Title

Fundamental studies of gas-to-particle conversion for nanoparticle synthesis in fames

Author

Dasappa, Shruthi

Publication Date

2021

UNIVERSITY OF CALIFORNIA SAN DIEGO

SAN DIEGO STATE UNIVERSITY

Fundamental studies of gas-to-particle conversion for nanoparticle synthesis in flames

A dissertation submitted in partial satisfaction of the
requirements for the degree Doctor of Philosophy

in

Engineering Sciences (Mechanical and Aerospace Engineering)

by

Shruthi Dasappa

Committee in charge:

San Diego State University

Professor Joaquin Camacho, Co-chair
Professor John Abraham

University of California San Diego

Professor Kalyanasundaram Seshadri, Co-chair
Professor Javier Garay
Professor Lynn Russell

2021

The Dissertation of Shruthi Dasappa is approved, and it is acceptable in quality and form for publication on microfilm and electronically:

Co-chair

Co-chair

University of California San Diego

San Diego State University

2021

DEDICATION

To my family, for the unconditional love and support

EPIGRAPH

Everything is energy and that's all there is to it.

Albert Einstein

It's nanotech. You like it?

IronMan, Avengers: Infinity War

TABLE OF CONTENTS

LIST OF FIGURES

LIST OF TABLES

LIST OF ABBREVIATIONS

CVD	Chemical Vapor Deposition
FSS	Flame Spray Synthesis
FSP	Flame Spray Pyrolysis
CNP	Carbon Nanoparticle
PSD	Particle Size Distribution
MMT	Methylcyclopentadienyl Manganese Tricarbonyl
PSDF	Particle Size Distribution Function
SMPS	Scanning Mobility Particle Sizer
XRD	X-Ray Diffraction
TEM	Transmission Electron Microscopy

LIST OF SYMBOLS

Symbols

x	Axial distance
r	Radial distance
u	Axial velocity
v	Radial velocity
a	Strain rate
L	Distance between burner nozzle and stagnation plate
$T_{stagnation}$	Temperature of stagnation plate
T_{nozzle}	Temperature of burner nozzle
T_f	Flame temperature
$T_{f,max}$	Peak flame temperature
t_p	Particle residence time/ particle age
$D_{orifice}$	Diameter of particle sampling orifice
DR	Dilution ratio
$D_{p,SMPS}$	Mobility particle diameter
D_p	True particle diameter
N	Number density of gas phase molecules
GS	Greyscale intensity
X_i	Mole fraction of species i
P_i	Partial pressure of species i
$G_{R,i}$	Gibbs free energy of reaction for $i = nano,\ bulk$
d	Particle diameter

S_i	Saturation ratio of reaction i
r^*	Kelvin radius
k_B	Boltzmann's constant
ν_{1i}	Molecular volume
K_{ii}	Coagulation coefficient

Greek Symbols

ϕ	Equivalence ratio
α	Dispersion exponent of carbon nanoparticle
ρ	Density
λ	Wavelength
γ	Surface energy

ACKNOWLEDGEMENTS

Going back to graduate school to pursue a PhD was a well-thought decision. As I am finishing, I am very lucky to have been provided the opportunity to make this wonderful journey happen. I have met very kind hearted and friendly people from whom I have learned a lot.

I would like to start by thanking Prof. Joaquin Camacho from San Diego State University for his guidance and support. He has not only taught me to be a better researcher but also a better person. His passion for research and eagerness to learn is captivating. His kindness and willingness to help is inspiring. I am grateful to have worked and learned from him.

I would like to thank Prof. Kalyanasundaram Seshadri, my advisor from University of California San Diego for following my progress and providing input on my work. His first principle's approach to teaching is specifically engaging. He has definitely taught me skills to be a well-rounded scientist.

I would also like to thank Prof. John Abraham from SDSU for all the guidance and support including introducing me to Prof. Camacho. Prof. Javier Garay introduced me to the world of material science and nanoparticles and this opened new doors for me. I am thankful to him for all the feedback. I am also thankful for feedback and discussions with Prof. Lynn Russell from UCSD. Special thanks to Dr. Joseph Libera at the Materials Engineering Research Facility at Argonne National Laboratory for providing me to opportunity to work with him. His methodical experimental techniques has taught me skills that I will use for a long time.

My time in San Diego has been a wonderful experience, mainly because of the kind hearted people I have met. They not only made my experience in the lab an enjoyable one but I have found life-long friendships in all of them. I am also lucky to have friends who have become like family. I thank them for all the support they have provided through this journey and for being people I can always count on.

I saved the best for the last in thanking my family for their endless love and for being my strongest influence my in life. They have been a pillar of support through all hardships. Their faith in me is a motivation to be a better person. The immense patience my family has shown in me has made this journey smoother. My family has taught me to believe that I can aim higher and reach farther and for this I will be always grateful to them.

Parts of Chapter 1 have been published in Fuel (Dasappa, S., Camacho, J., Evolution in size and structural order for incipient soot formed at flame temperatures greater than 2100 Kelvin : Materials and methods, 291, 120196), Fuel (Dasappa, S., Camacho, J., Fuel molecular structure effect on soot mobility size in premixed C6 hydrocarbon flames : Experimental methods, 300, 15, 120973), Energy and Fuels (Dasappa, S., Camacho, J., "Thermodynamic barrier to nucleation for manganese oxide nanoparticles synthesized by high-temperature gas-to-particle conversion: Computational methods and Experimental methods, 35, 2, 1874-1884) and CrystEngComm (Dasappa, S., Camacho, J., Formation of nanocrystalline manganese oxide in flames: oxide phase governed by classical nucleation and size dependent equilibria: Computational and Experimental , 22, 5509-5521). The dissertation author is the primary investigator for the publications.

The flame-formed carbon nanoparticle system description in Chapter 2, in part, has been published in Fuel (Dasappa, S., Camacho, J., Evolution in size and structural order for incipient soot formed at flame temperatures greater than 2100 Kelvin : Materials and methods, 291, 120196), Fuel (Dasappa, S., Camacho, J., Fuel molecular structure effect on soot mobility size in premixed C6 hydrocarbon flames : Experimental methods, 300, 15, 120973) and Data in Brief (Dasappa, S., Camacho, J., Raman spectroscopy, mobility size and radiative emissions data for soot formed at increasing temperature and equivalence ratio in flames hotter than conventional combustion applications : Experimental Design, Materials and Methods, 36, 107064). Parts of Chapter 2 regarding flame-formed manganese oxide synthesis has been published in Energy and Fuels (Dasappa, S., Camacho, J., "Thermodynamic barrier to nucleation for manganese oxide nanoparticles synthesized by high-temperature gas-to-particle conversion: Computational methods and Experimental methods, 35, 2, 1874-1884) and CrystEngComm (Dasappa, S., Camacho, J., Formation of nanocrystalline manganese oxide in flames: oxide phase governed by classical nucleation and size dependent equilibria: Computational and Experimental , 22, 5509-5521). The dissertation author is the primary investigator for the publications.

The flame-formed carbon nanoparticle studies in Chapter 3, in part, has been published in Fuel (Dasappa, S., Camacho, J., Evolution in size and structural order for incipient soot formed at flame temperatures greater than 2100 Kelvin : Materials and methods, 291, 120196), Fuel (Dasappa, S., Camacho, J., Fuel molecular structure effect on soot mobility size in premixed C6 hydrocarbon flames : Experimental methods, 300, 15, 120973) and Data in Brief (Dasappa, S., Camacho, J., Raman spectroscopy, mobility size and radiative emissions data for soot formed at increasing temperature and equivalence ratio in flames hotter than conventional combustion applications : Experimental Design, Materials and Methods, 36, 107064). The dissertation author is the primary investigator for the publications.

The flame-formed manganese oxide nanoparticle formation studies described in Chapter 4 has been published in CrystEngComm (Dasappa, S., Camacho, J., Formation of nanocrystalline manganese oxide in flames: oxide phase governed by classical nucleation and size dependent equilibria: Computational and Experimental , 22, 5509-5521). The dissertation author is the primary investigator for the publication.

The flame-formed manganese oxide nanoparticle formation studies described in Chapter 5 has been published in Energy and Fuels (Dasappa, S., Camacho, J., "Thermodynamic barrier to nucleation for manganese oxide nanoparticles synthesized by high-temperature gas-to-particle conversion: Computational methods and Experimental methods, 35, 2, 1874-1884). The dissertation author is the primary investigator for the publication.

The coal tar flame spray synthesis work presented in Chapter 6 has been submitted to

Applied Sciences for publication (Rodriguez-Fernandez, H., Dasappa, S., Dones Sabado, K., Camacho, J., “Production of carbon black in turbulent spray flames of coal tar distillates”, Applied Sciences, 11(21), 10001 (2021))

The work presented in Chapter 7 was done at the Materials Engineering Research Facility at Argonne National Laboratory with Dr. Joseph Libera. The dissertation author is the primary contributor for this work.

VITA

2012	Bachelor of Engineering in Mechanical Engineering, M S Ramaiah Institute of Technology, India
2014	Master of Science in Mechanical Engineering, Purdue University, USA
2014 - 2018	Senior Thermal and Fluid Science Engineer, Cummins Inc., Columbus, IN
2020 - 2021	IGE Technology Management Fellow, Rady School of Management, University of California San Diego
2021	Doctor of Philosophy in Engineering Sciences (Mechanical and Aerospace Engineering), University of California San Diego, San Diego State University, USA.

PUBLICATIONS

Rodriguez-Fernandez, H., **Dasappa, S.**, Dones Sabado, K., Camacho, J., “Production of carbon black in turbulent spray flames of coal tar distillates”, Applied Sciences, 11(21), 10001 (2021)

Dasappa, S., Camacho, J., “Ultrafine Particulate Matter in Methane-Air Premixed Flames With Oxygen Enrichment”, Front. Mech. Eng., 7, 739914 (2021)

Dasappa, S., Camacho, J., “Fuel molecular structure effect on soot mobility size in premixed C6 hydrocarbon flames”, Fuel, 300, 15, 120973 (2021)

Dasappa, S., Camacho, J., “Raman spectroscopy, mobility size and radiative emissions data for soot formed at increasing temperature and equivalence ratio in flames hotter than conventional combustion applications”, Data in brief, 36, 107064 (2021)

Dasappa, S., Camacho, J., “Thermodynamic barrier to nucleation for manganese oxide nanoparticles synthesized by high-temperature gas-to-particle conversion", Energy and Fuel, 35, 2, 1874-1884 (2021)

Dasappa, S., Camacho, J., "Evolution in size and structural order for incipient soot formed at flame temperatures greater than 2100 Kelvin", Fuel, 291, 120196 (2021)

Dasappa, S., Camacho, J., "Formation of nanocrystalline manganese oxide in flames: oxide phase governed by classical nucleation and size dependent equilibria", CrystEngComm, 22, 5509-5521 (2020)

Bonpua, J., Yagües, Y., Aleshin, A., **Dasappa, S.**, Camacho, J., "Flame temperature effect on sp^2 bonds on nascent carbon nanoparticles formed in premixed flames ($T_{f,max}$ >2100 K): A Raman spectroscopy and mobility sizing study", Proc. of the Combustion Institute, 37, 943-951, (2018)

FIELDS OF STUDY

Major Field: Mechanical Engineering

Studies in Combustion and Material Science

Prof. Joaquin Camacho and Prof. Kalyanasundaram Seshadri

ABSTRACT OF THE DISSERTATION

Fundamental studies of gas-to-particle conversion for nanoparticle synthesis in flames

by

Shruthi Dasappa

Doctor of Philosophy in Engineering Sciences (Mechanical and Aerospace Engineering)

University of California San Diego, 2021
San Diego State University, 2021

Professor Joaquin Camacho, Co-Chair
Professor Kalyanasundaram Seshadri, Co-Chair

The dissertation focuses on fundamental processes involved in the formation of carbon and manganese oxide nanoparticles by gas-to-particle conversion. A systematic approach through complementary experimental and modeling studies is implemented to study the evolution of flame formed particles and their dependence on flame conditions and growth environment.

Stretch stabilized stagnation flames are utilized to assess flame temperature and equivalence ratio effects for soot formed in higher-temperature regimes. This unique condition ($T_f > 2100\ K$) results in a new combination of "young", nucleation sized particles with a "mature" carbon structure. A significant transformation in carbon structure observed from the evolution in Raman spectra promises development of functional high-surface area sp^2 carbon materials.

Particle nucleation and growth of manganese oxide nanoparticles is examined in a complementary experimental and modeling study of high temperature premixed stagnation flames. Manganese oxide nanoparticles having varying oxidation states are observed depending on the flame conditions. Analysis of the formation of MnO indicates that a thermodynamic barrier limits nucleation.

Fundamental insights gained from simple laboratory flames inform particle formation in turbulent spray flames. The dissertation provides insight into flame spray synthesis (FSS), facilitating scaled, cost-effective, and versatile nanoparticle synthesis. FSS of carbon black is studied using coal tar distillate diluted in toluene as a carbon particle feedstock. Although the precursor is the same, this synthesis differs from conventional furnace black processes. Particles are formed directly in the flame rather than through downstream pyrolysis. Resulting carbon black particles are small but could potentially be tailored based on growth conditions.

A new diagnostic for determining chemical species information is introduced in collaboration with Argonne National Laboratory. Multi-probe optical emission spectroscopy is performed to analyze the axial evolution of manganese during FSS. "Optical Emission Spectroscopy Tool (OSAT)" is developed to enable data analysis, systematic feature recognition and axial species evolution. The axial evolution of Mn(I) through the flame provides fundamental insight such as the location of oxide formation.

This dissertation focusses on fundamental gas-to-particle conversion processes. Understanding the fundamental dependence of nanoparticles on the flame growth conditions is key towards engineering the size, structure, and morphology.

Part I

Background

Chapter 1

Introduction

The idea of nanotechnology appeared for the first time in the famous talk *"There is plenty of room at the bottom"* given by world renowned physicist Prof. Richard Feynman at the American Physical Society meeting on December 29, 1959. Prof. Feynman described the ability to manipulate individual atoms and molecules down to the needed scale using a top-down approach. Over time, nanotechnology has become a prominent field with bearings in medicine, electronics, energy storage and catalysis to name a few. Nanoparticles are the building blocks of nanotechnology, with properties and functionalities inherently different from their bulk counterparts. The performance and properties of nanomaterials depend on atomic structure, particle size, composition, defects etc. which are controlled by the thermodynamics and kinetics of the synthesis process [1].

Advances in nanomaterial synthesis for functional material emphasize a bottom-up approach of assembling from an atomic scale to a macroscopic scale. Chemical synthesis supports this approach through techniques in solid, liquid and gaseous phase. Solid phase synthesis involves grinding and mixing of solid precursors followed by high temperature heat treatment to facilitate diffusion controlled chemical reactions to form the final nanoscale product. This method, along with being labor intensive, can result in large grain sizes if not controlled. Nanomaterial synthesis in liquid or gas phase provides the flexibility of multi-component and multi-phase precursors with production at lower temperatures when compared to solid phase synthesis. Gas phase synthesis of nanomaterials produce better homogeneity and require relatively shorter production time with easy scalability when compared to liquid phase production. Compared to the wet chemistry approach, gas phase synthesis or aerosol synthesis has proven beneficial due to its high throughput with a continuous one step process, faster processing time, and simpler manufacturing and processing designs. Aerosol synthesis of nanomaterials is also considered to be environmentally cleaner when compared to wet chemistry [2].

1.1 Flame Synthesis

Flame aerosol synthesis is the most widely used gas phase technique. The technique dates back to ancient times as a pigment in cave paintings, Chinese ink in artwork and flame soot as a black pigment for India ink. Recent advances in flame synthesis for nanoparticle production have allowed its adaptability in the field of catalysis, dye-synthesized solar cells and biomedical devices. Further, titania as the white pigment in paints, silica in fiber optics applications, palladium and palladium oxide nanoparticles fuel ignition enhancer at lower temperatures, manganese oxide in energy storage materials and carbon nanoparticles in cathode catalysis are products of flame aerosol synthesis. Flame aerosol synthesis is a synergy of combustion science, aerosol technology and nanomaterial science [3, 4]. In this technique, liquid droplets and/or solid nanoparticles are dispersed in the flame. This synthesis technique can have two pathways depending on the nature of the precursor feeding conditions - vapor-fed and liquid-fed aerosol flame synthesis [5].

1.1.1 Vapor-Fed Aerosol Flame Synthesis

Vapor-fed aerosol flame synthesis is a classic gas-to-particle conversion process where particles are formed through the chemical reaction of gaseous precursors transforming the precursor vapor to product nanoparticles. The particle formation occurs via nucleation of low-vapor pressure species. This is followed by growth through competing mechanism of collision and coalescence among the nascent nanoparticles. This process produces nanoparticles with controlled crystallinity, ultra-fine diameter and narrow size distribution. While industrial flame aerosol reactors are employed for scalable and economical material synthesis, laboratory flame configurations are designed to study the fundamental thermodynamics and kinetics involved in the gas-to-particle conversion and particle growth mechanisms (Fig. 1.1) [6]. Premixed stagnation flames have been shown to be an effective flame configuration for fundamental process analysis [7, 8]. Detailed description of the flame configuration is provided in Chapter 2.

1.1.2 Liquid-Fed Aerosol Flame Synthesis

Liquid-fed aerosol synthesis utilizes economical and low-volatile precursors for easy handling, solubility of precursors in solvents and capability of using a mixture of precursors. In liquid-fed aerosol processes, the particle formation is a combination of gas to particle conversion and intra-particle reactions due to the spray processes as depicted in Fig. 1.1 [5]. If the liquid precursor solution drives the combustion process by dominating the energy contribution, then this liquid-fed aerosol flame synthesis is termed as flame spray pyrolysis (FSP). If the energy contribution of the liquid-fed precursor is not the primary source, then it is categorized as flame spray synthesis. Industrial nanoparticle synthesis of carbon black and metal oxides like Al_2O_3, TiO_2 and ZrO_2 adopts flame spray pyrolysis techniques [3]. The detailed description of the FSP configuration is provided in Chapter 2.

A systematic understanding of the underlying processes involved is key towards engineering functional nanomaterials. The interdependence of thermodynamics and kinetics of the flame and aerosols provide insight into the process controls. This study focuses on the flame synthesis of carbon and manganese oxide nanoparticles in the high temperature regime including the fundamental processes and the impact of its growth environment on the nanoparticle size, structure, composition and material properties. High temperature pre-

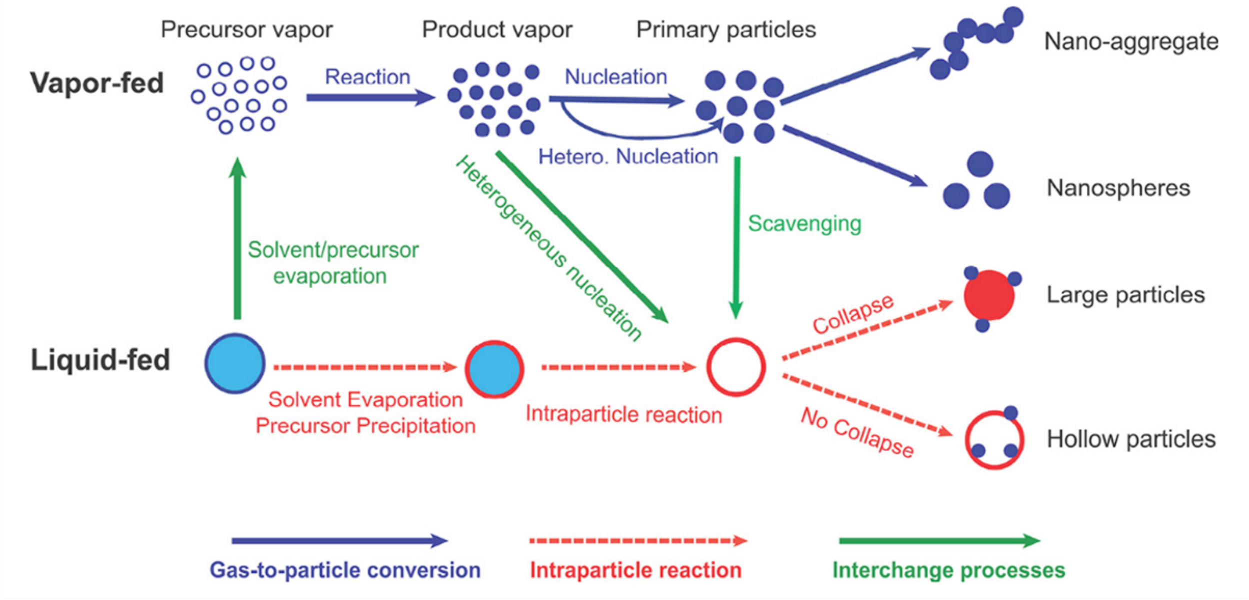

Figure 1.1: Particle formation processes during vapor-fed or liquid-fed flame synthesis through mechanisms [5]

mixed laminar stagnation flames are employed, and the underlying flame thermodynamics and kinetics are studied to provide a comprehensive understanding of the synthesis process to establish control parameters for engineering the nanoparticle size, structure, composition and properties. Carbon and manganese oxide nanoparticles are the focus due to their diverse uses. Carbon as a by-product of combustion, has a wide range of structures from disordered soot structures to ordered graphitic structures [4]. The work presented here concentrates on determining the dependance of the governing growth environment on the flame formed carbon. Manganese oxide's wide range of oxidation states and structural variety makes it key to establish the principal growth conditions and control factors. This study enables systematic observations evaluating nucleation, growth and equilibrium behavior in the flame formed manganese oxides formed. A complementary modeling and experimental approach adopted here enables determination of control parameters providing insight into nanomaterial engineering.

Flame spray synthesis is a scalable, cost-effective and versatile nanoparticle synthesis process. FSS's self-sustaining flame, usage of liquid fuels, requirement of less volatile precursors and proven scalability makes it heavily explored. Due to its high temperature flames and large temperature gradient capabilities FSS has been employed to synthesize a wide range of nanomaterials including oxides, salts and pure metals. Notable applications are in the area of catalysis, optics and photonics, health care, sensors, magnetic materials, fuel cells and composite materials. FSS is a convenient tool for synthesizing nanomaterials at large scales while tailoring materials properties. Carbon black and manganese oxide are synthesized using flame spray synthesis. A preliminary analysis of scalable flame spray techniques is also performed for carbon black and manganese oxide nanoparticle formation. Insights gained from fundamental studies using high temperature premixed stagnation flames are adopted towards determining growth environment control factors to engineer nanoparticles.

1.2 Flame-formed carbon nanoparticles (CNPs)

Soot formation is ubiquitous to hydrocarbon combustion, affecting engine performance, public health and the environment. The climate impacts of soot in the atmosphere is multifold. Soot contributes to air pollution via reactions with nitrogen dioxide, sulfur dioxide, and ozone .Soot particles cause warming of the Earth's atmosphere through absorption of radiation heating up the local atmosphere, changing the humidity and altering cloud formation processes [9]. Soot particles deposited on snow and ice absorbs radiation, hastening glacial melt. The health ramifications of soot particles can be as severe as cardiovascular and respiratory diseases including cancer [10]. Interestingly, flame-formed carbon also has a long history as a useful material. Soot was used in prehistoric cave paintings, soot provided the black pigment for India ink, and today, carbon black is used in automobile tires, as a pigment in laser printers, a cathode catalyst to name a few applications [11–13].

Over the last few decades, research has been focused towards establishing soot formation and flame-formed carbon analysis. Fig. 1.2 summarizes the soot formation and its evolution. Chemical initiation and fuel decomposition to form radicals like OH, O, H, CH and CH_2 act as starting points. In hydrocarbon-rich regions, these small radicals facilitate reactions that generate larger hydrocarbon radicals and polycyclic aromatic hydrocarbons (PAH). These PAH acts as precursors for soot formation through particle formation processes. The PAH precursors nucleate and grow to form incipient soot particles of diameters 1 - 6 nm. The incipient particles grow further through coalescence and surface addition to become larger particles with diameters of 10 - 50 nm. These primary particles undergo dehydrogenation, coagulation and surface growth to form graphitic aggregates [4, 14].

The great versatility of carbon makes it a highly researched material [11]. Most research in flame-formed carbon is focused towards the reduction of soot emissions, improvement of combustion efficiency, meeting regulations and reducing negative health effects [8, 15]. The study of flame-formed carbon as a functional nanomaterial is becoming more prominent [2, 5, 16]. Understanding of carbonization in flames is key towards engineering the structure of flame formed carbon. Soot is made of spherically shaped primary particles which aggregate together to form chain-like structures. The structure of the soot or flame formed carbon is dependent on its formation condition with impacts on its physical properties and chemical reactivity [17]. The growth environment factors like fuel structure, growth time/ particle age, temperature and gas-phase composition play vital roles in determining the nanostructure of the flame formed carbon. The soot formation is shown to be highly sensitive to competing processes, like nucleation, coagulation and gas-surface reactions, which are in turn functions of flame temperature and equivalence ratio [14]. Soot yield has been shown to decrease with increasing flame temperature. Particle size distribution studies show a continuous shift towards smaller particle size and less pronounced nucleation tail. The higher flame temperatures limits thermal decomposition of the chemical precursors, leading to limiting particle size growth. Soot formed in pyrolysis conditions showed amorphous structure at lower flame temperatures but with increasing temperature, a core-shell structure appeared [18, 19]. With fuel rich flames, soot yield has been shown to increase due to the increase in precursor concentration and the formation of PAHs with five membered rings. Soot structure and composition are dependent on the fuel structure. This is confirmed in

[20] where onion-like soot structures are observed in young soot formed in benzene flames, whereas soot in ethylene flames were seen to be more amorphous and disordered structure. Differences in growth mechanisms led to the formation of the onion-like structures in the benzene flame. This structure is found to be the result of two smaller particles combining into a single spherical particle after coalescing together and experiencing surface growth.

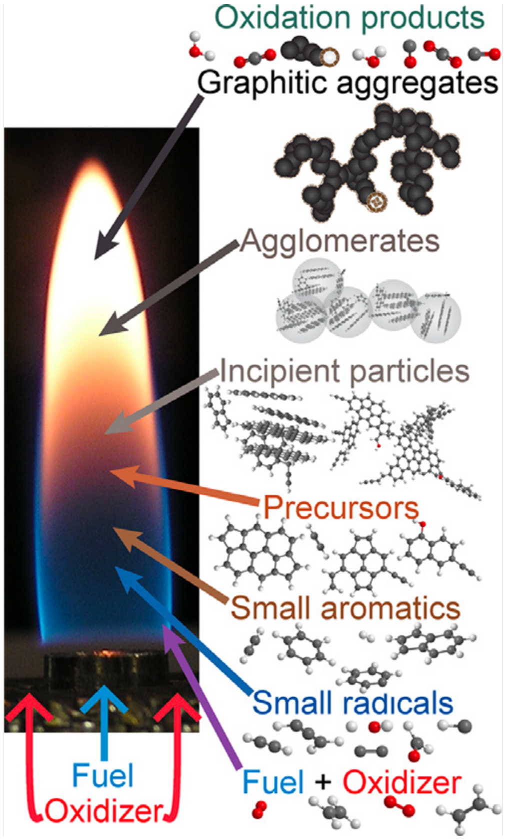

Figure 1.2: Schematic representation of soot formation and evolution in a flame [14]

Through decades of research, Raman spectroscopy has emerged as a remarkable and powerful tool for gaining chemical, structural and electronic information of CNPs [16, 21]. Analysis of flame formed carbon through Raman spectra has greatly contributed to the refinement of soot parameters such as the absorption cross-section [22], optical band gap [19, 23–25], graphitic crystallite size and structural defects [21, 26] . Investigations of soot formed in engines exist but more systematic observations in terms of fundamental formation and growth factors have been carried out in laboratory flames. The Raman spectra of flame-formed carbon has been analyzed in laminar premixed flames, co-flow diffusion flames, inverted diffusion flames and inverse flames. The carbon bonds are studied through Raman spectroscopy to elucidate the fine structural details. sp^2 bonded carbons have various degrees of graphitic ordering, ranging from microcrystalline graphite to glassy carbon. An amorphous carbon can have any mixture of sp^3 and sp^2. Raman spectroscopy for disordered carbon, like flame-formed CNPs, depends on the ordering of sp^2 sites and indirectly on the fraction of sp^3 cites [22, 27]. Commodo et al. [28] demonstrated in richer flames, the particles become more graphitic as the size of the graphitic planes increase. Miller et al. [29] used Raman spectroscopy to evaluate soot particulate structure and correlated the observed Raman spectra to particulate with modest-sized π conjugation lengths which are expected for clusters of PAH with individual masses between 500 and 1000 Da. Studying soot formation through Raman spectra at different wavelengths for diverse fuels in fuel rich laminar premixed flames showed the impact of hydrogenation on the extent of disorder and sp^2 aromatic character in the deposited soot [30, 31]. Details regarding Raman spectroscopy as a tool to study CNPs will be discussed in Chapter 3.

While there is extensive research directed towards understanding flame formed CNPs, a deficit observed is a systematic study aimed towards demonstrating the impact of the flame growth environment on the deposited CNPs specifically at high temperatures ($T_{\mathrm{f,max}} > 1900K$). A methodical approach establishing and understanding an evolution in flame formed carbon and manganese oxide nanoparticles in high temperature premixed stagnation flames is adopted here. Specifically, the flame conditions studied for CNPs correspond to the formation of incipient soot at the earliest growth stages. High-surface area carbon nanoparticles corresponding to freshly nucleated soot is expected, but the relatively high flame temperature may also induce carbonization only observed in so-called "mature" soot. The unique combination of "young", nucleation sized particles having relatively low defect density may be useful for applications of functional carbon black and hard carbon. Characterization of particle formation processes and material properties for flame-formed carbon shed light on the higher temperature regime and inform potential applications of the material produced. The study here involves a systematic isolation of the effects of equivalence ratio and flame temperature on flame formed carbon structure in the high temperature regime.

1.3 Manganese Oxide Nanoparticles

Manganese oxide nanomaterials and its derivatives have been of great interest in the field of energy storage, bioimaging, drug delivery, catalysis and waste water treatment for the last two decades due to its tunable structure, morphology, physical and chemical properties and cost effectiveness [1, 5, 32, 33]. Nanoscale MnO and MnO_2 have attracted attention due to their high energy capacities, environmentally benign and low-cost properties specifically as electrode materials in Lithium-ion batteries [34, 35]. Several novel and effective routes like hydrothermal synthesis, sol-gel synthesis and wet chemical route have been researched to prepare manganese oxide nanomaterials with various shapes and properties [34, 35]. Flame synthesis is a continuous, inexpensive process with high throughput making it a viable solution for manganese oxide nanoparticle production. Flame made manganese oxide nanoparticles have mostly been prepared through flame spray pyrolysis. As in any flame synthesis process, the growth environment plays a vital role in determining the oxidation state of the flame formed particles resulting in Mn_3O_4, Mn_2O_3, MnO_2 or MnO [5]. The particle size, structure and composition also depend on the gas-phase environment in which they were formed.

Synthesis of metal oxides have been previously studied using premixed flames to provide insight into competing processes and applied to design more complex, yet scaled up, processes such as flame spray synthesis. Formation of manganese oxide nanoparticles through flame synthesis is less explored than titanium oxide and iron oxide. A flame stabilized on a rotating surface was previously used to produce manganese oxide nanoparticles and selective oxidation was observed with oxidation states of Mn_3O_4, Mn_2O_3, MnO_2 or MnO based on precursor concentration and flame growth conditions [36]. This is contrary to flame formed titanium oxide and iron oxide studies where a range of crystal phases have been reported with full oxidation state of TiO_2 and Fe_2O_3 unlike that for manganese oxide [37–39]. This range of phases has been explained on the basis of shifts to bulk phase equilibrium driven by the surface energy of nanoparticles. Kraft et al. [40] showed an exception where TiO_2 - II in flame stabilized on a rotating surface studies at fuel rich conditions. This result of manganese oxide having multiple oxidation states when compared to other flame formed metal oxides gives rise to the need for systematic study of competing processes to understand and leverage the wide range of possible manganese oxide products.

Premixed stagnation flames are employed to provide a one-dimensional system for synthesis and growth processes for a range of well-characterized time-temperature-oxygen conditions. The size-dependent phase diagram is the basis to assess the degree to which phase equilibrium is established among the nano-crystalline manganese oxides formed. In addition, the wide range of physical properties of the manganese oxides calls into question the validity of the coagulation limited nucleation mechanism adopted for flame synthesis of TiO_2 nanoparticles. These considerations are also examined by systematic observation of manganese oxide formed in a flame with a well-characterized temperature - oxygen- time history. Manganese oxide's wide range of oxidation states and structural variety makes it key to establish the principal growth conditions and control factors. This study enables systematic observations evaluating nucleation, growth and equilibrium behavior in the flame formed manganese oxides. A complementary modeling and experimental approach adopted here enables determination of control parameters providing insight into nanomaterial engineering.

1.4 Dissertation Organization

The work presented here is aimed at studying the fundamentals involved in the flame synthesis of carbon and manganese oxide nanoparticles. The systematic study is aimed towards understanding the fundamentals involved in the flame synthesis process to engineer

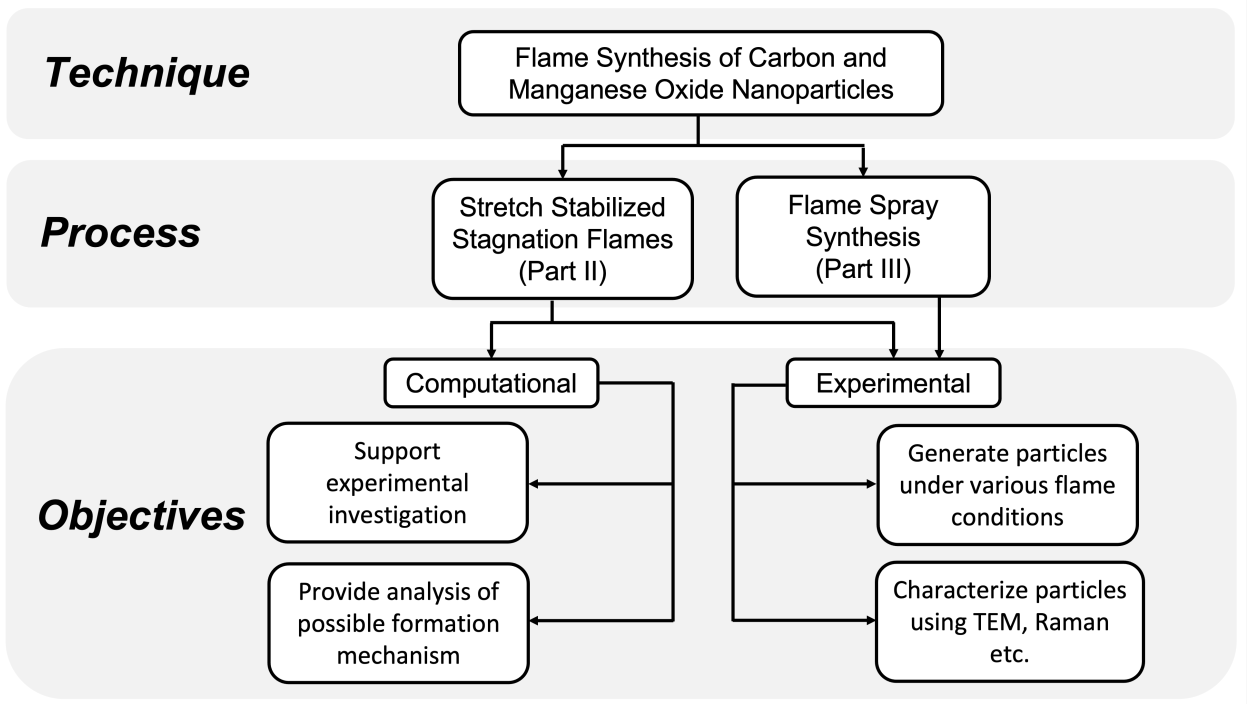

Figure 1.3: Flowchart regarding the overall objective and approach of the dissertation

nanoparticles with defined size, structure and morphology. Fig. 1.3 is a flowchart depicting the overall objective and approach of this dissertation. The approach involves detailed experimental and computational methodologies to analyze the flame structure, flame formed particle, size, structure and composition.

The dissertation is divided into three sections - Part I, Part II and Part III. Part I consists of the Background of this dissertation including Chapter 1 and 2. The experimental designs, computational techniques and characterization methods are introduced in Chapter 2.

Part II, consisting of Chapters 3, 4 and 5, discusses the synthesis of carbon and manganese oxide nanoparticles using stretch stabilized stagnation flames. Chapter 3 discusses the studies involving flame formed CNPs. The evolution in size and structural order for incipient soot formed at flame temperatures greater than 2100 K is discussed. Chapter 4 delves into the systematic observation of manganese oxide formed in stretch stabilized stagnation flames with a well-characterized temperature - oxygen - time history. A complementary experimental and modeling study is investigated for the nucleation of manganese oxide nanoparticles in premixed stagnation flames is carried out in Chapter 5.

Part III, consisting of Chapters 6 and 7, examines the synthesis of carbon and manganese oxide nanoparticles using flame spray synthesis. Chapter 6 studies the production of carbon black in spray flames of coal tar distillates. Chapter 7 conducts an optical emission spectroscopy analysis of manganese oxide nanoparticles in spray flames.

Parts of Chapter 1 have been published in Fuel (Dasappa, S., Camacho, J., Evolution in size and structural order for incipient soot formed at flame temperatures greater than 2100 Kelvin : Materials and methods, 291, 120196), Fuel (Dasappa, S., Camacho, J., Fuel molecular structure effect on soot mobility size in premixed C6 hydrocarbon flames : Experimental methods, 300, 15, 120973), Energy and Fuels (Dasappa, S., Camacho, J., "Thermodynamic barrier to nucleation for manganese oxide nanoparticles synthesized by high-temperature gas-to-particle conversion: Computational methods and Experimental methods, 35, 2, 1874-1884) and CrystEngComm (Dasappa, S., Camacho, J., Formation of nanocrystalline manganese oxide in flames: oxide phase governed by classical nucleation and size dependent equilibria: Computational and Experimental , 22, 5509-5521). The dissertation author is the primary investigator for the publications.

Chapter 2

Experimental and Computational Methods

The fundamental processes involved in the gas-to-particle conversion for nanoparticle synthesis are investigated in this dissertation. This chapter discusses the experimental and computational methods implemented. Several experimental techniques are designed during this work. In addition, commercially available instruments are utilized for characterization of nanoparticle size, structure and composition. Novel computational methods are developed to establish the flame structure, perform thermodynamic analysis and connect experimental observations to fundamental chemical kinetic processes.

2.1 Stretch Stabilized Stagnation Flames

Typical laboratory flames are designed to ease the analysis of elementary process like chemical kinetics, fluid mechanics and particle formation in the flames. Stationary premixed planar flames in stagnation flow (alternatively known as premixed stretch stabilized stagnation flames) are commonly used as an effective flame configuration for investigating fundamental particle formation processes. A photographic representation of the stretch stabilized stagnation flame is illustrated in Fig. 2.1. It has a simple, pseudo one-dimensional axisymmetric flow field. This along with its stabilization mechanism makes it a well-established flame structure [41]. Premixed flames in a stagnation flow are stabilized by flow stretch rather than by heat loss unlike the burner-stabilized flames. For this reason, the maximum flame temperatures in these flames approach the adiabatic flame temperatures. In many cases, they also exceed the adiabatic flame temperature due to the Lewis number effects [8]. These flames are stabilized in a laminar stagnation flow with a steady position given by the balance between the decelerating convective velocity and the opposing flame speed. The pseudo one-dimensional nature and the large temperature gradient between the flat flame and cold stagnation surface produces a thermophoretic force on the growing particles in the flame forcing them to be deposited on the cold stagnation surface [7]. The residence time of the particles from nucleation and growth to surface deposition is off the order of milliseconds and hence prevents it from reaching large sizes and resulting in particles have a narrow size distribution [7, 42, 43]. This well-established flame structure allows for systematic study through computations and experiments.

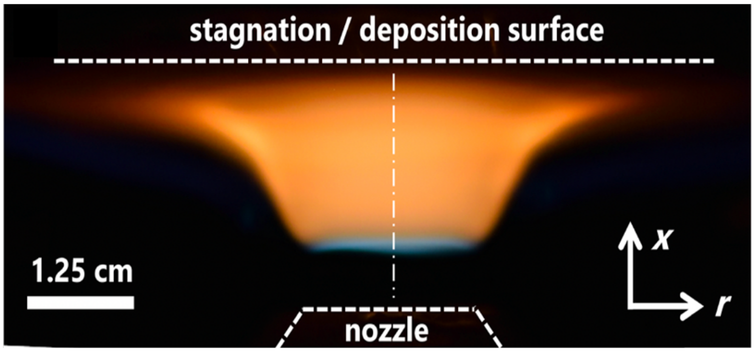

Figure 2.1: Photographic representation of the stretch stabilized stagnation flame.

2.1.1 Experimental Setup

The experimental setup, illustrated in Fig. 2.2, includes an aerodynamically shaped nozzle and a stagnation/deposition surface.The aerodynamic shape of the burner nozzle is designed to achieve plug flow at the burner exit. The gas flow rates of the fuel, oxygen, argon and nitrogen are controlled by critical orifices. The critical orifices are calibrated by measuring the flow rate of gas flowing into the orifice by bubble-flow meter (mini-Buck M-1). The flow stagnation is induced by a solid aluminum plate. The stagnation surface also acts as a deposition surface for flame formed particles. Aluminum is used as the stagnation/ deposition surface because of its high thermal conductivity property. The deposition efficiency is seen to approach zero as the hottest flames heat the deposition surface excessively causing loss in thermophoresis and particle attraction. This is resolved using an ice bath in a thin-walled stainless steel vessel placed over the deposition surface. This ensures deposition of the flame formed particles and a steady boundary condition at the stagnation surface for modeling purposes. The temperature of the deposition surface is monitored by a thin wire (0.125 micron) type K thermocouple placed on the non-deposition side of the aluminum plate and under the ice bath.The deposition surface temperature ($T_{stagnation}$) is maintained at $430 \pm 20K$ for all flame conditions. The temperature of the burner nozzle is measured using a K type thermocouple and is maintained at $T_{nozzle} = 330 \pm 20K$. The distance between the burner nozzle and the stagnation plate (L) is varied based on the experimental requirements of the study. The standing distance between the flame and the stagnation plate, L_s, may be varied by changing the unburned gas flow rate to manipulate the balance between the flow velocity and laminar speed. A concentric shroud of nitrogen shrouds the flame to reduce perturbations from the surrounding environment. The burner setup employed for flame formed carbon nanoparticle study (Fig. 2.2). The nozzle diameter, $D_{nozzle} = 1.43\,cm$, and the nozzle to stagnation distance is $L = 2.54\,cm$ for all flames studied but each flame has a different standoff distance designed for comparable particle time across all flames.

Flame synthesis of manganese oxide nanoparticles is carried out in premixed stagnation flames with subsequent deposition onto a stationary surface similar to the Fig. 2.2 with specific changes to the burner setup to include a precursor feed system. A diagram of the modified burner setup is shown in Fig. 2.3. Manganese oxide nanoparticles are formed in the flame and deposited onto a stationary deposition surface. The precursor, methylcyclopentadienyl manganese tricarbonyl (MMT, Sigma- Aldrich), in its liquid state, into the heated

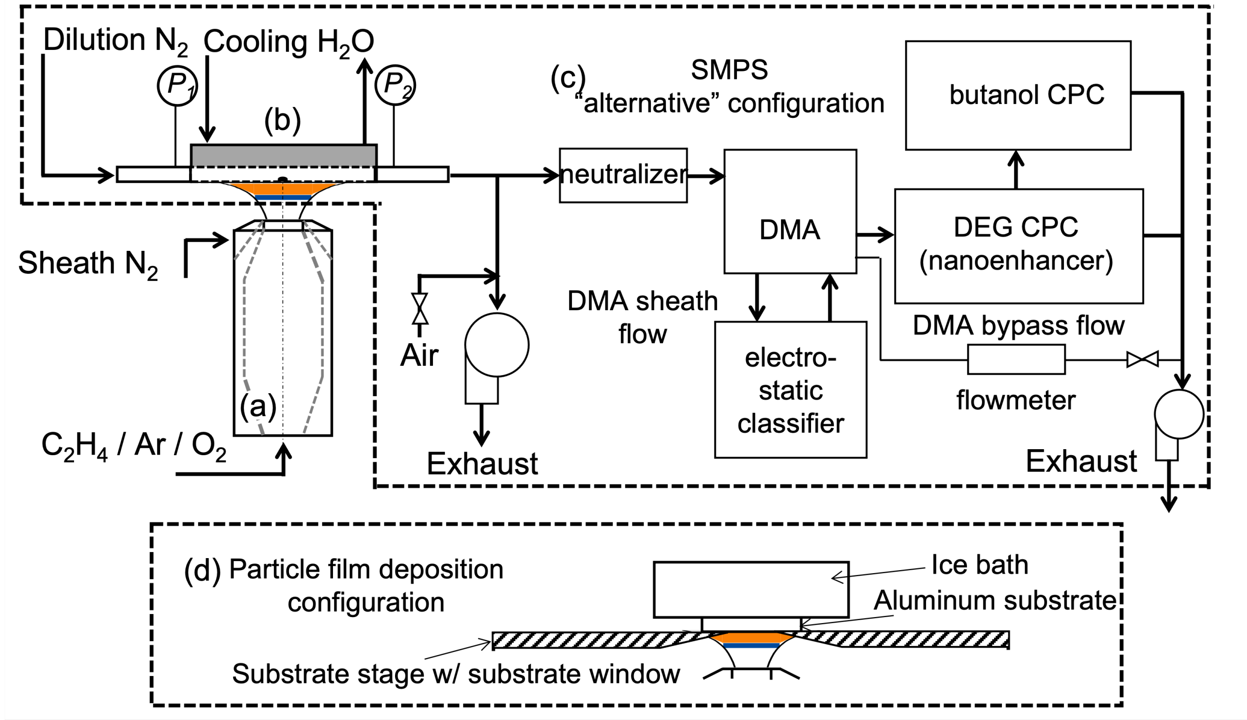

Figure 2.2: Experimental setup including the aerodynamic burner nozzle (a) a stagnation surface/sampling probe assembly (b) an SMPS in the "compact"configuration defined by the vendor (c), and the setup for collecting flame formed carbon deposits for off-line analysis (d)

fuel line by gas-assisted nebulizer (Precision 500-75P, 10 micron droplet rating) driven by 1 lpm argon flow. This is mixed with the unburned gas mixture and vaporized before leaving the fuel line. The liquid flow is precisely regulated by syringe pump, but the uncertainty of the doping concentration is ±10% based on measurable liquid volume draining from the spray chamber walls after experiments. The spray and the unburned gases are kept at 390 K to accelerate vaporization and prevent condensation at cold spots. The 2s residence time in the fuel line provides ample time for mixing and vaporization. The aluminum nozzle has a nozzle diameter $D_{nozzle} = 1cm$ and the wall thickness is 0.2 cm at the nozzle exit. Manganese oxide products are deposited from the flame onto a stationary aluminum substrate with the nozzle-to-stagnation separation kept at $L = 2.54\,cm$ for all experiments. In the flame, the precursor (gas-phase MMT) decomposes, burns and the oxide product nucleates to form an aerosol.

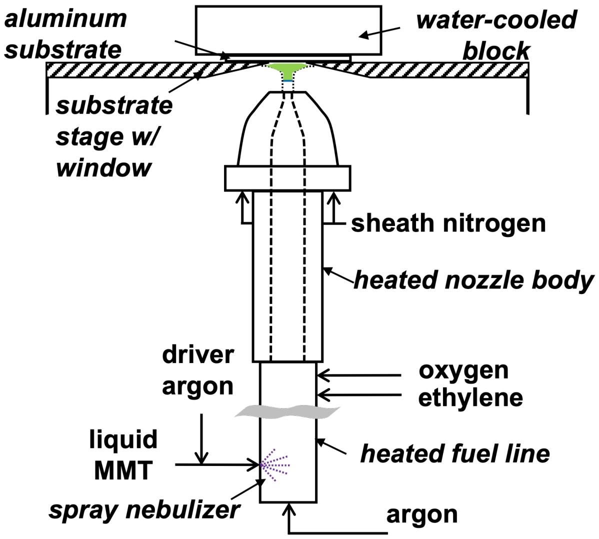

Figure 2.3: Experimental setup for manganese oxide flame-assisted deposition process

2.1.2 Computational methods

Flame structure computations are carried out using both a pseudo one-dimensional formulation and solution to the two dimensional axisymmetric flow field. The pseudo one dimensional flame structure computations are carried out using Fortran based OPPDIF [44] modified to include CO_2 and H_2O radiation. OPPDIF adopts a similarity transformation to reduce the two dimensional axisymmetric flow field to a one dimensional field developed by von Karman [41]. The radial component of the velocity is assumed to be linear in terms of r allowing for the dependent terms to be functions of the axial direction only and is defined as (Eq. 2.1):

$$\begin{aligned} & G(x) = -\frac{\rho v}{r} \qquad \textit{and} \qquad F(x) = \frac{\rho u}{2} \\ \textit{continuity equation:} \qquad & G(x) = \frac{dF(x)}{dx} \end{aligned} \tag{2.1}$$

where ρ is the mass density and u and v are the axial and radial convective velocities.

OPPDIF computations aid in the design of flame series experiments and are used to gain insight into the particle growth conditions in the flame by solving for the flame temperature, species mole fractions and axial and radial velocity components. A uniform plug flow (zero radial velocity) with a mass flux of $\dot{m}_o$ is assumed at the burner nozzle, $x = 0$, given by the cold flow velocity, reactant composition and burner nozzle temperature, T_{nozzle}. Diffusion of species is allowed into the nozzle boundary. The OPPDIF code is modified to accommodate the stretch stabilized stagnation flame by introducing a stagnation surface at $x = L$ in the form of a no slip boundary condition [37, 42]. The surface has a measured temperature $T = T_{stagnation}$. The axial, radial and diffusive velocities are zero at the stagnation surface and the zero diffusive velocity for each gas-phase species is the result of counteracting Fickian and thermal diffusion processes. The boundary conditions at the burner nozzle and the stagnation surface are expressed as (Eq. 2.2)

$$\begin{aligned}
&\text{Burner nozzle } (x = 0): \quad && F = \rho_o u_o/2 = \dot{m}_o/2 \qquad G = -\rho v/r = 0 \\
& && T = T_{nozzle} \qquad \rho Y_k \left(u + V_k\right) = \dot{m}_0 Y_{k,0} \\
&\text{Stagnation surface } (x = L): \quad && u = v = V_k = 0 \\
& && F = G = 0 \qquad T = T_{stagnation}
\end{aligned} \tag{2.2}$$

V_k is the axial diffusion velocity of species k.

The numerical simulations used windward differencing, the multicomponent transport formulation and thermal diffusion. Thermodynamic and transport properties are considered within the Sandia CHEMKIN [45] framework for the reacting flow problems. USC Mech II is used primary reaction chemistry model, consisting of 111 species and 784 reactions, to determine the flame structure in the absence of soot [46]. Separate reaction chemistry models are adopted for soot precursor assessment studied. Computations for sooting flames using the KAUST PAH Mechanism 2 (KM2) [47], Appel, Frenklach, Bockhorn (ABF) [48] and Blanquart, Pepiot, Pitsch (BPP) [15] mechanisms are performed to provide a comparison of PAH predictions among the three models for the flames of interest. The KM2 mechanism is a gasoline surrogate mechanism built from USC Mech II foundational chemistry. ABF is a classic mechanism for PAH chemistry based on GRI-Mech 3.0 foundational chemistry. The BPP mechanism is developed for engine relevant fuels with GRI-Mech 3.0 foundational chemistry incorporating several updates beyond the original GRI-Mech 3.0. The computed PAH profiles are intended to provide insight into agreement among models that are extrapolated to higher temperature.

The OPPDIF computed flame structure profile is used to provide insight into the particle residence/ growth time, t_p. The particle growth time is defined as the time for a Lagrangian particle to travel from the location of the flame zone ($T = T_{f,max}$) to the stagnation surface location. This is determined by establishing the thermophoretic velocity of the particle. The particles are assumed to flow at the gas convective velocity until the thermophoretic force induces additional drift towards the stagnation surface. Thermophoresis is the result of the significant temperature gradient between the flame and the stagnation surface. In this work, the thermophoretic velocity is assumed to be in the free molecular regime [49] and is given by Eq. 2.3

$$V_T = \frac{\lambda \, \partial T/\partial x}{5\left(1 + \frac{\pi\varphi}{8}\right) NkT} \tag{2.3}$$

λ is the thermal conductivity of the gas-phase. Momentum accommodation factor, $\varphi = 0.9$ based on Millikan's oil droplet experiments, N is the number density of the gas phase molecules, k, the Boltzmann constant and T, the local flame temperature. The thermophoretic velocity is calculated numerically and added to the total velocity. This is used to determine the particle residence time.

The two-dimensional axisymmetric computations are carried out to establish the accuracy of the pseudo 1D assumption and analyze the effect of the particle sampling probe on the flame flow field. These comutations are carried out in ANSYS Workbench (v.19.2) incorporating Fluent and CHEMKIN. USC Mech II chemistry model is imported for kinetics, thermal and transport mechanism. The governing equations for continuity, momentum, energy and species conservation are solved in the axial and radial directions using CHEMKIN - CFD invoked through Fluent. The 2D axisymmetric domain is defined along the axis of the burner nozzle and the width and height of the domain are 7.0 and 2.54 cm, respectively, for

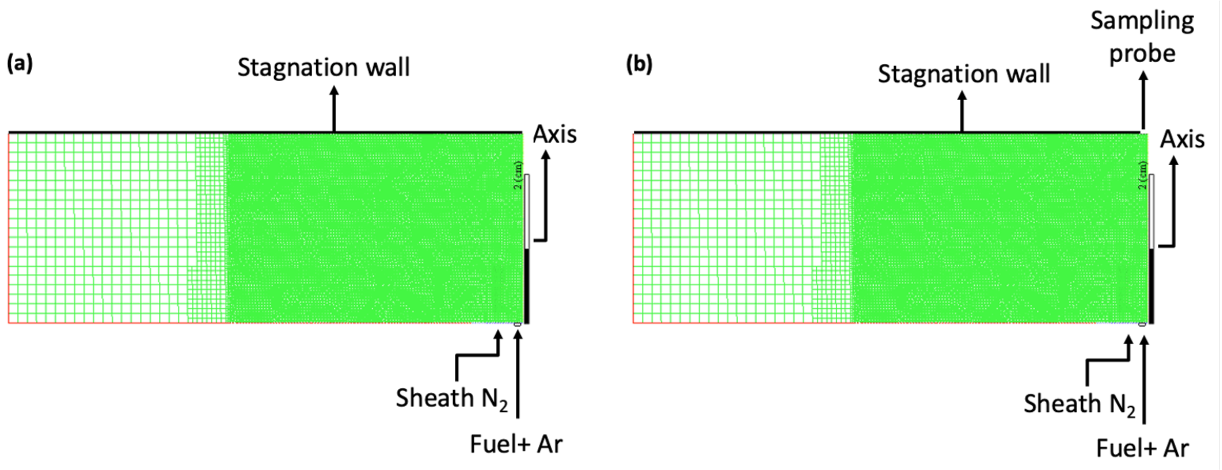

Figure 2.4: 2D ANSYS mesh setup (a) - without sampling probe (b) - with sampling probe

all flames. The domain is a simple projection of flame configuration without consideration of confinement or entrainment effects. The nozzle inlet, a boundary of the domain, is modeled as a slit normal to the centerline (Fig.2.4 (a)). The N_2 sheath flow channel is an opening adjacent to the nozzle opening. The computational mesh is 40800 cells mostly concentrated within 4 cm of the axis (99 %).The side faces of the domain are pressure outlets; the stagnation surface face is specified as a wall boundary. The nozzle and sheath openings are set as velocity inlets. The Fluent viscosity model is set to laminar and the CHEMKIN USC Mech II mechanism is uploaded into the species transport module. Radiation is not considered. Thermal diffusion and multicomponent transport are accounted for in the computations. An initial guess is provided to initiate the numerical modeling based on the 1D OPPDIF solution for temperature and flame position. During initialization, the temperature, O, H and OH concentrations are applied to a thin region on the mesh where OPPDIF predicts the flame position to be.

Aerosol probe sampling is carried out to analyze the in-situ particle size distribution of flame formed particles by mobility sizing. Experimental and modeling investigation of perturbations to the flame synthesis process due to probe sampling have indicated that precise characterization of process parameters and material properties requires consideration of probe effects. The premixed stagnation flames studied are probed by embedding a sampling orifice flush with the flat stagnation surface (Fig. 2.5). This design enables probe sampling with more clearly defined effects on the flame structure caused by flow stagnation and suction. For sampling perturbation studies, the two-dimensional computations include the sampling probe as an orifice at the centerline of an otherwise flat stagnation surface. This is modeled as a slit at the stagnation plate boundary centered on the axis of the two dimensional axisymmetric domain (Fig. 2.4). The flow velocity measured during dilution ratio calibration is set as a boundary condition at this face to assess the perturbation of aerosol sampling to the flame structure and growth time. For manganese oxide studies, computations of the flame structure are carried out without precursor chemistry or oxide particle formation processes.

2.2 Flame Spray Synthesis

Vapor fed flame reactors are limited due to the insufficient availability and complex handling of suitable gaseous precursors. FSS is convenient due to its simple precursor preparation technique. Combustible liquid precursor - solvent mixtures are available in a wide variety of elements with varying compositions making it convenient. This solution is delivered through a two fluid nozzle with oxygen, nitrogen or sometimes air is employed as the dispersion gas. The precursor solution is atomized and dispersed into fine droplets with mass median diameters of several micrometers. The sprayed droplets of a precursor/fuel mixture are ignited by surrounding flamelets, which serve as pilot flames for stabilizing combustion. The pilot flame enables spray ignition, droplet evaporation and precursor conversion. A sheath gas is used to cool the burner and quench particle growth. A photographic representation of the flame spray synthesis process is illustrated in Fig. 2.5.

The flame parameters like temperature, growth time, the liquid and gaseous thermophysicochemical properties determine the particle formation and growth mechanism. The precursor/solvent droplets in FSS can display disruptive combustion behavior unlike pure solvent drops which burn uniformly and quasi-steady. The mechanism of disruptive droplet

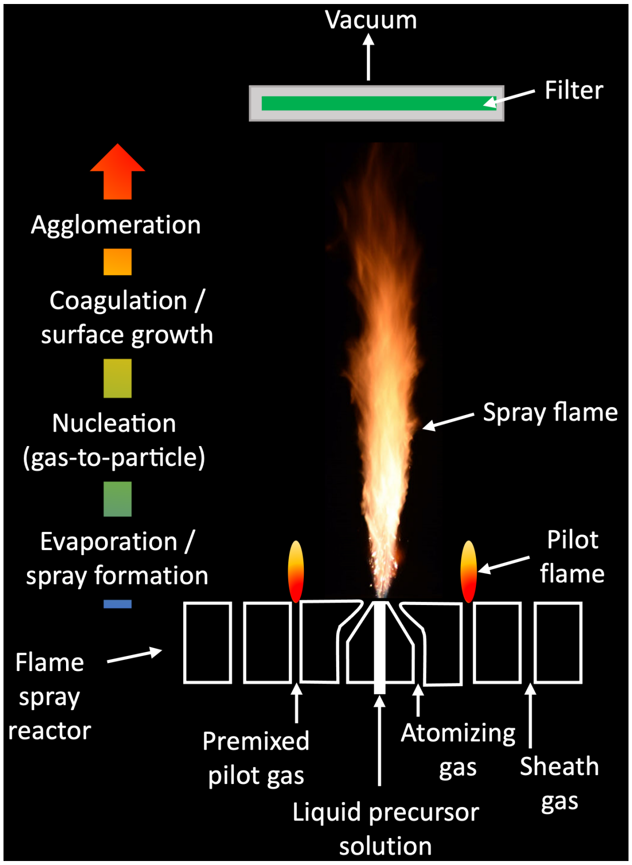

Figure 2.5: Photographic representation of the flame spray flame.

burning is similar to that of slurry droplets, consisting of three main steps: diffusion-controlled burning of the high-volatile solvent, viscous-shell formation due to decomposition of the low-volatile precursor, and subsequent disruption due to heterogeneous nucleation [5]. It is shown that the concentration and decomposition characteristics of the precursor are of significance in determining the time sequence of these three steps. Two possible particle formation mechanisms are "gas-to-particle" conversion where the particle nucleation and growth occur after precursor evaporation and "droplet-to particle" conversion which occurs inside the liquid droplet. These complexities make vapor-fed flames more suitable for experimental and theoretical studies than the FSS process because FSS includes droplet formation and precursor release constitute additional challenges in understanding the fundamental mechanisms for engineering the nanoparticle characteristics [50].

Flame spray synthesis is used to synthesize carbon black and manganese oxide. Two slightly different designs are used for this. The standardized SpraySyn burner is used to synthesize carbon black. Manganese oxide is made using a flame spray pyrolysis setup at the Materials Engineering Research Facility at Argonne National Laboratory. The FSP setup is similar to that of Mädler et al [50, 51]. Details regarding both the setups and the study are provided in 6 and 7 respectively.

2.3 Particle Characterization

Analysis of flame formed nanoparticles is key towards providing insights into the synthesis process, growth mechanism and nanoparticle properties. Scanning mobility particle sizing is employed to determine particle size. Raman spectroscopy, X-ray diffraction and transmission electron microscopy are adopted to study the composition and properties of the flame formed nanoparticles. Color-ratio pyrometry is a technique to measure the flame temperature and soot dispersion index. Further details regarding each of these characterization techniques are provided in this section.

2.3.1 Scanning Mobility Particle Sizing

Mobility particle sizing for the soot particle size distribution (PSDF) measurement is carried out by aerosol sampling at the stagnation surface. An effective technique established for sampling soot from flames under well-characterized boundary conditions is applied here to investigate nucleation of flame formed nanoparticles nanoparticles [7, 42, 43, 52]. Extensive studies on the evolution of nascent soot PSDF exist in terms of flame temperature [53–55], fuel structure[42, 43, 56–60], sooting level or equivalence ratio [55, 61] and age [28, 60] but systematic measurements of PSDFs from relatively high-temperature ($T_{f,max} > 2100K$) flames have been recently been achieved with the introduction of probed premixed flat flames [7]. Embedding a probe at the stagnation surface enables probe sampling and sample deposition with boundary conditions more precisely defined than other probe and deposition geometries [52]. The schematic of the burner system along with the sizing system is shown in Fig. 2.2 (b). An 8 cm diameter by 1.3 cm thick aluminum disk acts as the flow stagnation surface with a 0.635 cm stainless steel tubular sampling probe embedded into the disk. The tube wall is embedded flush with the stagnation surface and parallel to the flat flame. The flame sample was drawn into the probe through a laser-drilled micro-orifice. The orifice is positioned on the center axis of the burner facing the incoming flame gas. The aerosol sampling system for manganese oxide burner system has a laser-drilled micro-orifice, $D_{orifice} = 800\mu m$ and for the micro-orifice diameter carbon nanoparticle burner system is $D_{orifice} = 130\mu m$. Particle deposits accumulate in the orifice over time and should be regularly cleaned for reproducible results. Established aerosol sampling techniques are applied here to minimize loss of the smallest particles due to diffusion and artificial probe-induced coagulation [52, 55].

A TSI 1 nm Scanning Mobility Particle Sizer (SMPS) (TSI 3838E77) is used for particle sizing by differential mobility analysis. This system is composed of a dual voltage classifier (TSI 308,202), a Kr-85 bi-polar diffusion charger (Neutralizer TSI 3077A), 1 nm differential mobility analyzer (DMA) (TSI 3086), a diethylene glycol-based (DEG) condensation particle counter (CPC) (so-called Nanoenhancer, TSI 3777) and a butanol- based CPC (TSI 3772). TSI Aerosol Instrument Manager Software (version 10.2) is used to collect and export the PSDFs. As the aerosol sample is sucked into the sampling probe and into the SMPS, the neutralizer creates a well-characterized charge distribution on the particles. The DMA analyzes the charged particles for particle size. The trajectory of the particles is controlled within the known DMA geometry by applying an electric field. A monodisperse aerosol flow is created through a well designed DMA geometry such that the particle trajectory leads to a particle collection flow. Mobility sizing of particles in the DMA can classify particles approaching 1 nm but counting particles in this size range has required faraday cup electrometers or DEG-based CPCs [60, 62, 63].The DEG-based CPC facilitates counting of particles with mobility diameters as small as 1.4 nm.

The SMPS is in the "compact" configuration as suggested by TSI to minimize diffusion losses before the CPCs. The flame gas flow into the neutralizer is 5 SLPM of which 2.5 SLPM flows into the DMA, the balance of which bypasses to exhaust. The nitrogen sheath flow through the DMA (25 SLPM) is controlled in the electrostatic classifier housing and this gives a 10:1 sheath to aerosol flow concentration. The DMA polarity is set to positive. An insert supplied by the vendor is mounted onto the inlet of the neutralizer to minimize flow recirculation for more predictable attainment of the equilibrium charge distribution. A new diffusion correction is applied to the measured PSDF based on TSI's measurement of the penetration factor of ultra-fine particles through the system flow path. To ensure that the particle loss is negligible in the sampling line, a dilution procedure is employed. A wide range of dilution probe techniques were previously reported to investigate flame synthesis processes and material properties starting from the straight-tube design of Ulrich [12]. Kasper applied aerosol sampling using a quartz probe to investigate TiO_2 flame synthesis processes and other designs such as water-cooled and multistage dilution quartz sampling probes have since been employed for a variety of flame studies [39, 64–68]. For low sample dilution, the relatively high number density undergoes rapid coagulation across the sampling orifice causing artificial drop in the number density and increase in median diameter. Similarly, for high dilution, the relatively long residence time across the orifice allows significant diffusion loss of small particles to the wall. At an optimum range of dilution ratio, the dilution corrected number density and median diameter are insensitive to the applied dilution minimizing the sampling artifacts. Calibration of the aerosol sampling probe dilution is carried out by measuring the flow rate of air flowing into the probe orifice by bubble-flow meter (mini-Buck M-1). The dilution ratio is determined empirically by calibrating the flow through the orifice as a function of pressure drop (ΔP) across the orifice given by Eq. 2.4 [42]

$$log\, DR = a + \frac{b}{log\,(c\;\Delta P)} \tag{2.4}$$

where $a = 1.61$, $b = 0.1$ and $c = 0.04\,(mm\,H_2O)^{-1}$ for manganese oxide nanoparticle system.

$a = 1.89$, $b = 0.28$ and $c = 0.0233\ (mm\ H_2O)^{-1}$ are the probe parameters for the carbon nanoparticle burner system [52]. The pressure drop in Eq. 2.4 is the average pressure drop determined by monometers placed at the inlet and outlet of sampling probe tube. The details of the dilution ratio study is presented in the subsequent chapters. The measured mobility diameters are the average of 8 –10 separate scans (30 s scan of DMA voltages for 1 –20 nm mobility diameter) with error bars representing typical deviation across runs.

For soot, the SMPS mobility diameter is corrected to yield the real diameter on the basis of nanoparticle transport theory. The correlation between the SMPS measured mobility diameter $D_{p,SMPS}$ and true diameter D_p of a particle is given by Eq. 2.5. The data as obtained by the SMPS along with a log-normal curve and the curve fitting parameters are studied to provide insight into the competing soot formation processes in terms of global properties of the size distribution [52].

$$\frac{D_p}{D_{p,SMPS}} = \tanh\left(1.4334 + 0.01248 D_{p,SMPS}\right)\left(1.0676 - \frac{0.4463}{D_{p,SMPS}}\right) \tag{2.5}$$

2.3.2 Raman Spectroscopy

Raman spectra of soot and related carbon materials can be used to elucidate fine structural details [16]. Raman spectroscopy is carried out off-line for flame formed particles collected from each flame. A stagnation surface, shown in Fig. 2.2 (d), is designed to serve as a stage for deposition substrates over the flame. The stage is a 2 mm thick aluminum, water-cooled stagnation surface that is designed with a 3 cm diameter window to mount 1 mm thick aluminum plates over the area of the flat flame. The window is tapered such that deposition plates are effectively flush giving a nozzle-to-stagnation separation distance identical to the corresponding probe sampling experiments . A Thermo DXR2 Raman Microscope with a 532 nm excitation source is used to measure Raman spectra with Raman shifts spanning 100 – 3500 cm^{-1}. The detailed structural analysis of carbon nanoparticles includes a 785 nm excitation source in addition to the 532 nm source. The laser is focused under a 50x objective at 1 mW power and care is taken to prevent modifications to the flame formed structure by laser excitation.

For flame formed carbon nanoparticles, the measured spectra are analyzed for first order spectra (Raman shift: 1000 – 1800 cm^{-1}) and second order spectra (Raman shift: 1800 – 3500 cm^{-1}). A temporary fluorescence background was observed (which is evidence that adsorbed gas - phase PAH is not present in the samples) but spectra are only analyzed after the background intensity reached a steady level. Spectral intensities are normalized to the highest intensity value measured in the spectrum and a linear correction is used in MATLAB to correct the luminescent background. A five peak deconvolution is performed on the measured first order Raman spectra to examine the structure of flame formed carbon. The curve fitting included 4 Lorentzian curves (G, D, D', D4) and a Gaussian curve (D3). A four peak ($2D_1$, $2D_2$, D + G and 2D') deconvolution is performed on the second order Raman spectra using Lorentzian curve fitting. The peak positions of the curves were moderately constrained while the other parameters were allowed to vary to match the measured spectra [16, 69].

2.3.3 X-Ray Diffraction

X-ray diffraction is carried out to characterize manganese oxide nanoparticles. Manganese oxide nanoparticles condense in the flame and deposit onto the stagnation surface. The analyzed sample is a mesoporous film which grows on a deposition plate mounted flush with the water-cooled stagnation surface. The temperature of the film depends on the heat transfer to the water-cooling and the heat flux from the synthesis flame. Aluminum sample plates are used to enhance cooling heat transfer, and the deposition time is minimized (1 min) to reduce artificial sintering of the delicate film by prolonged exposure to the flame.The deposited samples are transferred from the aluminum deposition substrate to glass for XRD analysis to avoid diffraction from aluminum. XRD measurements are carried out on a PANalytical X'pert Pro diffractometer equipped with a Cu X-ray tube operating at 45 kV and

40 mA. Counts are made for 1.5s for each 0.02s increment for $20 < 2\theta < 60$.

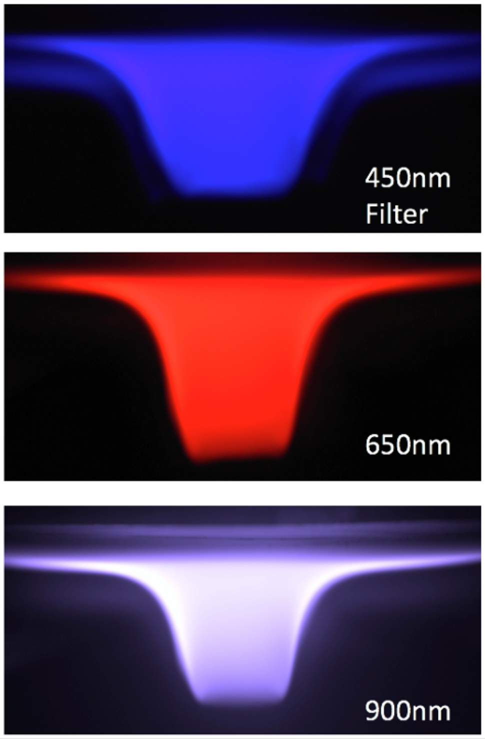

Figure 2.6: Ethylene - oxygen - argon flame image captured with 3 different bandpass filters (450nm, 650nm and 900nm)

2.3.4 Transmission Electron Microscopy

The structure of the flame formed nanoparticles are closely analyzed using transmission electron microscopy (TEM). A FEC Tecnai 12 Transmission Electron Microscope is employed with a Teitz 214 high resolution bottom mounted digital camera. TEM samples are prepared by scraping the as deposited flame formed film from the deposition plate, suspending the loose particles in tetrahydrofuran, and drop casting the suspension onto holey carbon - copper TEM grids.

2.3.5 X-Ray Photoelectron Spectroscopy

Structural measurements of carbon nanoparticles are carried out using a XPS (PHI 5600). The chamber is pumped to a pressure of 5 x 10^{-9} torr and the whole measurement was carried out at room temperature. Al Kα is used as the light source. The sample is sputtered with Ar+ for 3 mins at 2 kV and 1μ A. The XPS samples are prepared by scraping the as deposited flame formed film from the deposition plate, suspending the loose particles in tetrahydrofuran, and drop casting the suspension onto a thin nickel foil for analysis.

The curve fitting is done using CasaXPS software v 2.3.24 [70]. A Shirley background correction is used to correct the spectrum for background. The XPS curve is fitted using two curve fitting methods [71]. The curves are fit using a Lorentzian asymmetric lineshape which is a numerical convolution of a Lorentzian with a Gaussian to produce a lineshape which is a superset of the Voigt functions in the sense that asymmetric Voigt like lineshapes are possible as well as the traditional Voigt profiles [72]. The sp^3 is fitted allowing both the FWHM and binding energy to vary. The sp^2 peak has a variable FWHM but the peak position is constrained to be $E_{sp} - 0.5$ eV [73].

2.3.6 Color Ratio Pyrometry

Color-ratio pyrometry is a valuable, non-intrusive measurement technique based on the in- candescence nature of soot. Color-ratio pyrometry is carried out to analyze radiative emissions of the flame-formed carbon in-situ. A commercial DSLR camera (NIKON D3400) with the ultraviolet filter removed was employed for capturing radiative emissions emanating from flame-formed carbon. Three separate images were recorded with different bandpass filters (Andover FS420, 450 nm, 650 nm and 900 nm) placed in front of the camera lens. The images as captured from through the filters are shown Fig. 2.6.

Analysis is performed on an average of 10 frames. The camera captures the flame in a RAW format which is converted into TIF format using Nikon ViewNX-I. The images are further processed in MATLAB. The workflow used to compute the soot structure from the captured flame images is shown in Fig. 2.7. The images are cropped to the user defined flame height above burner such that the axis of symmetry is in the center. The 3 point inverse Abel transform algorithm is used to translate the image into an axisymmetric radial profile. The color ratio of the greyscale translated images are used for soot temperature calculations. The measurement technique proposed by Sunderland and co-workers [74] is adopted here with an additional modification to account for the evolution of optical properties as the soot structure evolves through the flame. The dispersion constant, α, accounts for the local properties of soot such as the H/C ratio which varies as the soot matures from a high H/C structure to a more carbonaceous structure. The wavelength dependent soot emissivity $\varepsilon\left(\lambda\right)$ is proportional to λ^{α} where λ is the filter wavelength and α is the light absorption dispersion exponent. The evolution in dispersion exponent was described by Gomez and co-workers [63, 75] using this assumption. With the inclusion of α, color ratio could be interpreted in terms of Planck's Law as follows:

$$\frac{GS_{\lambda_1}}{GS_{\lambda_1}} = \frac{b_1\tau_1\Delta\lambda_1\lambda_2^{5+\alpha}exp\left(\frac{hc}{\lambda_2 kT}\right)}{b_2\tau_2\Delta\lambda_2\lambda_1^{5+\alpha}exp\left(\frac{hc}{\lambda_1 kT}\right)} \tag{2.6}$$

h is the Planck's constant, k is the Boltzmann's constant, T is the temperature of the particle (assumed to be equal to the surrounding gas) and λ_i is the rated wavelength of the bandpass filter. $GS_i\left(r\right)$ is the post Abel transform radial greyscale output from the camera sensor through the respective filter and b_i is the wavelength specific fitting constant relating the camera response to spectral intensity through the Planck's law, τ_i is the transmissivity of the filter and $\Delta\lambda_i$ is the FWHM of the filter. b_i is calibrated using a blackbody furnace (Newport Oriel 67,032) with temperatures ranging from 1173 K to 1473 K while confirming the linear response of the camera. The temperature contours reported correspond to $\alpha = 1$ which is typical of mature soot [76, 77]. α is further evaluated as a function of local radiative properties of flame formed tuned to agree with the well-established computed temperature profile. Interpretation of radiative emissions from the flames is subject to experimental uncertainties associated with the camera sensor. This includes error in the blackbody furnace intensity during calibration, positional errors and errors in the filter properties. For assessment of dispersion coefficient, this also includes uncertainties in the computed flame temperature. A conservative estimated of the error on the measured dispersion coefficient is ±5% based on convolution of these errors.

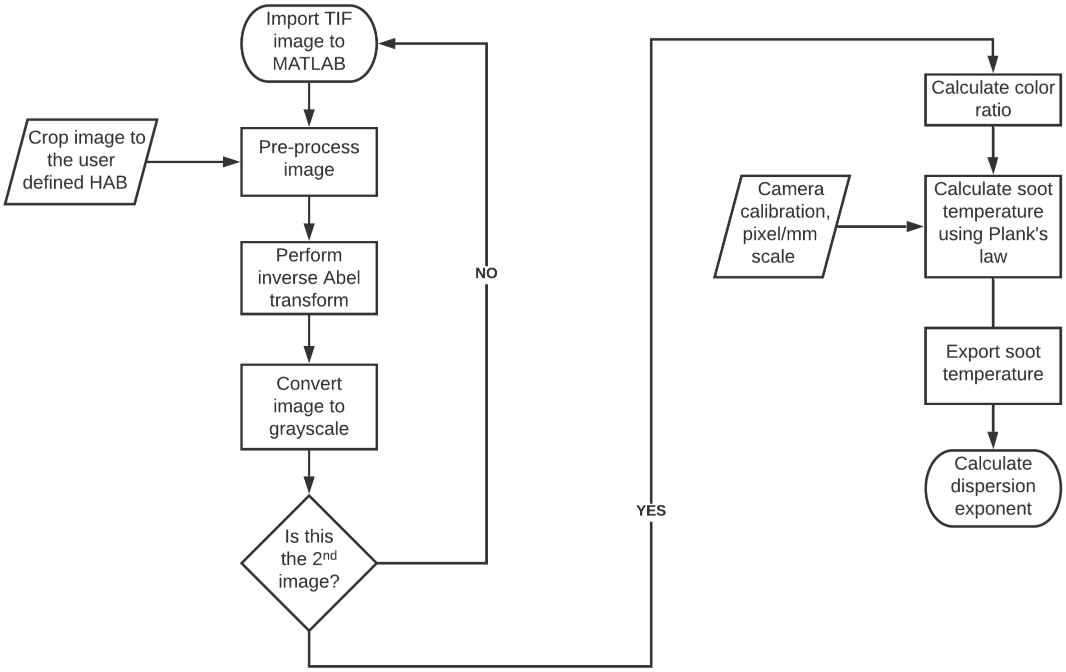

Figure 2.7: Typical workflow for color-ratio measurements and interpretation of radiative emissions

The description of the experimental and computational methods is provided in detail in this chapter along with particle characterization techniques. Details regarding the flame configuration of stretch stabilized stagnation flames and flame spray synthesis are further discussed. The fundamental processes involved in the gas-to-particle conversion for nanoparticle synthesis are investigated in the following chapters.

The flame-formed carbon nanoparticle system description in Chapter 2, in part, has been published in Fuel (Dasappa, S., Camacho, J., Evolution in size and structural order for incipient soot formed at flame temperatures greater than 2100 Kelvin : Materials and methods, 291, 120196), Fuel (Dasappa, S., Camacho, J., Fuel molecular structure effect on soot mobility size in premixed C6 hydrocarbon flames : Experimental methods, 300, 15, 120973) and Data in Brief (Dasappa, S., Camacho, J., Raman spectroscopy, mobility size and radiative emissions data for soot formed at increasing temperature and equivalence ratio in flames hotter than conventional combustion applications : Experimental Design, Materials and Methods, 36, 107064). Parts of Chapter 2 regarding flame-formed manganese oxide synthesis has been published in Energy and Fuels (Dasappa, S., Camacho, J., "Thermodynamic barrier to nucleation for manganese oxide nanoparticles synthesized by high-temperature gas-to-particle conversion: Computational methods and Experimental methods, 35, 2, 1874-1884) and CrystEngComm (Dasappa, S., Camacho, J., Formation of nanocrystalline manganese oxide in flames: oxide phase governed by classical nucleation and size dependent equilibria: Computational and Experimental , 22, 5509-5521). The dissertation author is the primary investigator for the publications.

Part II

Stretch Stabilized Stagnation Flames

Chapter 3

Evolution in size and structural order of flame formed carbon

Soot formation remains an unavoidable combustion problem affecting performance [78], public health [79] and the environment [80]. Interestingly, flame-formed carbon also has a long history as a useful material [11, 12]. The work focuses on the production of flame formed carbon nanoparticles in flames hotter than typical combustion applications. Processes designed for flame temperatures much greater than typical engines include rocket propulsion [81], oxy-fuel combustion [82] and enriched / preheated air applications [83]. A complementary experimental and modeling approach focusing on this temperature range is taken to shed light on distinctive higher-temperature ($T > 2100K$) soot formation processes. Soot yield is known to decrease at elevated flame temperatures [53, 55, 84, 85] but systematic studies of particle size distribution, carbon structure and other detailed properties rarely venture beyond 2100 K. Investigation of soot formed in this regime is relevant to higher-temperature combustion applications and characterization of the carbon structure may reveal unique and potentially useful properties.

Evolution in soot particle size distribution and carbon bonds is examined in laminar stretch-stabilized flames having maximum flame temperatures hotter than previously reported. Premixed stretch stabilized flames have been shown [7, 86] to be an effective flame configuration for investigating fundamental soot formation processes close to the adiabatic flame temperature. The pseudo one-dimensional configuration enables systematic study of detailed processes in a flow field amenable to computational reacting flow modeling [7, 87]. A series of flame experiments is established for isolation of the equivalence ratio and flame temperature effects on soot formation in the higher-temperature regime. Computation of the flame structure is also carried out for insight into the growth conditions in terms of the temperature–time history and polycyclic aromatic hydrocarbon (PAH) precursors. Elevated temperature is known to cause a decrease in soot precursor production [4, 84] a decrease in particle collision efficiency [88, 89] and an increase in particle carbonization rate [90–92].

Raman spectra of carbon deposited from flames at increasing flame temperature and equivalence ratio are analyzed to observe increase carbon structural ordering under a range of fuel-rich conditions. Raman spectroscopy is a valuable tool for probing carbon structure and elucidating soot properties such as absorption cross-section [93], optical band gap [94] and crystallite size [29]. A wealth of knowledge has been obtained from analysis of Raman spectra for soot formed in premixed flames [28, 95–100] diffusion flames [29, 95, 101–103] and engines [16, 69]. Although the range of flame conditions is large, the characteristics of the Raman spectra fall within a narrow range. That is to say, the nature of sp^2 bonding, sp^3 bonding and crystallite size do not change drastically under the conventional range of sooting flame conditions. In contrast, the authors have previously reported a transformation in the Raman signature for flame-formed carbon in the higher-temperature regime [86]. Rather than subtle changes to the characteristic D and G peaks of the Raman spectra, a dramatic shift in the relative heights and widths occurs as the flame temperature increases beyond 2100 K. If the correlation of Ferrari for highly defective graphite is applied [21, 24] the evolution in Raman spectra indicates that the distance between crystalline defects becomes significantly larger with increasing temperature. This analysis is expanded upon to assess flame formed carbon at increasing equivalence ratio in terms of defect density for the higher-temperature regime.

The flame conditions correspond to formation of incipient soot at the earliest growth stages. High-surface area carbon nanoparticles corresponding to freshly formed soot is expected, but, the relatively high flame temperature may also induce carbonization only observed in so-called “mature” soot. In fact, the unique combination of “young”, nucleation sized particles having relatively low defect density may be useful for applications of functional carbon black and hard carbon. Characterization of particle formation processes and material properties for flame-formed carbon will shed light on the higher temperature regime and inform potential applications of the material produced.

3.1 Computational Analysis

A series of stretch-stabilized ethylene-oxygen-argon flames is designed to track the effect of increasing flame temperature and equivalence ratio on flame-formed carbon size and structure. These flames are stabilized in a laminar stagnation flow with a steady position given by the balance between the decelerating convective velocity and opposing local flame speed [8]. A summary of the flames studied is shown in Table 3.1. For a given equivalence ratio, ϕ, the flame temperature and flame position are tuned by the flame diluent argon concentration, X_{Ar} and total flow rate. The use of argon instead of nitrogen enables higher flame temperatures to be established due to the heat capacity effect. Flame structure computations, carried out by OPPDIF are used to guide the design of the flame series and to gain insight into the growth conditions of the flame-formed carbon. The pseudo one-dimensional formulation taken in OPPDIF [44] is most accurate for domains in which the nozzle diameter is much greater than the nozzle-to-stagnation surface distance [104–106]. In some cases, however, OPPDIF was recently shown to perform as a fast and reasonably accurate approach for flame structure calculation even for more narrow aspect ratio domains [107].

OPPDIF is used to determine the maximum flame temperature, $T_{f,max}$, and particle growth time, t_p, for a given inlet composition and flow rate. The particle growth time is given by the time for a Lagrangian particle to travel from the location of the flame zone to the stagnation surface location. Carbon particles are assumed to follow the gas convective velocity until the thermophoretic force induces additional drift towards the colder stagnation surface. The details of the OPPDIF computations are provided in Section 2.1.2. Flame series for $\phi = 2.4$, 2.5 and 2.6 with increasing flame temperature ($1950K < T_{f,max} < 2250K$) and comparable growth time are established. Soot formation processes are not considered in the flame modeling study carried. Rather, detailed combustion chemistry models are used to determine the flame structure in the absence of soot. USC Mech II [46] is used as a baseline model (foundational chemistry up to benzene) to calculate the flame structure as previous work showed relatively accurate prediction of measured flame structure compared to other models applied to sooting stretch-stabilized flames [7]. Separate flame computations are also carried out with combustion chemistry models incorporating PAH to assess soot precursor predictions. Computations for each flame using the KAUST PAH Mechanism 2 (KM2) [47], Appel, Frenklach, Bockhorn (ABF) [48] and Blanquart, Pepiot, Pitsch (BPP) [15] mechanisms are performed to provide a comparison of PAH predictions among the three models for the flames of interest. The KM2 mechanism is a gasoline surrogate mechanism built from USC Mech II foundational chemistry [47, 108]. ABF is a classic mechanism for PAH chemistry based on GRI-Mech 3.0 foundational chemistry. The BPP mechanism was developed for engine relevant fuels with GRI-Mech 3.0 foundational chemistry incorporating several updates [15] beyond the original GRI-Mech 3.0. Experimental PAH measurements do not exist in the higher-temperature regime. As such, the computed PAH profiles provide insight into agreement among models that are extrapolated to higher temperature.

3.2 Experimental Conditions

Evolution in carbon structure and size distribution is observed experimentally to examine unique soot formation behavior at flame temperatures greater than conventional combustion applications. The experimental flame configuration centers upon laminar, premixed stretch-stabilized flames in a setup as described in Section 2.1.1. The flame formed

Table 3.1: Summary of flame synthesis conditions

ϕ	$X_{C_2H_4}$	X_{O_2}	X_{Ar}	$T_{f,max}$ (K)	T_{ad} (K)	$t_p(L)$ (ms)	v_o $(cm\ s^{-1})$	a (s^{-1})
2.40	0.138	0.173	0.689	2035	1945	18	91	36
2.40	0.146	0.183	0.671	2085	2010	15	101	40
2.40	0.150	0.188	0.662	2110	2025	15	98	39
2.40	0.152	0.191	0.658	2140	2040	15	97	38
2.40	0.166	0.207	0.627	2190	2120	14	90	35
2.40	0.173	0.217	0.610	2240	2160	14	86	34
2.50	0.145	0.174	0.681	1980	1905	14	104	41
2.50	0.151	0.180	0.670	2015	1950	18	87	34
2.50	0.160	0.192	0.648	2080	2005	16	90	35
2.50	0.175	0.210	0.615	2150	2075	13	101	40
2.50	0.183	0.220	0.597	2195	2110	13	97	38
2.50	0.196	0.236	0.569	2260	2180	12	88	35
2.60	0.153	0.176	0.670	1950	1840	18	91	36
2.60	0.162	0.188	0.650	2050	1920	16	95	37
2.60	0.177	0.204	0.618	2080	1980	16	86	34
2.60	0.184	0.212	0.605	2110	2005	16	83	33
2.60	0.189	0.218	0.592	2135	2030	16	80	31
2.60	0.209	0.240	0.551	2205	2105	14	79	31
2.60	0.223	0.258	0.518	2270	2220	11	92	36
2.77	0.260	0.282	0.458	2240	2170	11	81	32

$T_{f,max}$ computed using OPPDIF with measured boundary conditions ($L = 2.54cm$, $T_{nozzle} = 330K$ and $T_{stagnation} = 400K$) , v_o - cold gas velocity at 273 K and 1 atm, a - strain rate carbon is analyzed for structure, particle size and radiative emissions through Raman spectroscopy, X-ray photelectron spectroscopy, mobility particle sizing and color ratio pyrometry. The details of the experimental techniques are provided in Section 2.3.2, 2.3.1 and 2.3.6.

3.3 Results and Discussion

3.3.1 Computational PAH analysis

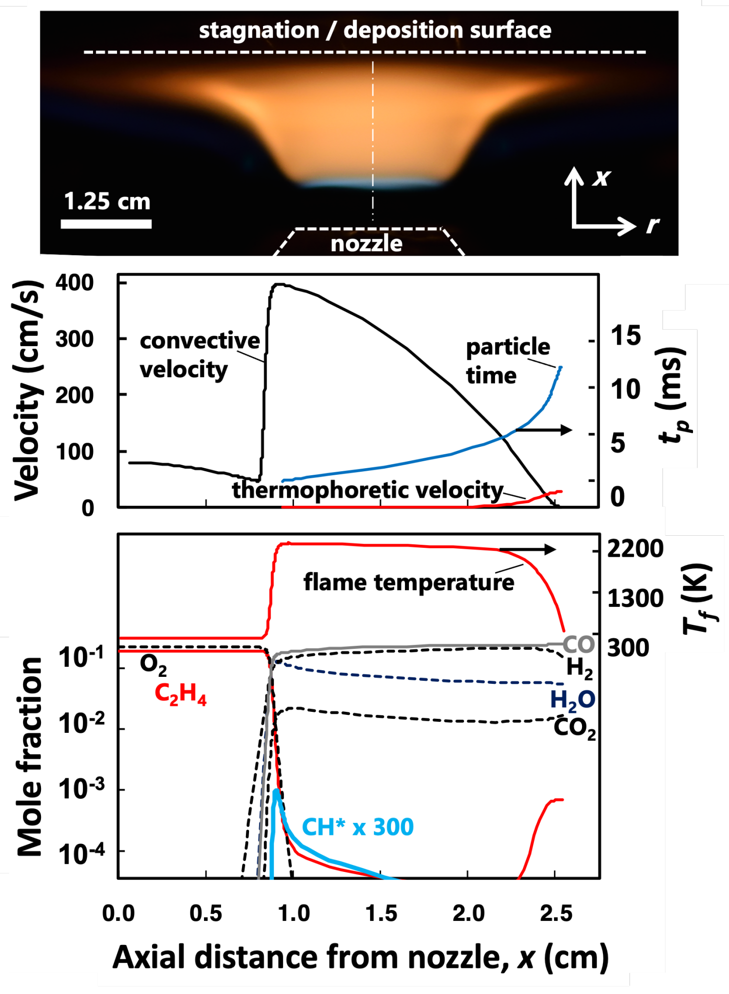

Figure 3.1: Flame image (top), computed centerline axial profiles for velocity and particle time (middle) and flame temperature and major species (bottom) for the $\phi = 2.6$, $T_{f,max} = 2205K$ flame case.

Complementary flame structure calculations provide insight into particle temperature-time history and gas-phase soot precursors. Computational flame structure results obtained by OPPDIF are shown in Fig. 3.1 for the centerline of the $\phi = 2.6$, $T_{f,max} = 2205K$ case. An image of this flame is also shown as representation of the sooting premixed stretch-stabilized flames studied. The position of the flame front is distinguished in flame images by the onset of luminosity. In the computations, the flame position is associated with sharp features of the computed flame structure such as a temperature rise, a velocity increase and a narrow peak of combustion intermediates. Particle inception occurs immediately after the flame zone as evidenced by the observed yellow luminosity next to the blue flame disc. The flame-formed particles then grow in the post flame region and eventually deposit onto the stagnation surface. The flame conditions are designed to isolate flame temperature and equivalence ratio effects for comparable particle times. Accompanying color-ratio pyrometry experiments are used to assess the consistency of the flame structure calculations.

Flame computations are also carried out with combustion chemistry models incorporating PAH to assess soot precursor predictions. Computations for each flame using the KM2, ABF and BPP mechanisms are performed to provide a comparison of PAH predictions among the three models for the flames of interest. The temperature profile is fixed to match the flame structure solution from USC Mech II for all comparisons between PAH mechanisms. The flame temperature predicted for stretch-stabilized flames is not primarily sensitive to a given fuel mechanism employed, but the flame position does strongly depend on the fuel kinetics. This effect is demonstrated in Fig. 3.2 in terms of computed flame temperature profiles obtained by independently solving the energy equation for each combustion mechanism flame calculation. Substantial differences in computed flame position are observed among the PAH mechanisms due to deviations in ethylene combustion chemistry leading to differences in predicted fuel burning velocity. The USC Mech II based solution has been shown to predict the measured flame position in previous studies of sooting stretch-stabilized flames [7]. As such, the flame structure solutions for the three PAH mechanisms are constrained to adopt the flame temperature profile from USC Mech II rather than inde-

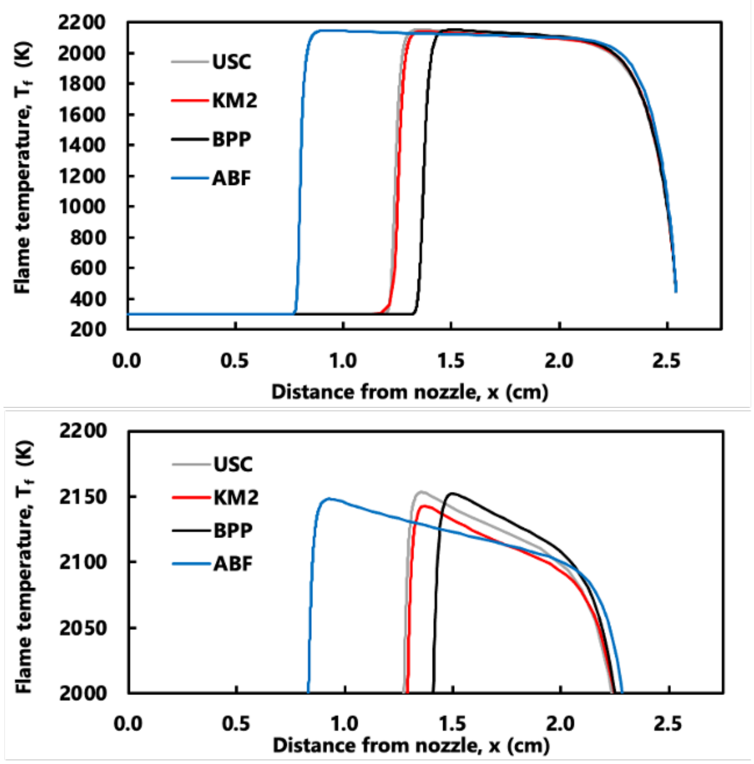

Figure 3.2: Computed temperature profiles for the $\phi = 2.5$, $T_{f,max} = 2150K$ flame case using the four combustion chemistry models studied. The computed temperature is based on solution of the energy equation rather than constraining the temperature profile. The full profile is shown (top) along with a profile emphasizing the peak flame temperatures (bottom).

pendently solving the energy equation. Assessment of this assumption is carried out below by comparing flame position predicted by USC Mech II to the measured flame. The KM2 mechanism is a PAH flame chemistry model based on foundational chemistry taken from USC Mech II. As such, the agreement in measured flame temperature and position between USC and KM2 mechanisms is expected.

The flame position and particle time is fixed across all models by imposing the USC Mech II based temperature profile in the OPPDIF computations running the KM2, ABF and BPP mechanisms. An example set of the computed species profiles for soot precursors shown in Fig. 3.3 as a function of space and particle time. The profiles shown in Fig. 3.3 are the same flame conditions shown in Fig. 3.1 using KM2 chemistry and the constrained temperature profile. Non-monotonic profiles are predicted for the computed PAH concentrations.

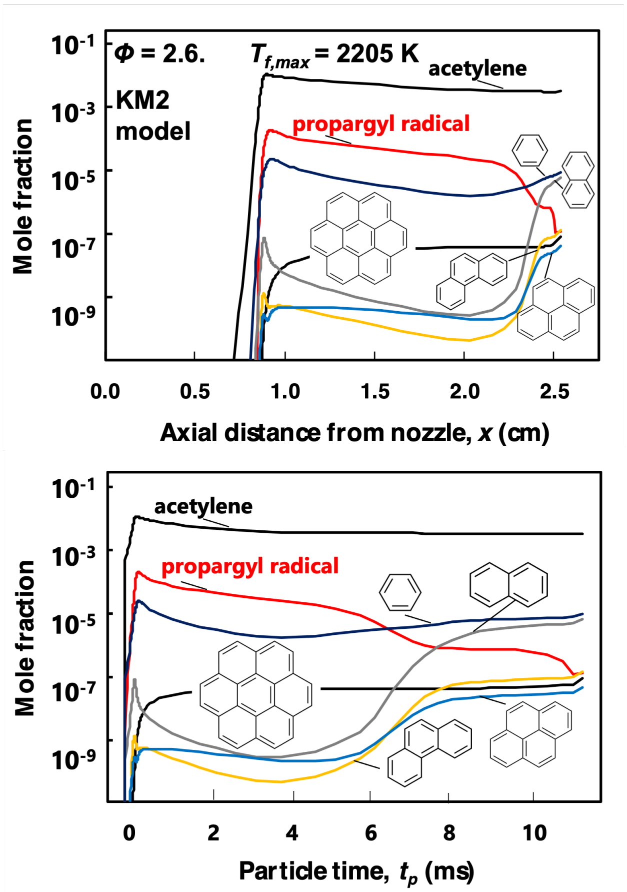

Figure 3.3: Computed gas-phase soot precursor profiles in terms of axial position (top) and particle time (bottom) based on the KM2 combustion chemistry model for the $\phi = 2.6$, $T_{f,max} = 2205K$ flame case.

A sharp rise occurs in the flame zone where the fuel is converted to PAH due to fuel-rich kinetic processes. The subsequent drop and rise seen in post-flame region is primarily governed by equilibrium effects. Equilibrium PAH concentrations typically peak at moderate flame temperatures and decrease for relatively hot flames [109]. The flame temperature profile computed evolves from high to low temperature as the burned gases approach the water-cooled stagnation surface. This causes a corresponding shift in equilibrium PAH concentrations. The temperature gradient in the vicinity of the water-cooled stagnation surface also induces thermal diffusivity of large and small gas phase species, which is a secondary cause for minor, additional shifts in the concentration.

Flame structure calculations are carried out for each flame using ABF, BPP and KM2

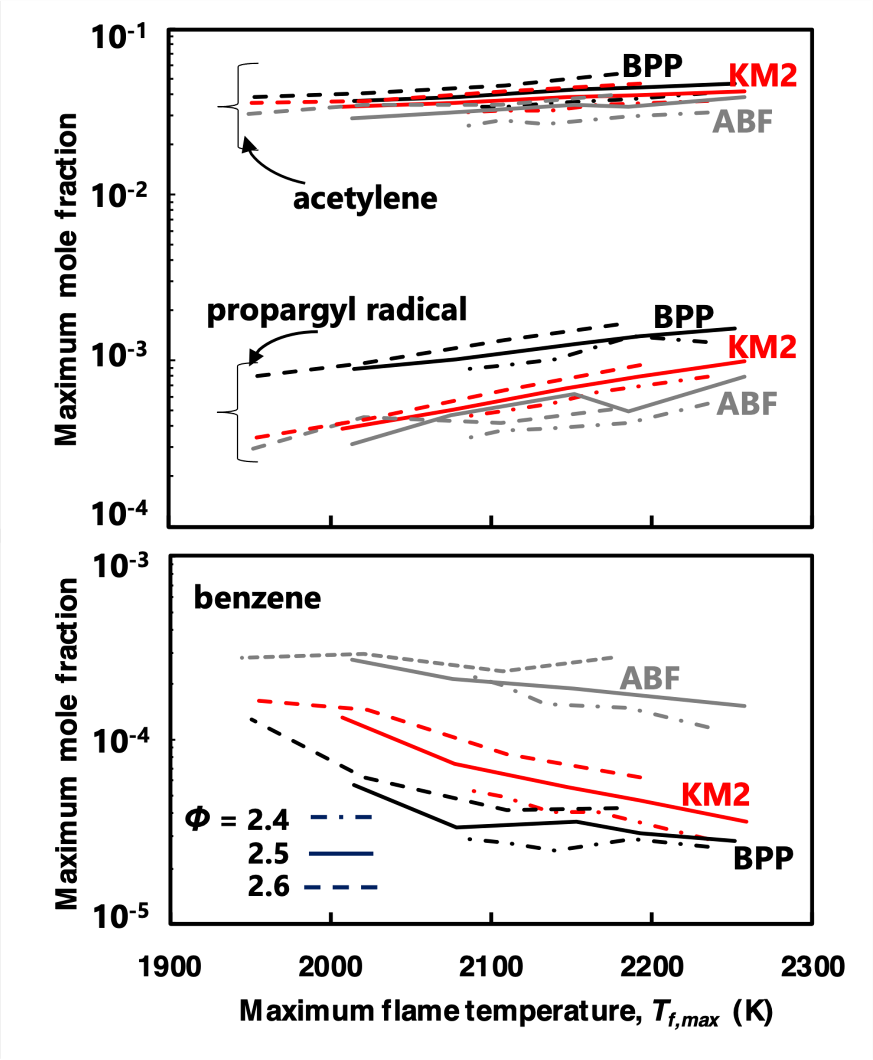

Figure 3.4: Maximum concentration in computed centerline axial profiles as a function of maximum flame temperature. The line follows computations for six flame temperature conditions for each equivalence ratio (see Table 3.1). Results for each chemistry model (ABF, BPP, KM2) is shown for acetylene and propargyl radical (top) and benzene (bottom).

mechanisms to evaluate the gas-phase environment under which the flame formed carbon develops. A summary of computed profiles is carried out by determining the maximum mole fraction computed for a species in a certain flame and designating each flame by the maximum flame temperature. This summary is shown in Fig. 3.4 for acetylene, propargyl and benzene to establish predictions based on foundational C0 - C6 chemistry. As Fig. 3.4 shows, disagreement in computed concentration is observed among the three PAH chemistry models despite having the same temperature profile constrained by the USC Mech II solution. The computed acetylene concentration increases with equivalence ratio as expected and the predicted trend with flame temperature is relatively similar among the models. In contrast, disagreement among the three models is observed for the predicted concentration of propargyl radical and benzene. The BPP model predicts a significantly higher propargyl radical concentration for the whole range of flame temperature conditions. The predicted species concentration for benzene has a much stronger dependence on the PAH mechanism employed rather than the equivalence ratio. The ABF model predicts benzene concentrations almost an order of magnitude higher than the other models.

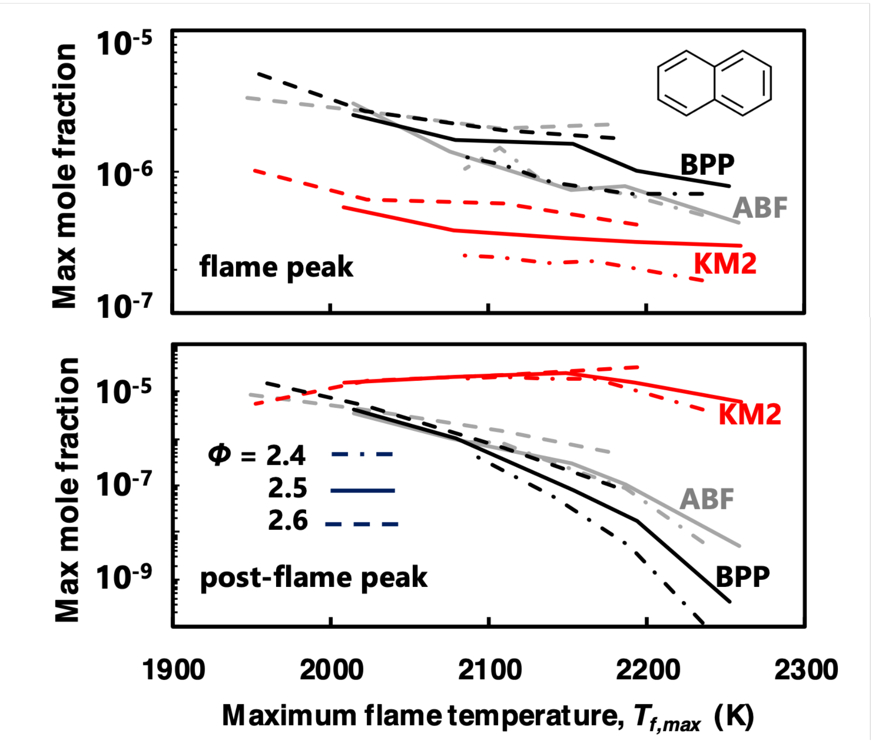

Figure 3.5: Summary of predicted naphthalene concentrations for the series of flame computations using the three PAH mechanisms. The maximum mole fraction in the computed profile is plotted for each flame taking the maximum at the flame zone (top) and the maximum in the post-flame region (bottom).

The observed divergence in computed foundational chemistry is expected to propagate into predictions for larger species. Computed naphthalene, phenanthrene and pyrene profiles for all flames and PAH mechanisms. As shown in Fig. 3.2, the PAH profiles are non-monotonic as the maximum concentration could occur in the kinetically-driven flame zone or in equilibrium-driven post flame region. The series of PAH profiles demonstrate the sensitivity of soot precursors to flame temperature and the kinetic mechanism. The profiles of these aromatic soot precursors show peak locations at the flame zone and the post-flame region with relative magnitudes depending on the mechanism employed. The maximum mole fraction computed for naphthalene is shown in Fig. 3.5 with peak concentration values taken from both the flame zone and the post-flame region. Predicted naphthalene concentrations are more sensitive the kinetic model employed than the equivalence ratio. The BPP and ABF models predict comparable concentrations in the flame zone and post-flame zone for the series of flame temperatures. On the other hand, the KM2 mechanism predicts different behavior in that a relatively low concentration of naphthalene in the flame occurs while more naphthalene is predicted in the post-flame zone. This comparison demonstrates the competing kinetic and thermodynamic processes with regards to PAH chemistry.

A summary of PAH predictions is shown in Fig. 3.6 for phenanthrene formation. The KM2 and BPP predictions for phenanthrene are comparable in the flame zone while the concentration predicted by ABF is an order of magnitude higher. In the post-flame zone, the phenanthrene concentrations span six decades among the three PAH mechanisms. The summary for pyrene concentrations shown in Fig. 3.7 is similar to phenanthrene in that the ABF model predicts an order of magnitude higher concentration in the flame zone. In the post-flame zone, the pyrene concentration predicted by the BPP mechanism is an order of magnitude lower than the other mechanisms. The computed PAH profiles would change with the addition of a soot formation model due to a split between gas-phase and soot-bound carbon depending on particle inception models and kinetic growth rates. PAH chemistry is a notorious bottleneck in quantitative understanding of soot formation and the analysis demonstrates this challenge for the higher-temperature regime.

The range of PAH profiles predicted among the three PAH mechanisms are due to different pathways and rate parameters adopted. The dominant reactions producing naph-

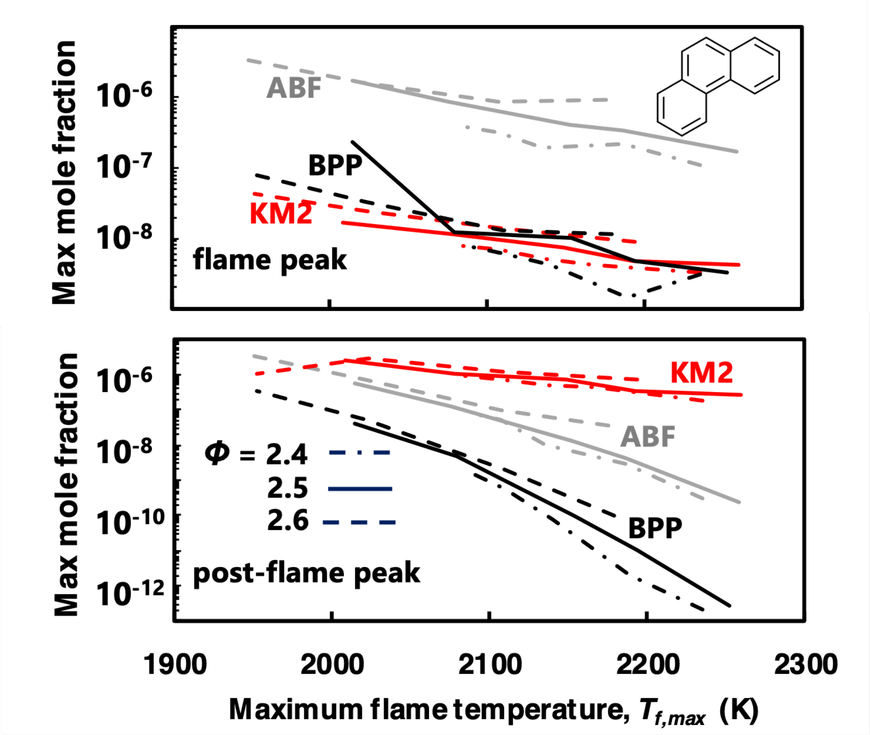

Figure 3.6: Summary of predicted phenanthrene concentrations for the series of flame computations using the three PAH mechanisms. The maximum mole fraction in the computed profile is plotted for each flame taking the maximum at the flame zone (top) and the maximum in the post-flame region (bottom).

thalene are plotted as a function of distance in Fig. 3.8 for $\phi = 2.6$, $T_{f,max} = 1950K$ flame case. This example demonstrates overlaps and divergence in pathways and reaction rates among the three PAH mechanisms. The combination of phenyl and butadienyl to form naphthalene is considered in all three mechanisms but significant discrepancies in rates of production are predicted along the flame profile. Naphthalene production from the naphthalene radical occurs at a comparable rate for the ABF and KM2 models but this is not a dominant pathway for BPP mechanism. Routes to naphthalene from ethylene substituted benzene and methylated naphthalene are dominant only in the KM2 and BPP mechanisms. The lack of experimental observations of PAH formation in this regime makes assessing chemical reversibility effects and competing mechanism pathways a difficult task. Moreover, application of these PAH mechanisms to soot formation modeling should first consider limitations in PAH chemistry.

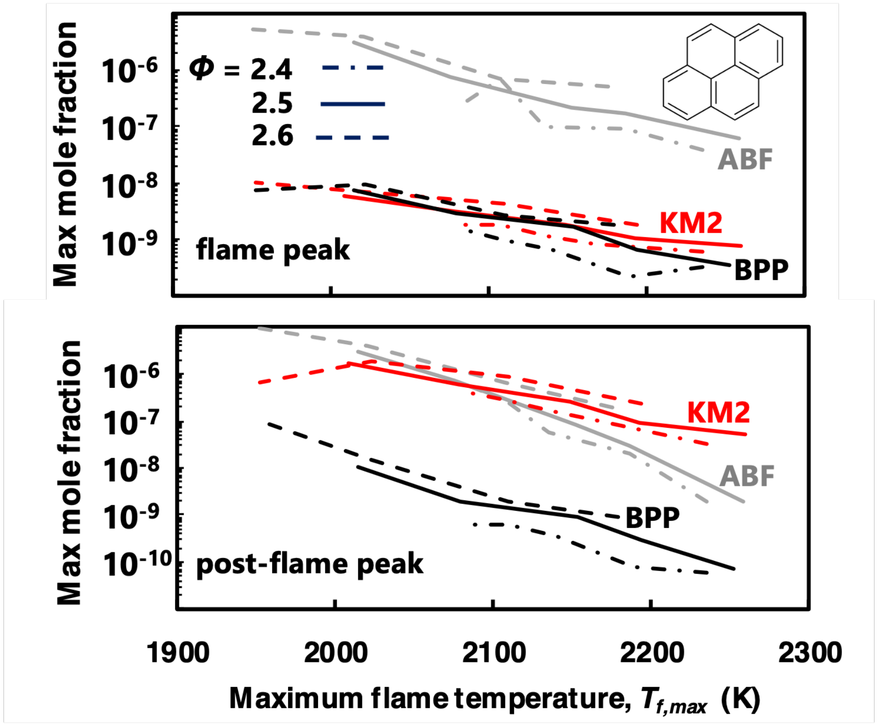

Figure 3.7: Summary of predicted pyrene concentrations for the series of flame computations using the three PAH mechanisms. The maximum mole fraction in the computed profile is plotted for each flame taking the maximum at the flame zone (top) and the maximum in the post-flame region (bottom).

3.3.2 Carbon Structure as Inferred by Soot Pyrometry

Color-ratio pyrometry measurements provide insight into the consistency of OPPDIF and USC Mech II for computing flame structure in the higher-temperature regime. Measured temperature fields are shown in Fig. 3.9 for the two hottest flame conditions of each equivalence ratio. The temperature reported in Fig. 3.9 is based on the assumption that the particle emissivity is proportional to λ^{-1} which is a typical dispersion exponent applied to mature soot [76]. Under this assumption, the measured maximum temperature is much greater than the maximum computed by OPPDIF. The observed discrepancy and the axial variation in measured flame temperature may be due to evolution in soot particle properties rather than an actual property of the measured flame structure. Gomez and co-workers recently [63, 75] showed that evolution in soot particle properties should be considered when interpreting radiative emissions from incipient soot. Soot is expected to form close

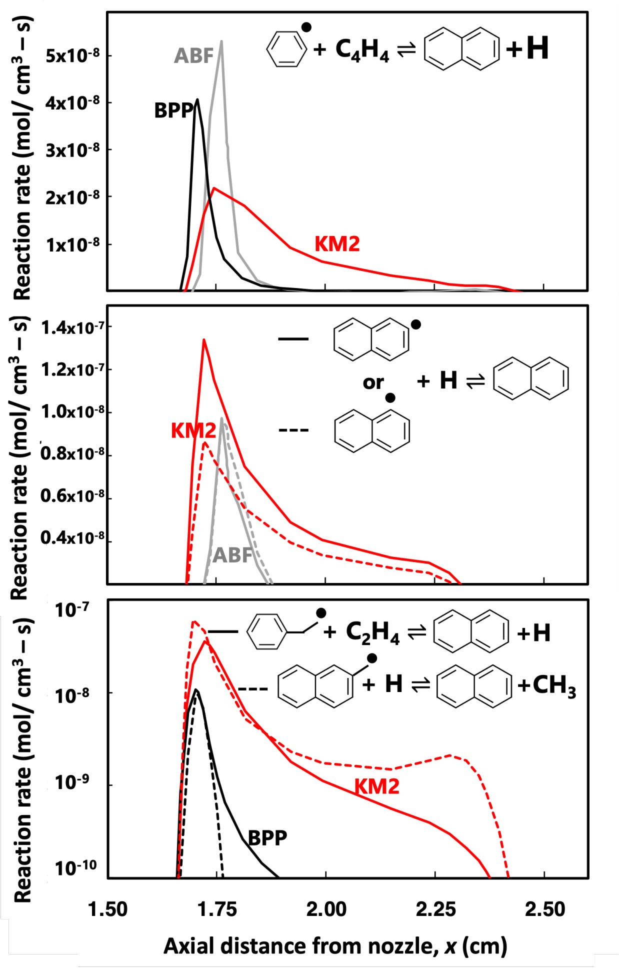

Figure 3.8: Rate of production of naphthalene predicted from reactions considered in the three PAH mechanisms studied including a phenyl based pathway (top), a naphthalene radical based pathway (middle), ethylene substituted benzene pathway (bottom) and methylated naphthalene pathway (bottom).

to the flame-front and grow over time as the C/H ratio and carbon structure also evolve for premixed stagnation flames. This evolution is also expected to depend on the particle temperature-time history and gas-phase environment (temperature and equivalence ratio effects).

An independent temperature diagnostic would shed light on the interpretation of measured particle radiative emissions for extracting flame temperature. Thermocouple measurements are simple and readily accessible, but this method is not reliable for stretch stabilized flames as the aerodynamic balance would be heavily disturbed by flame anchoring

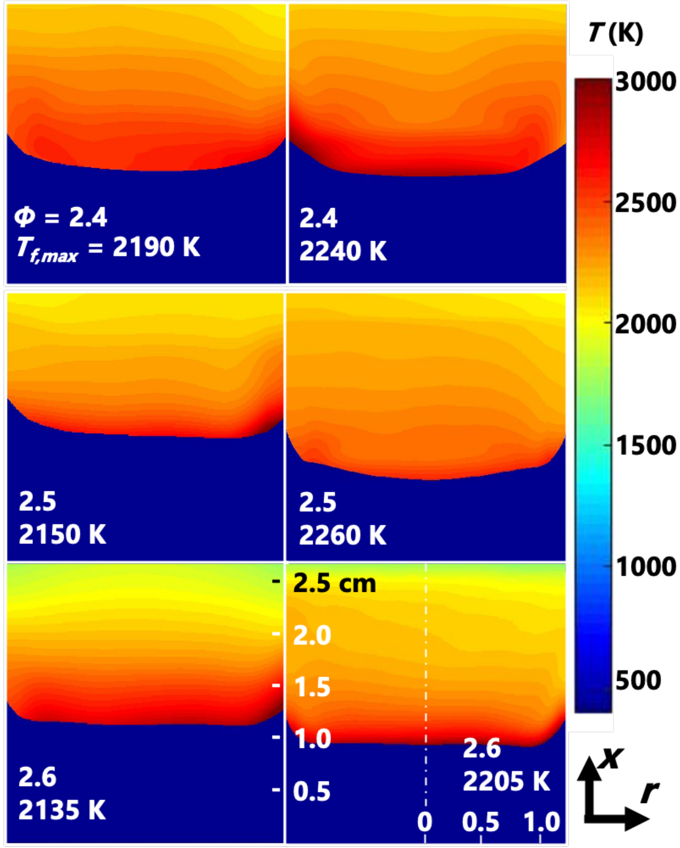

Figure 3.9: Axisymmetric flame temperature field, $T_f(x, r)$ extracted from measured color-ratio field for $\alpha = 1$.

onto thermocouple wires. In the absence of an independent diagnostic, the computed flame temperature profile is used to gain insight into the measured radiative intensity and flame temperature. A summary of comparisons between the measured and computed axial, centerline temperature profiles is shown in Fig. 3.10. Soot radiative emissions are detected in the post-flame region of the domain. The position where emissions are first detected above the nozzle coincide fairly closely with the flame position predicted by USC Mech II. The sharp rise in computed flame temperature overlaps the start of the emission profile or falls within 1 mm.

Flame temperature in the post-flame region of stretch-stabilized flames is expected to approach the adiabatic flame temperature with minor deviations based on strain, radiation and Lewis number effects [8]. The computed flame structure predicts this behavior with a

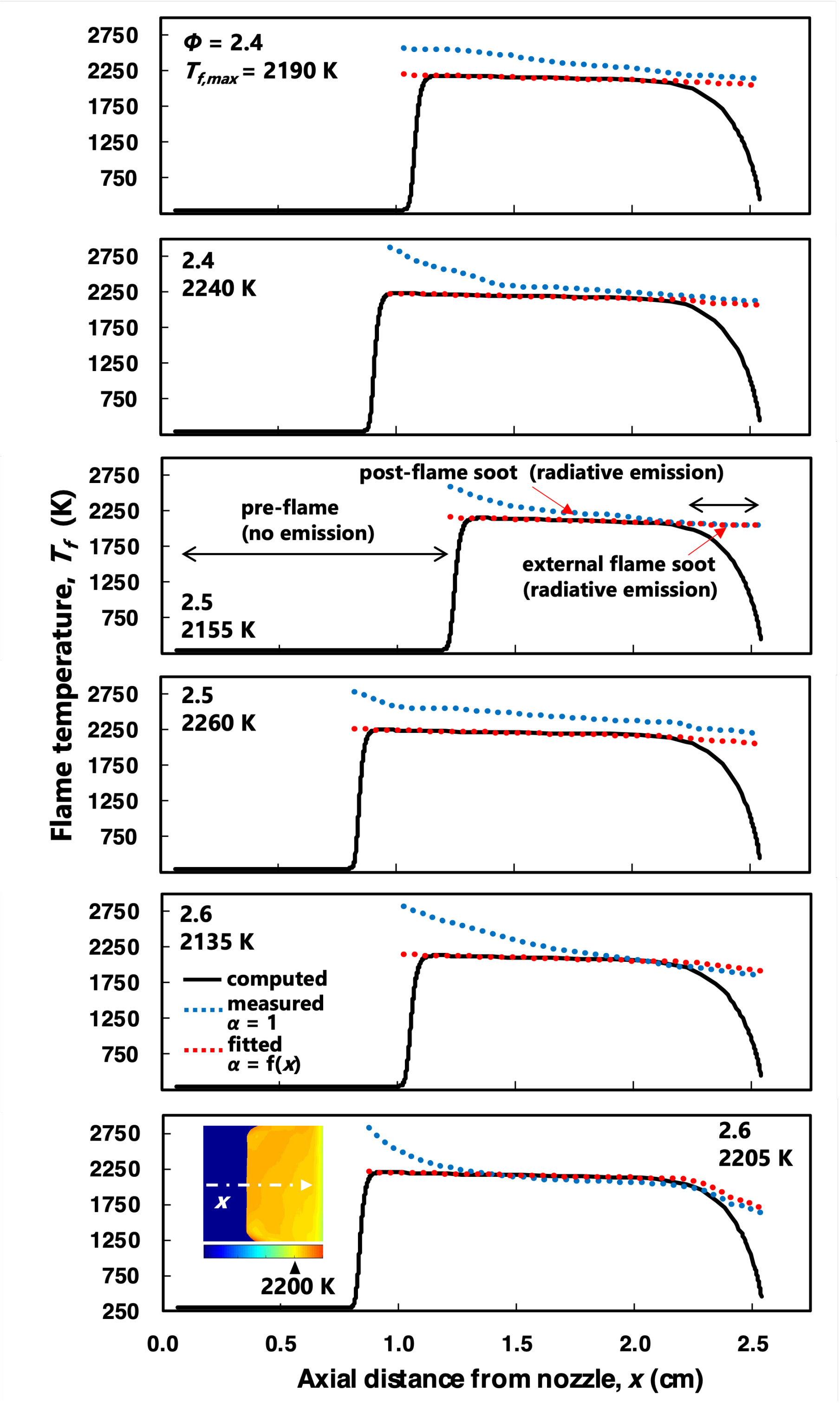

Figure 3.10: Measured and computed axial temperature profiles at the centerline. The measured profiles are shown for α = 1 and for α(x) fitted to match the computed temperature profile. The inset shows the measured temperature field for the $\phi = 2.4$, $T_{f,max} = 2205K$ case determined using the fitted $\alpha(x)$ profile.

plateau in flame temperature for most of the post-flame region. The measured flame temperature profile assuming the particle dispersion exponent is constant at $\alpha = 1$ shows a decrease in flame temperature with increasing distance from the nozzle. The measured decrease in temperature may be an artifact of the constant dispersion exponent assumption. The evolution of soot structure with time is expected to drive evolution in dispersion exponent and this should be considered when extracting the particle temperature.

Using the computed flame temperature as a constraint, a dispersion exponent profile is extracted for the measured grey scale intensity ratios based on Eq. 2.6 and the resulting exponent profiles are shown in Fig. 3.11. The measured temperature profile based on this fitted dispersion exponent profile is also included in Fig. 3.10 to demonstrate convergence after applying the computed temperature profile as a constraint. If the computed flame temperature is a reasonable reference point, the fitted profile should fall within physically relevant values. This is indeed the case as the trend and magnitude of the fitted dispersion exponents shown in Fig. 3.11 could be explained in terms expected soot formation behavior. Namely, the range of values observed ($0.5 < \alpha < 3$) falls with dispersion exponents reported for low C/H organic materials, soot and carbon [63, 76, 77, 110]. Interpretation of radiative emissions from the flames is subject to experimental uncertainties associated with the camera sensor. This includes error in the Blackbody furnace intensity during calibration, positional errors and errors in the filter properties. For assessment of dispersion coefficient, this also includes uncertainties in the computed flame temperature. A conservative estimated of the error on the measured dispersion coefficient is ±5% based on convolution of these errors.

The higher values obtained at the flame-zone correspond to incipient soot which is known to have low C/H structure. The fitted profiles indicate that the dispersion exponent may progress over time towards values on the order of unity corresponding to mature soot. The inset of Fig. 3.10 shows an example measured temperature field using the fitted axial dispersion exponent profile. A relative trend showing decreasing dispersion exponent for increasing flame temperature and equivalence ratio is also observed across the flames. Color

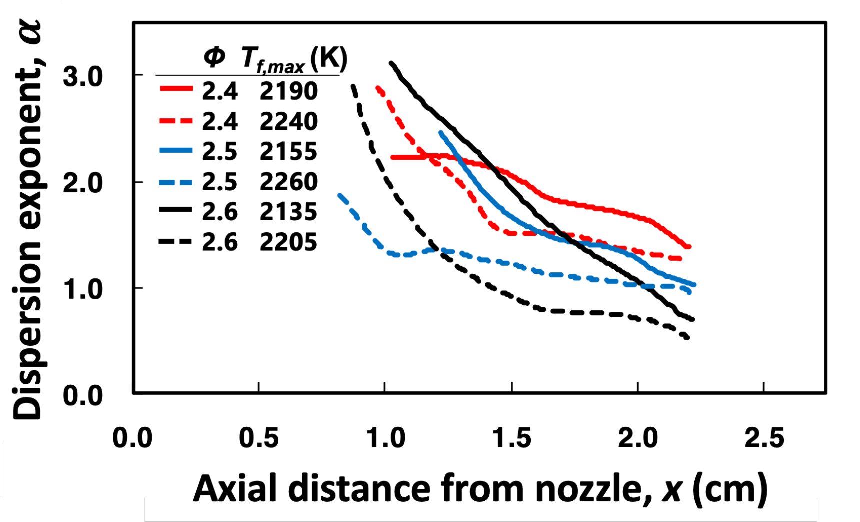

Figure 3.11: Dispersion exponent profiles based on fitting measured centerline radiative emission profiles to the computed axial flame temperature profile.

ratio measurements show reasonable agreement to the computed flame position. In addition, constraining the measured particle radiative emissions to match the computed flame temperature results in optical properties consistent with known physical values. The agreement between the measured and computed flame position is assessed by comparing the position of the luminous region with the computed temperature profile. The largest discrepancy occurs for the $\phi = 2.4$, $T_{f,max} = 2190K$ case as the measured onset of radiative emissions is approximately 1 mm upstream of the computed pre-heat zone. This upstream shift in position may explain the off-trend dip observed in the dispersion exponent for this case. The expected trend is for the hotter temperature case to have a lower dispersion exponent. This off-trend behavior may be due to artifacts of fitting the temperature profile that does not overlap in space as close as the other cases.

Color-ratio pyrometry provides insight into the optical dispersion exponent (α) of the carbon nanoparticles being formed in the flame. Color-ratio pyrometry is also performed for 2 flame conditions, $\Phi = 2.60, T_{\mathrm{f,max}} = 2270K$ and $\Phi = 2.77, T_{\mathrm{f,max}} = 2240K$. The temperature field as measured with $\alpha = 1$ is shown in Fig. 3.12(a). The discrepancy between the measured and the OPPDIF computed temperature profiles is due to a constant

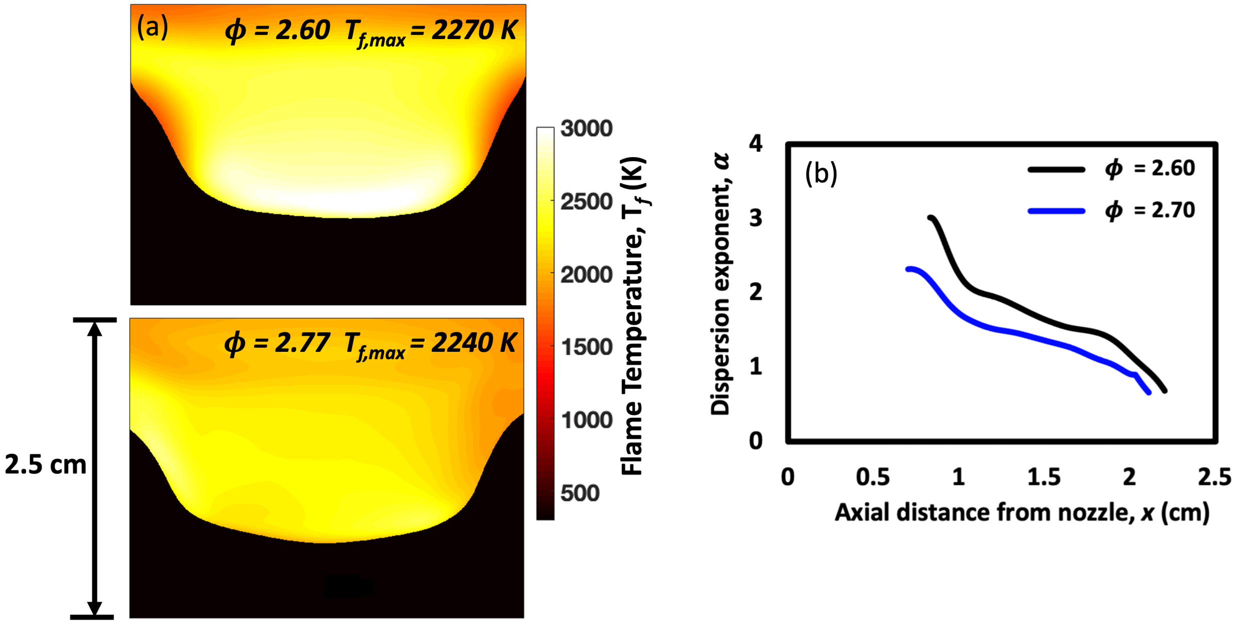

Figure 3.12: (a) - Temperature field as measured with $\alpha = 1$, (b) - Dispersion exponent profiles based on fitting measured centerline radiative emission profiles to the computed axial flame temperature profile

α, since the value of the dispersion exponent depends on local properties of soot such as the H/C ratio. The properties of flame formed carbon changes as it ages from PAH formed near the burner nozzle to carbonaceous particles near the stagnation plate. Due to this evolution in properties, color ratio pyrometry has been implemented by using α as a free parameter tuned to impose agreement with the well-established OPPDIF temperature profile.

The trend of the optical dispersion exponent along the axial distance above the burner is shown in Fig. 3.12(b). α shows a decreasing trend from values close to 3.2 typical of hydrocarbons with a unity H/C ratio close to the burner nozzle. The initial increase in soot volume fraction at high temperatures in proximity of the flame front, is accompanied by a sharp decrease in dispersion exponent. This behavior suggests a high temperature inception of visible transparent particles with a relatively large hydrogen content [63, 110, 111]. This high temperature inception stage is followed by carbonization and further growth highlighted by a decreasing α. As soot matures, the H/C ratio becomes increasingly smaller through dehydrogenation and surface growth (e.g., via the HACA mechanism), with α approaching the 0.5 value typical of graphite. Values even larger than 3.2 can be reached for nascent soot, since nanosized particles of organic carbon are essentially transparent in the visible and absorb in the UV, which would yield a value of α diverging in the visible spectrum. Color-ratio pyrometry analysis for the carbon nanoparticles formed in flame conditions being studied show optical dispersion exponent values close to that of typical graphite indicating graphitization of carbon nanoparticles in the flame.

3.3.3 Carbon Structure as Inferred by Raman Spectroscopy

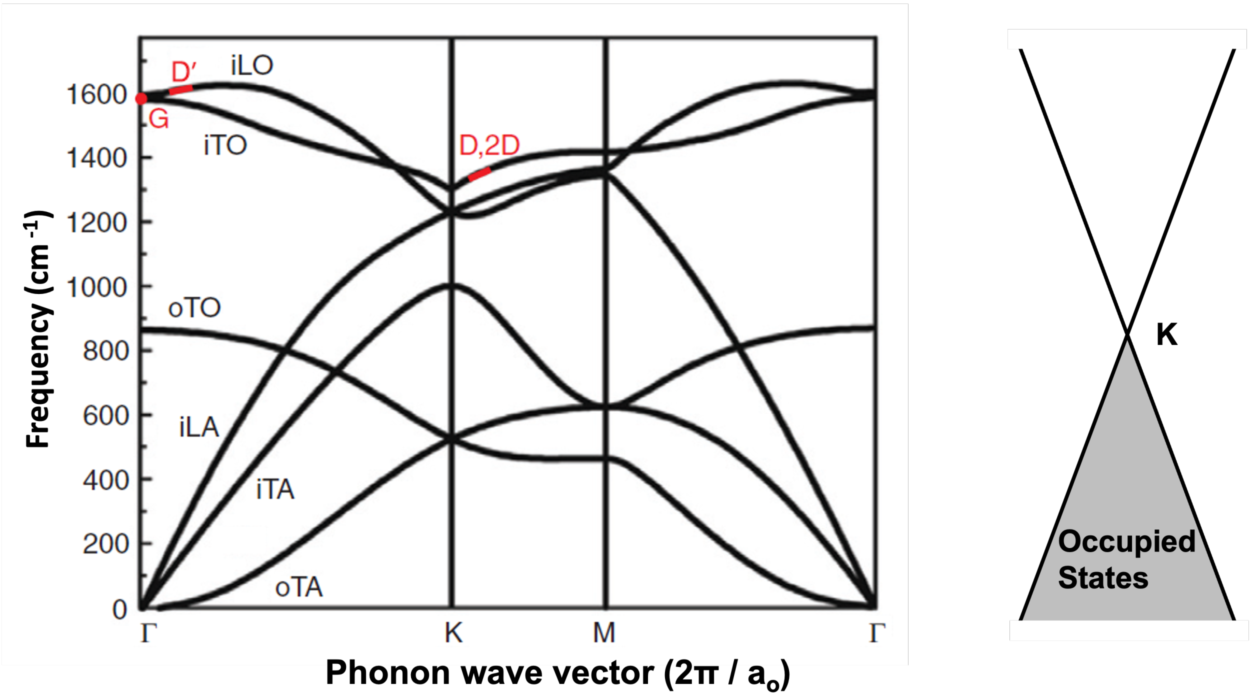

Figure 3.13: Phonon dispersion profile (left) and electron dispersion profile of graphite (right) [112]

With the gas-phase environment established, properties of flame formed carbon particles are now assessed. Raman spectroscopy is an effective tool for detecting precise structural information of carbon structure in soot and other graphitic materials. Raman scattering is a small fraction of the scattering that occurs when a photon is introduced to the material of interest but analysis of this process provides a wealth of information. Most photons simply scatter with only a change in direction (Rayleigh) but Raman scattering is also accompanied by a shift in photon energy due to interaction with phonon (vibrational) modes. The most likely Raman process (Stokes) results in a detection of a red-shifted photon that forms after an incident photon of known energy interacts with the material to induce an electron-hole pair and a new phonon (vibrational mode) [113]. The detected photon is characterized by a Raman shift caused by a loss in energy in accordance with the energy of the new phonon. Raman-active vibrational modes of carbon materials are related to the phonon dispersion profile of graphene. A map of graphene vibrational modes in reciprocal space is shown in Fig. 3.13 along with prominent Raman-active features. Electron dispersion is centered around the K symmetry points with energy bands bounded by the Dirac cones also shown in Fig. 3.13. The vibrational modes of graphene are in-plane longitudinal optical (iLO), in-plane transverse optical (iTO), out-of-plane transverse optical (oTA), in-plane longitudinal acoustic (iLA), in-plane transverse acoustic (iTA) and out-of-plane transverse acoustic (oTA).

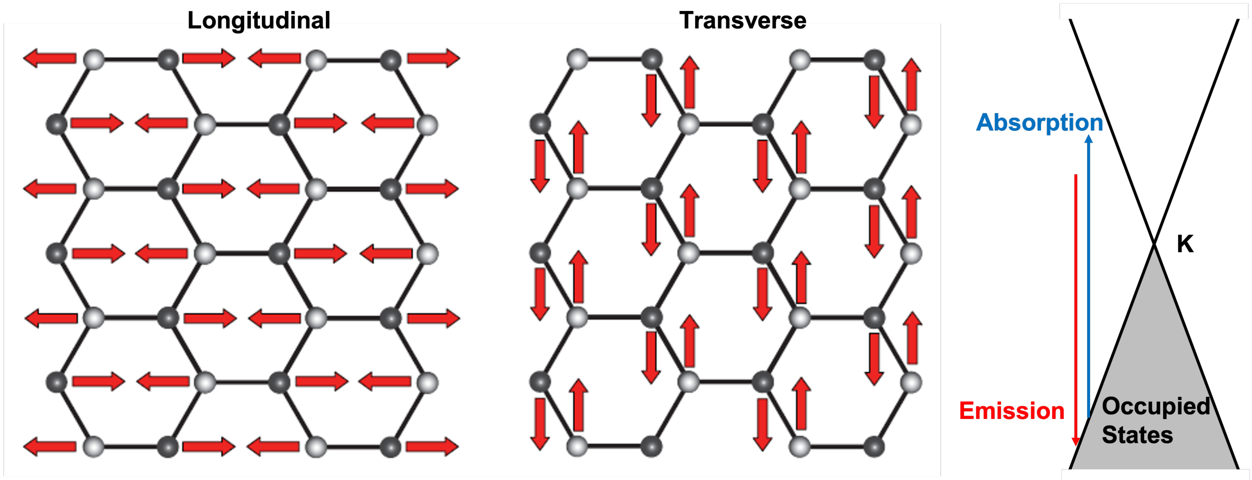

Figure 3.14: Degenerate E2g vibrational mode giving rise to the Raman G-band (left) and a diagram summarizing the role of electron dispersion cones in this Raman scattering process (right) [114]

The most prominent bands in Raman spectra of carbon materials are the so-called G and D bands. The origin of the G-band is the translational vibration of the sp^2 lattice shown in Fig. 3.14. In-plane optical phonons in the transverse and longitudinal coordinates give rise to the degenerate mode known as the E_{2g} mode [24, 115]. Another vibrational mode in the sp^2 lattice is the A_{1g} breathing mode that is only allowed in the presence of defects in the graphene lattice. After much debate, the Raman process giving rise to the D band is explained by the double - resonant process in involving two adjacent electron regions shown in Fig. 3.15.

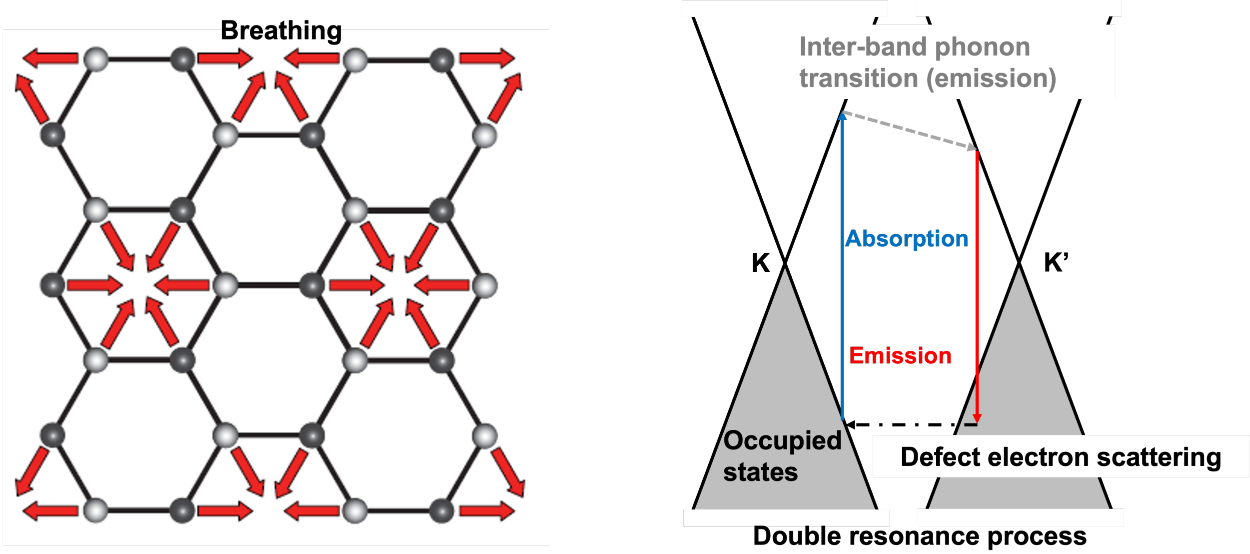

Figure 3.15: Breathing A1g vibrational mode giving rise to the Raman D - band (left) and a diagram summarizing the role of electron dispersion cones in this double-resonance Raman scattering process (right) [114]

The Raman signature for soot formed in the higher-temperature regime was previously shown to drastically transform from spectra traditionally reported [86]. This was explained in terms of the known response of carbon structures exposed to increasing temperature. This was explained in terms of the known response of carbon structures exposed to increasing temperature. TEM images, shown in Fig. 3.16, and mobility sizing measurements of carbon nanoparticles formed at higher - flame temperatures (discussed below) show the particles are also on the smallest nanoparticle size scale. This unique combination of ultra - fine particle size with an ordered carbon structure has only been reported by this laboratory and further investigation is carried out as part of this dissertation work. Previous Raman spectroscopy concepts borrowed from the graphite and graphene materials communities are used to interpret the measured spectra of the current materials. Soot formed at traditional flame temperature does not share Raman features with these materials but this unique flame formed carbon does.

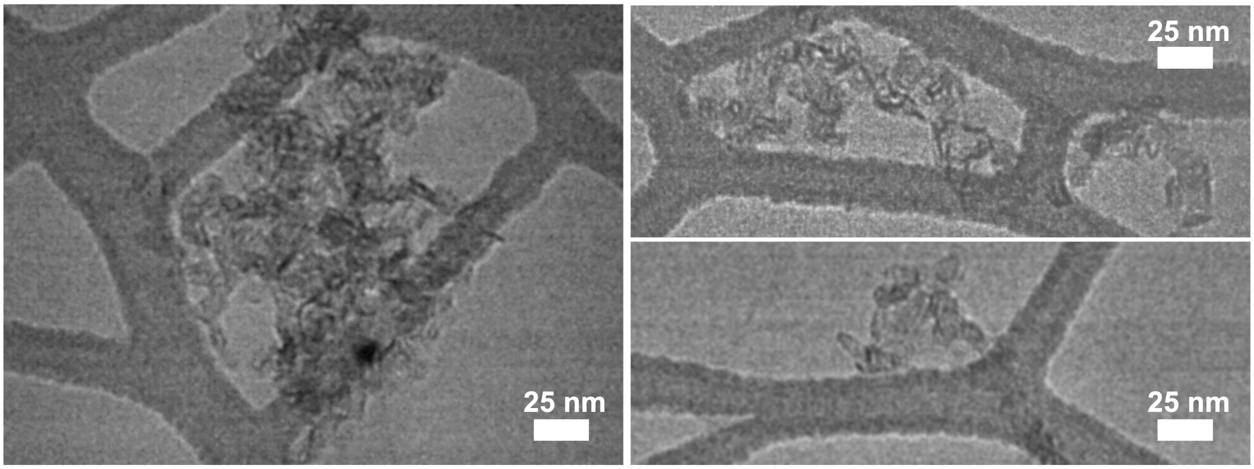

Figure 3.16: TEM images of flame formed carbon produced at flame temperatures higher than conventional flame temperatures.

Soot particles take on a variety of structures depending on the growth condition and age. At traditional flame temperatures, soot structure shows a slight resemblance to graphite properties only when the particle has matured long enough in the flame. Previous Raman measurements indicated that soot formed at higher than conventional flame temperatures exhibits graphite and graphene Raman features after a much shorter residence time in the flame [86]. Raman spectroscopy is further employed here to characterize the new carbon particles in terms of solid state chemistry of graphite and graphene materials. This approach begins with the unit cell of graphene shown in Fig. 3.17. Many of the physical properties are explained based in the reciprocal space representation for graphite and graphite also shown in Fig. 3.17. Evolution from typical soot spectra to Raman features resembling graphitic materials was previously observed for increasing flame temperature [86]. The current work expands on this to also show the evolution for increasing temperature and equivalence ratio. Further carbon structure information is obtained by observing dispersion effects due to different excitation wavelengths introduced to the sample. The evolution of carbon structure with increasing flame temperature could be understood from the so - called amorphization trajectory introduced by Ferrari and Robertson for a range of amorphous and graphitic carbons [21, 26]. The Raman response of the sample to different excitation wavelengths manifests in terms of the D band Raman shift position shift [116] and the increase G band intensity expected for higher excitation energy [117].

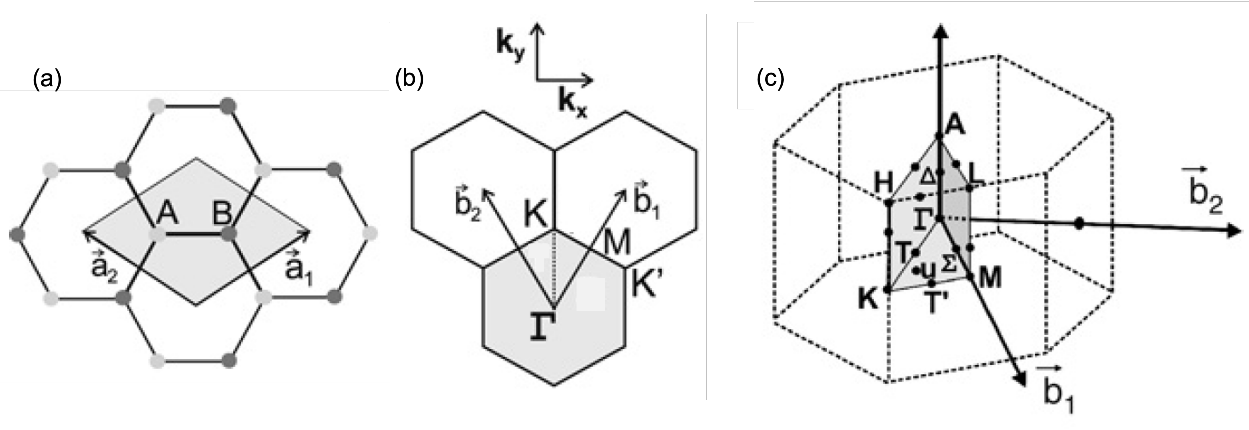

Figure 3.17: Graphene unit cell in real space (a), graphene unit cell in reciprocal space (1st Brillouin Zone, b) and 3D graphite unit cell in reciprocal space (1st Brillouin Zone, c) [115]

This approach is expanded to also examine the effect of increasing equivalence ratio. This analysis provides valuable insights into unique higher-temperature soot formation processes and material properties. Raman spectra for primary peaks of deposited films excited with a 532 nm source are shown in Fig. 3.18 for each flame series. The 5-band deconvolution approach established by Sadezky and co-workers [16] for flame-formed carbon is used to examine known Raman-active modes. Nomenclature of Sadezky is used only for the Raman bands unique to soot (D3 and D4) with the remaining peaks taking labels more commonly reported in the broader carbon literature. As discussed below, D and D' are commonly observed primary bands with corresponding 2D and 2D' secondary bands. Another secondary band is D + G commonly reported at 2945 cm^{-1} for 514.5 nm excitation wavelength. This nomenclature is adopted to compare the observations to other Raman studies of disordered carbon, which unlike soot, show well-defined secondary bands. Baseline correction and deconvolution procedures are described in Section 2.3.2. The highest peak intensity is identified in each measured spectrum and this is used to normalize the intensities. The highest peak intensity either appears in the G or D band for the conditions being studied.

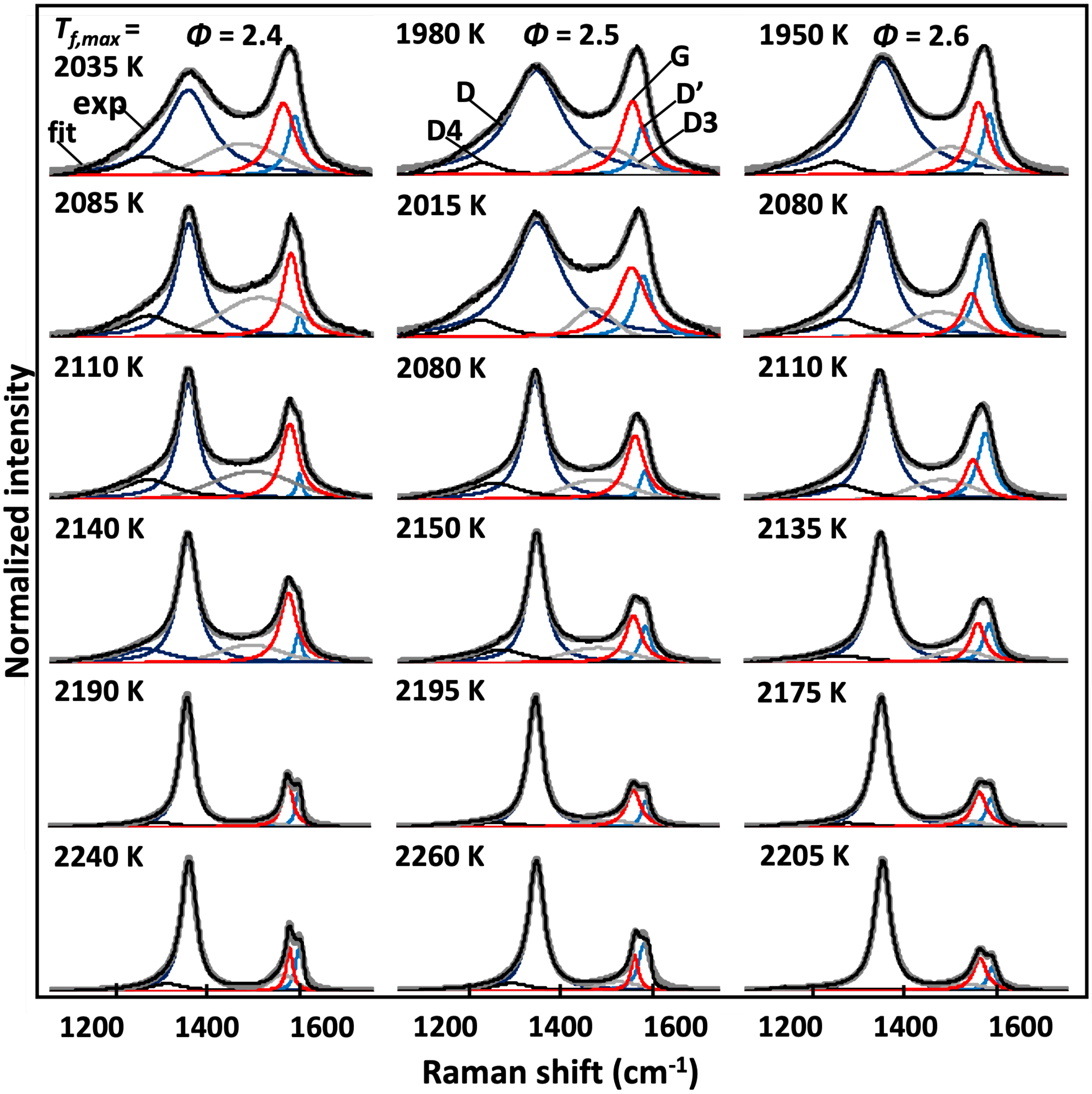

Figure 3.18: Baseline-corrected Raman spectra of primary peaks for all flame conditions (532 nm excitation source). The measured spectra are fitted according to the five-band deconvolution.

For each equivalence ratio series, a striking evolution in the spectra occurs with increasing flame temperature. The series begin with a signature typically reported for soot followed by a drastic shift in relative intensity and peak width. Signatures commonly reported for soot are partially composed of D3 and D4 bands which have been attributed to amorphous components and sp^3 bonds, respectively [16]. Disappearance of the "soot" bands (D3 and D4) with increasing flame temperature may be an indication that material properties of carbon particles formed in the higher-temperature regime differ from soot. Peaks corresponding to the so-called D, G and D' bands also evolve indicating a progression in sp^2 carbon bonding. The G band is attributed to stretching modes of all sp^2 bond pairs. Although highly order graphite only shows a G band, this mode does not require an aromatic ring [21, 22, 118, 119]. In contrast, the breathing motion of sp^2 bonded carbon in 6-member rings gives rise to the D band and is only observed in lattices deviating from perfect graphite [21, 22]. The D' band has been associated with surface sp^2 bonds also in the context of defects to a pristine graphite lattice [16, 120].

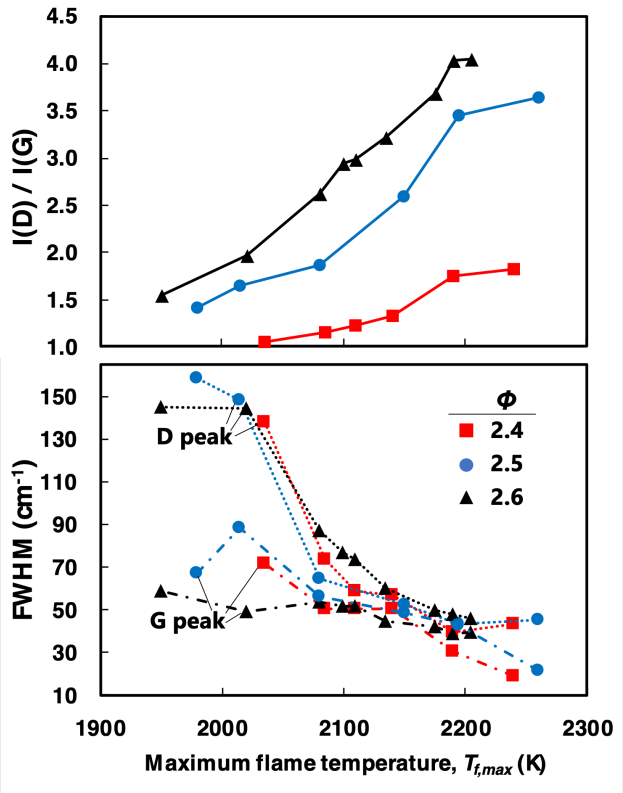

Figure 3.19: Evolution in I(D)/I(G) (top) and peak FWHM (bottom) based on Raman spectra of deposited carbon films for all flame conditions studied. Lines are drawn to guide the eye.

The width and relative intensity of characteristic Raman bands have been correlated to carbon structural order and crystallinity [21, 24, 26, 118, 121]. The ratio of peak intensities for the D and G band (I(D)/I(G)) and the peak widths have been used for quantitative characterization based on phenomenological analysis. The observed evolution in the D and G ratio and peak widths (FWHM) is shown in Fig. 3.1. At lower flame temperatures, the FWHM of the D peak is much wider than the G peak but significant narrowing of the D peak is observed for the higher temperature conditions. The disappearance of the "soot" bands and significant narrowing of the peaks may indicate that soot formed in the higher-temperature regime approaches the structure reported for other sp^2 carbon materials. Semi-empirical relations developed by Tuinstra and Koenig [121], Ferrari and Robertson [21], Pimenta and coworkers [122], Jorio and co-workers [123], and, more recently, Ferrari have related the relative intensity of the D and G bands to the characteristic size of an uninterrupted sp^2 lattice which, among other labels, has been referred to as the in-plane crystallite size, L_a. Now famous experiments by Jorio and co-workers [123] illustrated the response of Raman scattering to systematic addition of graphene defects by ion bombardment. This work introduced a wide-ranging phenomenological expression for predicting behavior in high and low defect regimes. The so-called defect distance, L_d, was introduced for the ion bombardment experiment to acknowledge that the defect surface density was being measured by Scanning Tunneling Microscopy and this could be related to the length scale of the undisturbed lattice [123].

The phenomenological expression introduced by Jorio and co-workers is applied for illustrative purposes [123]:

$$\frac{I(D)}{I(G)} = C_A \frac{(r_A^2 - r_S^2)}{(r_A^2 - 2r_S^2)} \left(exp\Big(\frac{-\pi r_S^2}{L_D^2}\Big) - exp\Big(\frac{-\pi (r_A^2 - r_S^2)}{L_D^2}\Big) \right) + C_S \Big(1 - exp\Big(\frac{-\pi r_S^2}{L_D^2}\Big)\Big) \quad (3.1)$$

where I(D) / I(G) is the relative intensity of the D and G peaks in the Raman spectrum and the rest of the parameters are established based on the ion bombardment experiment on graphene. The defect induced by bombardment of Ar+ creates a "structurally disordered" area with radius r_S. A larger area also surrounds the defect with radius r_A having a mixture states due to proximity to the defect. The coefficient C_A has been characterized as a measure of the maximum I(D)/I(G) ratio with a theoretical limit tied to electron-phonon coupling [123]. The C_S coefficient is related to the I(D)/I(G) ratio in the highly disorder limit. Parameter values from the ion bombardment experiments are adopted ($r_A = 3.0nm,\ r_S = 1.0nm,\ C_A = 4.6,\ C_S = 0.87$) to extract the defect distance, L_D, of the flame-formed carbon. Although the parameters may not precisely correspond to the flame formed carbon being investigated, the above expression may shed light on the evolution in carbon structure with increasing flame temperature. In fact, the narrow bands, prominent D' band and evolution of the Raman spectra are features shared with reported spectra for studies on evolution of disorder for multi-layer graphene [123–125].

The classical formulation relating L_a to I(D)/I(G) postulated by Tuinstra and Koenig [121] has been predicted to be limited for applications to graphitic materials with $L_a > 3nm$ [21, 24, 123, 124]. Using this limit to separate high and low disordered regimes, Ferrari introduced semi-empirical relations to correlate the defect distance to intensity ratio and the excitation energy with separate equations for the high and low defects [24]. Raman spectra of the flame-formed carbon may correspond to the high-defect density regime reported in several systematic studies where the I(D) / I(G) ratio was shown to increase with the defect distance [21, 22, 24, 26, 119]. The expression given in the context of high defect graphene by Ferrari and Basko [24] is used as a second method to correlate to the defect distance for the flame-formed carbon. The following is applied for the regime in which $L_a < 3nm$:

$$L_D^2 = 5.4 \times 10^{-2}\ E_L^4 \frac{I(D)}{I(G)} \tag{3.2}$$

where E_L is the excitation energy in electron volts. The excitation energy is $E_L = 2.33eV$ corresponding to the 532 nm excitation source used in this work. The dependence on excitation energy in Eq. 3.2 is also based on ion bombardment experiments [125] and the empirical expression $C_A = (160 \pm 48\ eV^4)E_L^{-4}$ is embedded to account for dispersion effects observed in the bombardment experiments.

The evolution in defect distance computed from the above expressions is shown in

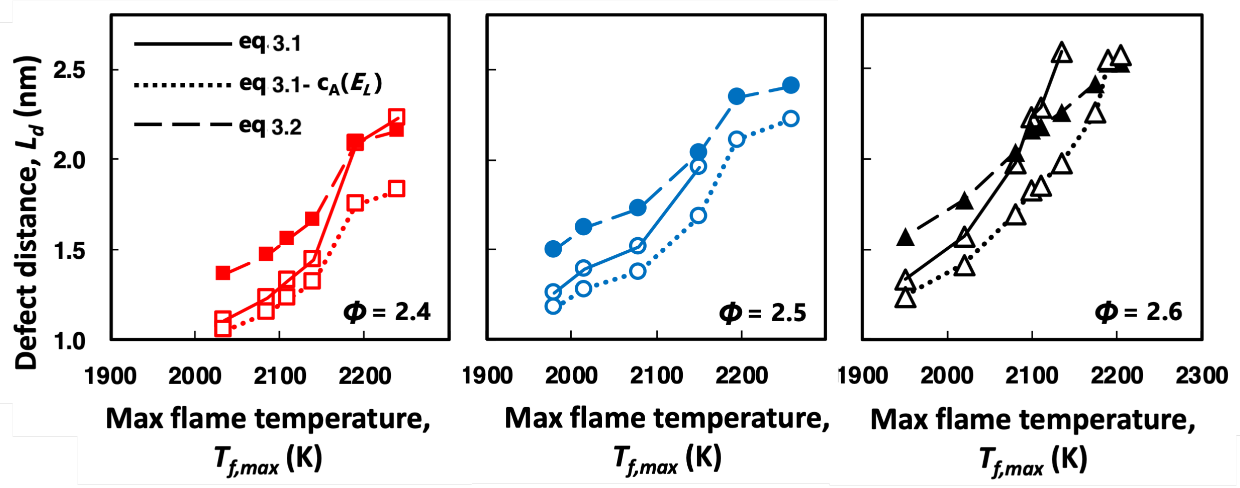

Figure 3.20: Evolution in defect distance based on Raman spectra of deposited carbon films for all flame conditions studied. The $\phi = 2.4$ (left), $\phi = 2.5$ (middle) and $\phi = 2.6$ (right) predictions are shown for three different correlations. The lines are drawn to guide the eye.

Fig. 3.20. A defect distance on the order of unity observed for the lower flame temperatures is in agreement with reports for typical flame soot. Miller and co-workers have interpreted this size to correspond to a building block of soot on the order of 4-5 aromatic rings [29]. For all equivalence ratio conditions, the observed defect distance increases with increasing flame temperature. This trend is in line with known carbon annealing behavior [119, 126] and entropy-driven carbonization processes [127, 128]. In addition, a systematic trend is observed showing, for a given flame temperature, the defect distance increases with equivalence ratio. That is, a larger region of crystalline carbon structure is observed with higher equivalence ratio.This observation may be explained on the basis of carbon lattice defects. Namely, the greater abundance of gas-phase PAH surrounding the carbon may facilitate development or "healing" of an ordered lattice during formation and growth.

The I(D)/I(G) ratio measured for the current flame-formed carbon is higher than the peak ratio of ~ 3.5 reported by Jorio and co-workers and this may be due to the slightly different excitation energy [123] applied or carbon structural differences. As such, the Jorio expression does not converge for the $\phi = 2.5$ and 2.6 cases above 2150 K due to the relatively high I(D)/I(G). A third expression is applied here which combines the original

Jorio expression with the excitation energy dependence. The 2.33 eV excitation applied in the current measurements corresponds to $C_A = 5.4$ according to the $\mathrm{C_A(E_L)}$ correlation embedded in Eq. 3.2 [125]. The predictions based on the Jorio expression incorporating this modified parameter is also included here. As Fig. 3.20 shows, there is up to a 30 % discrepancy observed between the three defect distance predictions. These correlations were developed for graphene materials and specifically calibrated for separate ion bombardment experiments. As such, application to the current flame-formed carbon is an extrapolation of these correlations and disagreement among the predictions is expected. Nonetheless, the qualitative trends of increasing order with increasing temperature and equivalence ratio still hold despite limitations of the current assumptions. Although, the parameters and correlations are borrowed from bombardment studies on graphene materials, the trends predicted for the current flame-formed carbon are informative. Typical Raman spectra reported for soot show mild changes for studies done at typical flame temperatures. In contrast, the response of the Raman spectra of flame-formed carbon to higher temperature conditions is dramatic and this can be interpreted to indicate that the carbon structure is more ordered than typical soot.

Secondary bands are not typically analyzed for soot formed at conventional flame temperature because soot is relatively disordered. In contrast, Raman spectra from the current high-temperature carbon products show distinct secondary bands. The evolution in secondary peaks is shown in Fig. 3.21 for all flame conditions studied. Secondary peaks corresponding to overtones of the D, G and D' bands are discernible for carbon formed at flame temperature hotter than 2050 K. In literature for disordered sp^2 carbon materials, these are bands are denoted as 2D and 2D' with an additional secondary band denoted as D + G. The secondary peaks become narrower and more resolved as flame temperature is increased. Interestingly, the 2D band is commonly considered to be the most prominent peak in the secondary spectra of disordered carbon [119, 129]but the D + G band is only dominant for the middle range of flame temperatures currently studied. The observed evolution in Raman

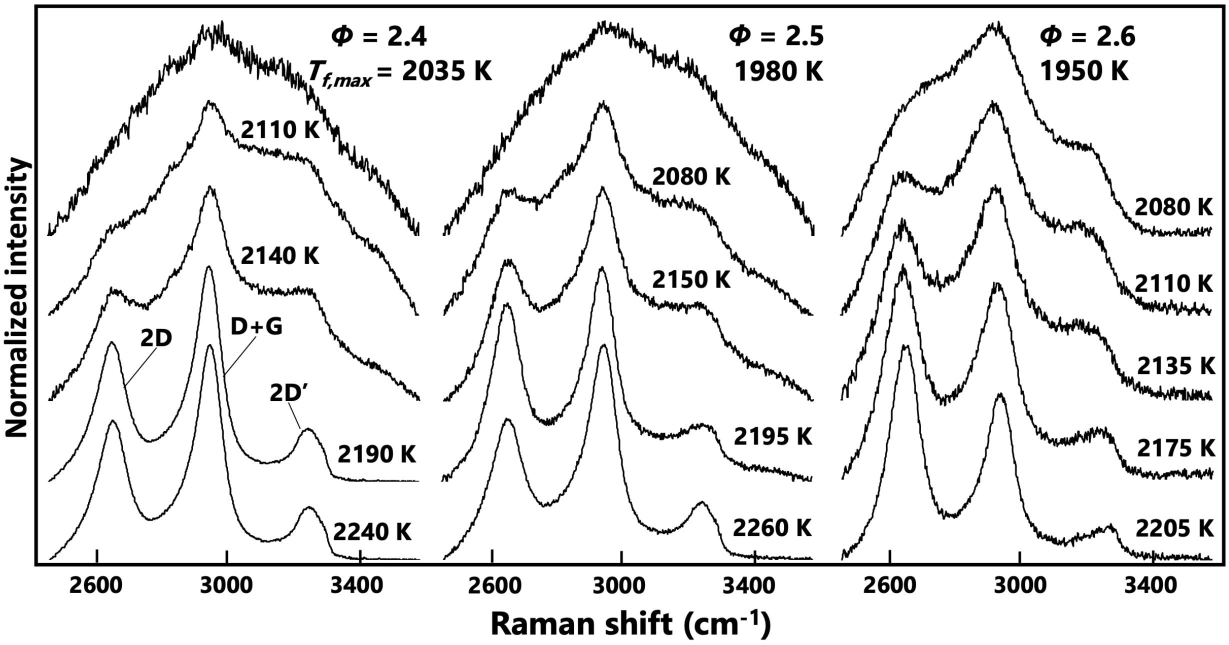

Figure 3.21: Evolution in baseline-corrected secondary Raman peaks for all flame conditions studied.

signature may indicate the current flame-formed carbon transitions from conventional soot to structure observed in high-defect sp^2 carbon.

The higher equivalence ratio series shows the most resolved secondary peaks in accord with the relative evolution of the primary peaks. Deconvolution of the 2D band into 2D$_1$ and 2D$_2$ bands is carried out as established in literature for disordered graphite an graphene materials [22, 129]. Deconvolution for the highest temperature conditions of the $\phi = 2.6$ case is shown in Fig. 3.22. A transition occurs whereby the 2D$_1$ is greatest at the 2110 K flame condition and becomes usurped by the 2D$_2$ peak at higher flame temperature. These relative intensities has been reported as a transition from powdered graphite to a carbon structure approaching highly ordered pyrolytic graphite [129]. Analysis on flame-formed carbon nano-discs reported by D'Anna and co-workers [25] provides an additional example of a unique structure having features of both stacked graphitic carbons and three-dimensional turbostratic structures. The secondary peaks observed in the intermediate temperature range of the current work may correspond to the aforementioned features of the nano-disc Raman

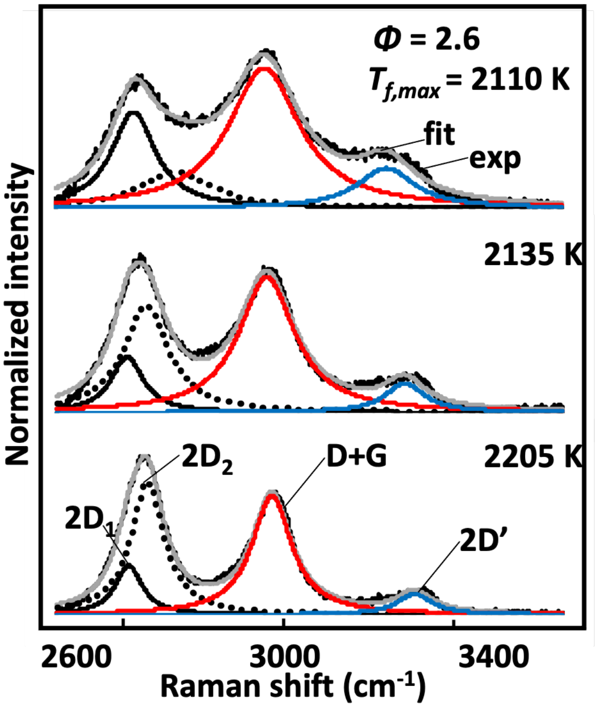

Figure 3.22: Baseline-corrected deconvoluted Raman peaks (2D band) for the $\phi = 2.6$ case with increasing flame temperature.

spectra followed by evolution to more ordered structure with increasing temperature. The Raman active modes of carbon enable the subtle variation in carbon structure to be examined for the series of flame conditions currently studied. The Raman spectra provide evidence that carbon structure approaching sp^2 carbon materials could be obtained. This is especially promising if the precise carbon structure could be functionalized for tuned material behavior.

A detailed structural analysis of flame formed carbon is performed for two flame conditions (Table. 3.1) and industry grade hard carbon (MSE Supplies, Particle size : 8 - 12 μm). Multi-wavelength Raman spectroscopy is employed to characterize the nanoparticles and their properties. Soot primarily consists of agglomerated primary particles with diameters on the order of 10 - 30 nm comprising of crystalline and amorphous components. The graphite-like crystalline structure consists of a few turbostratically stacked graphene layers [16].

An ideal graphite lattice has layers arranged in an alternating sequence corresponding to a hexagonal crystal structure with unit cells of four C atoms at two types of lattice sites with different coordination numbers. Amorphous soot is composed of polycyclic aromatic hydrocarbons with irregular onion-like structure [16]. The structure of flame formed carbon is dependent on its growth conditions as seen in the previous section. The fuel structure and composition, equivalence ratio, flame temperature and residence times play a vital role in determining the carbon structure. The structure of carbon nanoparticles as formed in high temperature flames are investigated. The structures are compared to that of industry grade hard carbon.

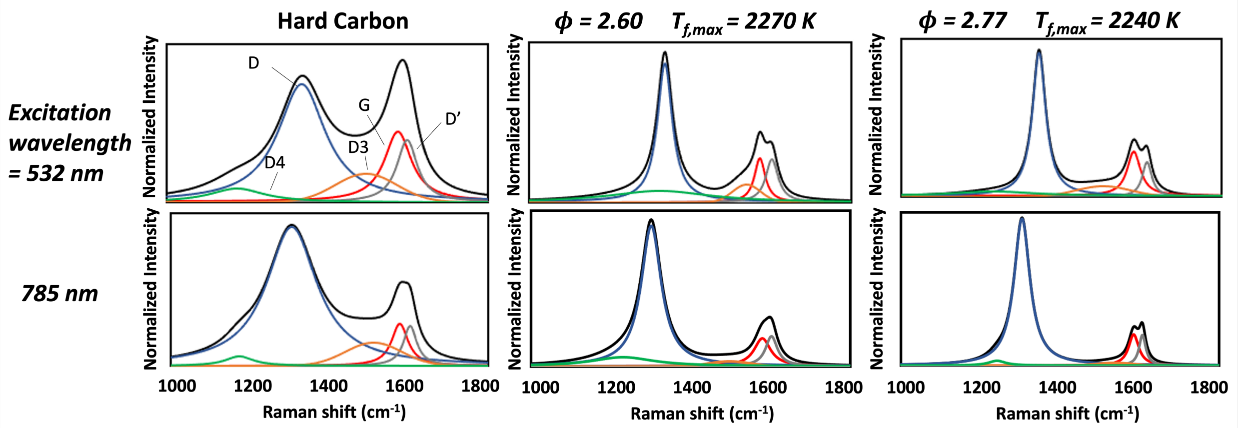

Figure 3.23: Baseline-corrected Raman spectra of primary peaks (532 nm (top panel) and 785 nm (bottom panel) excitation source). The measured spectra are fitted according to the five-band deconvolution.

For disordered materials like soot and flame formed carbon, Raman spectroscopy is sensitive to the crystal structures and the molecular structures. The Raman signals of graphite structures are due to lattice vibrations and is sensitive to the degree of disorder in the structure. Rosen and Novakov used Raman spectroscopy to show the presence of graphite like carbon in soot formed in diesel engines [130, 131]. Further, soot structure investigations through Raman spectroscopy found different soot structures with varying degrees of graphitization [16, 132]. The graphitization of soot and flame formed carbon have been measured through spectral parameters from different correlations (eg. Eq. 3.1 and Eq. 3.2). Multi-wavelength Raman spectroscopy is performed to investigate the flame formed

Table 3.2: Detailed Raman spectroscopy results

Material	**Position**		**FWHM**		I_D/I_G	L_d	L_d
	(G)	**(D)**	**(G)**	**(D)**		**(Eq. 3.1)**	**(Eq. 3.2)**
	(cm^{-1})	(cm^{-1})	(cm^{-1})	(cm^{-1})		(nm)	(nm)
Wavelength: 532 nm, Excitation Energy: 2.33 eV							
Hard Carbon	1575	1336	81	143	1.68	1.28	1.63
FFC 2.60	1580	1344	41	41	3.12	1.96	2.25
FFC 2.77	1574	1338	32	45	3.22	1.98	2.26
Wavelength: 785 nm, Excitation Energy: 1.58 eV							
Hard Carbon	1577	1305	50	155	3.32	1.14	1.06
FFC 2.60	1586	1305	31	49	4.76	1.26	1.27
FFC 2.77	1580	1301	50	61	5.00	1.28	1.30

Position () - Peak position, FWHM () - Full width half maximum of peak,
L_d - Defect distance as calculated with respective equations.

carbon structure and the extents of graphitization. Two excitation wavelengths (532 nm and 785 nm) are employed for this analysis. The Raman spectra is analyzed using 5 peak deconvolution consisting of G, D, D', D3 and D4 bands. The spectral parameters of the Raman spectra are provided in Table 3.2.

Fig. 3.23 shows the primary peaks Raman spectra (Raman shift: 1000 cm^{-1} - 1800 cm^{-1}) for hard carbon and flame formed carbon. Hard carbon shows a disordered carbon or soot like Raman spectra with broad D and G peaks similar to signatures observed in the literature. G band is assigned to the E_{2g} phonon at the Brillouin zone center. The mechanism giving rise to the G band starts with an incident photon that resonantly excites a virtual electron - hold pair in the carbon structure. The electron - hole pair then radiatively re - combine and emits a photon that is red-shifted by the amount of energy that is transmitted to the phonon. This band exists for all sp^2 carbon structures [114]. The G band positions for hard carbon is 1575 cm^{-1} for an excitation wavelength of 532 nm and 1577 cm^{-1} for 785

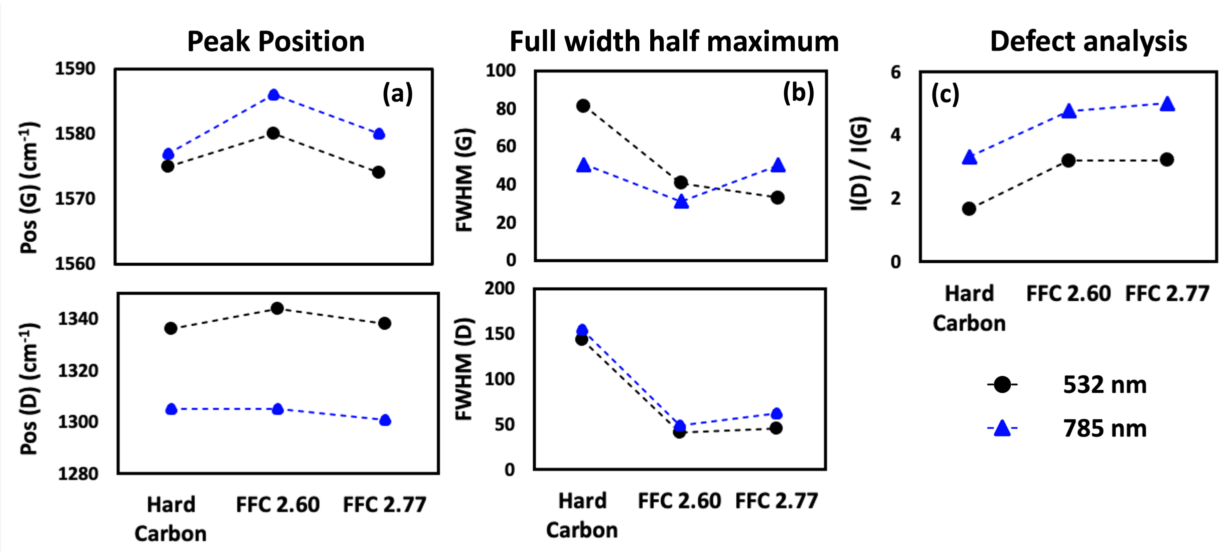

Figure 3.24: Analysis of Raman spectral parameters (a) Peak positions and (b) Full width half maximum of G and D peaks (c) I(D)/I(G) for different materials and excitation wavelengths.

nm. The D peak in hard carbon is a wide band with peaks at 1336 cm^{-1} and 1305 cm^{-1} based on the excitation wavelength of 532 nm and 785 nm respectively. The D band is due to the breathing modes of six atom rings and indicates the presence of defects [125]. The D peak is insensitive to the type of defects but only to the amount of disorder. D' peaks, observed at the shoulder of the G peak of the hard carbon sample, is about the same height and width as that of the G peak. The D' peak is due to the presence of defects in the carbon sample and is sensitive of the type of defect in the lattice. The D' peak arises due to the double resonance intravalley scattering [24, 133]. The D3 and D4 bands show significant contribution to the Raman spectra further indicating an amorphous disordered structure.

The Raman structure for flame formed carbon at $\Phi = 2.60$ and $\Phi = 2.77$ for excitation wavelengths of 532 nm and 785 nm are also shown in Fig. 3.23. Both samples show signs of significant graphitization and resemble Raman signatures similar to that of defective graphene [125, 134]. From Table. 3.2 and Fig. 3.24, the mean position of the G band is noted to be 1580 cm^{-1} with a standard deviation (s.d.) up to 5 cm^{-1}. This is in line with the spectra observed for hard carbon indicating that the position of the G band does not significantly depend on the excitation wavelength or the significant differences between soot

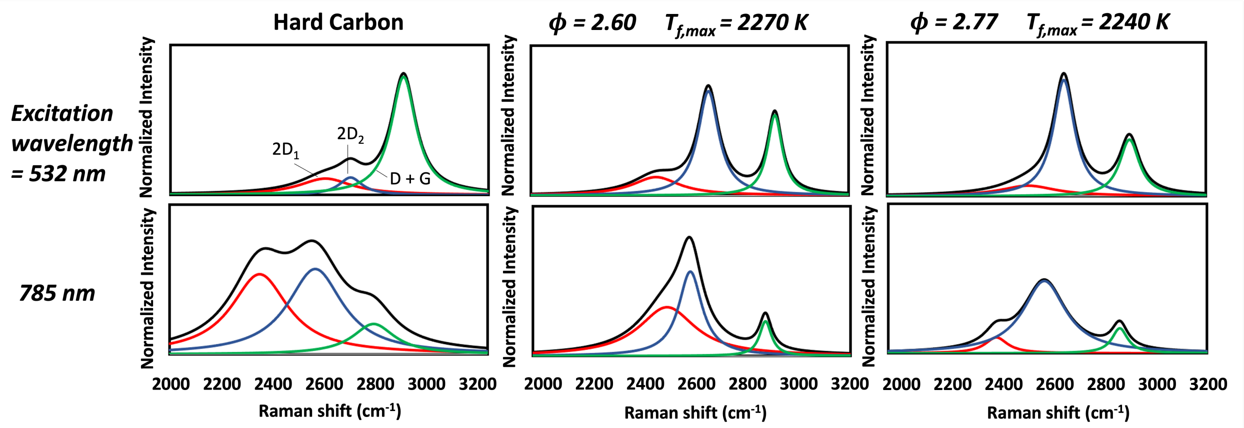

Figure 3.25: Baseline-corrected Raman spectra of secondary peaks (532 nm (top panel) and 785 nm (bottom panel) excitation source). The measured spectra are fitted according to the three-band deconvolution.

and graphite [16, 125]. D band on the other hand, has a mean position of 1341 cm^{-1} (s.d. $\leq$ 4) for 532 nm excitation wavelength and 1303 cm^{-1} (s.d. $\leq$ 3 cm^{-1}) for 785 nm excitation wavelength. The D band position exhibits pronounced dependancies on the laser excitation wavelength without significant differences between hard carbon and flame formed carbon. The dependance of D band position on the excitation wavelength is attributed to resonance effects [24]. The FWHM of G and D band is shown in Fig. 3.24(b) are significantly low for flame formed carbon when compared to hard carbon for both excitation wavelengths. In contrast to the band position, FWHM does not show any significant dependence on excitation wavelength. For carbon samples formed at $\Phi = 2.60$ and $\Phi = 2.77$ flame conditions, G and D' become narrow and split into obtain a doublet structure indicating graphitization of nanocrystalline carbon [22, 24, 26].

The quantification of defects in carbon through Raman spectroscopy, the D and G intensity ratios (I_D/I_G) are used. The Fig. 3.24(c) show the intensity ratio for different samples and excitation wavelengths. The I_D/I_G increases with increasing excitation wavelength. The ratio also increased significantly between hard carbon and flame formed carbon. The I_D/I_G ratio increases slightly on increasing equivalence ratio from $\Phi = 2.60$ to $\Phi = 2.77$. The increase in I_D/I_G ratio is indicative of graphitization of the carbon nanoparticles and evolution of carbon from sp_2 amorphous carbon to nanocrystalline structure.

The secondary peaks (Raman shift: 2000 cm^{-1} - 3200 cm^{-1}) of Raman spectra is shown in Fig. 3.25. The secondary peaks are attributed the overtones and combinations of graphitic vibration modes. Hard carbon samples exhibits broad signals when compared to the flame formed carbon being analyzed. This behavior is observed for both excitation wavelengths. The flame formed carbon samples at $\Phi = 2.60$ and $\Phi = 2.77$ have narrower $2D_1$, $2D_2$ and D+G and lower FWHM when compared to hard carbon. This indicates graphitization of flame formed carbon. The secondary peak of flame formed carbon is less pronounced for an excitation wavelength of 785 nm than that of 532 nm. The $2D_1$ band is less intense than the $2D_2$ and the D+G for flame formed carbon than hard carbon. This is related to the larger number of layers present in hard carbon when compared to flame formed carbon [133]. The increase in the number of layers leads to an increase in the intensity of the higher frequency, $2D_2$ band when compared to the $2D_1$ [135]. The results observed, specifically for the flame formed carbon samples, show Raman spectra similar to that of nanocrystalline graphite and signs of defective graphene structure.

3.3.4 Carbon Structure as Inferred by X-Ray Photoelectron Microscopy

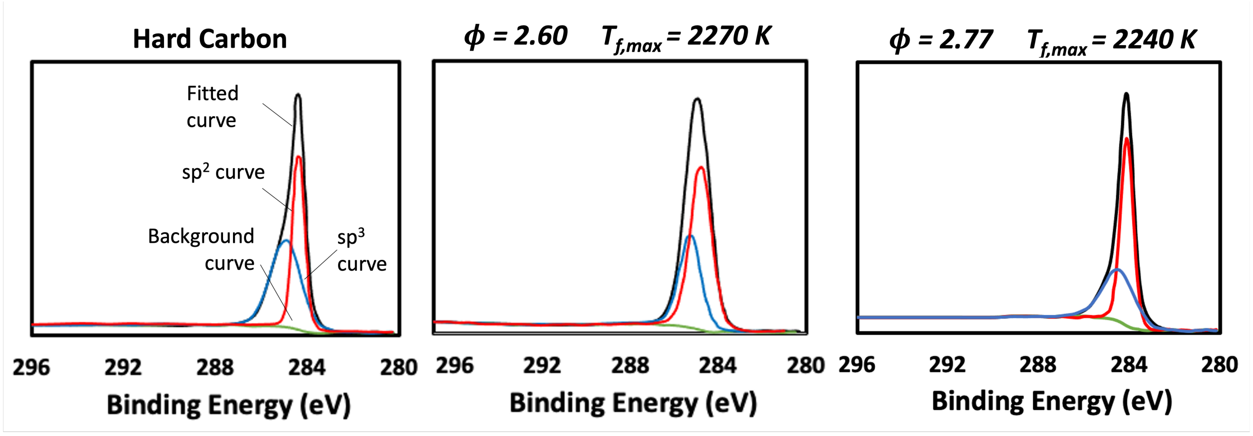

Figure 3.26: C1s XPS spectra for hard carbon, $\Phi = 2.60, T_{\text{f,max}} = 2270K$ and $\Phi = 2.77, T_{\text{f,max}} = 2240K$

X-ray photoelectron spectroscopy (XPS) is a convenient technique to determine the sp^3/sp^2 bonding ratio. The ideal graphite exhibits sp^2 at a binding energy of 284.5 eV [136]. Typical XPS spectra of carbon structures with sp^3 and sp^2 hybridization are positioned between 284.25 and 285.0 eV with the sp^2 bond between -1.1 and - 0.5 eV. The values of C sp^2/sp^3 binding energy separation obtained by Fujimoto et al. for carbon-hydrogen-oxygen structures showed that the assignment of the C sp^2 and C sp^3 peak and C sp^2/sp^3 separation value depend on hydrogen content, whereas experimental results for diamond in graphite are influenced by charging effect of diamond C sp^3 domains [137, 138].

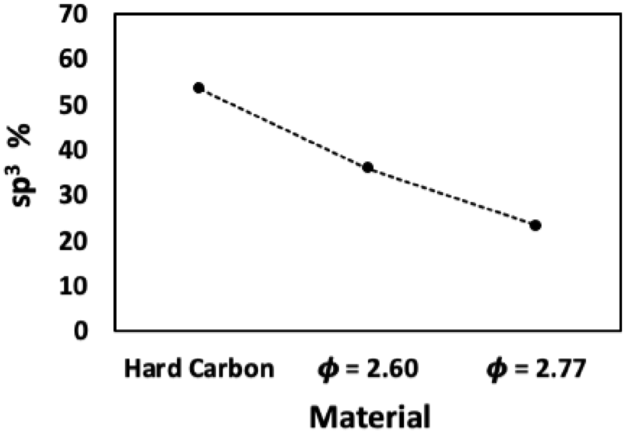

Figure 3.27: Percentage of sp^3 hybridization in hard carbon, and flame formed carbon samples at $\Phi = 2.60, T_{\text{f,max}} = 2270K$ and $\Phi = 2.77, T_{\text{f,max}} = 2240K$

The C1s XPS spectra of hard carbon and flame formed carbon samples are provided in Fig. 3.26. The two curve fitting method is employed as described in Section 2.3.5. The peaks are observed at ∼284.9 eV due photoelectrons excited from C1s. The C1s is assumed to consist of 2 peaks, sp^3 and sp^2 peaks and deconvoluted accordingly [73]. The average binding energy separation between the sp^3 and sp^2 peaks ∼-0.50 eV which agrees with the available literature. The sp^3 % is shown in Fig. 3.27. The areas under the sp^3 and sp^2 curves are used for this calculation. The hard carbon sample exhibits the highest sp^3 % at ∼50% implying a higher amorphous content. The flame formed carbon samples show significantly lower sp^3 hybridization indicating more graphite like nature [73, 136, 138]. This result is in accordance with the results observed from Raman spectroscopy.

3.3.5 Carbon Structure as Inferred by Scanning Mobility Particle Sizing

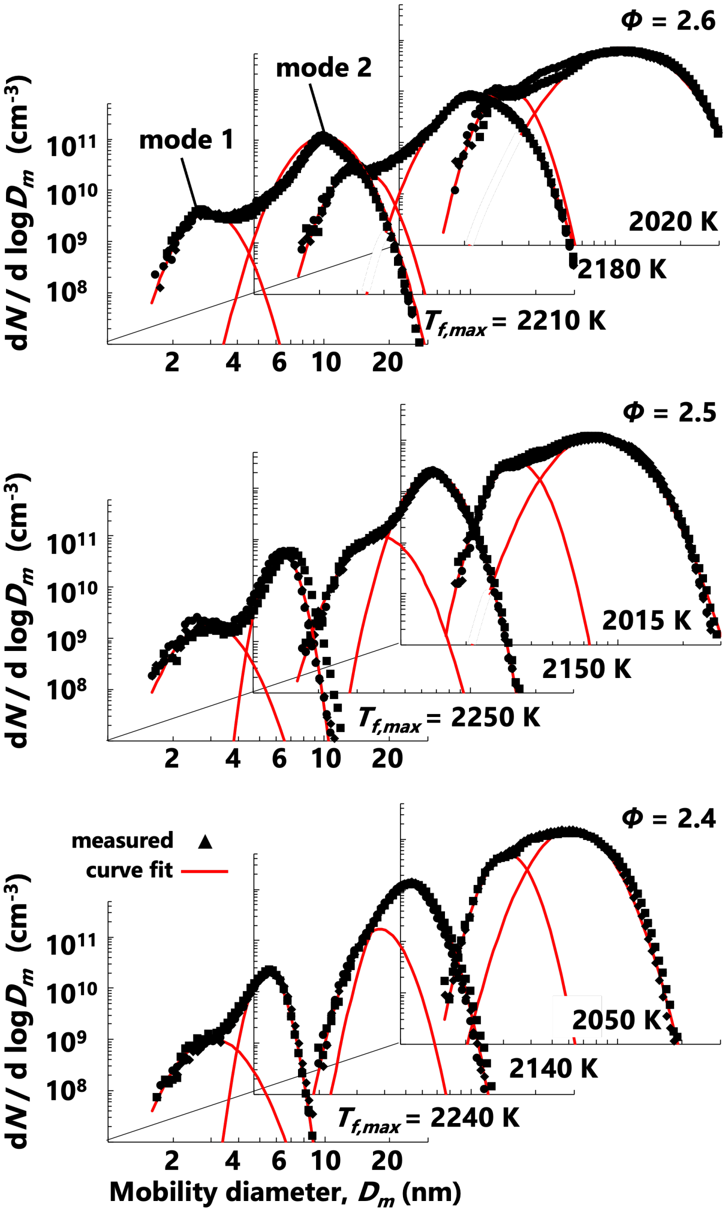

Figure 3.28: Measured PSDF for selected flame conditions. Symbols are measurements and lines are curve fits to a lognormal distribution for each size mode.

Direct observations of unique higher-temperature soot formation processes are also reported here in terms of detailed PSDF measured by mobility particle sizing. An established aerosol sampling method [7, 42] is applied to quantitatively follow evolution in the size distribution for increasing flame temperature and equivalence ratio. Measured PSDF for each flame series is shown in Fig. 3.28 along with lognormal curve fits of the observed bimodal distribution. The observed decrease in number and size range with increasing flame temperature for each equivalence ratio series is expected based on reversibility in precursor formation and reduced collision efficiency. A bimodal distribution consisting of nucleation-sized particles and a slightly larger mode of growth particles is observed in all cases. For the highest temperature cases, a visible split between the size modes becomes apparent as the width of the growth mode significantly narrows. PSDF in premixed sooting flames at conventional flame temperature (see e.g [53, 55]) have reported a bimodal distribution with a dominant nucleation mode relative to the growth mode. The magnitude of the nucleation mode is lower in the PSDF currently observed which may indicate that nucleation processes are not as persistent in the higher-temperature soot formation regime.

Parameters of the log-normal curve fitting provide further insight into competing soot formation processes in terms of global properties of the size distribution. The global parameters are plotted for each maximum flame temperature condition in Fig. 3.29. The median diameter of the growth mode varies by nearly a factor of two between the lowest and highest equivalence ratio cases. In contrast, the nucleation-size mode has a median of 3 nm across all conditions. The observed size range corresponds to isolated primary particles and small particle clusters rather than larger aggregates. Evolution in the geometric standard deviation occurs in opposing directions for the two size modes which may indicate size-dependent particle growth processes are occurring. The number density is nearly an order of magnitude greater for the growth mode particles and reduction in soot yield with increasing flame temperature is observed in terms of number density and volume fraction.

The particle size distribution is also measured for $\Phi = 2.60, T_{\text{f,max}} = 2270K$ and $\Phi = 2.77, T_{\text{f,max}} = 2240K$ as shown in 3.30. Particles with a median diameter of ~ 9 nm and 13 nm are observed in both cases respectively. The volume fraction observed in $\Phi = 2.60$ case is an order of magnitude lower than that of $\Phi = 2.77$ for a 30K peak temperature

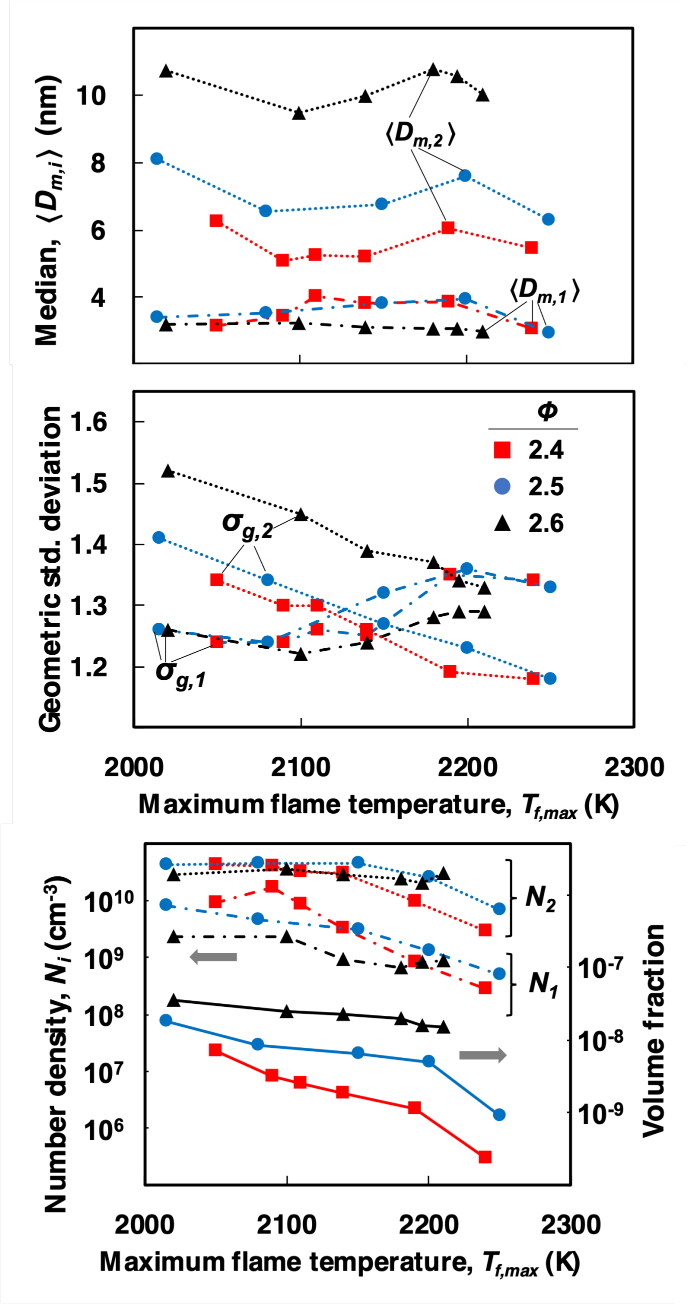

Figure 3.29: Global properties determined from log-normal curve fits of the bimodal PSDF including median diameter (top), geometric standard deviation (middle), number density and PSDF volume fraction (bottom).

difference highlighting the effect of equivalence ratios on the flame formed carbon. These measurements further reiterate that ultra-fine carbon nanoparticles with relatively narrow size distribution is produced for the flame conditions studied. The observed evolution in size distribution and carbon structure provides insight for soot formation modeling in the higher-

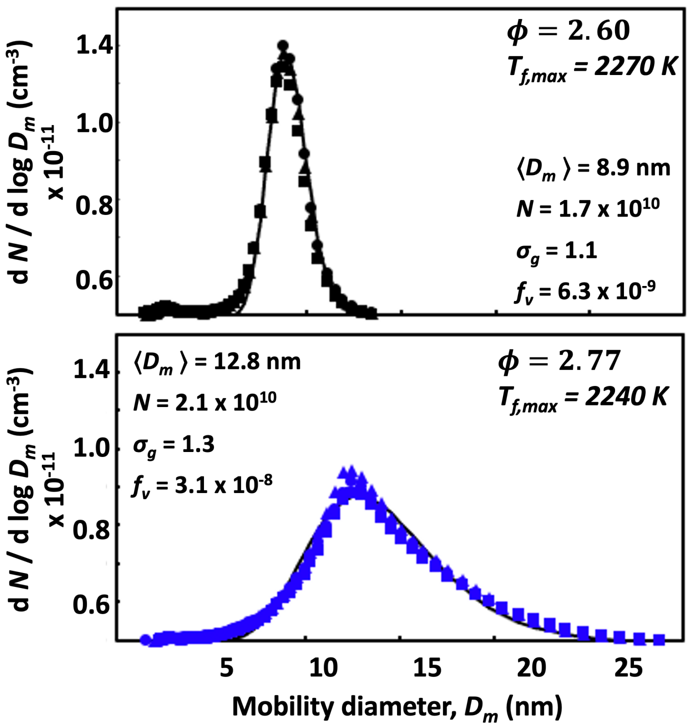

Figure 3.30: Measured PSDF for $\Phi = 2.60, T_{\mathrm{f,max}} = 2270K$ and $\Phi = 2.77, T_{\mathrm{f,max}} = 2240K$. Symbols are measurements and lines are curve fits to a lognormal distribution for each size mode.

temperature regime. Moreover, the observed transition from soot to structure corresponding to disordered sp^2 carbon may be promising for functional high-surface area carbon materials. Relatively high flame temperatures explored here enable soot produced with unique characteristics. The ultrafine particle size characteristic to incipient soot is combined with a carbon structure more ordered than that of mature soot. Functional material properties arising from this unique structure to be explored in the future include electrical conductivity and electrochemical behavior.

3.4 Summary

A complementary experimental and modeling study is reported to shed light on formation processes and material properties for soot formed in the higher-temperature regime ($T_f > 2100K$). The effects of flame temperature and equivalence ratio are isolated in a series of premixed stretch-stabilized flames. Flame structure computations show reasonable agreement to measured color-ratio intensity profiles in terms of the flame position and interpretation of the particle optical dispersion exponent. Computations using KM2, ABF and BPP combustion chemistry models show that predictions of PAH concentration profiles for the current higher-temperature flames are more sensitive to the choice in mechanism rather than specific flame conditions.

As for material properties, the particles produced in the current study are a new type of flame formed carbon. TEM and particle sizing indicates that these are nanoparticles of the order of 10 nm and Raman spectra show features resembling graphite and graphene materials. The Raman signatures transition from a typical soot spectrum to features observed in disordered sp^2 carbon materials with increasing flame temperatures. This is inferred from the disappearance of D3 and D4 bands and significant narrowing of all Raman peaks. Shift in the relative intensity of D and G bands and increased definition of the corresponding overtones are another indication that the structure is more ordered than typical soot. A shift in relative intensity of the $2D_1$ and $2D_2$ secondary bands is observed which tends towards increasing carbon structural order. The defect distance extracted from the Raman spectra begins on the order of unity for flame temperatures close to conventional flame studies and nearly doubles as the flame temperature exceeds 2200 K. Higher concentrations of gas-phase precursors may facilitate development of an ordered carbon structure as indicated by the relatively high defect distance observed for the highest equivalence ratio series.

Measured particle size distributions provide further insight into unique soot formation processes in the higher-temperature regime. As expected, the size and yield of soot decreases with increasing flame temperature due to expected reduction in precursor formation and collision efficiency. The observed ultra-fine size range is also expected, even for the larger growth mode of the bimodal distribution. Unlike PSDF reported for conventional flame temperature conditions, the mode of nucleation-sized particles does not dominate in the higher temperature regime. In addition, the median diameter for the nucleation mode is close to 4 nm for all flame conditions while the growth mode for the higher equivalence ratio cases have significantly larger median diameters.

The detailed material characterization of flame formed carbon has shown carbon nanoparticles formed in high equivalence ratio and high temperature flames show graphitization and Raman spectra similar to that of defective graphene. Multi-wavelength Raman spectroscopy shows similar trends as observed in the literature. High I_D/I_G ratios are seen for flame formed carbon when compared to hard carbon. The flame formed carbon structures analyzed show higher sp^3 content when compared to that of hard carbon as inferred from XPS. Systematic observation of size distribution and carbon structure provides a sound basis for developing soot formation models in the higher-temperature regime. This is especially promising if the significant transformation in carbon structure inferred from the evolution in Raman spectra enables development of functional high surface area sp^2 carbon materials.

The flame-formed carbon nanoparticle studies in Chapter 3, in part, has been published in Fuel (Dasappa, S., Camacho, J., Evolution in size and structural order for incipient soot formed at flame temperatures greater than 2100 Kelvin : Materials and methods, 291, 120196) and Data in Brief (Dasappa, S., Camacho, J., Raman spectroscopy, mobility size and radiative emissions data for soot formed at increasing temperature and equivalence ratio in flames hotter than conventional combustion applications : Experimental Design, Materials and Methods, 36, 107064). The dissertation author is the primary investigator for the publications.

Chapter 4

Formation of Nanocrystalline Manganese Oxide in Flames

Flame-based processes enable precise and scalable production of functional nanomaterials. Advantages of flame synthesis routes over wet-chemistry include fewer synthesis steps, much faster conversion, and continuous production. Several flame configurations have proven useful for tailoring material properties of nanoscale products including carbon (graphene, nanotubes), metals, and metal oxides. Manganese oxide nano-materials have been incorporated into many promising technologies including energy storage materials [139, 140], MRI contrast agents [141, 142] and in catalysis [143, 144]. Flame formed manganese oxide nanomaterials, mostly produced by flame spray pyrolysis [5, 34, 35, 145], have been reported for a variety of applications. Manganese oxide nanoparticles produced by flame stabilized on a rotating surface (FSRS) was reported previously [36] and it was observed that either Mn_2O_3, Mn_3O_4 or MnO_2 are formed depending on growth conditions in the premixed flame. This is unlike many titanium oxide and iron oxide premixed flames studies where full oxidation to TiO_2 and Fe_2O_3 are reported. There are notable exceptions such as a recent report of TiO_2-II formation in fuel rich FSRS conditions [146]. This work is a complementary experimental and modeling study examining formation of nanocrystalline manganese oxides in flames with analysis of thermodynamic barriers to particle nucleation and oxidation.

Formation of manganese oxide nanoparticles through flame synthesis is less explored than titanium oxide and iron oxide. Flame synthesis of titania has been carried out on the industrial scale for a century and academic studies exist going back decades. There is evidence that formation mechanisms for manganese oxides in flames may differ from those observed for titania like varying in oxidation states as discussed above. A range of crystal phases has been reported for titanium oxide nanoparticles formed in flames [37, 146, 147] but the oxidation state observed was mostly Titanium(IV) oxide. This range of phases has been explained on the basis of shifts to bulk phase equilibrium driven by the surface energy of nanoparticles [37, 148]. Birkner and Navrotsky assessed phase-stability for nano-scale manganese oxide under oxygen by drop-solution calorimetry for MnO_2 , Mn_2O_3 and Mn_3O_4 and surface energies were reported as MnO_2 surface energy: 2.05 J m^{-2}, Mn_2O_3: 1.77 J m^{-2} and Mn_3O_4: 1.62 J m^{-2} [149]. A phase stability diagram incorporating the surface energy effect is shown in Fig. 4.1 with an extension to the MnO (surface energy: 1.13 J m^{-2}) phase [150] based on established phase-stability for nano-scale manganese oxide under oxygen. The size-dependent phase diagram is the basis to assess the degree to which phase equilibrium is established among the nano-crystalline manganese oxides formed. In addition, the wide range of physical properties of the manganese oxides calls into question the validity of the coagulation limited nucleation mechanism adopted for flame synthesis of TiO_2 nanoparticles. These considerations are examined by systematic observation of manganese oxide formed in a flame with a well-characterized temperature- oxygen- time history.

Synthesis of manganese oxide nanoparticles is carried out in a flame-assisted chemical vapor deposition process. The process is similar to previous FSRS reports [37, 38, 146] except that a stationary deposition surface is used rather than deposition onto a rotating substrate. The stationary deposition surface enables rigorous modeling of the CVD domain and examination of competing processes leading to the final oxide product. Manganese oxide nanoparticles are synthesized by gas-to-particle conversion driven by premixed stagnation flames with well-characterized flame structure and boundary conditions. Competing oxidation and growth mechanisms for manganese oxide are examined in terms of systematic variation of the flame environment.

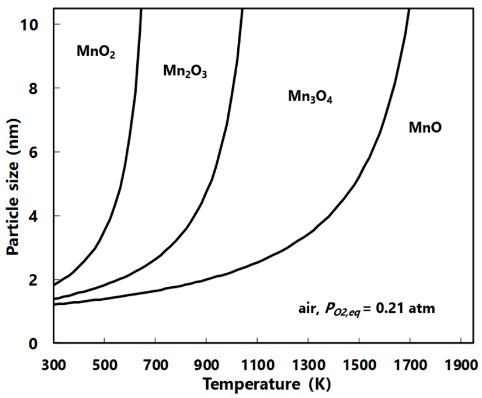

Figure 4.1: Phase stability diagram based on particle size for nano-scale manganese oxide under air.

4.1 Computational Analysis

Premixed stagnation flames on a stationary surface are modeled using a pseudo one-dimensional model and a full two-dimensional axisymmetric computation. The flame computations do not include particle precursor, nor do they consider nanoparticle synthesis processes in the flame. Rather, the flame structure resulting from the base ethylene-oxygen-argon mixture is calculated. An experimental comparison between flame positions with and without precursor doping is carried out to assess the range, if any, for neglecting role of the Mn oxide precursor on the flame structure. Thermodynamic analysis of manganese oxide nucleation and phase stability is carried out after the structure of the base flame is computed. An objective of the study is to determine the accuracy of using the pseudo one-dimensional computation for material synthesis processes having geometry at the limits of the self-similar range. The premixed stagnation flame is a flat reaction zone with axisymmetric two-dimensional geometry similar to conventional CVD domains. As first outlined by Kee [87], this type of flame structure could be solved using a similarity formulation in which the radial component is expressed in terms of the axial component. This pseudo one-dimensional approach enables efficient yet a powerful process design for material synthesis by simplifying the flow field and enabling detailed chemistry and physics to be incorporated. The similarity scaling of a linear dependence on r for radial velocity is most accurate for domains with a wide inlet boundary to stagnation boundary aspect ratio [105, 151]. The aspect ratio of the burner to stagnation studied is relatively narrow as it is closer to some CVD geometries [147]. Solutions obtained using the pseudo one-dimensional (self-similar) formulation for the current aspect ratio are compared to a separate computation of the two-dimensional axis-symmetric flame structure. The comparison between the one and two-dimensional flame computations provides insight into efficient flame structure calculation for the narrow aspect ratio domain and relatively large flame standoff distance studied here. Further details of the pseudo one-dimensional flame structure solution obtained using OPPDIF [44] and two-dimensional ANSYS computations are described in detail in Section 2.1.2.

Manganese oxide nanoparticles are formed in the flame and deposited onto a stationary deposition surface. The precursor, methylcyclopentadienyl manganese tricarbonyl (MMT, Sigma- Aldrich), is sprayed into the fuel line in its initial liquid state, mixed with the unburned gas mixture and vaporized before leaving the fuel line. The gas-to-particle conversion is assumed to occur after the flame front which, in this case, is a flat plane at a steady distance from the deposition surface. The calculations of the flame structure described enable rigorous definition of the particle trajectory as the precursor breaks down at the flame front and forms manganese oxide in the post-flame region. All the oxide formation and growth processes are assumed to occur after passing the flame front.

The reaction time, t, is considered to be the time for a Langrangian particle to traverse the location of the flame front (position where the temperature inflects sharply upwards) to the location of the stagnation surface. The particles are transported to the deposition surface by following the streamlines and by an additional thermophoretic force in the vicinity of the deposition surface. The details of this computation is provided in Section 2.1.2. The reaction time is considered to approximate the time for MMT precursor breakdown, Mn oxidation and particle nucleation/growth to occur before deposition. Examination of the relationship between the oxide product properties and the synthesis flame structure is expected to shed light on the competing oxidation, nucleation and growth time scales.

The mechanism for thermal decomposition of MMT precursor and subsequent formation of oxides is unknown and beyond the scope of this study. However, an analogous flame synthesis system, iron oxide from iron pentacarbonyl, guides initial assumptions. Extensive modeling [152, 153] and experimental studies of conversion of iron pentacarbonyl indicated the metal oxidation process begins from metallic iron. It is assumed the MMT precursor used here also produces metallic Mn. If this assumption is valid, then it follows that MnO is the first oxide to form. Nucleation from the gas-phase is hypothesized to occur by condensation of MnO after oxidation of gas-phase manganese:

$$\mathrm{Mn\,(g)} + \frac{1}{2}\,\mathrm{O_2} \rightleftharpoons \mathrm{MnO\,(s)}, \quad \mathrm{K}_{p,o} \tag{4.1}$$

Equilibrium partial pressures over MnO(s) measured at high temperature by Knudsen effusion mass spectrometry have been reported [153] and the partial pressure of Mn gas was orders of magnitude higher than that of MnO. This is evidence that metallic manganese, Mn, is not the first to nucleate due to the higher volatility. In addition, MnO is the first oxidation state so the higher oxides are assumed to evolve from MnO particles in the flame. Equilibria among manganese oxides under molecular oxygen are known to behave as follows:

$$6\,\mathrm{MnO\,(s)} + \mathrm{O_2} \rightleftharpoons 2\,\mathrm{Mn_2O_4\,(s)}, \quad \mathrm{K}_{p,1} \tag{4.2}$$

$$4\,\mathrm{Mn_3O_4\,(s)} + \mathrm{O_2} \rightleftharpoons 6\,\mathrm{Mn_2O_3\,(s)}, \quad \mathrm{K}_{p,2} \tag{4.3}$$

$$2\,\mathrm{Mn_2O_3\,(s)} + \mathrm{O_2} \rightleftharpoons 4\,\mathrm{MnO_2\,(s)}, \quad \mathrm{K}_{p,3} \tag{4.4}$$

The thermodynamic barrier to nucleation from the gas phase is quantified by the saturation ratio, S, which compares the concentration of relevant species to the equilibrium concentrations. For nucleation of MnO, this is given by:

$$S_o = \frac{P_{Mn} P_{O_2}^{1/2}}{P_{Mn,eq} P_{O_2,eq}^{1/2}} \tag{4.5}$$

where P_{Mn} and P_{O_2} are the local partial pressure of the relevant components in the flame derived from the flame structure computation. Calculated equilibrium partial pressures, $P_{Mn,eq}$ and $P_{O_2,eq}$ are determined by high-temperature equilibria reported for 4.1.

Equilibria between the manganese oxides depends on local temperature and oxygen partial pressure. Further, an additional surface energy effect has been seen to significantly shift oxidation-reduction equilibria between nano-scale transition metal oxides [148, 154] as follows:

$$\Delta G_{R,nano} = \Delta G_{R,bulk} + \frac{6}{d}\Big(\frac{bM_b}{\rho_b}\gamma_b - \frac{aM_a}{\rho_a}\gamma_a\Big) \tag{4.6}$$

where ΔG_R is the free energy of reaction for nano-scale and bulk processes, d is the particle diameter, b is the product stoichiometric coefficient, a is the reactant stoichiometric coefficient, M is the molecular weight, ρ is the mass density of the bulk oxide and γ is the surface energy of the oxide. Eq.4.6 is applied to the manganese oxide equilibrium reactions listed above with surface energy values listed above.

For a given temperature, the equilibrium oxygen partial pressure between two oxides of the same size are determined from an equilibrium constant based on Eq.4.6. Further, a saturation ratio is defined to describe the local oxygen partial pressure relative to the equilibrium oxygen partial pressure. Among the nano-scale manganese oxides the saturation ratio is defined as follows:

$$S_i = \frac{P_{O_2,flames}}{P_{O_{2,eq,i}}} \quad i = 1, 2, 3 \tag{4.7}$$

where the i subscript denotes equilibria for the second, third and fourth manganese oxidation steps listed in Eqs. 4.2, 4.3 and 4.4. The equilibrium values calculated by Eqs. 4.5, 4.6 and 4.7 is based on local temperatures along the computed flame spatial and time domains. The well-defined trajectory of the particle during formation in the flame allows for equilibrium conditions to be defined as the manganese oxide traverses the reaction zone.

4.2 Experimental Conditions

The objective of the experiments is to examine the competition between MMT concentration, temperature, oxygen and time effects in terms of fundamental processes. The well-characterized boundary conditions and flame structure enable systematic observations that could be explained based on thermodynamic or kinetics considerations. The thermodynamic framework outlined above is the basis to evaluate nucleation, growth and equilibrium behavior for the manganese oxides formed. This complementary modeling and experiment approach enables determination of parameters that could be generalized for any synthesis process.

The flame synthesis of manganese oxide nanoparticles are carried out in a premixed stagnation flame setup. The details regarding the experimental setup are described in Section 2.1.1. A summary of the flame conditions studied is provided in Table 4.1. Experimental sets (A, B, C and D) are defined by flame temperature, reaction time, oxygen environment and precursor concentration. Design of the experimental flame synthesis conditions are based on OPPDIF computations of the flame structure. The gas-phase oxygen levels during synthesis are characterized by the equivalence ratio, ϕ, of the unburned mixture. This is the ratio of inlet fuel to O_2 over the stoichiometric fuel to O_2 such that $\phi < 1$ corresponds to an oxygen-rich post-flame zone. For $\phi > 1$, a small amount of oxygen remains after the flame and this approaches zero as $\phi \gg 1$.

The first set of experiments, labelled as the A series of flames, examines manganese oxide nanoparticle formation in the same oxygen-rich flame but at increasing levels of MMT precursor loading (Flames A1-A3). The inlet flow rate for flame A corresponds to a cold gas velocity of $\mathrm{v_o}$ = 335 cm/s and the mixture has $\phi = 0.40$ with argon mole fraction of $\mathrm{X_{Ar}} = 0.46$. For L = 2.54 cm with this inlet flow, OPPDIF predicts the maximum flame temperature as $\mathrm{T_{f,max}}$ = 2600 K and t = 4 ms. As reported previously [36], the competition

Table 4.1: Summary of flame synthesis conditions

Flame	$\boldsymbol{\phi}$	$\boldsymbol{X_{C_2H_4}}$	$\boldsymbol{X_{O_2}}$	$\boldsymbol{X_{Ar}}$	$\boldsymbol{T^1_{f,max}}$ (K)	$\boldsymbol{T^1_{ad}}$ (K)	$\boldsymbol{t_p(L)^1}$ (ms)	$\boldsymbol{v^2_o}$ (cms^{-1})	$\boldsymbol{a^3}$ (s^{-1})	**MMT** (ppm)
A1	0.4	0.063	0.477	0.460	2600	2586	4	335	132	200
A2	0.4	0.063	0.477	0.460	2600	2586	4	335	132	300
A3	0.4	0.063	0.477	0.460	2600	2586	4	335	132	500
B1	0.4	0.056	0.423	0.520	2510	2509	4	301	119	100
B2	0.4	0.063	0.477	0.460	2600	2586	4	335	132	100
B3	0.4	0.056	0.423	0.520	2510	2509	4	301	119	200
B4	0.4	0.063	0.477	0.460	2600	2586	4	335	132	200
B5	0.4	0.045	0.335	0.620	2340	2333	7	252	99	500
B6	0.4	0.051	0.384	0.560	2450	2439	6	290	114	500
B7	0.4	0.056	0.423	0.520	2510	2509	4	301	119	500
B8	0.4	0.063	0.477	0.460	2600	2586	4	335	132	500
C1	0.4	0.063	0.477	0.460	2600	2586	4	335	132	100
C2	0.5	0.056	0.336	0.610	2560	2549	5	299	118	100
C3	0.6	0.055	0.277	0.670	2590	2560	5	305	120	100
C4	0.8	0.060	0.225	0.720	2620	2631	5	316	124	100
D1	1.2	0.054	0.135	0.810	2390	2425	7	267	105	200
D2	1.3	0.064	0.149	0.790	2480	2491	6	279	110	200
D3	1.4	0.067	0.144	0.790	2400	2410	7	269	106	200
D4	1.5	0.074	0.149	0.780	2390	2395	6	279	110	200

[1] Computed using OPPDIF and USC Mech II with $T_{burner} = 400K$ and $T_{probe} = 473K$,
[2] Unburned gas velocity at 400 K and 1 atm,[3] Strain rate

between manganese oxidation and particle growth is expected to be affected by precursor concentration for a given flame condition. The nanoparticle products are expected to form under the same temperature oxygen- time history while undergoing different rates of particle growth. For series A flames, the precursor loading effect on synthesis products is isolated from temperature, oxygen and time effects. The oxygen-rich condition ($\phi = 0.40$) is used again in the B series of flames to observe manganese oxide formation for a series of increasing flame temperature conditions ($2340K < T_{f,max} < 2600K$) all at comparable reaction time, t (Flames B1- B8). Precursor loadings of 100, 200 and 500 ppm are used in the B series to investigate competing growth and temperature effects. Comparable temperature and particle time is used in the C series to examine the role of gas-phase oxygen ($0.4 < \phi < 0.8$). Low MMT loading (100 ppm) is used to emphasize the role of gas-phase oxygen and the extent to which this limits oxidation. The D series further explores oxygen concentration effects by focusing on oxygen-lean growth conditions. This series of flames having $1.2 < \phi < 1.5$ is expected to produce lower oxidation states of manganese oxide.

The flame formed manganese oxide particles are characterized off-line using Raman Spectroscopy, X-ray diffraction and transmission electron microscopy. The details regarding the characterization are depicted in Section 2.3.2, 2.3.3 and 2.3.4. The flame position is measured by analyzing the flame projection captured by DSLR camera.

4.3 Results and Discussion

Modeling tools are used to design flame conditions with desired temperature-oxygen-time histories in the post flame region. Computed flame structures, neglecting precursor doping, are the basis for determining the particle growth environment. Premixed stagnation flames are steady with a disc-like flame front having a stand-off distance where opposing convective and burning velocities are balanced. The comparison between experimental and computed flame structure is shown in Fig. 4.2 in terms of recorded flame images and computed 2D contours. The flame structure is characterized by a pre-flame zone where the velocity and temperature are very close to the inlet boundary conditions. The flame-front is a narrow region characterized by a sharp jump in temperature, velocity and sharp consumption of fuel and oxygen. The stagnation flame drives a chemical vapor deposition process where precursor decomposes at the flame zone and undergoes conversion to manganese oxide in the post-flame region. The flame image shows the MMT doped flame having a post-flame region illuminated by excited Mn oxide species. The illuminated region shifts from light blue next the flame zone to a light green shade which may be an indication of evolving manganese oxide species. The base flame is stabilized in approximately the same position as the precursor doped flame. The position of the 100 ppm of MMT flame is slightly closer to the nozzle boundary which may indicate that this mixture is more reactive than the base flame. This effect may be caused by catalytic behavior of manganese or by a mixture that is slightly more reactive due to being closer to the stoichiometric ratio. Recorded flame images for other flames with and without precursor doping ($2340K < T_{\mathrm{f,max}} < 2600K$, B5 - B8) are presented in Fig. 4.3. Inspection of the B series images indicates that the flame position is not affected significantly by precursor doping.

The two-dimensional computation of the flame structure shows reasonable agreement to the images in terms of the computed temperature contour. There are instabilities and influences from the environment which result in broadening of the flame position observed in the flame images. A small degree of chemiluminescence appears in a broad region surrounding the MMT doped flame which is caused by radial diffusion, minor flickering and oscillation instabilities. A comparison in terms of the flame structure at the centerline is also shown in Fig. 4.2. Measured pixel intensity at the centerline is compared to calculated temperature and CH* profiles. The doped flame pixel intensity maps out the region of high-temperature emission from manganese oxide species. Without precursor doping, the excited combustion intermediates (i.e CH*) are the only source of illumination. A comparison between the measured pixel intensity without precursor doping and computed CH* profiles is shown at the inset. Assuming the measured pixel intensity is due to CH*, the discrepancy in measured

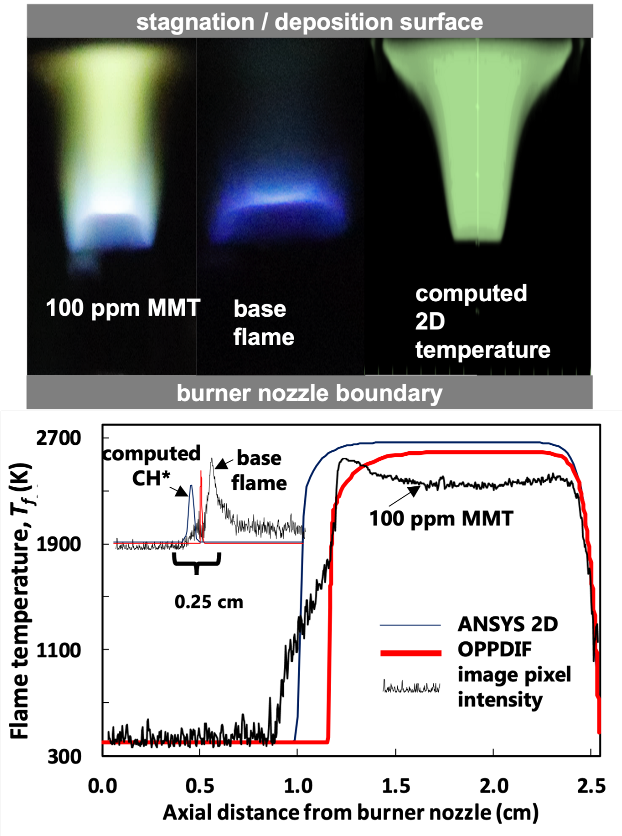

Figure 4.2: Comparison between measured and computed flame position in terms of flame images and 2D temperature contour computed using ANSYS (left). Also shown is comparison between centerline temperature profiles (right) and CH* concentration profiles (right-inset).

and computed flame position is 0.25 cm for the ANSYS solution. Comparison between the measured pixel intensity and the steep temperature gradient computed by OPPDIF shows good, fortuitous or not, agreement. The flame temperature gradient predicted by the ANSYS 2D solution lies within 0.15 cm of the doped flame pixel intensity. Both OPPDIF and ANSYS 2D compile USC Mech II in the Chemkin framework with the accompanying thermodynamic and transport models. One difference in the computation is that radiation effects are ignored in the ANSYS workbench and this could explain the higher temperature predicted in the ANSYS computation.

Many two-dimensional flame modeling studies have been carried out to evaluate the optimal counterflow conditions to achieve self-similar conditions [146]. A common focus is

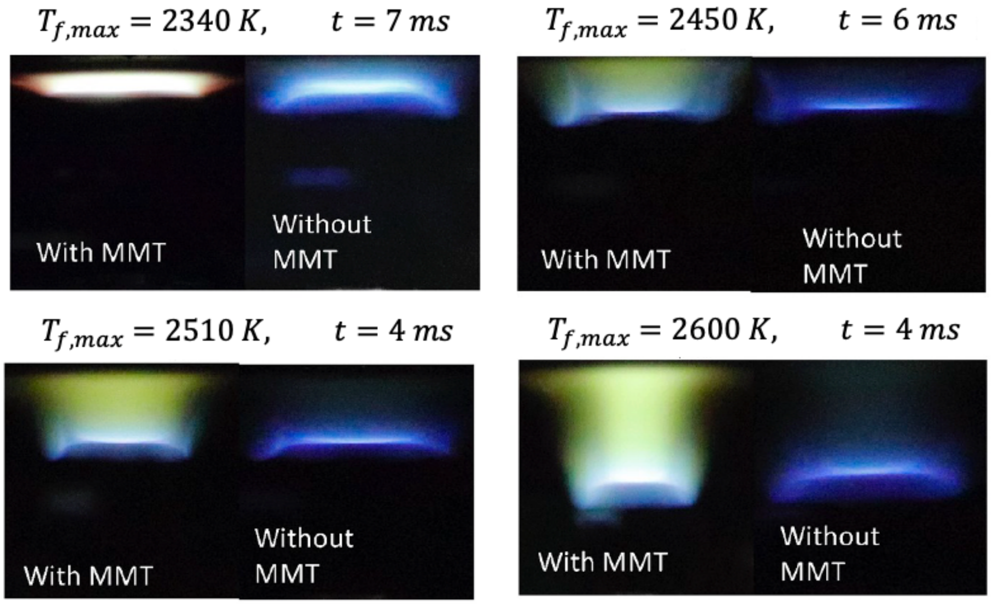

Figure 4.3: Comparison of measured flame position between MMT doped flames and base flames without doping for B5-B8 ($\phi = 0.40$)

the inlet boundary in which plug-flow is important for accurately extrapolating the laminar flame speed from low-strain premixed flames [155]. More careful treatment of the boundary flow profile could extend the range of the self-similar computation for flame extinction [156] and for flames outside of the mixing layer [157]. A typical velocity and reaction time profile is shown in Fig.4.4 for both the self-similar (OPPDIF) and two dimensional (ANSYS) computation. The reaction time applies to Mn oxide synthesis thus the thermophoretic velocity is only added to the convective velocity after the flame front. Higher predicted flame temperatures for the two-dimensional calculation has been reported [157, 158] and radial momentum and energy equation considerations were shown to become significant for large aspect ratio stagnation configurations [157, 159]. Overall, the flame position is predicted reasonably well for OPPDIF and ANSYS two-dimensional methods. This comparison indicates that the self-similar assumption of OPPDIF provides a fast and accurate computation of the flame structure for a robust range of premixed stagnation flame conditions. Definition of the flame structure enables rigorous determination of the particle trajectory in terms of reaction time. This is especially promising if a quicker method (OPPDIF) could be used to provide insight into the temperature-oxygen-time history during synthesis of manganese oxide and other systems.

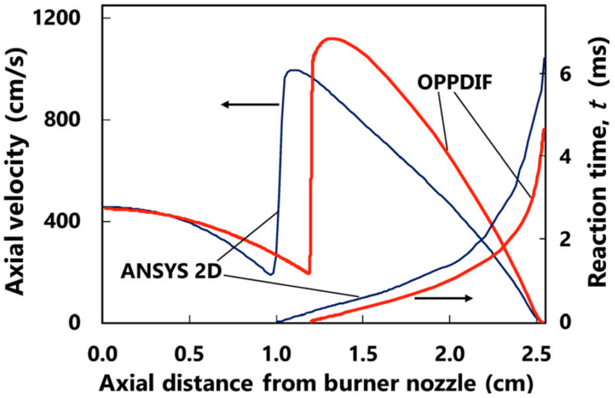

Figure 4.4: Comparison between typical velocity and reaction time profiles obtained from OPPDIF and ANSYS 2D computations.

The A series of flame synthesis experiments is designed to systematically examine the precursor loading effect isolated from temperature, time and oxygen effects. Flame A ($\phi = 0.40$, $T_{f,max} = 2600\ K\ and\ t = 4ms$) is examined with 200, 300 and 500 ppm levels of MMT loading. The gas-phase oxygen and temperature profiles computed using the pseudo one-dimensional method (OPPDIF) is shown in Fig. 4.5 in spatial dimensions. The series A flame has a structure characterized by a flame zone positioned ~1.3 cm from the burner nozzle with a maximum flame temperature of $T_{f,max} = 2600K$. The oxygen flows into the domain at a given partial pressure and gets consumed at the flame front with an excess amount remaining in the post flame region. The reaction time is calculated from the computed velocity-distance profile. It is assumed that the precursor breaks down to form metallic Mn and the oxidation process begins at the flame front. The top-axis of Fig. 4.5 shows the translation to reaction time based on these assumptions. As Fig. 4.5 shows, the manganese oxide spends $\sim$ 4 ms in the post flame zone of flame A before depositing onto the stagnation surface. A coagulation-limited nucleation mechanism applies if there is no thermodynamic barrier to manganese oxide condensation. The Kelvin equation has been applied to TiO_2 in previous reports [12, 160] of gas-phase synthesis to determine whether

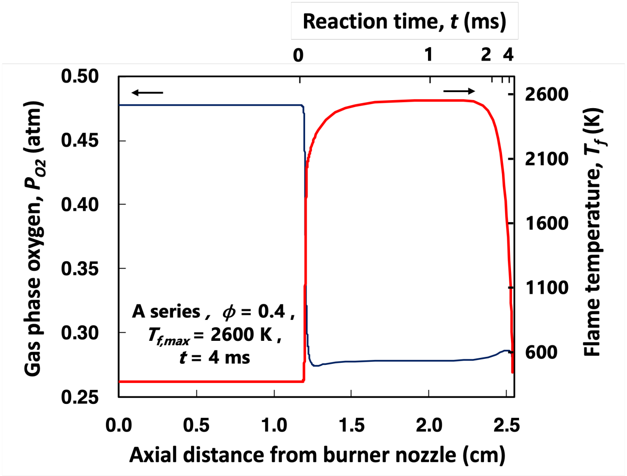

Figure 4.5: Computed gas phase oxygen and flame temperature profiles obtained with OPPDIF for the A series flame. Also shown is the reaction time computed for manganese oxide formation and growth (top-axis).

particle nucleation is limited by coagulation. The criterion is that nucleation does not have a thermodynamic barrier if the critical cluster size predicted by the Kelvin equation is smaller than the size of a single oxide molecule [12, 161]. In the current study, a similar analysis will be carried out by calculating the saturation ratio for formation of solid MnO from the gas phase (Eq. 4.5) along the computed temperature-oxygen-time history.

The computed saturation ratio-reaction time profile, shown in Fig. 4.6, indicates that condensation of MnO is not thermodynamically favored for a significant portion of the flame. Where the Kelvin equation applies $(S_o > 1, \gamma_{MnO} = 1.13\ J\ m^{-2})$, the predicted critical diameter for stable nuclei is smaller than the MnO monomer size for $T_f < 1800K$. This condition occurs at the sharp temperature rise in the flame zone and about 2 ms later as the flame temperature decreases upon approaching the water-cooled stagnation surface. If the thermodynamic barrier exists, particles would nucleate in the flame zone before reaching the maximum flame temperature, then vaporize (or stop growing) at the hottest portion of the flame followed by re-condensing as the flame temperature cools. Similar behavior has been reported by Schulz and co-workers in a previous experimental work on synthesis of iron oxide nanoparticles in premixed burner-stabilized flames [162]. Particles were detected by molecular beam mass spectrometry in the flame-front before becoming undetectable at the

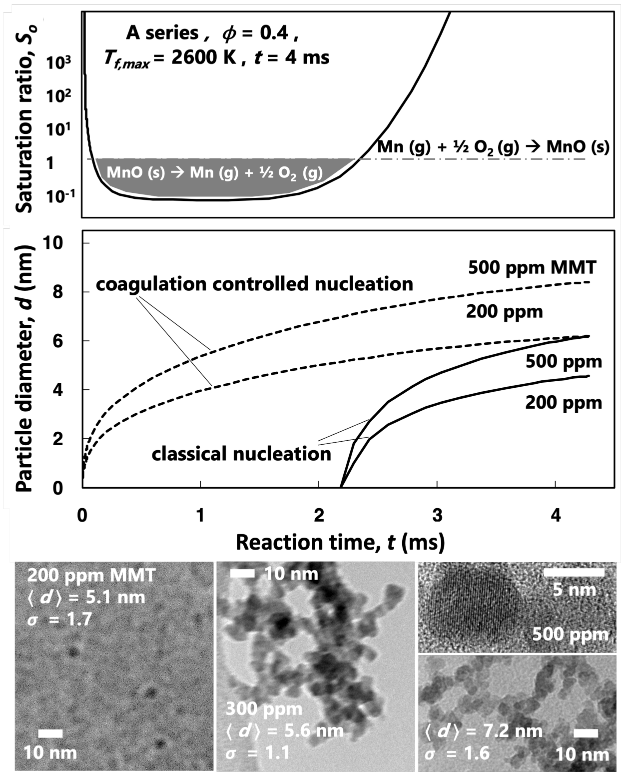

Figure 4.6: Analysis of nucleation and growth for particles formed in the A Series flame experiments. Saturation ratio profile in terms of reaction time in the flame (top), particle size profile assuming either coagulation controlled or classical nucleation (middle) and TEM images of synthesized nanoparticles (bottom).

maximum flame temperature only to reappear in the post-flame region. This observation was rationalized by classical nucleation behavior. Analysis of the saturation ratio for MnO condensation in the current flame indicates that nucleation could also be governed by a classical mechanism.

For classical nucleation, the size of the final manganese oxide nanoparticles would be smaller than predicted by a coagulation-limited process because the thermodynamic barrier prevents growth for a portion of the reaction time. The particle size is estimated here based on the simplified solution to the coagulation equation (Eq. 4.8):

$$\begin{aligned} d(t_i) &= d_{i-1}(1 + K_{ii}N_{i-1}t_{i-1})^{1/3} \\ K_{ii} &= 4\alpha\Big(\frac{6\ kTd_{i-1}}{\rho_p}\Big)^{1/2} \end{aligned} \tag{4.8}$$

where t_{i-1} is interval between the previous grid point, d_{i-1} is the particle diameter of the previous grid point, N_{i-1} is the number density of the previous grid point, K_{ii} the coagulation coefficient, α is the collision efficiency, k is the Boltzmann constant, T is temperature and ρ_p is the bulk density of the oxide. The coagulation coefficient used here is for collisions of like-sized particles in the free molecular regime [163]. Collision efficiency varies widely in this size range depending on particle size, temperature and material properties but the value was kept at $\alpha = 0.50$ as a compromise between the range of $0.10 < \alpha < 0.90$ commonly observed [163]. The coagulation equation was solved in discrete steps based on computed temperature-time history profile grid.

Two potential scenarios for growth by coagulation are summarized in Fig. 4.6. Nucleation and growth only limited by coagulation would result in particles with $d \sim 6nm$ assuming a mono-modal size distribution starting at the flame front from 200 ppm of MnO monomer ($d = 0.34nm$). The final particles would be $\sim 2nm$ smaller if growth did not begin until the saturation ratio reached unity in the post-flame region. The characterization of the particles is only carried out for materials deposited at the stagnation surface. Particle sizing by analysis of the TEM images in ImageJ, also shown in Fig. 4.6, indicates that the size of particles ranges from 5 -7 nm for the conditions studied. The measured particle sizes are significantly smaller than that predicted by the coagulation limited assumptions taken in Fig. 4.6. The above analysis is to provide preliminary justification for a classical nucleation mechanism. There are many details required to rigorously quantify the nucleation process. For example, the dependence of the saturation ratio on conversion of Mn(g) to MnO(s) (Fig. 4.7) would shift the unity crossover to later reaction time.

Characterization of the final manganese oxide products formed in Flame A is shown in Fig. 4.8 in terms of XRD and Raman spectroscopy. As expected, X-ray diffraction is not strong for these relatively disordered and ultrafine particles. The most prominent faces were observed on the 500 ppm case as (222) and (440) attributed to Mn_2O_3. Faint evidence of MnO_2 peaks appear as (101) and (110) in the lower ppm loading cases. Lattice fringes were

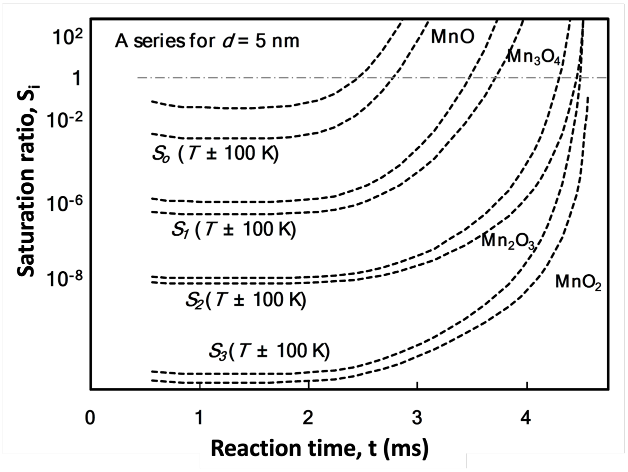

Figure 4.7: Saturation ratio-reaction time profiles for S_o–S_3 in the A series flame with saturation ratios calculated with a temperature-time history ± 100 K the base calculation.

detectable by TEM as shown in Fig. 4.6 for the 500 ppm case. Examination of short range order by Raman spectroscopy shows a more clear evolution at increasing particle loading. The A_{1g} breathing mode of Mn oxide octahedra is observed at 650 cm^{-1} for materials formed under higher precursor loading (300 and 500 ppm) and this is a characteristic of Mn_3O_4. Several studies attribute this to known thermal decomposition behavior of Mn_2O_3 under laser power [164, 165]. The flame synthesis origin of the manganese oxide may have caused this high-temperature feature to persist in the product structure rather than artifacts from the laser (1 mW). The Mn-O stretch mode is observed at 680 cm^{-1} for the 300 and 500 ppm cases which corresponds to Mn_2O_3 [164]. The Raman spectra of the 200 ppm loading case shows a clear departure in that the dominant mode A_{1g} is no longer present. Instead, broad A_g modes are observed above 600 cm^{-1} and these have been attributed to disordered MnO_2 structures [165].

For increasing precursor loading in the same oxygen-rich flame, the particle size increases and the manganese oxidation state decreases. This observation may be explained by equilibria between the oxides governed by size, temperature and oxygen partial pressure. The equilibrium conditions are mapped onto reaction time space in Fig. 4.9 in terms of the saturation ratios of the four manganese oxidation steps (Eqs. 4.1 - 4.4). Local tempera-

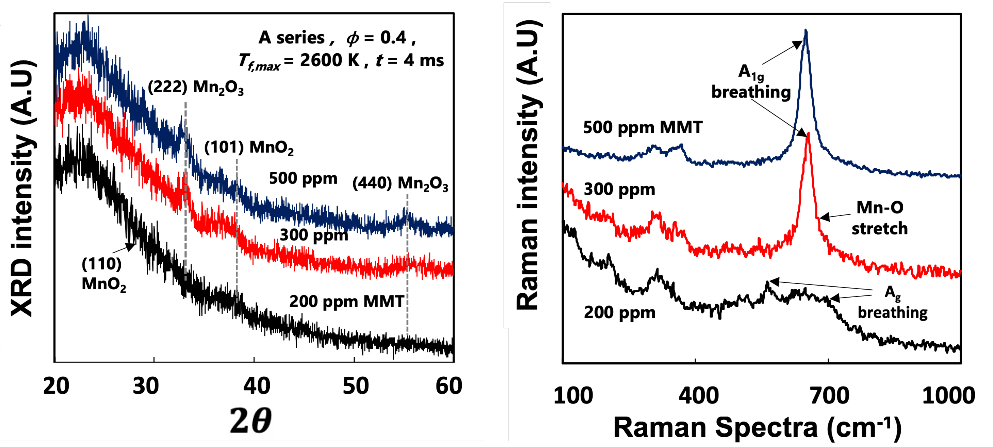

Figure 4.8: Characterization of nanocrystalline manganese oxide synthesized in A Series flame experiments. XRD patterns (top) and Raman spectra (bottom) for films deposited with 200 ppm, 300 ppm and 500 ppm MMT precursor loading

ture and oxygen partial pressure are known as the manganese oxide progresses through the synthesis domain and comparison to the equilibrium condition gives insight into the thermodynamically favored processes throughout. This is analysis is carried out for $d = 2nm$ and 5 nm to present conditions that overlap all three of the precursor conditions carried out in the A series of experiments. The surface energy effect causes a significant shift in the boundaries shown in Fig. 4.9 such that Mn_2O_3 and MnO_2 do not cross the unity saturation threshold for small particle size. If the boundaries shown are accurate, the higher oxidation states are only stable for larger particle sizes in this flame.

The computed saturation ratio profile ignores the minor discrepancy between the measured and computed flame position. The presence of precursor, particles and three dimensional flow effects are suspected of causing this discrepancy. The stretch effect does not cause a significant deviation from the adiabatic flame temperature for the global strain rates studied here. Computations as shown in Table 4.1 and in Fig 4.10, in the absence of particles, the calculated maximum flame temperature is effectively the adiabatic flame temperature and the stretch affect causes a 3% reduction in temperature in the flame zone for nearly twice the global strain rate. This is performed in conjunction with the assumption that the computed temperature is not affected by the presence of particles. Flame temperature profiles were

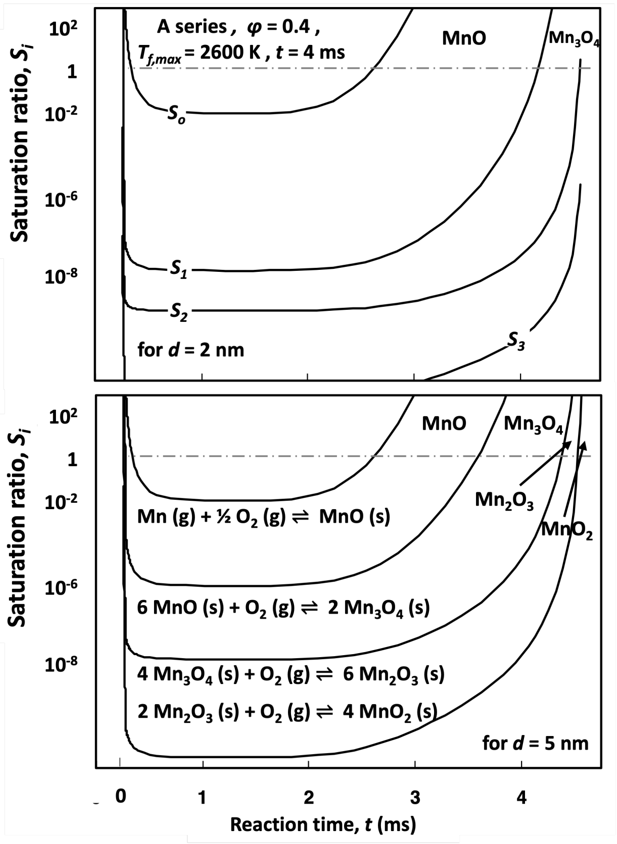

Figure 4.9: Analysis of local phase equilibria between manganese oxides with $d = 2nm$ (top) and $d = 5nm$ (bottom) in the A series flame in terms of saturation ratio – reaction time profiles.

measured by a thermocouple in previous reports on TiO_2 nanoparticle synthesis in stagnation flames [38, 166]. The particle concentration was in a similar range as studied here and the high-temperature emissivity is of the order of 0.50 for both Mn_3O_4 and TiO_2 [167]. Therefore, any effect of particle radiation is expected to be similar for the manganese oxide flames studied here. Measured temperatures were 40 K to 100 K lower than the adiabatic flame temperature in the TiO_2 synthesis flames depending on particle loading. Pratsinis and co-workers measured the flame temperature for TiO_2 synthesis in premixed flames as well but temperature was only 200 K higher than the un-doped flame even with two orders of magnitude greater precursor loading [168]. To account for the current uncertainty in the temperature due to particles, the saturation profile was calculated for a range of temperature 100 K from the original OPPDIF computation (Fig. 4.7). The range of saturation ratios changes moderately with temperature and the ±13% shift in boundaries does not alter the conclusions drawn.

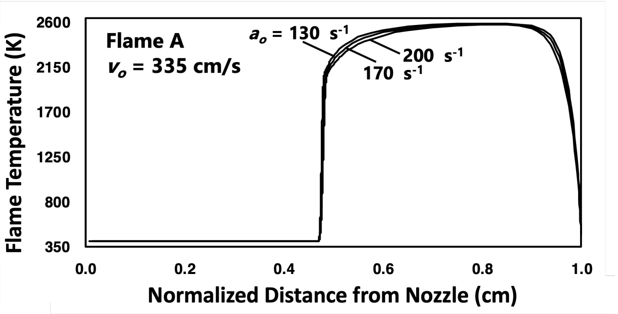

Figure 4.10: Computed axial temperature profile (OPPDIF) with increasing global strain rate for Flame A.

The saturation ratio leading to Mn_2O_3 and MnO_2 phases are predicted to reach $S > 1$ when $d > 5nm$. The thermodynamically predicted phase for the collected material is MnO_2 because the particles collected are $> 5nm$ and the final synthesis temperature is on the low range of the phase diagram. Characterization of the oxide products discussed above indicates that signatures of Mn_3O_4, Mn_2O_3 and MnO_2 are present depending on the level of precursor loading. This may indicate that phase equilibrium is only achieved when the particles are small enough to equilibrate on the millisecond timescale. The Mn_2O_3 and Mn_3O_4 features observed may be metastable characteristics which formed at higher temperature and were quenched as the particles deposited.

Temperature and precursor loading effects are explored further in the B series of flame experiments. The series is a set of flames with $\phi = 0.40$ having comparable reaction times at increasing flame temperatures ($2315K < T_{f,max} < 2600K$). The computed flame temperature-reaction time profiles based on the pseudo one-dimensional formulation is shown in Fig. 4.11. Images of these flames with and without precursor loading are shown in Fig. 4.3. The flame images show that the position of the flame does not change significantly due to the presence of MMT precursor. In addition, the position of the flame varies in order to keep the reaction time comparable for the given range of flame temperatures. By expressing the synthesis region in terms of reaction time, the systematic comparison of flame structure

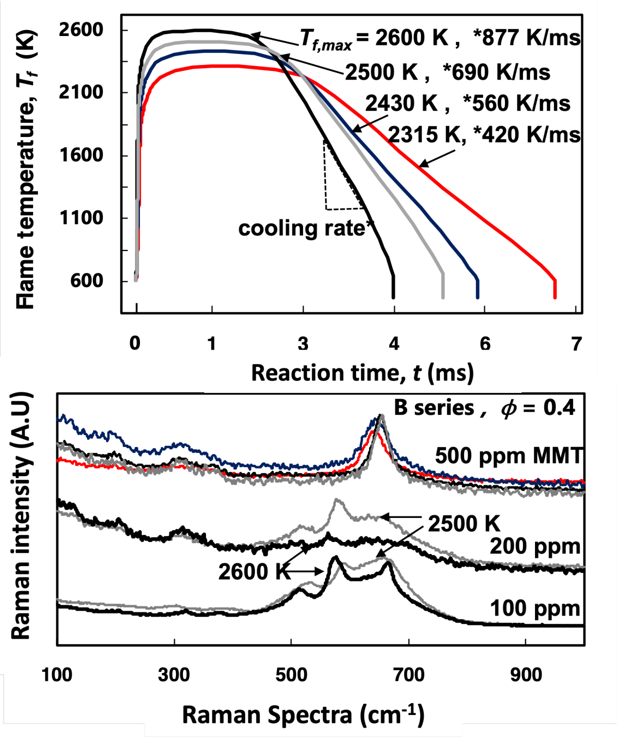

Figure 4.11: Temperature – reaction time profiles (top) and Raman spectra for nanocrystalline manganese oxide formed (bottom) in the B Series flame experiments.

shown in Fig. 4.11 is carried out. The computed flame structures show that the series also provides insight into the cooling rate effect as the hottest flame approaches the stagnation surface with twice the cooling rate as the coldest flame in the series. The cooling rate is expected to provide another means to control the properties of the material formed.

A summary of products formed in the B series is also shown in Fig. 4.11 in terms of Raman spectra. The spectra show the oxide formed does not depend on the temperature and cooling rate for the 500 ppm precursor loading condition. Features of Mn_2O_3 products are observed for 500 ppm MMT loading at all temperature conditions. If the equilibrium considerations discussed above hold, MnO_2 should be the thermodynamically favored phase due to the final size and synthesis temperature. Similar to the A series, the observed Mn2O3 products may be a metastable phase that is too massive to equilibrate even at a reduced cooling rate. The spectra corresponding to Mn_2O_3 is observed for the largest particles across a temperature range of 300 K and cooling rates spanning 400 K / ms. This is contrasted to the spectra for the lower ppm conditions of the same flames. Manganese oxides forming in the 100 and 200 ppm loading cases have Raman features corresponding to MnO_2 structures. The spectra attributed to products formed at the 100 ppm condition show signatures of the MnO_6 octahedra stretch modes corresponding to pyrolusite MnO_2 [165]. Pyrolusite is considered a relatively ordered MnO_2 structure and other MnO_2 structures have been characterized by degrees of pyrolusite inter-growth. The spectra observed for the 200 ppm cases may be described as MnO_2 with varying pyrolusite components [165] which, under the given cooling rate, did not fully become an ordered structure. Examination of competing particle growth and oxidation effects carried out in the A and B series of flame experiments shows both metastable and thermodynamically favored phases could be obtained depending on the details of the temperature-oxygen-time history during synthesis.

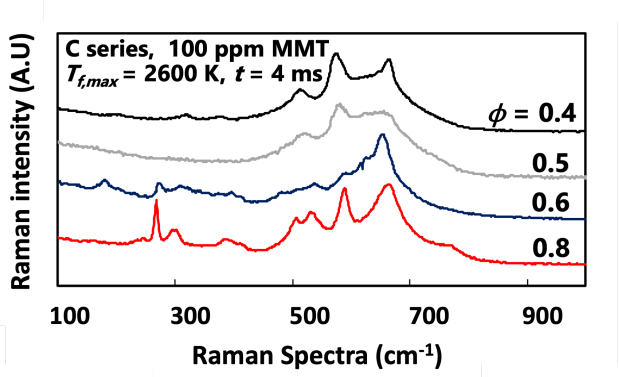

Figure 4.12: Raman spectra for nanocrystalline manganese oxide formed in the C Series flame experiments

The role of gas-phase oxygen is further examined for low precursor loading (100 ppm) in the C series of flame experiments ($0.40 < \phi < 0.80$). The flames are designed to have comparable temperature-time history while decreasing the partial pressure of oxygen during synthesis. Characterization of the final products is shown in Fig. 4.12 in terms of Raman spectra. The $\phi = 0.40$ spectrum is characteristic to pyrolusite MnO_2 [165]. As the series progresses to lower oxygen growth conditions, features of the Raman spectra appear to evolve from MnO_2 to Mn_2O_3. The variety of peaks observed from 500-700 cm^{-1} have been attributed to pyrolusite MnO_2 with various degrees of pyrolusite (order) [165]. At $\phi = 0.80$, features of

$_2O_3$ appear in terms of new low wavenumber features and a prominent A_{1g} breathing mode. Series C flame experiments demonstrate the role of gas-phase oxygen in tuning the properties of the deposited manganese oxide for a given size range and temperature-time history.

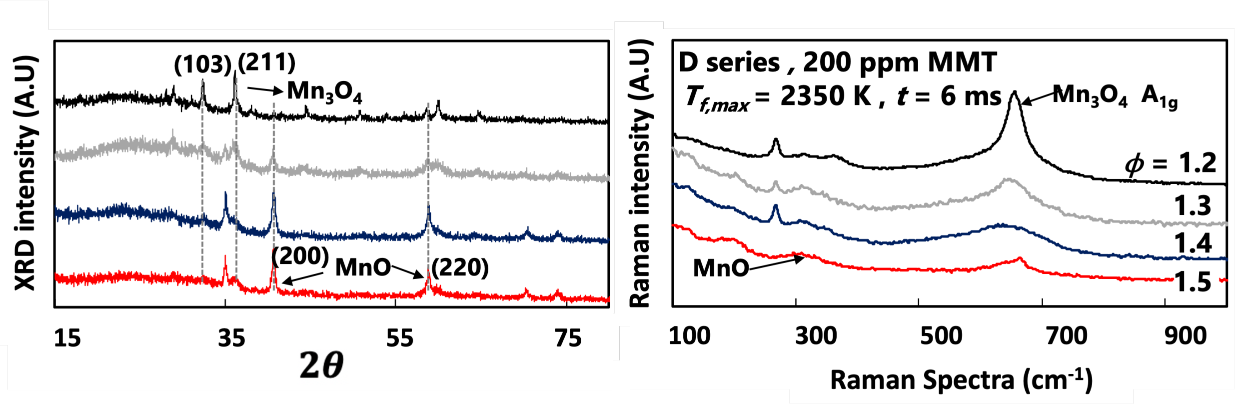

Figure 4.13: Characterization of nanocrystalline manganese oxide synthesized in the D Series flame experiments. XRD patterns (left) and Raman spectra (right) for materials deposited from the flame.

Oxygen-lean growth conditions were also examined to observe the formation of lower manganese oxidation states in series D flame experiments. Flames having $1.2 < \phi < 1.5$ were studied with comparable temperature-time history. Characterization of the products formed in these flames is shown in Fig. 4.13 in terms of XRD and Raman spectra. The formation of MnO is observed, for the first time by flame synthesis, in the most oxygen lean flame ($\phi = 1.5$). The XRD and Raman features show a systematic evolution from Mn_3O_4 products to MnO products as the equivalence ratio is increased (gas-phase O_2 decreases). A range of titanium oxide structures was reported for increasing equivalence ratio [40] but a range of metal oxide valence this extensive has never been reported.

Manipulation of O_2 during particle growth was systematically carried out in the C and D series of flame experiments to observe the role of gas-phase oxygen on resulting particle oxidation state / structure. Complementary experimental and modeling studies in the premixed stagnation flame configuration enables systematic study of competing thermodynamic and kinetic processes. Computed oxygen partial pressure - reaction time profiles are shown in Fig. 4.14 for the D series of flames. As the computed oxygen profiles show, manganese oxide forms under similar flame structure with oxygen being the only variation across the flames. The oxygen present in the post-flame region is much lower than the oxygen-rich flames studied above and this enables products having lower oxidation states to be favored. The given range of ϕ examined in the D series results in oxygen partial pressures spanning an order of magnitude relative to each other.

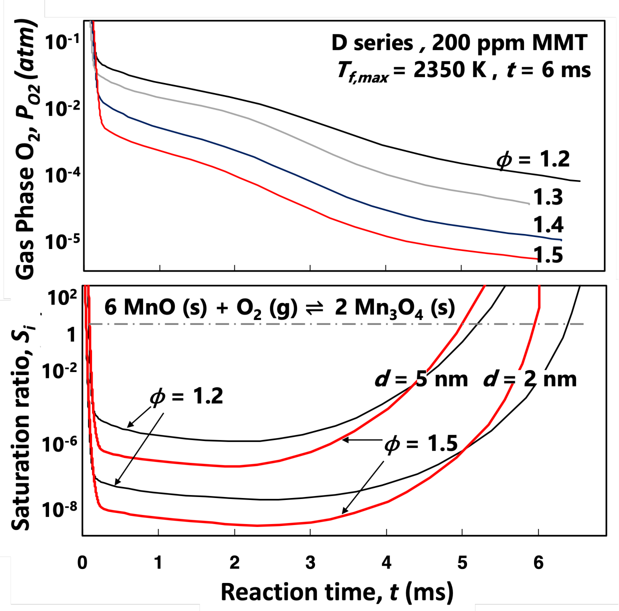

Figure 4.14: Computed oxygen partial pressure-reaction time profiles for the D series (top) and saturation ratio (S_1)-reaction time profiles (bottom) for selected conditions and particle size.

The saturation ratio for MnO-Mn_3O_4 equilibrium (S_1) is also mapped to the reaction time in Fig. 4.14 for the $\phi = 1.2$ and 1.5 cases. For early growth stages (i.e. $d = 2\ nm$) the window for Mn_3O_4 stability is narrow. As the particle grows, the surface energy effect widens the Mn_3O_4 stability zone for both flames. The saturation ratio analysis carried out here does not account for the oxygen consumed by the manganese during oxidation to MnO and Mn_3O_4. At these trace oxygen levels, the saturation ratios may actually cross the unity threshold later due to oxygen partial pressure lower than computed for the flame structure. This effect may be more pronounced in the most fuel lean case ($\phi = 1.5$) where the saturation ratio is an order of magnitude lower at the highest flame temperature. Nonetheless, the analysis shows that the lower oxides (MnO and Mn_3O_4) are thermodynamically favored in oxygen-lean flame synthesis conditions.

4.4 Summary

Formation of nanocrystalline manganese oxide nanoparticles in premixed stagnation flames was systematically examined. Comparisons among flame structure computations and experimentally determined flame position indicates that a pseudo one-dimensional model performs reasonably well for characterizing the structure of the synthesis domain. With the temperature-oxygen-time history defined, thermodynamic analysis was carried out by comparing local conditions to equilibrium values. Analysis of the saturation ratio for formation of condensed MnO in the flame indicates that nucleation may be limited by a thermodynamic barrier. This nucleation mechanism is supported by measured particle sizes smaller than what would be expected from a coagulation limited growth process.

Manganese oxide nanoparticles having II, II-III, III or IV oxidation states were observed depending on the flame conditions. Size-dependent equilibrium for oxygen partial pressure was compared to the computed local concentration to assess thermodynamically favored conditions. An oxygen-rich flame was examined with increasing particle loading (A series) and the thermodynamically favored product, MnO_2, was obtained only for the smallest particle size. Further examination of oxygen-rich conditions with a range of temperatures and cooling rates (B series) showed that phase equilibrium may be not be achieved for larger particle sizes due to longer times required for thermal equilibration. Nanocrystalline MnO, reported here for the first time by flame synthesis, was obtained in oxygen lean flames. Observations of manganese oxide formation under a range of oxygen conditions (C and D series) showed that the oxide phase produced could be tuned to some extent. Overall, definition of the temperature-oxygen-time history and size-dependent equilibria enable production of nanocrystalline manganese oxide with a range of properties.

The flame-formed manganese oxide nanoparticle formation studies described in Chapter 4 has been published in CrystEngComm (Dasappa, S., Camacho, J., Formation of nanocrystalline manganese oxide in flames: oxide phase governed by classical nucleation and size dependent equilibria: Computational and Experimental , 22, 5509-5521). The dissertation author is the primary investigator for the publication.

Chapter 5

Thermodynamic Barrier to Nucleation for Flame Formed Manganese Oxide Nanoparticles

In Chapter 4, it was shown that the temperature and oxygen growth conditions could be manipulated to produce manganese oxide nanoparticles in flames with some selectivity in the oxidation state and nanostructure. Phase equilibria among MnO, Mn_3O_4, Mn_2O_3, and MnO_2 largely governs the final product formed, while cooling and coagulation rates also contribute to the final product properties. The range of valences observed in stable products of manganese oxide is wider than has been reported for flame synthesized TiO_2 and Fe_2O_3. This gives rise to the need for systematic study of competing processes to understand and leverage the wide range of possible manganese oxide products. In the current work, nucleation of manganese oxide nanoparticles by gas-to-particle conversion is systematically examined. As in the previous chapter, premixed stagnation flames are employed to provide a one-dimensional growth process for isolation of the manganese oxide nucleation process under a well-characterized temperature-time history. Relatively high flame temperatures are achieved in premixed stagnation flames. Prior work on metal oxide phase stability in flames were performed for TiO_2 and manganese oxides at temperatures greater than 2200K.

The specific flame synthesis method adopted is amenable to fundamental studies of gas-to-particle conversion as well as application to film deposition processes for fabrication of functional films.

Condensation of nanoparticles from the gas phase is potentially limited by a thermodynamic barrier at high flame temperature and low precursor concentration. The Kelvin effect is used to quantify the thermodynamic barrier for conversion of gas-phase clusters to the condensed phase by accounting for the supersaturation of condensable species and the surface tension of the resulting particle or droplet. Particle nucleation and growth occur immediately after the product is formed (coagulation-limited) if the size of the monomer molecule is greater than the critical cluster size, r^*, given by the Kelvin equation [161, 163]:

$$r^* = \frac{2\sigma_s \nu_1}{k_B T ln(S)} \tag{5.1}$$

where σ_s is the surface energy or tension of the cluster, ν_1 is the molecular volume, k_B is Boltzmann's constant, T is the local temperature, and S is the saturation ratio. This criterion has been applied to SiO_2 [12] and TiO_2 [42] particle formation to show that coagulation governs particle nucleation and, hence, the final particle size for flame synthesis conditions with high supersaturation of precursors. Chapter 4 on manganese oxide synthesis in premixed stagnation flames provids evidence that the higher flame temperatures and parts per million (ppm) level of precursor doping may give rise to a thermodynamic barrier for particle nucleation. The range of oxidation states observed made application of simple coagulation models less accurate due to the additional contribution of oxidation to particle size. The lowest oxidation state product, MnO, is the focus of the current work to enable isolated study of nucleation and growth in the absence of further oxidation steps.

The work described in this chapter is a complementary experimental and modeling study of manganese oxide synthesis in premixed stagnation flames. The temperature-oxygen-time history of the particle is well-characterized during synthesis in premixed stagnation flames due to reliable numerical models of the flame structure. Thermodynamic analysis of the manganese-oxygen-manganese oxide system is applied for insight into equilibrium conditions based on the computed underlying flame structure. Measurements of the flame position and final particle size are used to evaluate assumptions of the flame structure computation and coagulation growth model. Aerosol probe sampling is carried out here to analyze the particle size distribution of flame-formed particles in real-time by mobility sizing. An effective technique established for sampling soot from flames under well-characterized boundary conditions is applied here to investigate nucleation of manganese oxide nanoparticles.

5.1 Computational Analysis

Computations of the flame structure are carried out here without precursor chemistry or oxide particle formation processes. A well-known antiknock agent, manganese methylcyclopentadienyl tricarbonyl (MMT), is fed into the premixed stagnation flames as a gas phase precursor. Inhibition chemistry for MMT has been established by Linteris for methane flames [169, 170], but the inhibition efficiency has been shown to be half as effective as iron pentacarbonyl with additional loss in inhibition for concentrations in which particles are formed. In addition, perturbation to the flame structure is not observed for premixed propane flames doped with MMT [171]. Chapter 4 shows comparable flame positions between base ethylene-oxygen-argon flames and flames doped with MMT. These reported observations for propane and ethylene flames may indicate that inhibition is weaker for larger hydrocarbon flame chemistry. The premixed stagnation flame (ethylene-oxygen-argon) is modeled here using both a pseudo-one-dimensional formulation and a solution to the two-dimensional axisymmetric flow field. The details regarding the modeling setup is discussed in detail in Section 2.1.2.

$$\mathrm{Mn\ (g)} + \frac{1}{2}\,\mathrm{O_2} \longrightarrow \mathrm{MnO\ (s)} \tag{5.2}$$

For the manganese-oxygen-manganese oxide system, the process given by reaction 5.2, is hypothesized for nucleation of manganese oxide in flames. Insights into the gas-to-particle conversion of manganese oxide could be gained from high-temperature studies of the solid-to-gas process. Gas-phase Mn and MnO are reported upon vaporization of solid MnO in high-temperature mass spectroscopy studies [172] which indicates dissociation occurs upon entering the gas phase. Other studies have confirmed that the partial pressure of metallic Mn is orders of magnitude higher than that of MnO at elevated temperature [169, 173]. Based on the reported stability of the high temperature Mn-MnO-O_2 system, it follows that condensation of MnO occurs more readily than condensation of metallic Mn. The enthalpy of reaction for sublimation of solid MnO to the gas phase has been reported at 532 kJ mol^{-1}, while the dissociative sublimation (reverse of 5.2) has been reported at 644 kJ mol^{-1} [173]. The combination of Mn and O_2 to condense MnO can be considered more thermodynamically favored than condensation of gas-phase MnO based on the reported enthalpies of reaction. The breakdown and flame chemistry associated with the MMT precursor is complex. Linteris introduced gas-phase chemistry of Mn oxidation based on studies of MMT doped flames [169, 170], but particle formation processes were not considered. Gas-to-particle conversion to manganese oxide is likely to stem from a variety of species to produce a range of initial particle types. A simple global model is applied here based on existing equilibrium parameters of the high-temperature Mn-MnO-O_2 system and nanoscale manganese oxides. The oxygen-deficient flame condition chosen is designed to minimize contributions from higher oxidation states of manganese such that nucleation and growth of MnO could be isolated. Errors associated by modeling nucleation and growth based on reaction 5.2 are counterbalanced with a well-characterized reaction environment and by narrowing the range of potential manganese oxide species.

High-temperature equilibrium partial pressures have been reported for this system from Knudsen effusion mass spectroscopy measurements [173] as follows:

$$ln\left(\frac{P_{Mn,eq}}{Pa}\right) = \frac{-64412}{T} + 35.688 \tag{5.3}$$

$$ln\left(\frac{P_{O_2,eq}}{Pa}\right) = \frac{-27064}{T} + 11.461 \tag{5.4}$$

where $P_{Mn,eq}$ and $P_{O_2,eq}$ are the equilibrium partial pressures of Mn and O_2 in Pascal. Local equilibrium partial pressures for Mn and O_2 are computed along the computed temperature profile for insight into supersaturation leading to manganese oxide condensation. In addition, the computed profiles are transformed from the space domain to a Lagrangian time profile using the computed axial convective and thermophoretic velocity [42, 86, 107]. Decomposition of MMT is expected to occur in the vicinity of the flame zone such that oxidation, nucleation, and growth of manganese oxide nanoparticles are a one-dimensional progression in time from the flame zone to the stagnation surface. If particle nucleation occurs upon formation of MnO and no further oxidation occurs, particle growth will be determined by coagulation of MnO particles over time. The computed particle size is based on coagulation of like-sized particles starting from a monodisperse distribution of MnO monomers [163] as follows:

$$\begin{gathered} d(t_i) = d_{i-1}\left(1 + \frac{K_{ii} N_{i-1} t_{i-1}}{2}\right)^{1/3} \\ K_{ii} = 4\alpha\left(\frac{6\ kT d_{i-1}}{\rho_p}\right)^{1/2} \end{gathered} \tag{5.5}$$

where d is the particle size computed discretely from the OPPDIF computed temperature-time profile. A one-to-one proportion of MMT molecules to Mn atoms to MnO monomers is assumed, and this gives the initial number density of monomers (MMT has a single Mn ligand). After each grid point denoted by time t_i, growth occurs from the size at the previous grid point, d_{i-1}. N_{i-1} is the number density of the previous grid point, K_{ii} the coagulation coefficient of like-sized particles in the free molecular regime, α is the collision efficiency, k is the Boltzmann constant, T is temperature and ρ_p is the bulk density of MnO. Nucleation-sized particles have collision efficiency as low as 10 % [174], but precise values for the current system are unknown. As such, Eq. 5.5 is computed for a range of collision efficiency to report feasible particle sizes for the given growth time.

5.2 Experimental Conditions

The experimental configuration centers on synthesis of manganese oxide nanoparticles in premixed stagnation flames. The base flame is 8.8% ethylene, 17.5% oxygen, and 73.7% argon by mole which is a fuel-rich mixture ($\phi = 1.50$) expected to produce MnO based on Chapter 4. The nozzle flow has a cold gas velocity of 315 cm s^{-1}, and the temperature is 400 ± 20 K at the nozzle exit as indicated by a fine-wire Type K thermocouple. The detailed experimental setup along with the burner schematic is depicted in Section 2.1.1. Analysis of the flame-formed aerosol is carried out in real-time by mobility particle sizing. X-ray diffraction (XRD) and TEM analysis are carried out to analyze particle structure. The flame position is measured by analysis of images of flame projections obtained from a Nikon D5300 DSLR camera.The analysis techniques are described in detail in Section 2.3.1, 2.3.3 and 2.3.4.

5.3 Results and Discussion

Known equilibrium concentrations for the nucleation reaction (Eq. 5.1) enable determination of the saturation ratio and Kelvin effect as a function of temperature. The saturation ratio for this process is given as:

$$S = \frac{P_{Mn} P_{O_2}^{1/2}}{P_{Mn,eq} P_{O_2,eq}^{1/2}} = K_P(T) P_{Mn} P_{O_2,eq}^{1/2} \tag{5.6}$$

where P_{Mn} and P_{O_2} are the local concentrations. The initial partial pressure of Mn is given by the known MMT feed concentration assuming oxidation of manganese begins from Mn atoms produced by decomposition of MMT at a one-to-one ratio. Evaluation of the equilibrium constant and critical radius for the nucleation reaction is shown in Fig. 5.1 as a function of temperature. Relatively low precursor concentrations of MMT precursor and O_2 are evaluated to assess the Kelvin effect in flames with low precursor loading. Under these conditions, production of MnO(s) is not thermodynamically favored above 1800 K. Application of the critical radius criterion for the MnO molecular radius ($r_{MnO} = 0.17nm$) indicates that condensation of MnO monomers is unstable above 2000 K even for fuel-lean flames ($P_{O_2} = 10^{-1}atm$).

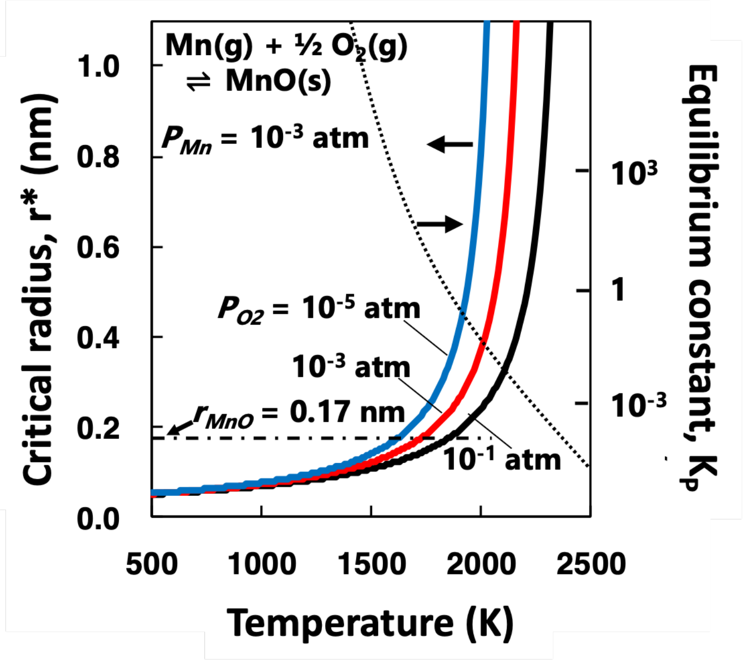

Figure 5.1: Critical Kelvin radius and equilibrium constant for the nucleation reaction as a function of temperature.

The effect of MMT precursor doping on the flame structure is assessed here in terms of the measured flame position. Images of flame projections for doped flames is compared to the base flame in Fig. 5.2. The flame standoff distances, L_s, reported in Fig. 5.2 are determined by analyzing the edges of the gray scale intensity profiles for 30 flame images. Inspection of the images and reported standoff distances show no significant effect of MMT precursor loading on the flame position. The position of the flame zone is determined by the kinematic balance between the local flow velocity and the local burning velocity toward the unburned mixture [170]. As such, the flame structure is intimately coupled to the underlying flame chemistry for premixed stagnation flames. Any inhibition due to MMT is expected to cause a decrease in flame speed and/or a reduction in flame temperature. In turn, the flame is expected to respond by a shift in position due to a perturbation in the flame speed or temperature. Lack of this response may indicate that MMT inhibition chemistry is quenched by the formation of particles or the radical recombination processes established by Linteris [170] are less impactful for fuels larger than methane.

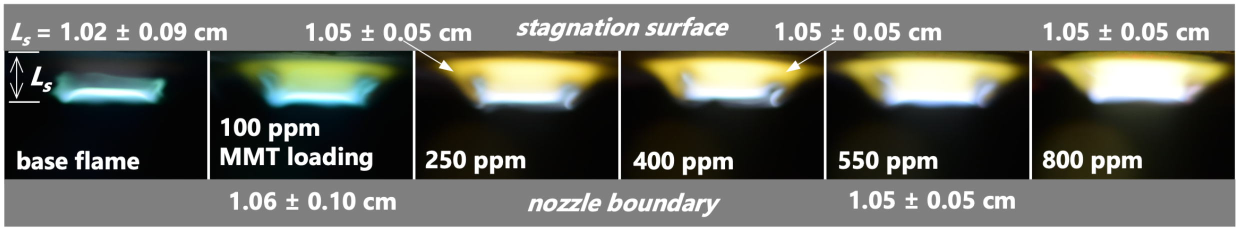

Figure 5.2: Flame images and measure flame standoff distances for the base flame and flames with increasing MMT loading.

Computations of the flame structure are carried out using the pseudo-one-dimensional formulation (OPPDIF) and solution to the two-dimensional axisymmetric flow field (ANSYS). Computed profiles at the centerline of the flame are compared to the experimental flame in terms of the measured gray scale intensity recorded by the camera. For the base flame, the luminosity detected by the camera is assumed to be comparable to the excited radical CH* position, and this comparison is shown in Fig. 5.3. The thin region of luminosity in premixed flat flames is due to chemiluminescence of excited radicals such as CH*, C_2*, and OH* [175]. A previous report on fuel-rich premixed flames [176] showed that emission of CH* and C_2* occurs in the same thin region in the flame zone. The comparison between computed CH* and measured intensity does not make a conclusion of CH* production. Rather, the computed CH* is a marker in space for the computed narrow flame region of where excited flame radicals exist. The computed temperature profile is compared to the measured intensity for MMT doped flames in the bottom frame of Fig. 5.3. No inference is made here to measure the CH* or temperature values based on camera intensity. Rather, the comparison shown in Fig. 5.3 is only to quantify any differences in measured flame position. The relatively good agreement between the flame position inferred from OPPDIF, ANSYS, and camera intensity is a basis for using the computed flame structure for analysis of nucleation and growth of MnO.

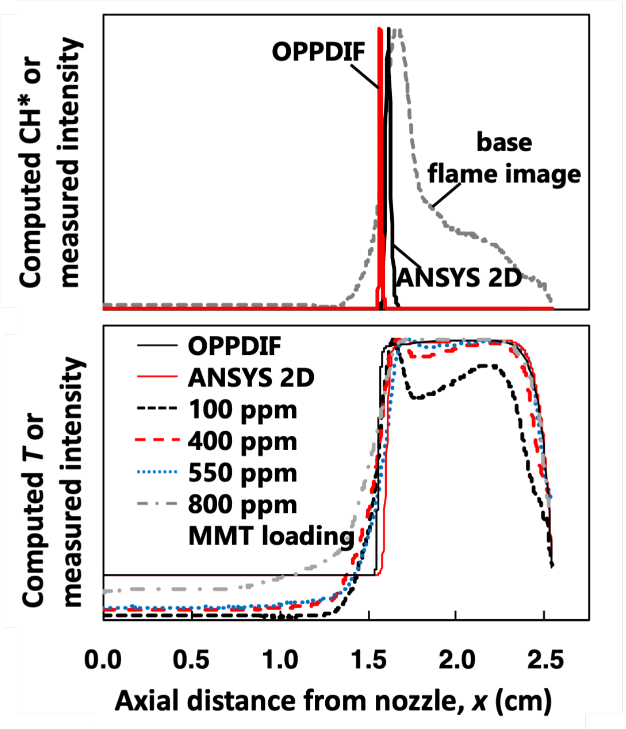

Figure 5.3: Computed centerline CH* profile compared to measured gray scale camera intensity from the base flame (top) and computed centerline temperature compared to measured gray scale camera intensity for increasing MMT precursor loading (bottom).

The particle size distribution of flame synthesized manganese oxide nanoparticles is measured here by mobility particle sizing and analysis of TEM images. Mobility sizing is a real-time measurement based on an aerosol sample pulled from the flame. The perturbation to the flame due to probe sampling is evaluated here by modeling the two-dimensional flame structure with a sampling flow applied to the stagnation surface boundary. The computed axial convective velocity and temperature contours are shown in Fig. 5.4 along with an image of a typical MMT doped flame. Without sampling suction, the convective velocity at the stagnation surface is zero due to the nonslip boundary condition, and the temperature is assigned the measured value of the water-cooled surface ($T_{stag} = 473K$). The flow rate into the orifice was measured, as discussed below, at various levels of suction. In Fig. 5.4, the flow velocity through the face of the sampling orifice is set to 200 cm s^{-1} to show the perturbation at the higher end of the experimentally applied suction. The computed profiles predict significant perturbations to the temperature and velocity field, but this effect is localized to a narrow region close to the sampling orifice. As expected, the flow induced by sampling suction increases the temperature of the flow entering the orifice.

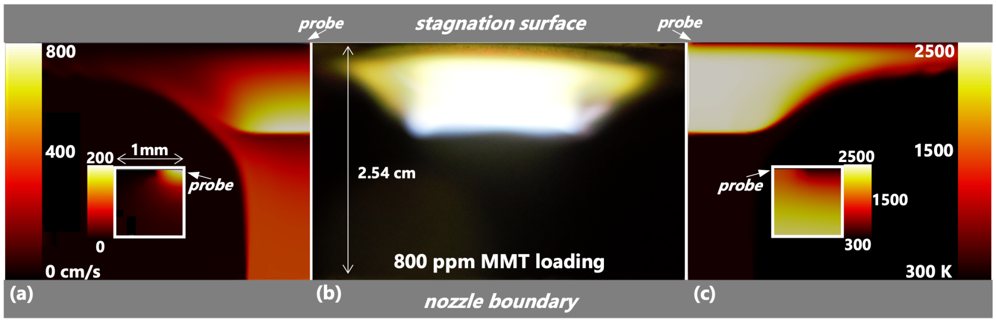

Figure 5.4: Computed axial velocity (a) and temperature (c) contours for the base flame with outflow through a sampling orifice ($r = 0.4mm$) at the centerline axis. The inset of the computed contours shows the perturbations to the velocity and temperature field in a 1 mm by 1 mm domain at the sampling probe boundary. Also shown is an image for a typical flame doped with MMT precursor without sample suction (b).

The probe perturbation is further illustrated in Fig 5.5 in terms of the computed centerline profiles of the two dimensional solution. The solution for a 100 cm s^{-1} sample flow rate is also included to represent the flow rate range adopted for optimal sampling conditions. The axial convective flow velocity deviates from the stagnation flow solution approximately 1 mm upstream of the sampling orifice boundary. Manganese oxide nanoparticles present in the flame are assumed to follow gas streamlines except in the vicinity of the stagnation surface where an additional force on the particle induces a thermophoretic velocity toward the colder surface. The computed thermophoretic velocity, shown in Fig. 5.5, decreases significantly as probe induced flow makes the temperature gradient less severe compared to the stagnation flow solution. The reaction time computation shown in Fig. 5.5 is based on the sum of convective and thermophoretic velocities. The reaction time label is based on the assumption that the time for conversion of manganese oxide precursors to the final product begins at the flame zone and ends at the stagnation surface boundary. The flow induced by the probe sampling speeds up the particle more than reduction in thermophoretic velocity. Thus, the reaction time is significantly lower than the stagnation flow solution when probe perturbation is accounted for. For the 100 cm s^{-1} sample flow condition, the reaction time is reduced by 20% relative to the time computed for the stagnation flow. This magnitude of flow perturbation is on the same order as the perturbation reported for sampling probe perturbation in premixed burner stabilized flames [177].

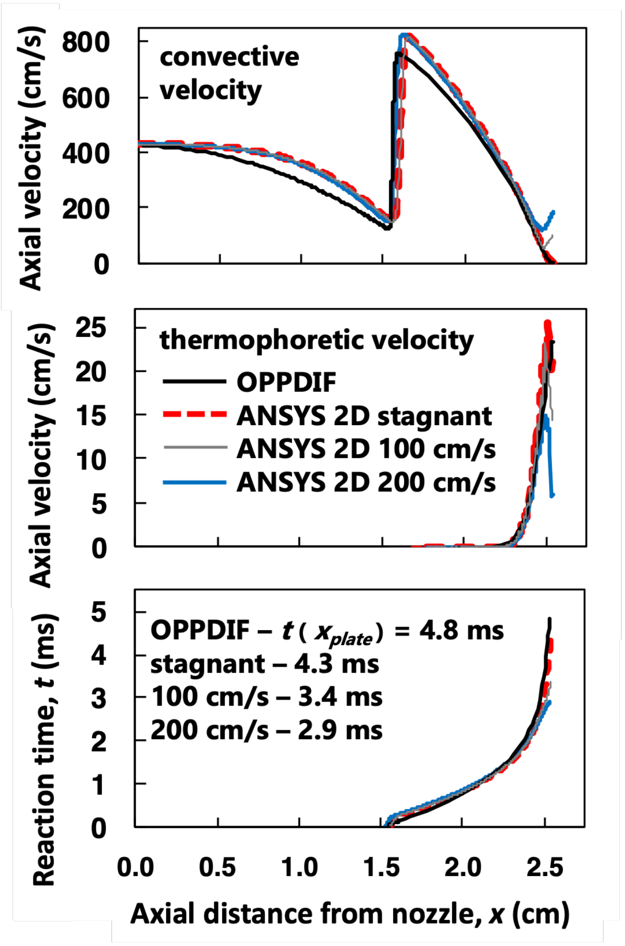

Figure 5.5: Computed centerline profiles of axial convective velocity (top), axial thermophoretic velocity (middle), and reaction time (bottom). Solutions for the stagnation flow is presented from OPPDIF and ANSYS along with the solution for sampling probe induced flows of 100 and 200 cm s^{-1}.

Analysis of the flame synthesized manganese oxide is carried out by XRD to characterize the oxide phase and structure. Diffraction patterns for films deposited from the 400 and 800 ppm MMT loading cases are shown in Fig. 5.6. Sintering during deposition is minimized by using aluminum substrates for efficient heat transfer from the water-cooled block. No significant diffraction was observed from samples deposited on aluminum which indicates that the film material is amorphous and/or any crystalline regions are very small. Faint evidence of the (200) face of MnO is observed for the as-deposited 800 ppm case, but most of the signal is an amorphous hump. A second deposition experiment was carried out using quartz deposition surfaces to inhibit heat transfer to the water-cooled block. This artificially induces sintering of the deposited film over the deposition period to provide an indication of the oxidation state of the flame synthesized product. Prominent, yet broad diffraction peaks corresponding to known MnO faces (JCPDS 07-0230) are observed after sintering is induced during deposition. Comparison of the relative intensities indicates that slight differences in stoichiometry may exist between the 400 and 800 ppm conditions. Nonetheless, the XRD analysis indicates that ultrafine particles with oxidation state at or close to MnO are produced. In the absence of significant oxidation beyond MnO, nucleation and growth processes could be examined in isolation.

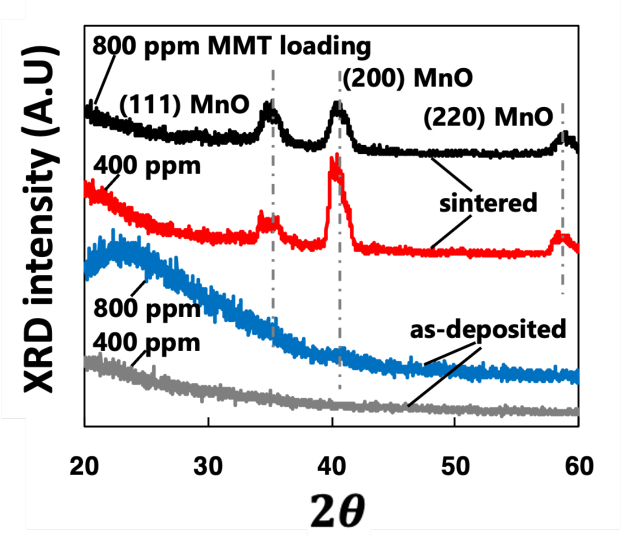

Figure 5.6: XRD patterns for as-deposited and sintered films deposited from the flame.

Thermodynamic analysis along the computed temperature and gas-phase oxygen profiles is carried out to assess the Kelvin effect on MnO nucleation in the flame. The computed flame structure obtained by OPPDIF is shown in Fig. 5.7 in terms of the temperature and gas-phase oxygen as a function of reaction time. The reaction time is a Langrangian reference frame where the position of the flame zone is $t = 0$, and the final reaction time occurs upon reaching the stagnation surface. For coagulation-limited growth, particles would form at $t = 0$ and grow over the entire reaction time. Stretch-stabilized flames are relatively hot, and this may introduce a condition in which condensation of MnO is not stable until the flame temperature decreases in the vicinity of the water-cooled stagnation surface. The OPPDIF stagnation flow solution is the basis of the thermodynamic analysis, but the conclusions also apply to the probe perturbed conditions after shifts in time and temperature are taken into account. The current flame is fuel-rich, but small amounts of gas-phase oxygen are predicted to remain in the post flame region. The flame zone is a very narrow region where the flame temperature quickly approaches the adiabatic flame temperature, and this temperature persists through most of the post flame region. On approach to the stagnation surface, the flame temperature approaches the temperature of the water-cooled surface. Any nanoparticles formed in the flame are assumed to follow the flow streamlines with exception to the cooling region where the thermophoretic force induces an additional particle velocity toward the stagnation surface.

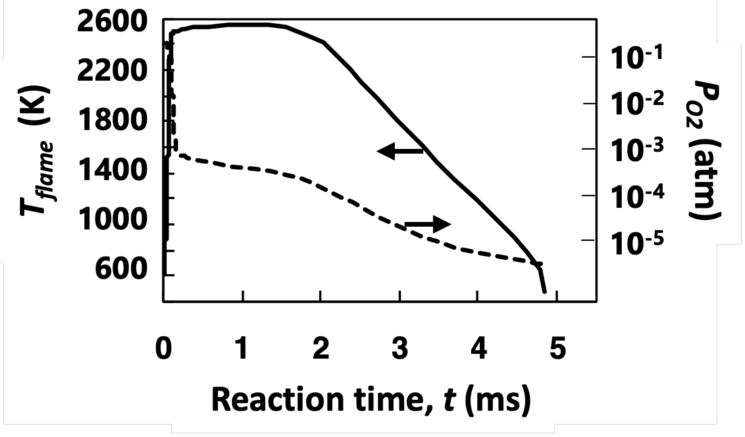

Figure 5.7: Temperature and oxygen as a function of reaction time determined by the pseudo-1D stagnation flow computation (OPPDIF).

The basis of the thermodynamic analysis is that the local gas-phase Mn and O_2 concentrations determine the saturation conditions according to Eqs. 5.1 and 5.6. The saturation ratio profile for zero Mn converted is shown along with the profile for 99% conversion of Mn in Fig. 5.8 to represent the limiting cases for the gas-to-particle conversion. Within this range, supersaturation is only achieved as the flame temperature decreases significantly from the peak temperature of 2600 K. The saturation ratio is not sensitive to the factor of 2 difference between precursor loading cases. This is evident in the overlapping curves in the cooling region where $S > 1$. As Fig. 5.8 shows, the Kelvin equation is also insensitive to the precursor loading conditions. Computation of the critical Kelvin diameter based on the local saturation ratio indicates that condensation of MnO monomers become stable 3-4 ms after the flame zone for both 400 and 800 ppm MMT precursor loading conditions. In other words, a thermodynamic barrier may delay nucleation and growth of MnO nanoparticles for the current flame temperature and precursor conditions. The barrier may play a role in flame synthesis conditions at relatively high-temperature, low precursor loading, and/or composite materials having a range of proportions. This analysis is a factor in interpreting the particle size measured for particles collected at the stagnation surface.

Calibration of the aerosol sampling probe dilution is carried out by measuring the flow rate of air flowing into the probe orifice by bubble-flow meter (mini-Buck M-1) in a procedure described previously [52, 178]. The dilution ratio calibration is shown in Fig. 5.9 as a function of indicated pressure drop across the orifice. The indicated pressure drop is the average pressure drop determined by monometers placed at the inlet and outlet of sampling probe tube. Reversal of the flow from positive to negative flow is observed as the average pressure drop approached 28 mm H_2O. The measured flow rates correspond to sample flow velocities spanning 50-400 cm s^{-1}.

The size distribution of the aerosol sample is measured by mobility sizing for a range of dilution ratio (probe suction) to assess artificial perturbations. For low sample dilution, the relatively high number density undergoes rapid coagulation growth across the sampling orifice causing an artificial drop in number density and increase in median diameter. For high dilution, the relatively long residence time across the orifice allows for significant diffusion

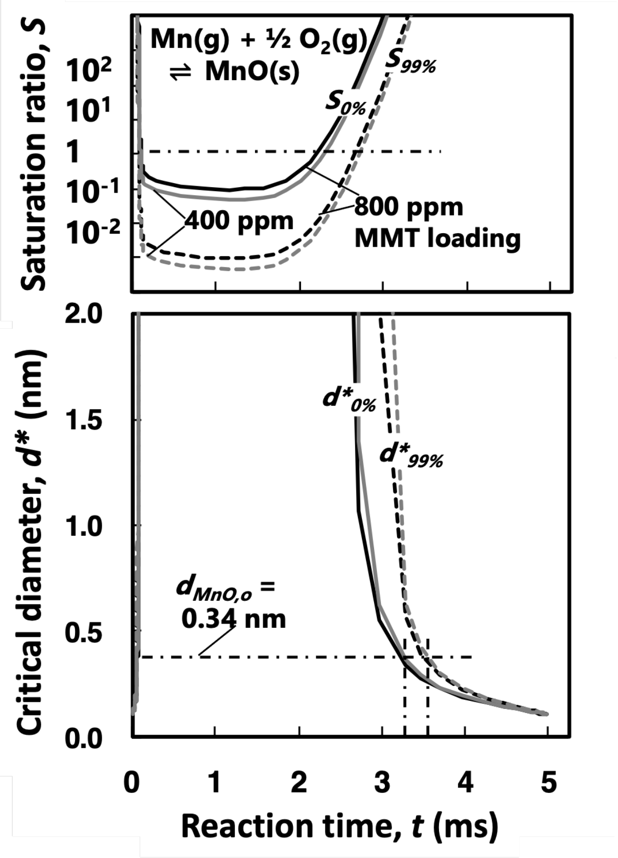

Figure 5.8: Thermodynamic analysis for MnO nucleation in terms of the saturation ratio (top) and critical Kelvin diameter (bottom) based on the computed temperature and oxygen profiles.

loss of small particles to the wall. Ideally, an optimum range of dilution ratio exists where the dilution corrected number density and median diameter are insensitive to the applied dilution [178]. Sampling artifacts to the measured PSDF are minimized in this optimal region.

Each measured PSDF is fit to a log-normal distribution to obtain the number density, median mobility diameter, and geometric standard deviation. Measured PSDF number density and median diameter for the 400 ppm MMT loading condition, shown in Figure 5.10, indicates that the optimal sampling dilution range is narrow. Namely, a peak in the dilution corrected number density occurs around 200 dilution ratio, and the median diameter is close to 4 nm within this dilution ratio range. The measured values are the average of

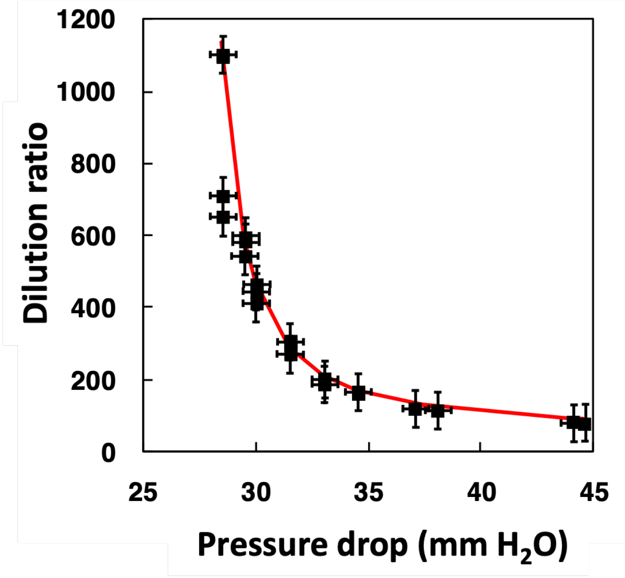

Figure 5.9: Measured dilution ratio calibration in terms of the indicatedpressure drop across the sampling orifice.

8-10 separate scans (30 s scan of DMA voltages for 1-20 nm mobility diameter) with error bars representing typical deviation across runs. The median mobility diameter and number density are determined to be 4 ± 1 nm and (2 ± 1) x 10^{11} cm^{-3} for the 400 ppm loading case based on conservative interpretation of the response of the PSDF to dilution ratio.

This measurement is also reported in Fig. 5.11 for the 800 ppm MMT loading condition. The optimal region where the PSDF number density and median diameter is clearer for the 800 ppm case. The median mobility diameter and number density are determined to be 5.5 ± 1 nm and (6 ± 1) x 10^{11} cm^{-3} based on interpretation of the response of the PSDF to dilution ratio. Dilution corrected PSDF are shown in Fig. 5.12 for the 400 and 800 ppm MMT loading conditions. Deviations in the PSDF are due to minor fluctuations in the flame and sampling conditions across and during scanning periods. These fluctuations include drift of the applied pressure drop and deposit accumulation at the sampling orifice. The observed increase in median diameter and geometric standard deviation provide insight into the underlying aerosol growth processes. Significant diffusional losses in the sampling line exist at the inlet valve and tubing where the flow splits and slows down in the final 10 cm before entering the mobility analyzer.

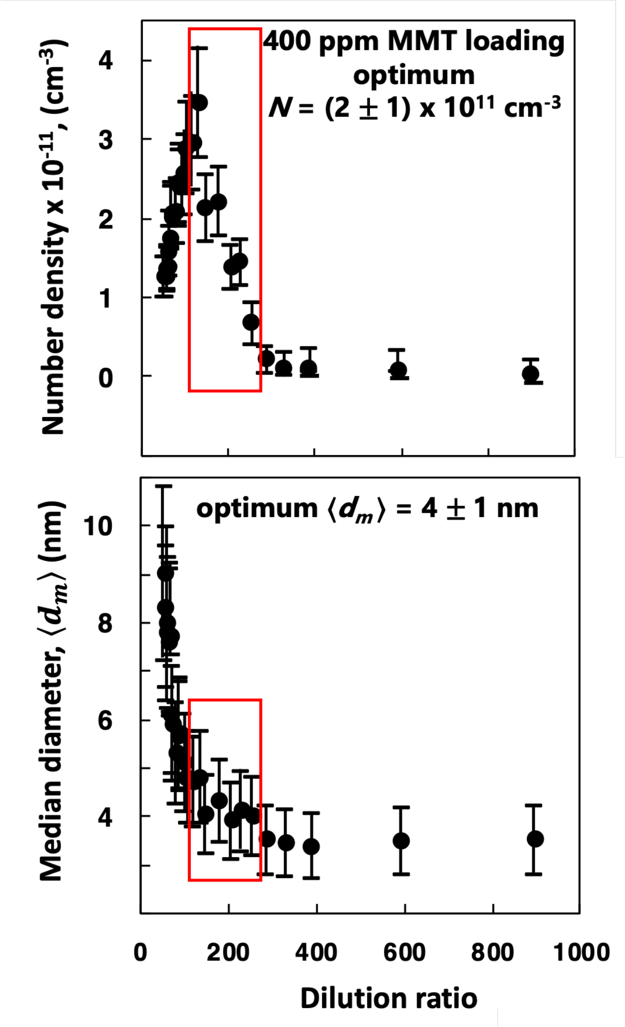

Figure 5.10: Measured PSDF number density and median diameter for the 400 ppm MMT loading condition for a range of sample dilution ratios.

The particle size distribution is also measured by analyzing TEM images for the 400 and 800 ppm MMT loading cases. The sample particles correspond to the "as-deposited" case shown in the XRD patterns which was obtained by depositing onto an aluminum substrate to minimize sintering. Example TEM images and the distribution of measured projection diameters are shown in Fig. 5.13. The histogram is a distribution for a total of 150 particles for each ppm loading case. The median diameter determined by TEM is in reasonable agreement with the mobility diameter-based distributions. The observed ultrafine size is also in line with the lack of XRD signal observed for the as-deposited films. The particle

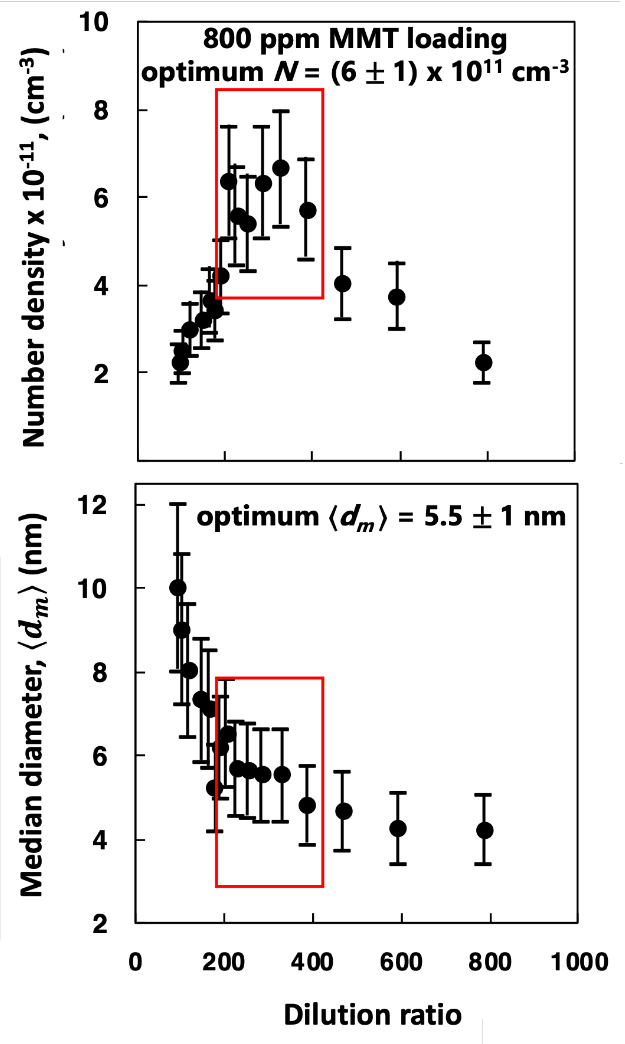

Figure 5.11: Measured PSDF number density and median diameter for the 800 ppm MMT loading condition for a range of sample dilution ratios.

size measured by mobility sizing and TEM corresponds to the end of the particle growth process. Gas-to-particle conversion occurs at some point upstream of the stagnation surface and measurement of the particle size at the stagnation boundary provides insight into the underlying nucleation and growth mechanisms in the flame. The measured particle sizes provide an experimental comparison to the particle size predicted from the gas-phase flame temperature-time profile.

The temperature-oxygen-time history of the particle during growth in flame can be inferred from the computed flame structure. Moreover, analysis of the thermodynamic bar-

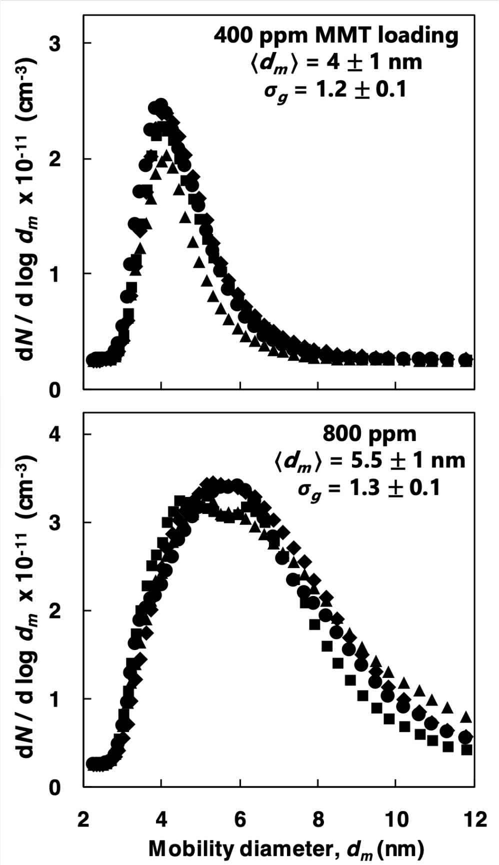

Figure 5.12: Measured PSDF at optimal sampling conditions for the 400 ppm (top) and 800 ppm MMT loading (bottom) cases. Different symbols are used to denote separate experimental runs which correspond to the optimal range of dilution ratio specified in Fig. 5.10 and Fig 5.10

rier provides insight into the time at which nucleation becomes stable. If a thermodynamic barrier for nucleation is present, the observed particle size would be smaller due to the delay in particle condensation and growth. This hypothesis is tested in Fig. 5.14 in terms of particle size profiles computed as a function of reaction time. Comparison of expected particle size for coagulation-limited and nucleation-limited regimes is done by application of the monodisperse coagulation rate expression starting from the position of the flame zone ($t = 0$) and at a downstream position determined by the critical Kelvin diameter.

Nucleation from MnO monomers is predicted to occur over 3 ms after the flame zone for both 400 and 800 ppm levels of precursor loading based on the critical diameter criterion. Assuming a constant collision efficiency of $\alpha = 0.65$, the final particle size computed for the

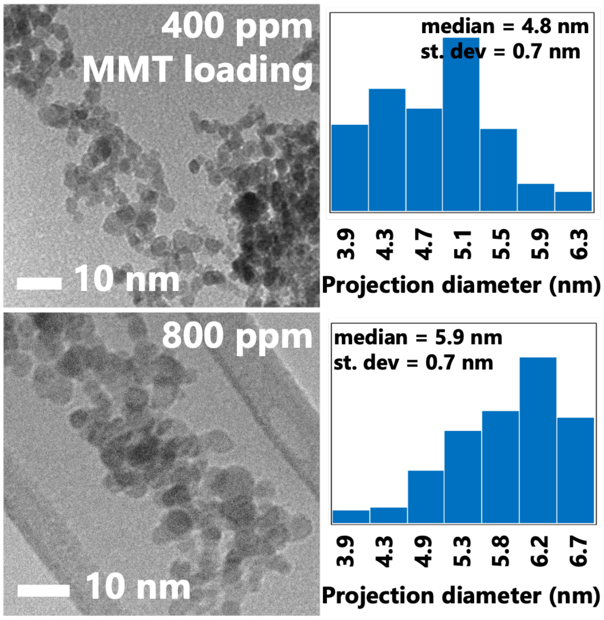

Figure 5.13: TEM images and particle size counts for the 400 ppm (top) and 800 ppm (bottom) MMT precursor loading conditions.

nucleation-limited regime is 4.8 and 5.9 nm for the 400 and 800 ppm cases, respectively. Computations are also shown for $\alpha = 0.3$ and 0.9 to represent the range of feasible particle sizes resulting from coagulation growth. The computed particle size is nearly double for coagulation-limited growth. The measured particle size is much closer to the size predicted for the nucleation-limited regime for both the 400 and 800 ppm loading cases. The mobility diameter is subject to uncertainty in the growth time induced by flow perturbation. However, the size measured by TEM indicates that the particle size is not significantly higher under full stagnation flow conditions. The applied sample suction amounts to 20 % faster reaction time which roughly accounts for the discrepancy between the size measurement techniques. Excessive suction was not applied, but Fig. 5.14 labels the reaction time computed for the lowest dilution ratio case to demonstrate that the coagulation-limited growth regime does not explain the relatively small particle size observed. The smaller than expected particle size is evidence that the current temperature and precursor conditions do not induce high levels of supersaturation, and the Kelvin effect may hinder nucleation.

This analysis is subject several assumptions and experimental uncertainties, but the

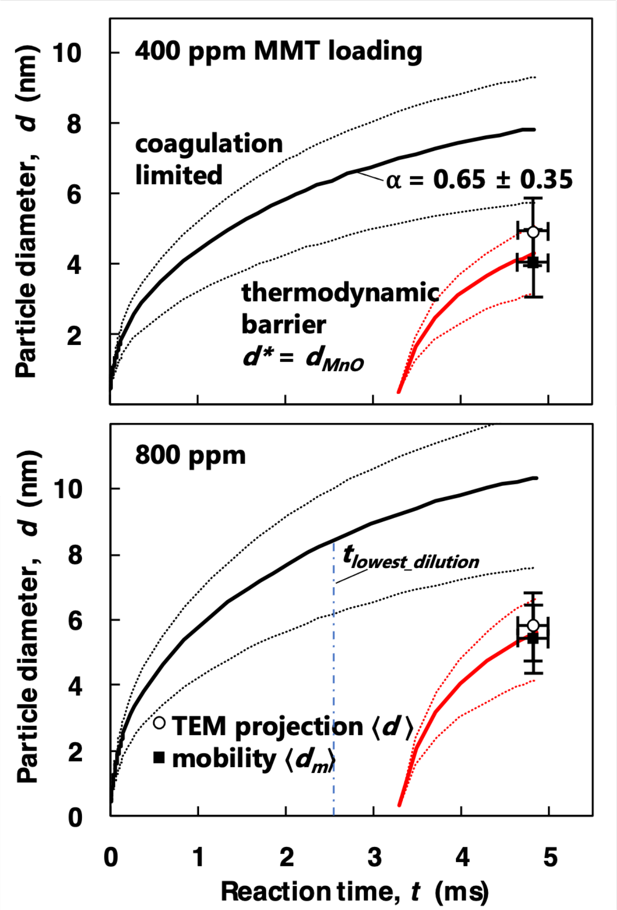

Figure 5.14: Computed particle diameter profile for the 400 ppm (top) and 800 ppm (bottom) MMT precursor loading conditions for coagulation-limited growth and growth limited by a thermodynamic barrier. Also included are particle sizes measured by mobility sizing and TEM projections.

results are conclusive in terms of observation of particle sizes significantly lower than predictions of coagulation-limited growth. Disappearance of nucleated particles at elevated temperatures has been reported for iron oxide synthesis in premixed flat flames [162] and TiO_2 production in turbulent flow reactors [160], but this effect is more pronounced in premixed stagnation flames due to flame stabilization at relatively high temperature. Isolated study of nucleation behavior carried out for the manganese oxide system is invaluable for elucidating competing thermodynamic and kinetic processes leading to the wide-range of manganese oxides obtainable by flame synthesis.

5.4 Summary

A complementary experimental and modeling study is performed for nucleation of manganese oxide nanoparticles in premixed stagnation flames. Flame synthesis occurs at relatively high temperature and precursor loading. Thermodynamic analysis based on the postulated nucleation process, $\mathrm{Mn\ (g)} + \frac{1}{2}\,\mathrm{O_2} \longrightarrow \mathrm{MnO\ (s)}$, is carried out to quantify precursor supersaturation and potential barriers to nucleation. The computed temperature-time-oxygen history is the basis used to analyze nucleation and growth. The effect of MMT on the flame chemistry is assessed by comparing measured flame position for the base flame to flames having precursor loading from 100 to 800 ppm. Measured flame standoff distances are unchanged relative to the base flame when MMT is added. This may indicate that the established inhibition flame chemistry is quenched by particle formation or less impactful for the fuels larger than methane. The measured flame position is in agreement with flame position predicted by pseudo one-dimensional and pseudo two-dimensional solutions of the flame structure. Agreement between measured and computed flame position is justification for basing the thermodynamic analysis on the computed flame structure.

Mobility particle sizing is carried out by aerosol sampling with probe perturbations characterized by two-dimensional flame structure computations including probe suction. Probe induced flow decreases the reaction time in the post flame region by 20 % compared to full stagnation flow. The observed discrepancy between median sizes measured by mobility sizing and TEM imaging may be due to differences in growth time. Thermodynamic analysis indicates that a thermodynamic barrier, quantified by the Kelvin effect, delays condensation of MnO for the flame synthesis conditions currently studied. The nucleation-limited growth mechanism explains the observed particle size much closer than growth predicted from a coagulation growth mechanism, even when probe perturbations are accounted for. Isolated study of nucleation behavior carried out for the manganese oxide system is invaluable for elucidating competing thermodynamic and kinetic processes leading to the wide-range of manganese oxides obtainable by flame synthesis. In addition, supersaturation should be examined for gas-phase processes producing composite materials having a range in proportions.

The flame-formed manganese oxide nanoparticle formation studies described in Chapter 5 has been published in Energy and Fuels (Dasappa, S., Camacho, J., “Thermodynamic barrier to nucleation for manganese oxide nanoparticles synthesized by high-temperature gas-to-particle conversion: Computational methods and Experimental methods, 35, 2, 1874-1884). The dissertation author is the primary investigator for the publication.

Part III

Flame Spray Synthesis

Chapter 6

Production of Carbon Black in Turbulent Spray Flames of Coal Tar Distillates

Over the centuries, carbon particles have been produced in a variety of processes but the furnace black process has been widely adopted as the most efficient and versatile method for industrial scale production [6, 11, 179]. The furnace black process relies on flames to achieve high reactor temperatures but the conversion of feedstock to carbon black particles occurs in a downstream pyrolysis process separated from the high - temperature oxidizing conditions. The carbon black industry has developed furnace processes for the production of aggregates with tailored primary particle size, aggregate morphology and surface functional groups. Selectivity in carbon black properties has been established for large-scale production by optimizing temperature, residence time and feedstock-to-air ratio with addition of coagulation suppressant in some cases [11]. Global models for conversion of a generic hydrocarbon precursor in furnace black reactors have been researched [11, 180, 181]. More recently, detailed chemical kinetic models have been presented based on methane [146, 182], acetylene [183], benzene [184], methylnaphthalene [185], and waste tire oil feedstocks [186]. Any experiments accompanying these modeling studies do not directly explain furnace black processes using petroleum or tar distillate precursors. The study uses a real heavy aromatic feedstock but the synthesis does not occur in a pyrolysis reactor. Nonetheless, the relatively simple turbulent spray flame configuration is a suitable approach to investigate physics-based combustion kinetics and particle growth from an industrially relevant feedstock. The study examines the high-temperature conversion of feedstock to carbon black particles in flames rather than a pyrolysis reactor. Flames introduce high-temperature oxidizing conditions which result in a loss of the particle precursor to the gas-phase. However, the unique flame environment may result in useful carbon structure and surface properties without a pyrolysis reactor stage and this may justify the lower particle yield.

The fossil fuel by-product known as carbon black feedstock is a mixture of heavy aromatic components originating from either cracking of petroleum oil or distillation of coal tars [6, 11, 179]. The feedstock employed is distilled from tar components produced during high-temperature coking of bituminous coal. Coal-sourced feedstocks were engineered to match the physical and chemical properties of the original petroleum-based feedstocks to ensure uniformity and compatibility with established carbon black processes. In the furnace black process, the heavy viscous feedstock is pre-heated to facilitate atomization and mixing before entering the pyrolysis reactor stage. The initial energy to reach the reaction temperature (typically 1500 - 2200 K) is furnished by the pre-combustion stage and partial combustion of the oil feedstock. The yield of the feedstock to carbon black is up to 70% but high-surface area grades require higher reactor temperatures which lowers the yield [6]. The study explores the formation of high-surface area carbon black without the use of a pyrolysis reactor. Rather, atomized carbon black feedstock is used to establish a piloted, turbulent spray flame at conditions conducive to carbon nanoparticle formation.

Similar to a flow reactor, flames have the potential provide tunable nanoparticle synthesis conditions within a certain range. The SpraySyn burner was introduced as a standardized spray flame configuration to systematically examine the conversion of non-volatile liquid precursors to nanoparticles [187]. The conversion of coal tar distillates to high-surface area carbon black is examined for a range of flame temperature and precursor feed rates. Spray flame synthesis has the potential for industrial scale production, and the implementation of the SpraySyn system may facilitate scale-up production [188–190].

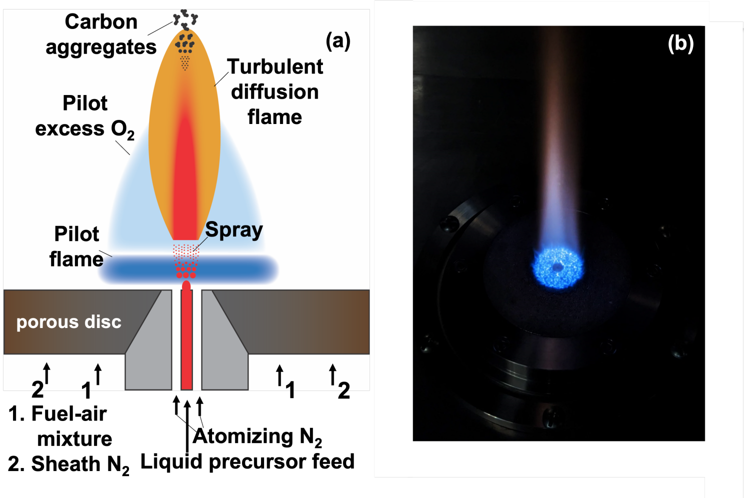

Figure 6.1: Schematic of the SpraySyn burner configuration (a) and an image of a typical flame used to pilot the synthesis spray flame (b).

6.1 Experimental Conditions

An experimental investigation of carbon black production in turbulent spray flames is performed. Conventional piloted, turbulent spray flame nozzles use co-axial jet or slot flames to support combustion of the central spray [190]. The narrow size scale of the pilot nozzle in conventional designs increases the required spatial resolution for flame modeling studies [187]. To facilitate systematic studies, the pilot flame of the SpraySyn burner configuration is designed as a burner-stabilized flame with a larger domain to facilitate flame modeling with a coarse grid. The schematic of the SpraySyn burner, shown in Fig. 6.1, includes a porous metal disc which distributes the flow of the laminar pilot premixed fuel-air mixture. A larger area of this porous disc is also used to homogeneously issue a concentric inert nitrogen flow to shield and stabilize the synthesis process. An image of a typical pilot flame stabilized on the porous surface is shown in Fig. 6.1. Atomization of the liquid precursor feed is carried

Table 6.1: Pilot and spray flame conditions.

Flame	**Pilot** ϕ	**Pilot** C_2H_4 (SLPM)	**Pilot** O_2 (SLPM)	**Pilot** N_2 (SLPM)	**Feed Toluene** (mL/min)	**Feed Coal Tar Distillate** (mL/min)
Series 1: 65% toluene - 35% coal tar distillate by volume						
Increasing pilot ϕ; Atomizing N_2 = 9.9 SLPM						
p40t65d35	0.40	1.65	12.36	10.4	1.95	1.05
p43t65d35L	0.43	1.65	11.46	10.4	1.95	1.05
p45t65d35	0.45	1.65	11.01	10.4	1.95	1.05
p50t65d35	0.50	1.65	9.89	10.4	1.95	1.05
Series 2: Pilot ϕ = 0.43						
Increasing coal tar distillate volume %; Atomizing N_2 = 10.8 SLPM						
p43t100d0	0.43	1.65	11.46	10.4	3.00	0
p43t65d35H	0.43	1.65	11.46	10.4	1.95	1.05
p43t40d60	0.43	1.65	11.46	10.4	1.20	1.80
p43t25d75	0.43	1.65	11.46	10.4	0.75	2.25

Feed total flow rate of 3 mL/min. Sheath N_2 gas co-flow: 120 SLPM.
Flame names: "*p*"- pilot flame equivalence ratio, "*t*"- liquid feed toluene % volume, "*d*"- liquid feed coal tar distillates % volume, "*L*" and "*H*"- flow atomizing N_2 flow rate.

out by a two - fluid nozzle. Nitrogen gas is the atomizing fluid and the coal tar distillates liquid precursor injection rate is controlled by a syringe pump (KDS 100). The gas flow rates are controlled by calibrated critical orifices. More details of the SpraySyn burner design are discussed by Schulz and co-workers in their original instrumentation publication. Carbon black feedstock (Koppers Inc.) is an aromatic tar distillates obtained between 600 K and 700 K. Approximate composition is up to 24 % phenanthrene, up to 22 % fluoranthene, up to 18 % pyrene, up to 7 % anthracene and up to 3 % naphthalene with many other aromatic components [191].

The burner system is housed in a closed polycarbonate chamber with height, width and depth of 1.2 m, 0.6 m and 0.8 m, respectively. Particles are captured from the flame

0.5 m above the burner surface from a 300 nm quartz filter (Sterlitch QR-200) attached to a vacuum pump. The product particles are examined under TEM using a FEC Tecnai 12 with a Teitz 214 high resolution bottom mounted digital camera. The TEM samples are prepared by collecting carbon black from the filter and suspending the particles in tetrahydrofuran. Raman spectra are obtained from the particle laden filter using a Thermo DXR2 Raman Microscope with a 532nm excitation source for spectra having Raman shifts spanning 300 to 3000 cm^{-1}. Flame images are obtained from a Nikon D5300 DSLR camera and the images are analyzed using a process designed by the developers of SpraySyn to define the spray flame height and width [107, 187, 192]. A separate set of flame images for two-color pyrometry studies to provide contour profiles of the soot particle temperature field. Thermocouple measurements of the pilot and spray flames are taken to complement the pyrometry measurements. A fine-wire type R thermocouple (125 micron wire, Omega P13R-005) is coated with a Y_2O_3/BeO ceramic as outlined in previous studies [52, 59] to minimize catalytic surface reactions on the platinum wire [193]. Thermocouple readings are corrected for energy losses at the thermocouple bead based on known heat transfer behavior of fine-wire thermocouples in flames [194, 195]. The details regarding the characterization techniques are provide in 2.1.1.

The two flame series currently studied are outlined in Table 6.1. The pilot fuel is ethylene gas kept at the same flow rate for all flames. Pilot nitrogen is also kept at the same flow rate across all flames in a flow kept independent of the pilot oxygen. The first series of flames examines the effect of excess oxygen in the pilot flame by systematically increasing the pilot oxygen flow rate to decrease the pilot flame equivalence ratio from 0.5 to 0.4. The liquid particle feedstock is coal tar distillates diluted in toluene (65% toluene, 35% distillate by volume in the first series) to decrease viscosity and to minimize the disruption due to liquid coking at the atomization nozzle. The second flame series keeps the pilot flow rates constant while steadily increasing the percent volume of coal tar distillate in the liquid feed from pure toluene to 75% coal tar distillates by volume (at 3 mL/min liquid feed flow rate).

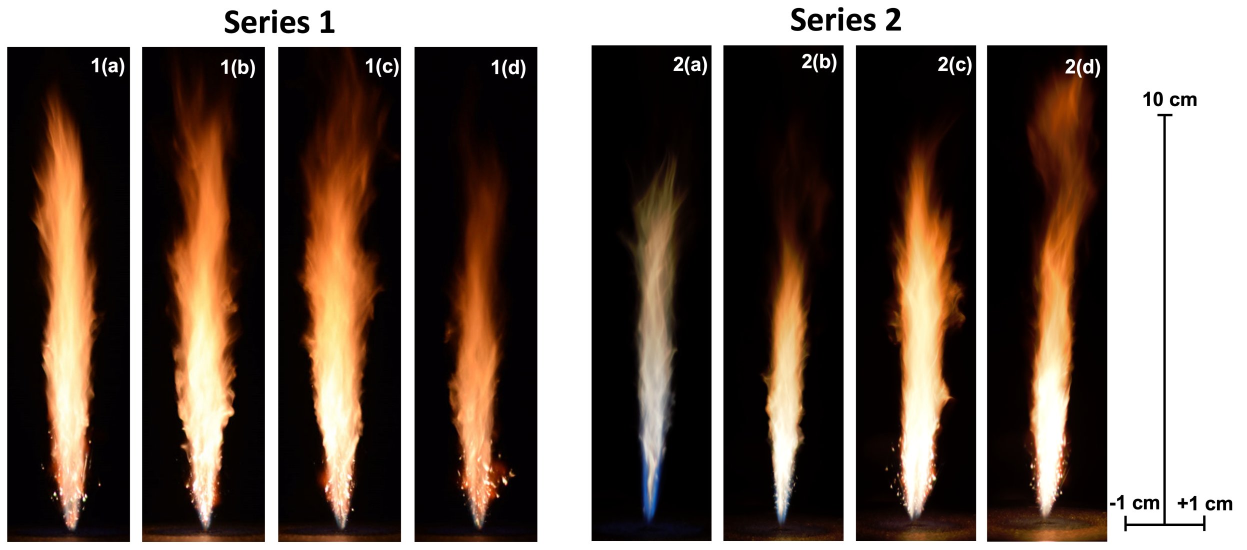

Figure 6.2: Left - Flame images of Series 1 flames; t65d35 with p40 (a), p43 (b), p45 (c) and p50 (d). Right - Flame images of Series 2 flames; p43 with t100d0 (a), t65d35 (b), t35d65 (c) and t25d75 (d).

6.2 Results and Discussion

Images of the spray flames provide insights into the flame dynamics and interaction with the pilot flame. Typical spray flame images for the Series 1 flames are shown in Fig. 6.2(left). In Series 1, the pilot flame is varied and the spray conditions are kept constant. The lowest pilot equivalence ratio (p40) corresponds to the highest oxygen flow entrainment to the spray because there is the most excess oxygen available. The p40 flame shows the tallest area of flame luminescence because the higher oxygen entrainment may result in a higher spray flame temperature. As the pilot oxygen flow rate is reduced, the equivalence ratio increases such that less excess oxygen is available for the spray flame. In general, the flame temperature of burner-stabilized flames decreases with decreasing flow rate and increases with increasing equivalence ratio. These two competing factors affect the appearance of Series 1 flames. Tall flame heights are maintained with increasing equivalence ratio perhaps due to increasing pilot flame temperature (Fig. 6.3(left)). Decreasing flame luminosity due to less available oxygen is also observed and the p50 pilot flame corresponding to the lowest oxygen is relatively short and dim. All flame images are captured at 1/3200 s shutter speed to prevent saturation in the brightest flame images and for comparable images across all flames. The observed range of flame conditions is expected to impact the production of flame-formed carbon black particles.

In Series 2 flames, the pilot flame is kept constant and the spray composition is modified to include a greater contribution of coal tar distillates. Typical flame spray images for Series 2 flames are shown in Fig. 6.2. Under this condition, the pure toluene spray flame shows lower visible emissions from the spray carbon flame particles. The addition of more coal tar distillate to the spray feed significantly increases the flame luminosity and the flame height (Fig. 6.3(right)). The greatest flame height observed for the 25% toluene / 75% distillates spray flame may be due to the more carbon dense feedstock that induces a longer and stronger spray flame for the same oxygen entrainment. The presence of heavier precursor components is evidenced by bright burning droplets extending into the pilot flame for increasing coal tar distillate feed. The series of flame images imply that the carbon is formed under a range of growth time, growth temperature and oxidation and these effects are discussed in terms of observed particle properties below.

Thirty flame images are taken for each flame condition and processed to obtain and averaged flame height and width. Before taking flame images, a calibration pattern placed on the burner is imaged and processed in a procedure defined by Schulz and co-workers for defining the camera pixel-to-millimeter ratio [187]. A peak flame height of 11.2 cm is observed for the p45 flame in Series 1 flames but the lower equivalence ratio conditions also have comparable flame height considering the standard deviation across the images (reported as error bars). The measured flame width for the Series 1 flames lay within 10% of each other. Stronger trends in flame dimensions are observed for the Series 2 flames. The toluene flame is relatively small and this corresponds to a spray flame height of 9.1 cm and width of 0.9 cm. Introduction of an increasing fraction of coal tar distillates to the spray feed increases the spray flame height and width up to 11.3 and 1.7 cm, respectively.

Flame temperature measured by thermocouple and soot pyrometry add further in-

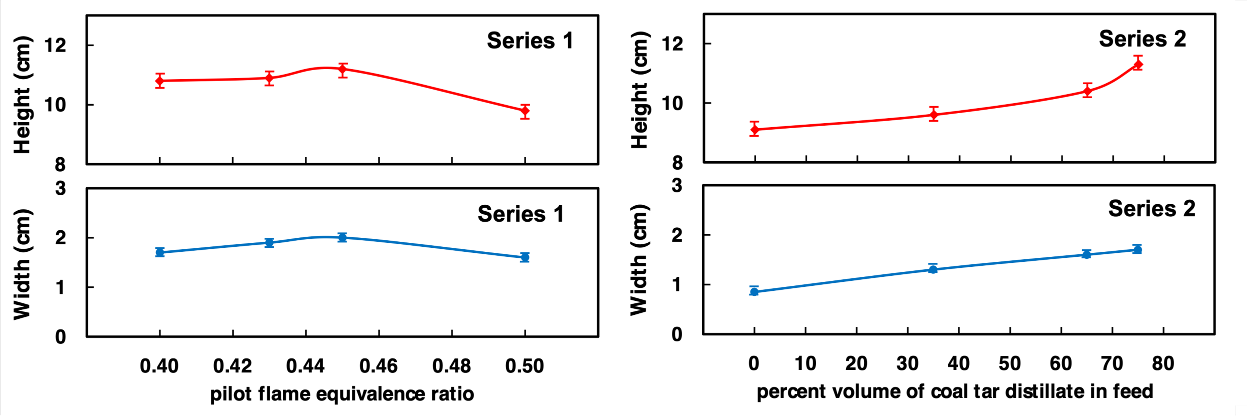

Figure 6.3: Measured flame heights and widths based on flame images for Series 1 (left) and Series 2 (right). Lines are drawn to guide the eye.

sights into the formation and growth environment of the carbon black particles. The temperature profile measured by thermocouple at the centerline of the pilot flames is shown in Fig. 5. As discussed above, the flame temperature of burner-stabilized flames depends on the inlet flow rate and equivalence ratio of the fuel-air mixture. The measured temperature profile indicates that increasing the flow rate of oxygen causes a net increase in flame temperature at all distances above the burner despite lower equivalence ratio. The pilot flames of the SpraySyn burner are unique burner-stabilized flames, however, because a 0.6 cm island housing the spray nozzle assembly exists at the center of the burner surface (see Fig. 6.1). Without the spray, a stagnant zone exists at the centerline and this impacts the lowest flow rate pilot flame, p50, as exhibited by the peak flame temperature delayed 2 cm downstream of the burner surface. The higher flow rate pilot flame temperature profiles are less impacted by this island. The maximum flame temperature is comparable across all equivalence ratio conditions but the lower flow rate of the p50 condition induces relatively lower temperatures at the burner boundary and further downstream. As discussed above, the temperature profile of the pilot flames is expected to directly impact the spray flame structure and carbon black particle properties.

The spray flame temperature is also measured by thermocouple at the centerline. The largest variation in spray flame temperature is expected to occur for Series 1 as the

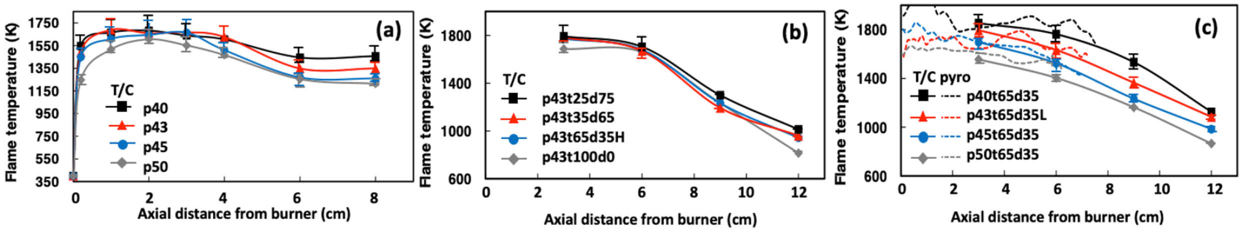

Figure 6.4: Measured temperatures at the centerline of the pilot flame without the spray flame using a thermocouple (a), centerline measurements of Series 1 spray flames using a thermocouple and soot pyrometry (b) and centerline measurements of Series 2 spray flames using a thermocouple (c). Lines are drawn to guide the eye.

pilot flame temperature varies for constant spray inlet conditions. As such, temperature measurements are also taken by thermocouple and soot pyrometry for Series 1 to gain insight into the 2D axisymmetric flow field. The centerline thermocouple measurements, shown in Fig. 6.4, indicate the low equivalence ratio pilot flame induces the highest flame temperature profile. The spray flame temperatures follow the same trend as the pilot flame center line temperature profiles with the highest flame spray temperature measured by thermocouple in Series 1 being 1850 K (flame p40) and the lowest spray flame temperature is 1555 K. The centerline thermocouple measurements for Series 2 flames are also shown in Fig 6.4. The effect of increasing flame coal tar distillate on the temperature profile is less distinct than the effect of pilot oxygen flow rate. The 75% distillates spray flame is approximately 100 K hotter than the flame of pure toluene and the temperature difference extends to approximately 200 K 12cm downstream of the burner. Overall, the trends in flame luminosity and size observed from the flame images carry over to the relative flame temperatures measured at the centerline.

Contour plots of the axisymmetric soot temperature field are extracted from images of the flame projection under 650 nm and 900 nm bandpass filters. Assuming a soot dispersion index of unity [76, 196], contour plots of the Series 1 flames are shown in Fig. 6.5. The pyrometry camera is calibrated to detect soot radiative emissions from 1400 K to 2500 K and this results in flame images with smaller dimensions than the full flame images shown in Figs. 6.2. The temperature contours are an average of 20 flame images taken under each filter. Asymmetry in the temperature contour is detected to some extent with flame temperatures exceeding 2000 K detected in local pockets of the turbulent spray flame. In principle, flame asymmetry could be minimized by more precise centering of the liquid feed nozzle. Overall, the flame temperatures determined by soot pyrometry at the spray flame centerline agree with the thermocouple measurements shown in Fig. 6.4. The constant dispersion index assumption taken in the pyrometry measurements and differences in turbulent flow field averaging may be the source of discrepancies between the temperature measurement methods.

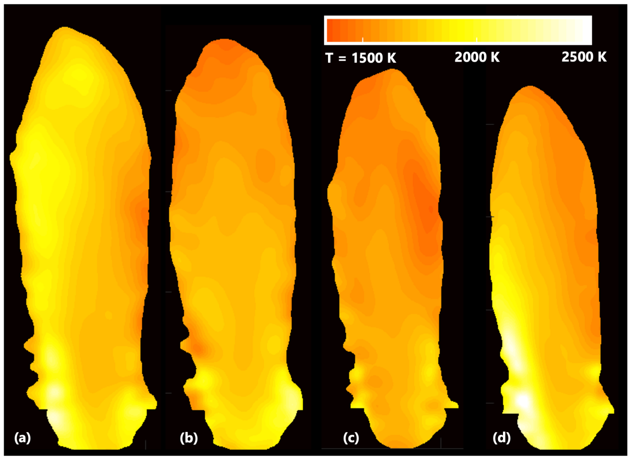

Figure 6.5: Soot pyrometry results for the Series 1 flames; t65d35 with p40 (a), p43 (b), p45 (c) and p50 (d).

With the flame structure established, properties of the flame-formed carbon could be examined more effectively. A summary of TEM images for carbon black formed in both flame series is shown in Fig. 6.6. The aggregate morphology is similar across all flame conditions but trends towards larger aggregates are noticeable for decreased equivalence ratio (Series 1) and increasing coal tar distillate spray feed (Series 2). Decreased oxygen levels in the flame are conducive to carbon particle formation but the impact of flame temperature on particle formation is not monotonic [6, 11]. The optimum flame temperature is typically understood to lie at approximately 1800 K for soot formation in flames [55, 183] and for yield in a carbon black pyrolysis furnace. Kinetics for growth of precursors is favored at higher temperatures but growth reactions eventually reverse at higher temperatures [4]. As such, the size of aggregates in Series 1 flames is a product of competing oxygen and temperature influences. For Series 2, increasing the fraction of coal tar distillates in the spray feed is expected to favor the formation and growth of carbon black due to the introduction of more aromatic particle precursors.

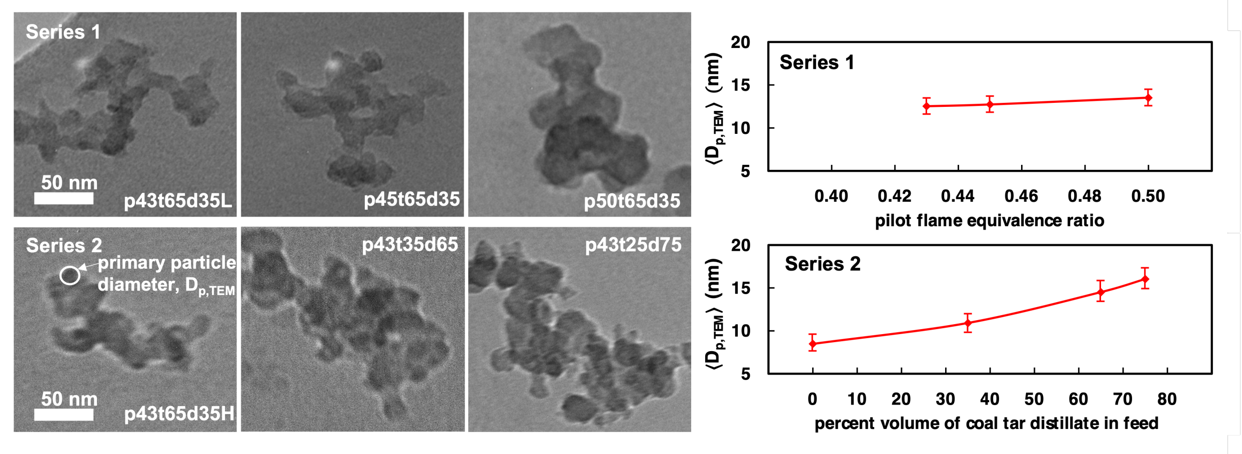

Figure 6.6: Right - Selected TEM images of aggregates formed in the flames currently studied. The top row contains an example aggregate particle from flame Series 1 and the bottom row contains an example aggregate from flame Series 2. Left - Median primary particle diameter based on analysis of TEM images of particles for flame Series 1 (top) and the flame Series 2 (bottom). Lines are drawn to guide the eye.

Primary particle diameters based on TEM particle projections are shown in Fig. 6.6 for both flame Series. The median diameter of the histogram obtained from counting over 200 primary particles for each condition is reported. The median primary particle for the Series 1 flames increases by approximately 1 nm as the pilot flame equivalence ratio increases from 0.43 to 0.50. At lower equivalence ratio, the hotter spray flame temperature may favor carbon black production but higher oxygen concentration in the spray increases particle oxidation thus hindering growth. Particle formation and growth kinetics are slower at lower flame temperature (p50) but lower oxygen concentrations may allow for larger primary particle diameter.

For flame Series 2, the trend with increasing coal tar distillates is more significant than the effect of oxygen concentration. The median primary particle diameter is 8.5 nm for particle flames from pure toluene spray flames and increases to 16.5 nm for spray containing

75% coal tar distillates by volume. Increasing atomizing nitrogen flow rate is expected to decrease the spray droplet size and increase entrainment of pilot flame gases into the spray. The p43t65d35 L and H conditions correspond to an increase in atomizing nitrogen flow rate by approximately 10%. The lower atomizing flow rate is more conducive to particle formation as the median primary particle diameter is over 1 nm larger. All flame synthesis conditions reported here approach ASTM N110 carbon black which is designated by primary particle sizes 15-19 nm [11]. The current flame conditions could readily be manipulated to increase the primary particle diameter to obtain larger grades.

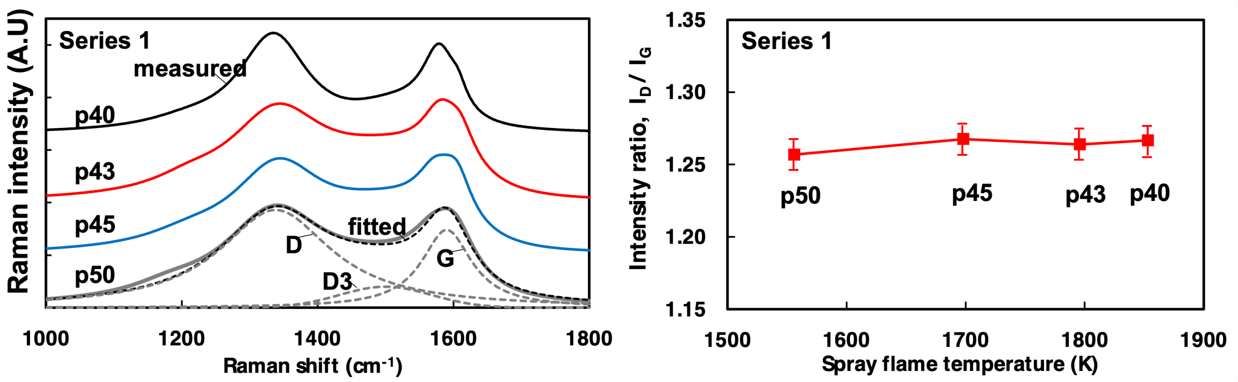

Figure 6.7: Raman spectra for carbon black formed in the Series 1 flames along with an example 3-peak curve fitting (left) and the ratio of the fitted D-band to G-band intensity extracted from the fitted spectra (right). Solid lines are measured, black dotted line is the fitted spectrum, and the 3 fitted peaks are shown in grey dotted lines.

The carbon structure is examined by Raman spectroscopy for further insights into the flame-formed carbon black properties. Raman spectra obtained directly from the particle laden collection filter are shown in Fig. 6.7 for Series 1 flames. Carbon materials are known be show prominent Raman scattering due to ordered graphitic sp^2 structural components (G peak) and disordered sp^2 components (D peak) [118, 121]. The spectra are fitted for the D and G peaks with Lorentzian functions and a third peak attributed to amorphous components is fitted with a Gaussian as defined previously for carbon black materials [29, 197, 198]. The widths and relative intensity of the G and D peaks resemble Raman spectra previously reported for various carbon black grades [16, 198]. The intensity ratio of the D and G peaks is not sensitive to the synthesis condition for the Series 1 flames even though the particles are formed under a range of oxygen and temperature conditions. Particle size and carbon structure analysis indicate that flame-formed carbon black resembles high-surface area carbon black grades. However, most furnace black production processes are designed to quench the pyrolysis reaction before excessive surface graphitization and other unwanted surface properties develop.

6.3 Summary

The carbon black synthesis method studied occurs under oxidizing conditions in contrast to the conventional pyrolysis process. Liquid coal tar distillate precursor is sprayed directly into the pilot flame to form a new turbulent spray flame from entrained oxygen. A significant portion of precursor and particles are lost to the gas-phase under high-temperature oxidizing conditions. Particles collected downstream are survivors of this hostile environment. Nonetheless, the compact configuration of the flame and control of synthesis parameters may justify the lower yield of carbon black particles. This is especially promising for high-surface area grades where the yield in pyrolysis processes is also known to decrease [6, 11, 179]. Carbon black produced has a high-surface area with primary particle diameters approaching ASTM N110. An optimal condition is found such that enough oxygen is supplied to the spray for full vaporization of the heavy precursor to form dry carbon particles which survive the oxidation zone.

The coal tar flame spray synthesis work presented in Chapter 6 has been submitted to Applied Sciences for publication (Rodriguez-Fernandez, H., Dasappa, S., Dones Sabado, K., Camacho, J., “Production of carbon black in turbulent spray flames of coal tar distillates”, Applied Sciences, 11(21), 10001 (2021))

Chapter 7

Optical Emission Spectroscopy Analysis of Manganese Oxide Nanoparticles in Spray Flames

Flame spray reactors are used in the industry to synthesize a variety of materials including carbon black, SiO_2, TiO_2, Al_2O_3 and other oxides [50]. Combustion of sprays is a favorable alternative to conventional vapor flame reactors due to the broad spectrum of liquid precursors that can be utilized [5]. FSP is capable of producing metal oxide powders in the range of 1-200 nm in size from low cost precursors with high production rates [1, 50]. While the final product and its material properties are key, understanding the evolution of the nanoparticles are important towards engineering and tailoring its morphology. Manganese oxide nano-materials have been incorporated into many promising technologies including energy storage materials [139, 140], MRI contrast agents [141, 142] and in catalysis [143, 144]. Flame formed manganese oxide nano-materials, mostly produced by flame spray pyrolysis [5, 34, 35, 145], have been reported for a variety of applications.

Multi-probe optical emission spectroscopy (OES) is adopted to study the formation of manganese oxide nanoparticles through flame spray pyrolysis. Multi-probe OES data presents measurement challenges like wavelength alignments and signal bleeding. An "OES

Spectral Analysis Tool" (OSAT) - is developed to address measurement challenges. OSAT is a data processing tool capable of multi-probe optical emission spectroscopy data analysis, systematic feature recognition and cataloging axial species evolution. The objective of the tool is to enable and enhance OES data analysis. Along with manganese oxide synthesis through FSP, details regarding new capabilities and implementation of the tool are provided in this chapter.

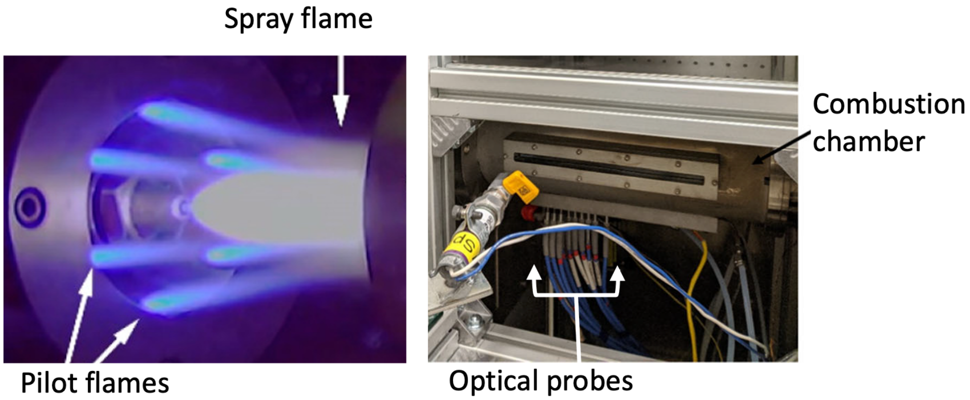

Figure 7.1: Optical microscope image of the flame spray pyrolysis burner (left). FSP pyrolysis chamber with 8 optical emission spectroscopy probes (right) [199]

7.1 Experimental Setup and Conditions

The experiments are performed using a flame spray pyrolysis setup at the Materials Engineering Research Facility at Argonne National Laboratory. The FSP setup is similar to that of Mädler et al [50, 51]. The optical microscope image of the FSP burner and the combustion chamber with 8 optical emission spectrometer probes is shown in Fig. 7.1. Precursor recipes are obtained by dissolving 0.1 mg/ml of manganese(II) acetylacetonate ($Mn(acac)_2$) in varying concentrations of acetonitrile (standard enthalpy of combustion $(\Delta H_C^o) = 1256.33\ kJ/mol$) and xylene ($\Delta H_C^o = 4552\ kJ/mol$). Varying concentrations of the solution are fed through an oxygen atomizing nozzle (Schlick Nozzle Model 970 S8, D4.1016/1 Version 1.0, Germany) as precursor solution. The details regarding the flame

Table 7.1: Summary of flame synthesis conditions

Flame	**Flow rate Acetonitrile** (*ml/min*)	**Flow rate Xylene** (*ml/min*)	**Driver O_2** (*L/min*)	**Sheath N_2** (*L/min*)
A 95 X 5	8.55	0.45	6	25
A 77 X 23	6.41	1.92	6	25
A 56 X 44	4.30	3.37	8	25
A 30 X 70	2.10	4.90	9	25

A - Acetonitrile, X - Xylene

conditions is provided in Table 7.1. Combustion of the spray is initiated and sustained by pilot flames. Six identical CH_4 and O_2 pilot flames with flow rates of 2 L/min and 4 L/min corresponding to an equivalence ratio of 1 are employed. Nitrogen gas is used as the sheath gas to prevent overheating during combustion. The products are transported through a tube furnace. The gas temperature of the tube furnace is measured to be approximately 973 K. After the combustion, additional N_2 gas (30 L/min) is added to the flow as the quench. Process analytic tools are installed in situ to track the intermediate products through optical emission spectrometers (OES). Details regarding the calibration of the spectrograph and OES data processing are provided in the next section along with the new capabilities of the tool.

7.1.1 Data Processing of OES Data

Optical emission spectroscopy is a non invasive method for determining the elemental composition. OES involves detection of chemically excited atoms and ions discharged in the flame to create a unique emission spectrum for each element. A single element generates numerous characteristic spectral lines. A typical OES spectra is shown in Fig. 7.2. Based on the flame conditions and the excited species, the spectral signatures can differ significantly. An ANDOR Kymera 328 spectrograph with 2400 l/mm grating and 1200 l/mm grating is employed to capture intermediate species at 8 different locations along axial length of the FSP

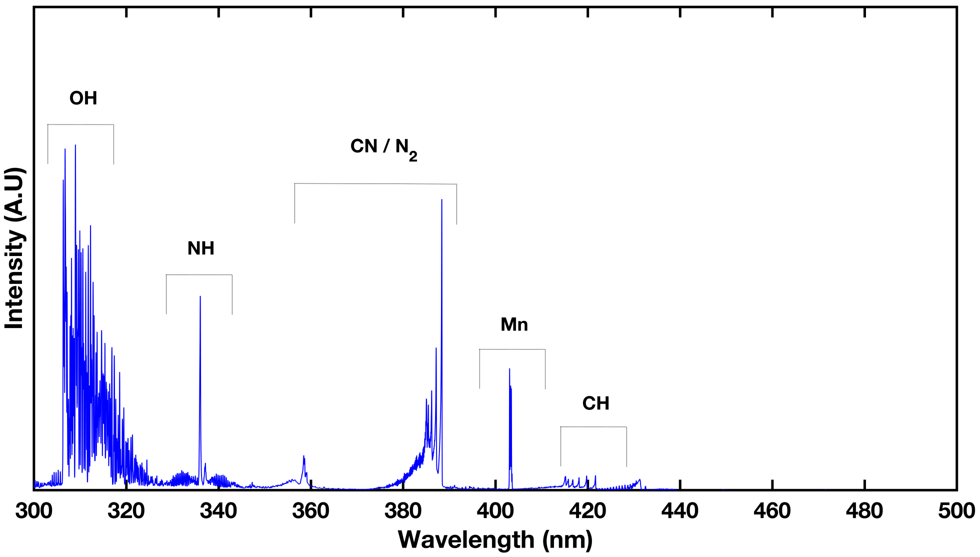

Figure 7.2: OES spectra for Flame A 77 X 23 for a single channel

burner. The OES Spectral Analysis Tool (OSAT) is an application developed in MATLAB framework to investigate multi-probe OES spectral features. OSAT is designed to have 3 tabs to post-process multi-probe OES data including signal calibration, peak identificartion and analyzing axial evolution. OSAT has been expanded in this work from the previous version by implementing multi-probe calibration capabilities, intensity gain correction and axial species profile evaluation. The main features of the new OSAT include:

1. **OES spectral calibration:**

   OES spectral calibration is performed to calibrate the wavelength and intensity axis of the multi-channel OES spectrograph. The peak position fidelity and repeatability is assured using a Hg calibration source. The OES spectra is calibrated using an Ocean Optics HG-2 spectrometer wavelength calibration source. The wavelength spans from 200nm to 700nm. Channel and grate specific calibration is performed across the captured sensor data. Peak fitting tools developed by O'Haver et al. [200] are employed to determine the x and y axis corrections and gain factors. Fig. 7.3 shows the calibration tab of the OSAT. This calibration exercise establishes alignment of spectral data from different channels hence facilitating comparison of spectra across the axial length of the reactor.

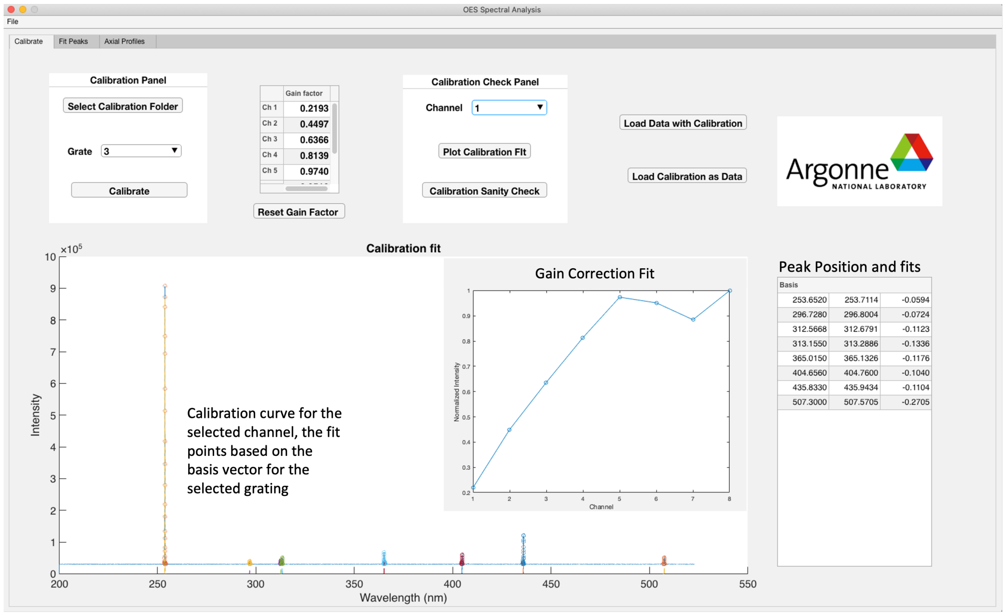

	Gain factor
Ch 1	0.2193
Ch 2	0.4497
Ch 3	0.6366
Ch 4	0.8139
Ch 5	0.9740

Calibration curve for the selected channel, the fit points based on the basis vector for the selected grating

Basis		
253.6520	253.7114	-0.0594
296.7280	296.8004	-0.0724
312.5668	312.6791	-0.1123
313.1550	313.2886	-0.1336
365.0150	365.1326	-0.1176
404.6560	404.7600	-0.1040
435.8330	435.9434	-0.1104
507.3000	507.5705	-0.2705

Figure 7.3: OES Spectral Analysis Tool - Calibration Tab

The measured wavelength in the optical emission spectra experiences a drift across channels. The measured wavelength needs to be calibrated to ensure accurate alignment. The optical emission spectral intensity as measured by the spectrometer shows differences across channels due to the “bleeding” or crossover of the signal across channels. These peak “drift” and signal “bleeding” issues are depicted in Fig. 7.4 (bottom left). Due to these discrepancies and concerns, a spectral data calibration is required to ensure fidelity of the measurement. The wavelength and intensity calibration is shown in Fig. 7.4 (top row). The wavelength calibration ensures alignment of the x-axis across channels. The difference in the peak positions as measured by the spectrometer capturing signatures Hg calibration source and the predetermined peak positions is used to establish the x-axis calibration. A linear correlation is calculated at intermediary wavelengths. This is corrected through a gain correction factor across channels. These wavelength and intensity calibrations ensure accurate engineering data acquisition.

2. **Spectral data analysis:**

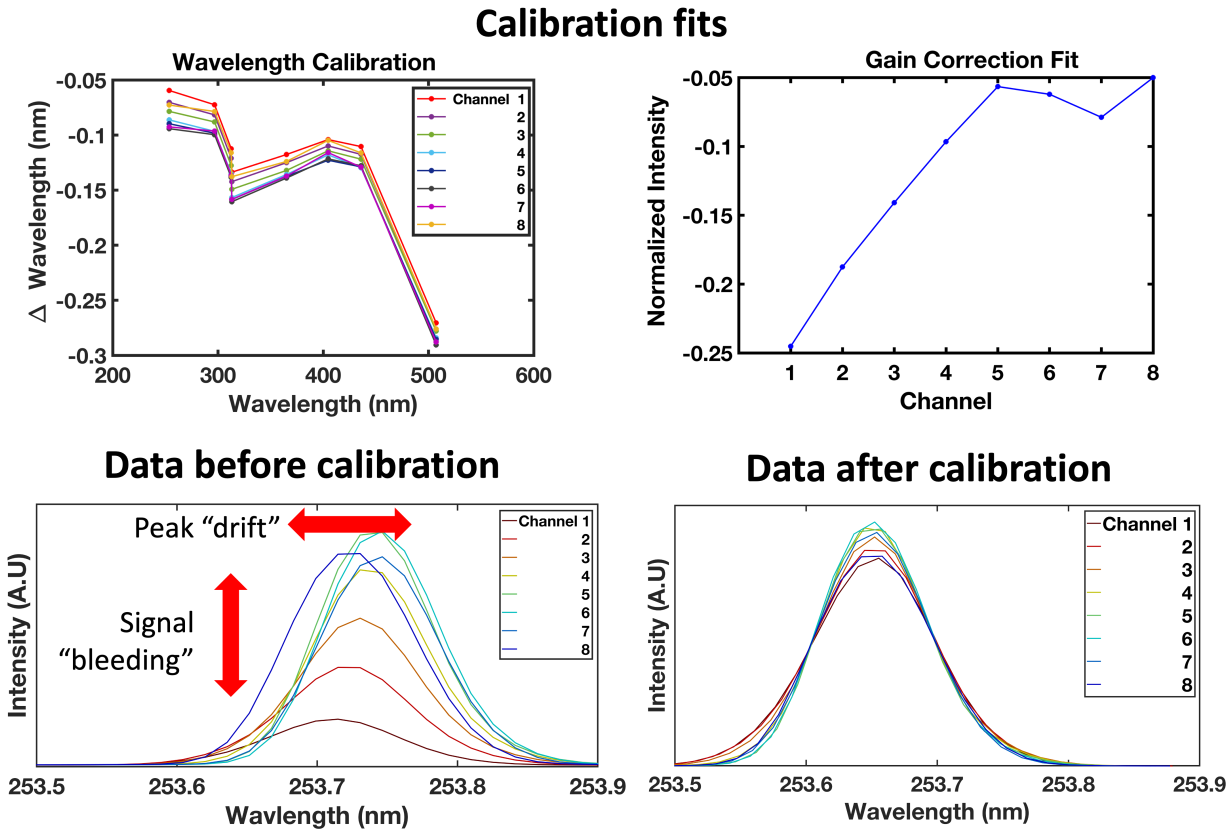

Figure 7.4: Optical emission spectral calibration - wavelength calibration (top left) and intensity gain correction (top right), spectra before calibration (bottom left) and spectra after calibration (bottom right)

The “Fit Peaks” tab focuses on identifying peaks representing specific species across channels, performing background correction and identifying trends through the reactor. OSAT is designed to identify spectral signatures of a few standard species like OH, NH, CH and C_2 with capability for expansion. Fig. 7.5 shows Peak fit tab from the OSAT tool. Peak fitting algorithms from [200] is adopted to identify and align peaks across channels and provide axial comparisons. The peak fitting algorithm accurately measures the peak parameters. The peak fitting function locates the positive peaks in a noisy data set, performs a least-squares curve-fit of a Gaussian function to the top part of the peak, and computes the position, height, and width (FWHM) of each peak from the least-squares fit.

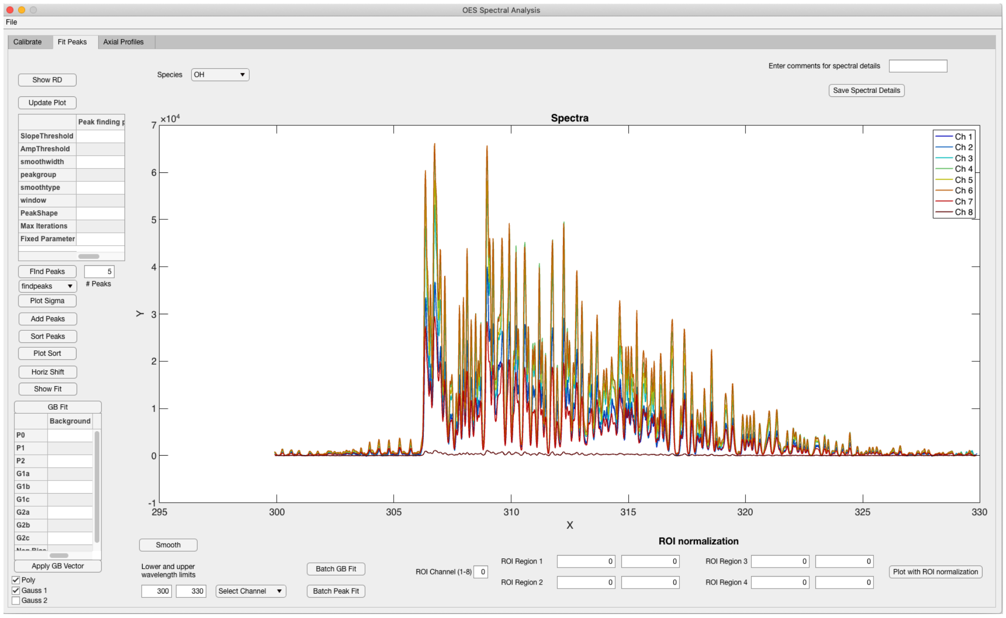

Species: OH

\# Peaks: 5

findpeaks

☑ Poly
☑ Gauss 1
☐ Gauss 2

Lower and upper wavelength limits: 300 330

ROI Channel (1-8): 0

ROI Region 1: 0 0

ROI Region 2: 0 0

ROI Region 3: 0 0

ROI Region 4: 0 0

Figure 7.5: OES Spectral Analysis Tool - Fit Peaks Tab

3. **Axial profile analysis:**

   The “Axial Profile” tab plots the axial profile of various species. Fig. shows 7.6 Peak fit tab from the OSAT tool.The axial profile of the average intensity, area under the peaks or the width of the peaks can be analyzed. Either predetermined species comparison or a custom region of intent areas can be chosen to analyze the axial profile. Multiple profiles can be examined simultaneously with parameter normalization capabilities.

7.2 Results and Discussion

In-situ optical emission spectroscopy (OES) is a powerful tool to estimate trace elements and excited reactive species in flames. The main objective of studying flame spectra is to identify intermediate chemical species and make quantitative measurements to determine the concentrations of various species and estimate species in different energy levels provides information about the formation processes. Multi-probe OES in flame spray pyrolysis facilitates evaluation of species evolution through the flame. This understanding helps to engineer nanoparticle by applying fundamental atomic and molecular species information. Evolution

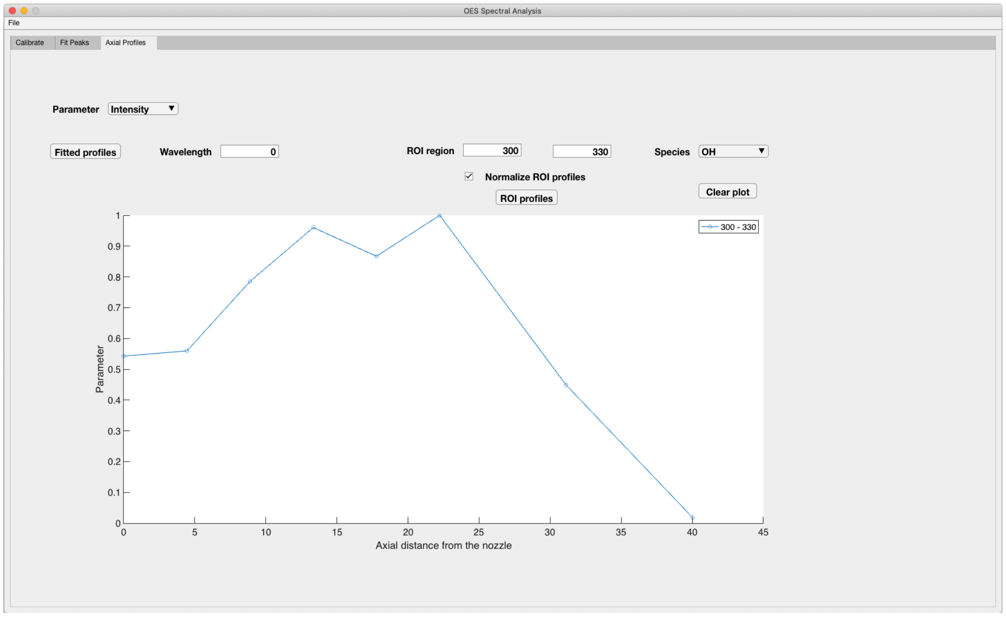

Parameter Intensity

Wavelength 0

ROI region 300 330

Species OH

☑ Normalize ROI profiles

Figure 7.6: OES Spectral Analysis Tool - Axial Profile Fit Tab

of manganese oxide in flames is studied through OES with specific focus on multi-probe sampling and its fidelity.

Optical emission spectra is captured for 4 different flame conditions as mentioned in Table 7.1. Both the solvent only and the solution spectra are analyzed for CH, OH and Mn species. Fig. 7.7 shows the emission spectra of OH, CH and Mn across different channels through the “A 95 X 5” flame. Different channels represent 8 axial points from 0 to 40 mm along the burner. One of the prominent features that appears between 305 and 325 nm corresponds to the transition of the OH radicals from the electronically excited to the ground state ($A^2\Sigma \rightarrow X^2\Pi$). An open but intense rotational structure is observed [201]. The OH band emissions may result form the dissociation of the burned gases.

CH bands are observed between 425 and 432 nm. The system shows an open rotational structure, a characteristic of a diatomic hydride with double branches, indicating a molecule with odd number of electrons. The strongest band is at 431.5 nm due to $A^2\Delta \rightarrow X^2\Pi$ transition. CH^+ transitions around 417.1 nm and 422.2 nm occur due to $A^1\Pi \rightarrow X^1\Sigma$ [176, 201]. Mn (I) bands are observed around 403.4 nm with the prominent transition being $4s\ 4p^6\ P^0_{3/2} \rightarrow 3d^5\ 4s^{26}\ S_{5/2}$ indicating the dissociation of the precursor from

$Mn(acac)_2$. N_2 peaks are observed around 390 nm [68, 202].

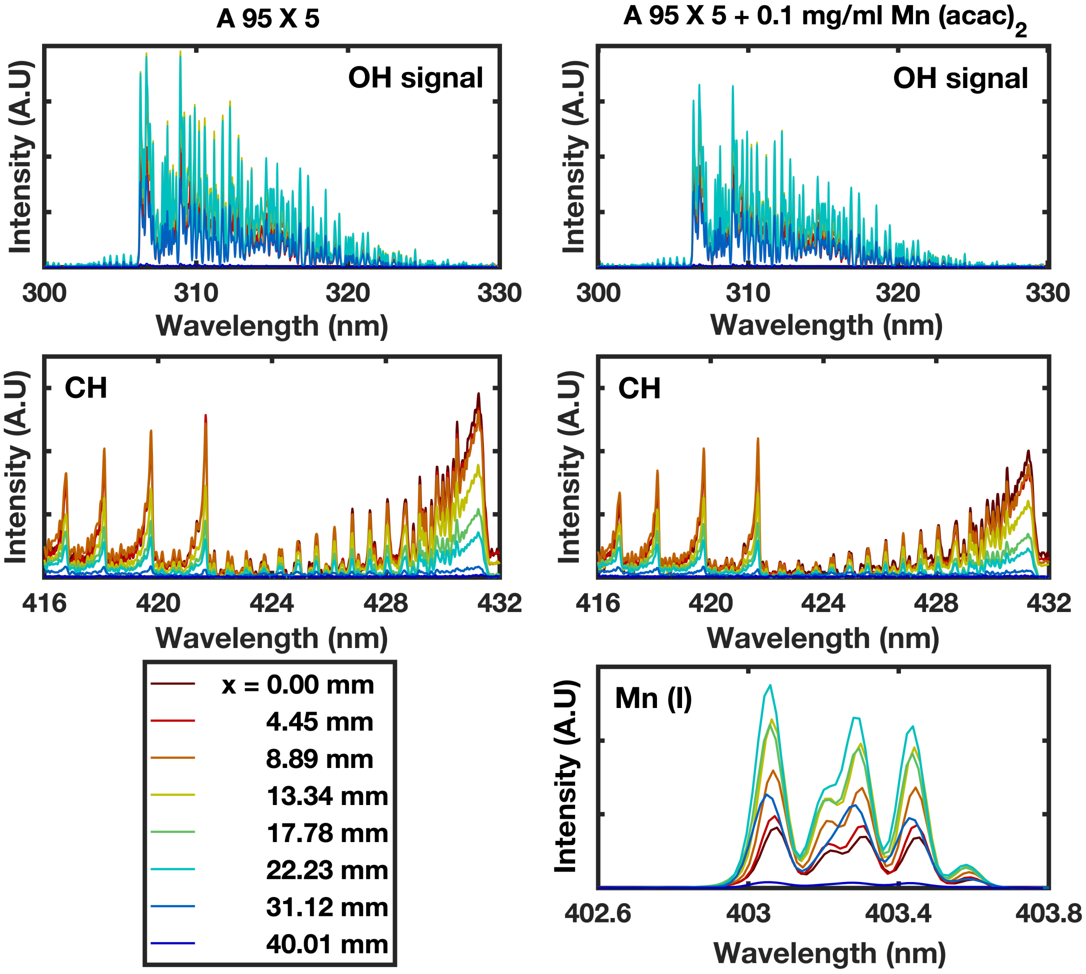

Figure 7.7: OH (top), CH (middle) and Mn (bottom) optical emission spectra for A95 X 5 solvent and solution ((left) - Solvent only, (right) - Solvent + $Mn(acac)_2$)

The axial evolution of OH, CH and Mn is presented in Fig. 7.8. The OH emission intensity reaches its peak at about 20 mm from the burner and linearly drops after that. Increasing xylene concentration in the solution increases OH concentration in the flame, probably from the increase of heat release due to the increase of fuel mass flow rate. CH concentration shows a similar increasing trend with increasing xylene concentration in the feedstock. CH emission intensity, however unlike OH, is the highest near the burner nozzle. A preliminary investigation of the rotational temperature of CH at the burner is estimated to be 5000 K at the burner nozzle for Flame A 56 X 44 based on [203, 204]. The OH and CH profile trends do not change with addition of Mn(acac)$_2$. Axial evolution of Mn (I) is indicative of

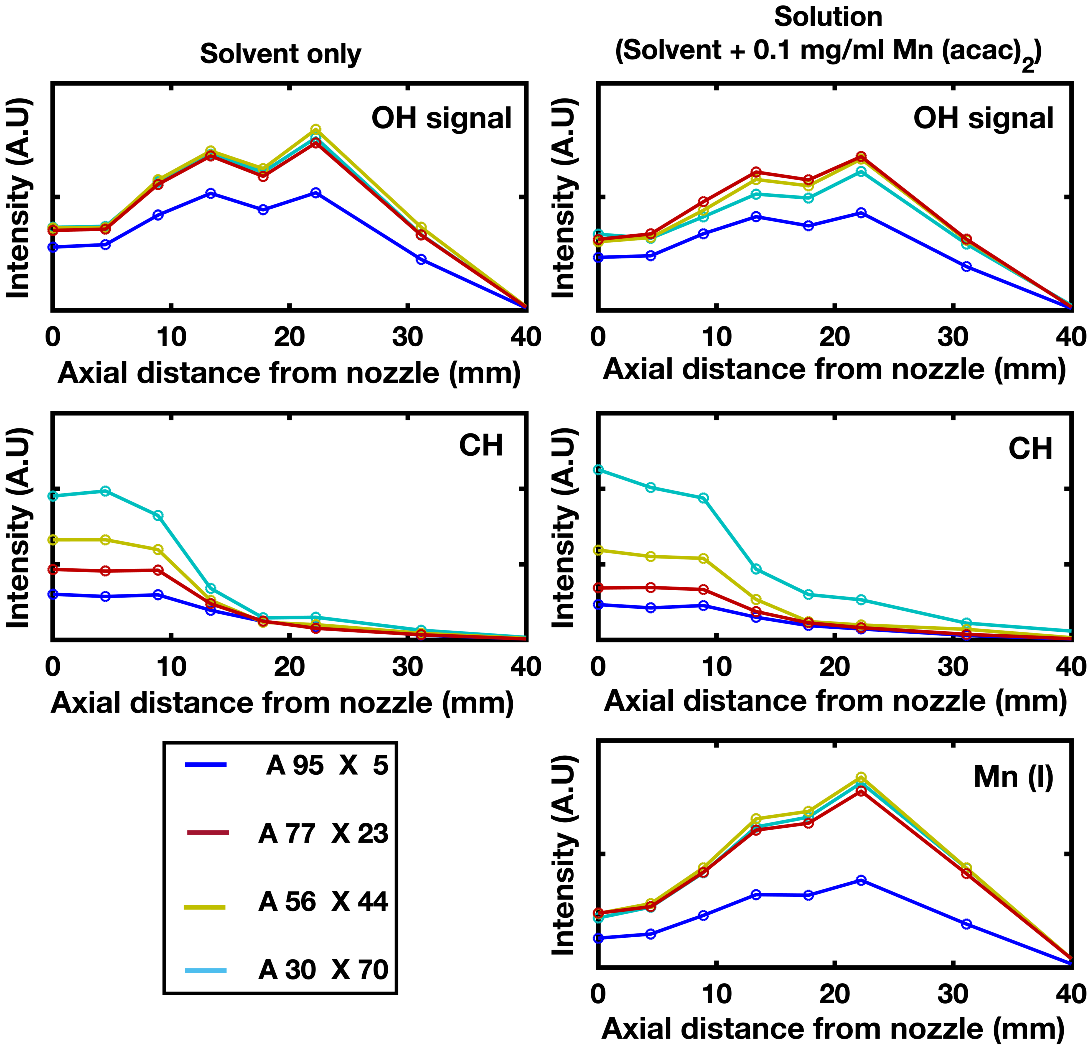

Figure 7.8: Axial profile of OH (top), CH (middle) and Mn (bottom) for varying concentrations ((left) - Solvent only, (right) - Solvent + Mn(acac)$_2$)

the flame location post which oxidation and particle formation of manganese oxide occurs. The peak concentration is at about 20 mm from the burner. The axial concentration profile is similar to that of OH. Addition of xylene, increases Mn (I) concentration and precursor conversion significantly. The higher enthalpy of combustion and adiabatic flame temperature of xylene in oxygen supports increased concentration on the Mn (I) and precursor conversion.

7.3 Summary

Optical emission spectra is an in-situ, non intrusive diagnostic technique used to identify intermediate species. The newly developed OSAT tool enables multi-probe spectral analysis of manganese oxide in flames. OSAT is designed to calibrate, correct the background, peak fit and analyze OES spectra. With new capabilities, analysis of up to 8 probes and axial evolution of intermediate species can be studied. The adequacy and efficiency of the tool is tested through the analysis of optical emissions spectra of manganese oxide formation through flame spray pyrolysis. The axial profiles of OH, CH and Mn (I) are examined with OSAT. The axial evolution of Mn (I) through the flame provides insight into the location of oxide formation. The tool is a powerful and reliable method for insight into the the axial spectra and insight into the fundamental processes.

The work presented in Chapter 7 was done at the Materials Engineering Research Facility at Argonne National Laboratory with Dr. Joseph Libera. The dissertation author is the primary contributor for this work.

Chapter 8

Concluding Remarks and Future Work

Fundamental processes involved in formation of nanoparticles by gas-to-particle conversion are investigated with a focus on production of carbon and manganese oxide. The dissertation examines pseudo one dimensional laminar flames and turbulent flame spray synthesis processes to enable systematic academic studies and processes with greater potential for industrial - scale production.

A unique and potentially new carbon material produced in sooting flames burning at a much higher temperature than conventional combustion applications is reported. Flame - formed carbon nanoparticles on the order of 10 nm with carbon structure resembling graphite and graphene materials are observed. Typical soot particles are larger and more amorphous than the carbon nanoparticles reported in the dissertation work. Synthesis conditions for this material is systematically characterized by non - intrusive pyrometry measurements and computation of the flame structure including temperature and PAH precursor profiles. Material properties are assessed by aerosol mobility particle sizing, TEM analysis and Raman spectroscopy. Experiments are designed to isolate flame temperature, growth time and fuel-to-air ratio such that evolution into the unique carbon structure could be examined.

Soot formed in flames hotter than conventional combustion applications is expected to undergo unique formation processes and develop a carbon structure distinct from typical soot. A complementary experimental and modeling approach using three separate combustion chemistry models show that predictions of PAH concentration are more sensitive to the choice in mechanism rather than specific flame conditions. The radiative emissions detected from the flame particles correspond to increasing C/H ratio with increasing flame temperature. Particle size distributions measured by mobility sizing show size and yield of soot decreases with increasing flame temperature and the bimodal distribution falls within the ultra - fine range for all flame conditions.

Several solid - state physics concepts are borrowed from the graphite and graphene research community to interpret the Raman spectra for the new carbon materials. The Raman signatures transition from a typical soot spectrum to features observed in disordered sp^2 carbon materials as the flame temperature increases. The defect distance extracted from the Raman bands nearly doubles from values typically reported for soot as the flame temperature exceeds 2200 K. Raman spectra at two different wavelengths highlight the expected shift in D - band position and G - band intensity. The evolution in Raman spectra from soot to a more ordered carbon structure could be explained by the "amorphization trajectory" reported by Ferrari and Robertson for evolution of graphite into nano - crystalline graphite. This is especially promising if the significant transformation in carbon structure inferred from the evolution in Raman spectra enables development of functional high-surface area sp^2 carbon materials. Namely, the current observations indicate that the flame-formed carbon structure evolves towards high - defect sp^2 carbon with size and carbon structure that can be tuned to some extent.

Carbon black nanoparticles were also synthesized in turbulent spray flames to extend the academic flame work to a configuration more suitable for industrial-scale production. Conventional carbon black production occurs by pyrolysis after heavy aromatic feedstock is injected into the post - combustor region of furnace black reactors. The current work examines the conversion of coal tar distillate in turbulent spray flames to demonstrate a more compact reactor configuration. Coal tar distillates diluted in toluene is atomized and burned in a standardized flame spray synthesis configuration known as SpraySyn. Flame conditions are characterized by thermocouple, soot pyrometry and image analysis and product particle properties are examined by TEM and Raman spectroscopy. The measured flame temperature corresponds to the range of temperatures used in the furnace black process, but the current synthesis includes oxidizing conditions and faster residence times. The resulting carbon black particles are aggregates having primary particle size on the small end of the carbon black size spectrum according to analysis of TEM images. Carbon black formed under a range of flame temperatures show Raman spectra with features resembling typical carbon black materials. Conversion of coal tar distillate to carbon black by direct flame synthesis may be a scalable method to produce high-surface area grades without a conventional pyrolysis reactor stage.

Particle nucleation and growth of crystalline manganese oxide nanoparticles was examined in a complementary experimental and modeling study. Gas-to-particle conversion occurred in a flame-assisted chemical vapor deposition process whereby a premixed stagnation flame drove the high - temperature synthesis. The structure of the stagnation flame was computed using pseudo one-dimensional and axisymmetric two - dimensional methods to assess the accuracy of using a faster similarity-based calculation for flame - deposition design. The pseudo one-dimensional computation performs reasonably well for the narrow aspect ratio stagnation flow currently studied as evidenced by reasonable agreement between the measured flame position and both computational methods. Manganese oxide nanoparticles having II, II-III, III or IV oxidation states were observed depending on the flame conditions. These observations may be explained by size-dependent equilibria between nano-scale manganese oxide and surrounding gas-phase oxygen. Local equilibrium was assessed during the particle temperature-oxygen-time history to gain insight into oxide formation in the flame. Analysis of the saturation ratio for formation of condensed MnO in the flame indicates that nucleation may be limited by a thermodynamic barrier. This nucleation mechanism is supported by measured particle sizes smaller than what would be expected from a coagulation limited growth process. Nanocrystalline MnO, reported here for the first time by flame synthesis, was obtained in oxygen lean flames. MnO_2 is the phase predicted to be thermally stable as the particles approach the deposition surface, yet other metastable oxide phases were produced in many of the flames examined. In fact, MnO_2 was only observed in the smallest particle size conditions which may indicate that high cooling rates limit phase equilibrium to less massive particles.

A complementary experimental and modeling study is investigated for nucleation of manganese oxide nanoparticles in premixed stagnation flames. The synthesis occurs at relatively high flame temperature and low precursor loading. Thermodynamic analysis based on the postulated nucleation process, $Mn(g) + O_2(g) \rightarrow MnO(s)$, is carried out to quantify precursor supersaturation and potential impacts of the Kelvin effect on particle formation. Nucleation and growth are analyzed based on the computed temperature-time-oxygen history in the post flame region. Agreement between measured and computed flame position for the base flame and precursor doped flames indicates that the manganese methylcyclopentadienyl tricarbonyl precursor does not inhibit flame chemistry for the conditions studied. Particle size distributions measured by mobility particle sizing and TEM images show reasonable agreement. Moreover, the measured particle size is predicted much more closely by a nucleation - limited mechanism rather than the size predicted by coagulation-limited growth.

Large - scale manganese oxide production in turbulent spray flames was also studied with collaboration from Argonne National Laboratory. New experimental capabilities were developed for this process as part of the current dissertation work. Optical emission spectral analysis of manganese oxide in flames is studied using the Optical Spectral Analysis Tool. The OSAT tool is designed to calibrate, correct the background, peak fit and analyze multi-probe OES spectra. The new tool enables fundamental chemical evolution in the flame to be determined. The adequacy and efficiency of the tool is tested through the analysis of optical emissions spectra of manganese oxide formation occurring during flame spray pyrolysis. The axial profiles of OH, CH and Mn (I) are examined with spatial resolution enabled by the new tool. The axial evolution of Mn (I) through the flame provides fundamental insight into the oxide formation and facilitates design of new manganese oxide synthesis processes.

The research has provided an understanding into the formation of manganese oxide and carbon nanoparticles using flame synthesis. This research can be further advanced. Below are a few possible routes to be explored:

1. **Mechanism and properties of carbon structure ordering in flames:**
   With an evaluation of carbon nanoparticle structure formed in high temperature premixed stagnation flames, new fundamental models of the gas-to-particle conversion of PAH precursors to graphitic particles could be developed.

2. **Flame spray pyrolysis for large scale production of carbon and manganese oxide nanomaterial:**
   Flame spray pyrolysis facilitates large scale production of nanomaterials. An understanding of the formation and structural features of manganese oxide and carbon nanoparticles in premixed stagnation flames and its dependance on temperature-time-oxygen has been established. A detailed analysis of the production of carbon and manganese oxide nanomaterials through flame spray pyrolysis will help evaluate the applicability of results obtained from premixed stagnation flames in flame spray pyrolysis.

3. **Electrochemical properties and energy storage device fabrication:**
   Establishing the electrochemical properties of flame formed carbon and manganese oxide will help integrating nanoparticles in electrodes and energy storage devices. Designing fabrication techniques like binary layered films of manganese oxide and carbon nanoparticles for energy storage electrodes is crucial for large scale production processes

Bibliography

[1] A. Mews. *Nanomaterials Handbook. Edited by Yury Gogotsi.* Vol. 46. 13. 2007, pp. 2143–2143.

[2] C. Koch. *Nanostructured Materials: Processing, Properties, and Applications: Second Edition.* 2006, pp. 1–760.

[3] J. Kemmler, S. O. Schopf, L. Mädler, N. Barsan, and U. Weimar. "New process technologies for the deposition of semiconducting metal oxide nanoparticles for sensing". *Procedia Engineering* 87 (2014), pp. 24–27.

[4] H. Wang. "Formation of nascent soot and other condensed-phase materials in flames". *Proceedings of the Combustion Institute* 33.1 (2011), pp. 41–67.

[5] S. Li, Y. Ren, P. Biswas, and S. D. Tse. "Flame aerosol synthesis of nanostructured materials and functional devices: Processing, modeling, and diagnostics". *Progress in Energy and Combustion Science* 55 (2016), pp. 1–59.

[6] E Pratsinis. "Flame aerosol synthesis of ceramic powders". *Fuel and Energy Abstracts* 39.5 (1998), p. 384.

[7] J. Camacho, A. V. Singh, W. Wang, R. Shan, E. K. Yapp, D. Chen, M. Kraft, and H. Wang. "Soot particle size distributions in premixed stretch-stabilized flat ethylene-oxygen-argon flames". *Proceedings of the Combustion Institute* 36.1 (2017), pp. 1001–1009.

[8] C. K. Law. *Combustion physics.* Vol. 9780521870. 2006, pp. 1–722.

[9] U. Lohmann, F. Friebel, Z. A. Kanji, F. Mahrt, A. A. Mensah, and D. Neubauer. "Future warming exacerbated by aged-soot effect on cloud formation". *Nature Geoscience* 13.10 (2020), pp. 674–680.

[10] National Toxicology Program. "Report on Carcinogens, Fourteenth Edition". *Report on Carcinogens* 1948.Ntp 2000 (2016), p. 5.

[11] J. Donnet and R. Bansal. *Carbon Black: Science and Technology, Second Edition.* 1993, p. 461.

[12] G. D. Ulrich, B. A. Milnes, and N. S. Subramanian. “Particle Growth in Flames. II: Experimental Results for Silica Particles”. *Combustion Science and Technology* 14.4-6 (1976), pp. 243–249.

[13] M. S. Dresselhaus and G Dresselhaus. “Nanotechnology in Carbon Materials Introduction to Carbon Materials Fullerenes as Nanostructures”. 9.97 (1997), pp. 33–42.

[14] H. A. Michelsen. “Probing soot formation, chemical and physical evolution, and oxidation: A review of in situ diagnostic techniques and needs”. *Proceedings of the Combustion Institute* 36.1 (2017), pp. 717–735.

[15] G. Blanquart, P. Pepiot-Desjardins, and H. Pitsch. “Chemical mechanism for high temperature combustion of engine relevant fuels with emphasis on soot precursors”. *Combustion and Flame* 156.3 (2009), pp. 588–607.

[16] A. Sadezky, H. Muckenhuber, H. Grothe, R. Niessner, and U. Pöschl. “Raman microspectroscopy of soot and related carbonaceous materials: Spectral analysis and structural information”. *Carbon* 43.8 (2005), pp. 1731–1742.

[17] R. L. Vander Wal and A. J. Tomasek. “Soot oxidation: Dependence upon initial nanostructure”. *Combustion and Flame* 134.1-2 (2003), pp. 1–9.

[18] R. L. Vander Wal and A. J. Tomasek. “Soot nanostructure: Dependence upon synthesis conditions”. *Combustion and Flame* 136.1-2 (2004), pp. 129–140.

[19] M. L. Botero, E. M. Adkins, S. González-Calera, H. Miller, and M. Kraft. “PAH structure analysis of soot in a non-premixed flame using high-resolution transmission electron microscopy and optical band gap analysis”. *Combustion and Flame* 164 (2016), pp. 250–258.

[20] M. Alfè, B. Apicella, R. Barbella, J. N. Rouzaud, A. Tregrossi, and A. Ciajolo. “Structure-property relationship in nanostructures of young and mature soot in premixed flames”. *Proceedings of the Combustion Institute* 32 I.1 (2009), pp. 697–704.

[21] A. C. Ferrari and J Robertson. “Interpretation of Raman spectra of disordered and amorphous carbon”. 61.20 (2000), pp. 95–107.

[22] A. C. Ferrari. “Raman spectroscopy of graphene and graphite: Disorder, electron-phonon coupling, doping and nonadiabatic effects”. *Solid State Communications* 143.1-2 (2007), pp. 47–57.

[23] C. Liu, A. V. Singh, C. Saggese, Q. Tang, D. Chen, and K. Wan. “Flame-formed carbon nanoparticles exhibit quantum dot behaviors” (2019), pp. 1–6.

[24] A. C. Ferrari and D. M. Basko. “Raman spectroscopy as a versatile tool for studying the properties of graphene”. *Nature Nanotechnology* 8.4 (2013), pp. 235–246.

[25] P. Minutolo, M. Commodo, A. Santamaria, G. De Falco, and A. D'Anna. "Characterization of flame-generated 2-D carbon nano-disks". *Carbon* 68 (2014), pp. 138–148.

[26] A. C. Ferrari and J Robertson. "Resonant Raman spectroscopy of disordered , amorphous , and diamondlike carbon". 64.October 2000 (2001), pp. 1–13.

[27] G. Gouadec and P. Colomban. "Raman Spectroscopy of nanomaterials: How spectra relate to disorder, particle size and mechanical properties". *Progress in Crystal Growth and Characterization of Materials* 53.1 (2007), pp. 1–56.

[28] M. Commodo, G. Tessitore, G. De Falco, A. Bruno, P. Minutolo, and A. D'Anna. "Further details on particle inception and growth in premixed flames". *Proceedings of the Combustion Institute* 35.2 (2015), pp. 1795–1802.

[29] J. D. Herdman, B. C. Connelly, M. D. Smooke, M. B. Long, and J. H. Miller. "A comparison of Raman signatures and laser-induced incandescence with direct numerical simulation of soot growth in non-premixed ethylene/air flames". *Carbon* 49.15 (2011), pp. 5298–5311.

[30] Y Kobayashi, S Tanaka, and M Arai. "PAHs Behavior and Graphitization Degree of Soot in a Hexane Diffusion Flame". 2.1 (2018), pp. 1–12.

[31] M. Salamanca, M. L. Botero, J. W. Martin, J. A. Dreyer, J. Akroyd, and M. Kraft. "The impact of cyclic fuels on the formation and structure of soot". *Combustion and Flame* 219 (2020), pp. 1–12.

[32] W. Li and S. T. Oyama. *Mechanism of Ozone Decomposition on a Manganese Oxide Catalyst. 2. Steady-State and Transient Kinetic Studies.* Tech. rep. 1998.

[33] A. Ramírez, P. Hillebrand, D. Stellmach, M. M. May, P. Bogdanoff, and S. Fiechter. "Evaluation of MnOx, Mn2O3, and Mn 3O4 electrodeposited films for the oxygen evolution reaction of water". *Journal of Physical Chemistry C* 118.26 (2014), pp. 14073–14081.

[34] F. O. Ernst, H. K. Kammler, A. Roessler, S. E. Pratsinis, W. J. Stark, J. Ufheil, and P. Novák. "Electrochemically active flame-made nanosized spinels: LiMn2O4, Li4Ti5O12 and LiFe5O8". *Materials Chemistry and Physics* 101.2-3 (2007), pp. 372–378.

[35] T. J. Patey, R. Büchel, S. H. Ng, F. Krumeich, S. E. Pratsinis, and P. Novák. "Flame co-synthesis of LiMn2O4 and carbon nanocomposites for high power batteries". *Journal of Power Sources* 189.1 (2009), pp. 149–154.

[36] J. Camacho, C. Liu, N. Montes, and H. Wang. "Ultrafine Manganese Oxide Nanoparticles Synthesized by Flame Stabilized on a Rotating Surface". *9th U. S. National Combustion Meeting* December 2017 (2015), 2B09.

[37] C. Liu, J. Camacho, and H. Wang. “Phase Equilibrium of TiO2 Nanocrystals in Flame-Assisted Chemical Vapor Deposition”. *ChemPhysChem* 19.2 (2018), pp. 180–186.

[38] B. Zhao, K. Uchikawa, J. R. McCormick, C. Y. Ni, J. G. Chen, and H. Wang. “Ultrafine anatase TiO2 nanoparticles produced in premixed ethylene stagnation flame at 1 atm”. *Proceedings of the Combustion Institute* 30 II (2005), pp. 2569–2576.

[39] H. Zhao, X. Liu, and S. D. Tse. “Effects of pressure and precursor loading in the flame synthesis of titania nanoparticles”. *Journal of Aerosol Science* 40.11 (2009), pp. 919–937.

[40] M. Y. Manuputty, J. A. Dreyer, Y. Sheng, E. J. Bringley, M. L. Botero, J. Akroyd, and M. Kraft. “Polymorphism of nanocrystalline TiO2 prepared in a stagnation flame: Formation of the TiO2-II phase”. *Chemical Science* 10.5 (2019), pp. 1342–1350.

[41] R. J.Kee, J. A.Miller, G. H.Evans, and G. Dixon-Lewis. “A computational model of the structure and extinction of strained, opposed flow, premixed methane-air flames”. *Symposium (International) on Combustion* 22.1 (1989), pp. 1479–1494.

[42] A. D. Abid, J. Camacho, D. A. Sheen, and H. Wang. “Quantitative measurement of soot particle size distribution in premixed flames - The burner-stabilized stagnation flame approach”. *Combustion and Flame* 156.10 (2009), pp. 1862–1870.

[43] H. Lin, C. Gu, J. Camacho, B. Lin, C. Shao, R. Li, H. Gu, B. Guan, H. Wang, and Z. Huang. “Mobility size distributions of soot in premixed propene flames”. *Combustion and Flame* 172 (2016), pp. 365–373.

[44] A. Lutz, R. Kee, J. Grcar, and F. Rupley. “3ss OPPDIF: A Fortran program for computing opposed-flow diffusion flames”. *Sandia National Laboratories …* May (1997), pp. 3–33.

[45] G.-p. Chemical. “Chemkin”. September (2000), pp. 1–181.

[46] F. E. &. C. K. L. Hai Wang, Xiaoqing You, Ameya V. Joshi, Scott G. Davis, Alexander Laskin. “USC Mech Version II. High-Temperature Combustion Reaction Model of H2/CO/C1-C4 Compounds” ().

[47] A. Raj, I. D. C. Prada, A. A. Amer, and S. H. Chung. “A reaction mechanism for gasoline surrogate fuels for large polycyclic aromatic hydrocarbons”. *Combustion and Flame* 159.2 (2012), pp. 500–515.

[48] J. Appel, H. Bockhorn, and M. Frenklach. “Kinetic modeling of soot formation with detailed chemistry and physics: Laminar premixed flames of C2 hydrocarbons”. *Combustion and Flame* 121.1-2 (2000), pp. 122–136.

[49] Z. Li and H. Wang. “Drag force, diffusion coefficient, and electric mobility of small particles. II. Application”. *Physical Review E - Statistical Physics, Plasmas, Fluids, and Related Interdisciplinary Topics* 68.6 (2003).

[50] F. Meierhofer, L. Mädler, and U. Fritsching. “Nanoparticle evolution in flame spray pyrolysis—Process design via experimental and computational analysis”. *AIChE Journal* 66.2 (2020), pp. 1–14.

[51] M. Levental, R. Chard, J. A. Libera, K. Chard, A. Koripelly, J. R. Elias, M. Schwarting, B. Blaiszik, M. Stan, S. Chaudhuri, and I. Foster. “Towards Online Steering of Flame Spray Pyrolysis Nanoparticle Synthesis”. *Proceedings of XLOOP 2020: 2nd Annual Workshop on Extreme-Scale Experiment-in-the-Loop Computing, Held in conjunction with SC 2020: The International Conference for High Performance Computing, Networking, Storage and Analysis* (2020), pp. 35–40.

[52] J. Camacho, C. Liu, C. Gu, H. Lin, Z. Huang, Q. Tang, X. You, C. Saggese, Y. Li, H. Jung, L. Deng, I. Wlokas, H. Wang, M. O. E. Engineering, and S. Jiao. “Mobility size and mass of nascent soot particles in a benchmark premixed ethylene flame”. *Combustion and Flame* 162.10 (2015), pp. 3810–3822.

[53] A. D. Abid, N. Heinz, E. D. Tolmachoff, D. J. Phares, C. S. Campbell, and H. Wang. “On evolution of particle size distribution functions of incipient soot in premixed ethylene-oxygen-argon flames”. *Combustion and Flame* 154.4 (2008), pp. 775–788.

[54] M. Sirignano and A. D’Anna. “Coagulation of combustion generated nanoparticles in low and intermediate temperature regimes: An experimental study”. *Proceedings of the Combustion Institute* 34.1 (2013), pp. 1877–1884.

[55] C. Gu, H. Lin, J. Camacho, B. Lin, C. Shao, R. Li, H. Gu, B. Guan, Z. Huang, and H. Wang. “Particle size distribution of nascent soot in lightly and heavily sooting premixed ethylene flames”. *Combustion and Flame* 165 (2016), pp. 177–187.

[56] M. M. Maricq. “A comparison of soot size and charge distributions from ethane, ethylene, acetylene, and benzene/ethylene premixed flames”. *Combustion and Flame* 144.4 (2006), pp. 730–743.

[57] C. A. Echavarria, A. F. Sarofim, J. A. S. Lighty, and A. D’Anna. “Evolution of soot size distribution in premixed ethylene/air and ethylene/benzene/air flames: Experimental and modeling study”. *Combustion and Flame* 158.1 (2011), pp. 98–104.

[58] J. Camacho, S. Lieb, and H. Wang. “Evolution of size distribution of nascent soot in n- and i-butanol flames”. *Proceedings of the Combustion Institute* 34.1 (2013), pp. 1853–1860.

[59] K. V. Puduppakkam, A. U. Modak, and E. Meeks. “A soot chemistry model that captures fuel effects” (2014), pp. 1–11.

[60] Q. Tang, B. Ge, Q. Ni, B. Nie, and X. You. "Soot formation characteristics of n-heptane/toluene mixtures in laminar premixed burner-stabilized stagnation flames". *Combustion and Flame* 187 (2018), pp. 239–246.

[61] L. A. Sgro, A. De Filippo, G. Lanzuolo, and A. D'Alessio. "Characterization of nanoparticles of organic carbon (NOC) produced in rich premixed flames by differential mobility analysis". *Proceedings of the Combustion Institute* 31 I.1 (2007), pp. 631–638.

[62] F. Carbone, M. Attoui, and A. Gomez. "Challenges of measuring nascent soot in flames as evidenced by high-resolution differential mobility analysis". *Aerosol Science and Technology* 50.7 (2016), pp. 740–757.

[63] F. Carbone, K. Gleason, and A. Gomez. "Probing gas-to-particle transition in a moderately sooting atmospheric pressure ethylene/air laminar premixed flame. Part I: gas phase and soot ensemble characterization". *Combustion and Flame* 181 (2017), pp. 315–328.

[64] M. Katzer, A. P. Weber, and G. Kasper. "The effects of electrical fields on growth of titania particles formed in a CH4-O2 diffusion flame". *Journal of Aerosol Science* 32.9 (2001), pp. 1045–1067.

[65] P. S. Fennell, J. S. Dennis, and A. N. Hayhurst. "The size distributions of nanoparticles of the oxides of Mg, Ba and Al in flames: Their measurement and dependence on the concentrations of free radicals in the flame". *Proceedings of the Combustion Institute* 31 II.2 (2007), pp. 1939–1945.

[66] P. S. Fennell, J. S. Dennis, and A. N. Hayhurst. "The sampling of nanoparticles of MgO formed when doping an oxygen-rich flame with magnesium: The measurement of the concentrations and size-distributions of these nanoparticles". *Combustion and Flame* 151.4 (2007), pp. 560–572.

[67] K. H. Ahn, C. H. Jung, M. Choi, and J. S. Lee. "Particle sampling and real time size distribution measurement in H2/O2/TEOS diffusion flame". *Journal of Nanoparticle Research* 3.2-3 (2001), pp. 161–170.

[68] N. Reed, J. Fang, S. Chavalmane, and P. Biswas. "Real-time measurement of size-resolved elemental composition ratio for flame synthesized composite nanoparticle aggregates using a tandem SMPS-ICP-OES". *Aerosol Science and Technology* 51.3 (2017), pp. 311–316.

[69] M. Saffaripour, L. L. Tay, K. A. Thomson, G. J. Smallwood, B. T. Brem, L. Durdina, and M. Johnson. "Raman spectroscopy and TEM characterization of solid particulate matter emitted from soot generators and aircraft turbine engines". *Aerosol Science and Technology* 51.4 (2017), pp. 518–531.

[70] *CasaXPS v 2.3.24*.

[71] K. Axis. “Peak Fitting in XPS”. *Casa XPS* (2006), pp. 1–29.

[72] J. Walton, P. Wincott, N. Fairley, and A. Carrick. “Peak Fitting with CasaXPS”. *Casa XPS* (2010), pp. 1–140.

[73] J. Filik, P. W. May, S. R. Pearce, R. K. Wild, and K. R. Hallam. “XPS and laser Raman analysis of hydrogenated amorphous carbon films”. *Diamond and Related Materials* 12.3-7 (2003), pp. 974–978.

[74] F. Xu, P. B. Sunderland, and G. M. Faeth. “Soot formation in laminar premixed ethylene/air flames at atmospheric pressure”. *Combustion and Flame* 108.4 (1997), pp. 471–493.

[75] K. Gleason, F. Carbone, and A. Gomez. “Effect of temperature on soot inception in highly controlled counterflow ethylene diffusion flames”. *Combustion and Flame* 192 (2018), pp. 283–294.

[76] H. Guo, J. A. Castillo, and P. B. Sunderland. “Digital camera measurements of soot temperature and soot volume fraction in axisymmetric flames”. *Applied Optics* 52.33 (2013), pp. 8040–8047.

[77] C. R. Millikan. “Optical Properties of Soot”. 51.6 (1961), pp. 698–699.

[78] John B. Heywood. *Internal Combustion Engine Fundamentals*. New York: McGraw-Hill, 2018.

[79] I. M. Kennedy. “The health effects of combustion-generated aerosols”. *Proceedings of the Combustion Institute* 31 II (2007), pp. 2757–2770.

[80] M. C. Jacobson and H Hansson. “ORGAN IC ATMOSPHERIC AEROSOLS’ REVIEW AN D STATE OF THE SCIENCE”. *Reviews of Geophysics* 1998 (2000), pp. 267–294.

[81] Ten-See Wang. “Thermophysics Characterization of Kerosene Combustion”. *Journal of Thermophysics Heat Transfer* 15.2 (2001), pp. 140–7.

[82] T. Ochs, D. Oryshchyn, R. Woodside, C. Summers, B. Patrick, D. Gross, M. Schoenfield, T. Weber, and D. O’Brien. “Results of initial operation of the Jupiter Oxygen Corporation oxy- fuel 15 MWth burner test facility”. *Energy Procedia* 1.1 (2009), pp. 511–518.

[83] C. R. Shaddix and T. C. Williams. “The effect of oxygen enrichment on soot formation and thermal radiation in turbulent, non-premixed methane flames”. *Proceedings of the Combustion Institute* 36.3 (2017), pp. 4051–4059.

[84] M. Frenklach, S. Taki, M. B. Durgaprasad, and R. A. Matula. “Soot formation in shock-tube pyrolysis of acetylene, allene, and 1,3-butadiene”. *Combustion and Flame* 54.1-3 (1983), pp. 81–101.

[85] M. H.Böhm, D.Hesse, H.Jander, B.Lüers, J.Pietscher, H.G.G.Wagner. “The influence of pressure and temperature on soot formation in premixed flames”. *Symposium (International) on Combustion* 22.1 (1989), pp. 403–411.

[86] J. Bonpua, Y. Yagües, A. Aleshin, S. Dasappa, and J. Camacho. “Flame temperature effect on sp2 bonds on nascent carbon nanoparticles formed in premixed flames (Tf,max > 2100 K): A Raman spectroscopy and particle mobility sizing study”. *Proceedings of the Combustion Institute* 37.1 (2019), pp. 943–951.

[87] E. Meeks, R. J. Kee, and D. S. Dandyt. “Computational Simulation of Diamond Chemical Vapor Deposition in Premixed C2H 2 / 0 2 / H 2 and CH 4 / O2-Strained Flames”. 160 (1993), pp. 144–160.

[88] A. D’Alessio, A. C. Barone, R. Cau, A. D’Anna, and P. Minutolo. “Surface deposition and coagulation efficiency of combustion generated nanoparticles in the size range from 1 to 10 nm”. *Proceedings of the Combustion Institute* 30.2 (2005), pp. 2595–2603.

[89] W. Pejpichestakul, A. Frassoldati, A. Parente, and T. Faravelli. “Kinetic modeling of soot formation in premixed burner-stabilized stagnation ethylene fl ames at heavily sooting condition”. *Fuel* 234.July (2018), pp. 199–206.

[90] M. R. Kholghy, A. Veshkini, and M. J. Thomson. “The core-shell internal nanostructure of soot - A criterion to model soot maturity”. *Carbon* 100 (2016), pp. 508–536.

[91] K. O. Johansson, F. El Gabaly, P. E. Schrader, M. F. Campbell, and H. A. Michelsen. “Evolution of maturity levels of the particle surface and bulk during soot growth and oxidation in a flame”. *Aerosol Science and Technology* 51.12 (2017), pp. 1333–1344.

[92] R. A. Dobbins. “Soot inception temperature and the carbonization rate of precursor particles”. *Combustion and Flame* 130.3 (2002), pp. 204–214.

[93] R. Dastanpour, A. Momenimovahed, K. Thomson, J. Olfert, and S. Rogak. “Variation of the optical properties of soot as a function of particle mass”. *Carbon* 124 (2017), pp. 201–211.

[94] C. Russo, B. Apicella, J. S. Lighty, A. Ciajolo, and A. Tregrossi. “Optical properties of organic carbon and soot produced in an inverse diffusion flame”. *Carbon* 124 (2017), pp. 372–379.

[95] M. Commodo, G. De Falco, A. Bruno, C. Borriello, P. Minutolo, and A. D’Anna. “Physicochemical evolution of nascent soot particles in a laminar premixed flame:

From nucleation to early growth". *Combustion and Flame* 162.10 (2015), pp. 3854–3863.

[96] M. Sirignano, A. Ciajolo, A. D'Anna, and C. Russo. "Chemical Features of Particles Generated in an Ethylene/Ethanol Premixed Flame". *Energy and Fuels* 31.3 (2017), pp. 2370–2377.

[97] C. Russo, A. D'Anna, A. Ciajolo, and M. Sirignano. "Analysis of the chemical features of particles generated from ethylene and ethylene/2,5 dimethyl furan flames". *Combustion and Flame* 167 (2016), pp. 268–273.

[98] M. Sirignano, D. Bartos, M. Conturso, M. Dunn, A. D'Anna, and A. R. Masri. "Detection of nanostructures and soot in laminar premixed flames". *Combustion and Flame* 176 (2017), pp. 299–308.

[99] F. Picca, G. De Falco, M. Commodo, G. Vitiello, G. D'Errico, P. Minutolo, and A. D'Anna. "Characteristics of flame-nucleated carbonaceous nanoparticles". *Chemical Engineering Transactions* 73.July 2018 (2019), pp. 61–66.

[100] M. Commodo, G. De Falco, P. Minutolo, and A. D'Anna. "Structure and size of soot nanoparticles in laminar premixed flames at different equivalence ratios". *Fuel* 216.November 2017 (2018), pp. 456–462.

[101] M. Commodo, P. H. Joo, G. De Falco, P. Minutolo, A. D'Anna, and Ö. L. Gülder. "Raman Spectroscopy of Soot Sampled in High-Pressure Diffusion Flames". *Energy and Fuels* 31.9 (2017), pp. 10158–10164.

[102] K. Hayashida, S. Nagaoka, and H. Ishitani. "Growth and oxidation of graphitic crystallites in soot particles within a laminar diffusion flame". *Fuel* 128 (2014), pp. 148–154.

[103] M. Commodo, A. E. Karataş, G. De Falco, P. Minutolo, A. D'Anna, and Ö. L. Gülder. "On the effect of pressure on soot nanostructure: A Raman spectroscopy investigation". *Combustion and Flame* 219 (2020), pp. 13–19.

[104] V. K. T. "On laminar and turbulent friction". *NATIONAL ADVISORY COMMITTEE FOR AERONAUTICS TECHNICAL MEMORANDUM* 1092 (1921).

[105] K.Seshadri and F.A.Williams. "Laminar flow between parallel plates with injection of a reactant at high Reynolds number". *International Journal of Heat and Mass Transfer* 21.2 (1978), pp. 251–253.

[106] V. Giovangigli and M. D. Smooke. "Extinction of Strained Premixed Laminar Flames With Complex Chemistry". *Combustion Science and Technology* 53.1 (1987), pp. 23–49.

[107] S. Dasappa and J. Camacho. “Formation of nanocrystalline manganese oxide in flames: oxide phase governed by classical nucleation and size-dependent equilibria”. *CrystEngComm* 22 (2020), pp. 5509–5521.

[108] Y. Wang, A. Raj, and S. H. Chung. “A PAH growth mechanism and synergistic effect on PAH formation in counterflow diffusion flames”. *Combustion and Flame* 160.9 (2013), pp. 1667–1676.

[109] M. Frenklach and J. Warnatz. “Detailed Modeling of PAH Profiles in a Sooting Low-Pressure Acetylene Flame”. *Combustion Science and Technology* 51.4-6 (1987), pp. 265–283.

[110] J. Simonsson, N. E. Olofsson, S. Török, P. E. Bengtsson, and H. Bladh. “Wavelength dependence of extinction in sooting flat premixed flames in the visible and near-infrared regimes”. *Applied Physics B: Lasers and Optics* 119.4 (2015), pp. 657–667.

[111] K. Gleason, F. Carbone, and A. Gomez. “Pressure and temperature dependence of soot in highly controlled counterflow ethylene diffusion flames”. *Proceedings of the Combustion Institute* 37.2 (2019), pp. 2057–2064.

[112] A. C. Ferrari and D. M. Basko. “Raman spectroscopy as a versatile tool for studying the properties of graphene”. *Nature Nanotechnology* 8.4 (2013), pp. 235–246.

[113] C. V. Raman and K. S. Krishnan. “A new type of secondary radiation [11]”. *Nature* 121.3048 (1928), pp. 501–502.

[114] R. Beams, L. Gustavo Cançado, and L. Novotny. “Raman characterization of defects and dopants in graphene”. *Journal of Physics Condensed Matter* 27.8 (2015).

[115] M. S. Dresselhaus, A. Jorio, A. G. Souza Filho, and R. Saito. “Defect characterization in graphene and carbon nanotubes using Raman spectroscopy”. *Philosophical Transactions of the Royal Society A: Mathematical, Physical and Engineering Sciences* 368.1932 (2010), pp. 5355–5377.

[116] I. Pócsik, M. Hundhausen, M. Koós, and L. Ley. “Origin of the D peak in the Raman spectrum of microcrystalline graphite”. *Journal of Non-Crystalline Solids* 227-230.PART 2 (1998), pp. 1083–1086.

[117] L. G. Cançado, A. Jorio, and M. A. Pimenta. “Measuring the absolute Raman cross section of nanographites as a function of laser energy and crystallite size”. *Physical Review B - Condensed Matter and Materials Physics* 76.6 (2007).

[118] P.Lespade, R.Al-Jishi, and M.S.Dresselhaus. “Model for Raman scattering from incompletely graphitized carbons”. *Carbon* 20.5 (1982), pp. 427–431.

[119] M. A. Pimenta, G. Dresselhaus, M. S. Dresselhaus, L. G. Cançado, A. Jorio, and R. Saito. “Studying disorder in graphite-based systems by Raman spectroscopy”. *Physical Chemistry Chemical Physics* 9.11 (2007), pp. 1276–1291.

[120] M. S. Dresselhaus and G. Dresselhaus. “Intercalation compounds of graphite”. *Advances in Physics* 51.1 (2002), pp. 1–186.

[121] F. Tuinstra and J. L. Koenig. “Raman Spectrum of Graphite”. *The Journal of Chemical Physics* 53.3 (1970), pp. 1126–1130.

[122] L. G. Caŋado, K. Takai, T. Enoki, M. Endo, Y. A. Kim, H. Mizusaki, A. Jorio, L. N. Coelho, R. Magalhães-Paniago, and M. A. Pimenta. “General equation for the determination of the crystallite size la of nanographite by Raman spectroscopy”. *Applied Physics Letters* 88.16 (2006), pp. 12–14.

[123] M. M. Lucchese, F. Stavale, E. H. Ferreira, C. Vilani, M. V. Moutinho, R. B. Capaz, C. A. Achete, and A. Jorio. “Quantifying ion-induced defects and Raman relaxation length in graphene”. *Carbon* 48.5 (2010), pp. 1592–1597.

[124] E. Henrique, M. Ferreira, M. Moutinho, and R. B. Capaz. “Evolution of the Raman Spectra From Single- , Few- , and Many-Layer Graphene With Increasing Disorder”. June 2014 (2010).

[125] L. G. Cançado, A. Jorio, E. H. Ferreira, F. Stavale, C. A. Achete, R. B. Capaz, M. V. Moutinho, A. Lombardo, T. S. Kulmala, and A. C. Ferrari. “Quantifying defects in graphene via Raman spectroscopy at different excitation energies”. *Nano Letters* 11.8 (2011), pp. 3190–3196.

[126] H. Marsh. “A tribute to Philip L. Walker”. *Carbon* 29.6 (1991), pp. 703–704.

[127] I.C.Lewis. “Chemistry of carbonization”. *Carbon* 20.6 (1982), pp. 519–529.

[128] R. A. Dobbins, G. J. Govatzidakis, W. Lu, A. F. Schwartzman, and R. A. Fletcher. “Carbonization rate of soot precursor particles”. *Combustion Science and Technology* 121.1-6 (1996), pp. 103–121.

[129] E. F. Antunes, A. O. Lobo, E. J. Corat, V. J. Trava-Airoldi, A. A. Martin, and C. Veríssimo. “Comparative study of first- and second-order Raman spectra of MWCNT at visible and infrared laser excitation”. *Carbon* 44.11 (2006), pp. 2202–2211.

[130] H. Rosen and T. Novakov. “Identification of primary particulate carbon and sulfate species by Raman spectroscopy”. *Atmospheric Environment (1967)* 12.4 (1978), pp. 923–927.

[131] H. Rosen and T. Novakov. “Raman scattering and the characterisation of atmospheric aerosol particles [14]”. *Nature* 266.5604 (1977), pp. 708–710.

[132] N. F. Raman, S. B. Dippel, and J Heintzenberg. “Soot Characterization in Atmospheric Particles From Different Sources”. *l. Aerosol ScL* 30 (1999), pp. 907–908.

[133] L. M. Malard, M. A. Pimenta, G. Dresselhaus, and M. S. Dresselhaus. “Raman spectroscopy in graphene”. *Physics Reports* 473.5-6 (2009), pp. 51–87.

[134] A. Eckmann, A. Felten, I. Verzhbitskiy, R. Davey, and C. Casiraghi. “Raman study on defective graphene: Effect of the excitation energy, type, and amount of defects”. *Physical Review B - Condensed Matter and Materials Physics* 88.3 (2013), pp. 1–11.

[135] A. Das, B. Chakraborty, and A. K. Sood. “Raman spectroscopy of graphene on different substrates and influence of defects”. *Bulletin of Materials Science* 31.3 (2008), pp. 579–584.

[136] S. T. Jackson and R. G. Nuzzo. “Determining hybridization differences for amorphous carbon from the XPS C 1s envelope”. *Applied Surface Science* 90.2 (1995), pp. 195–203.

[137] A. Fujimoto, Y. Yamada, M. Koinuma, and S. Sato. “Origins of sp3C peaks in C1s X-ray Photoelectron Spectra of Carbon Materials”. *Analytical Chemistry* 88.12 (2016), pp. 6110–6114.

[138] B. Lesiak, L. Kövér, J. Tóth, J. Zemek, P. Jiricek, A. Kromka, and N. Rangam. “C sp 2 /sp 3 hybridisations in carbon nanomaterials – XPS and (X)AES study”. *Applied Surface Science* 452 (2018), pp. 223–231.

[139] W. Wei, X. Cui, W. Chen, and D. G. Ivey. “Manganese oxide-based materials as electrochemical supercapacitor electrodes”. *Chemical Society Reviews* 40.3 (2011), pp. 1697–1721.

[140] M. M. Thackeray, C. S. Johnson, J. T. Vaughey, N. Li, and S. A. Hackney. “Advances in manganese-oxide ’composite’ electrodes for lithium-ion batteries”. *Journal of Materials Chemistry* 15.23 (2005), pp. 2257–2267.

[141] J. Shin, R. M. Anisur, M. K. Ko, G. H. Im, J. H. Lee, and I. S. Lee. “Hollow manganese oxide nanoparticles as multifunctional agents for magnetic resonance imaging and drug delivery”. *Angewandte Chemie - International Edition* 48.2 (2009), pp. 321–324.

[142] K. M. Taylor, W. J. Rieter, and W. Lin. “Manganese-based nanoscale metal-organic frameworks for magnetic resonance imaging”. *Journal of the American Chemical Society* 130.44 (2008), pp. 14358–14359.

[143] C. Liu, J. W. Shi, C. Gao, and C. Niu. “Manganese oxide-based catalysts for low-temperature selective catalytic reduction of NOx with NH3: A review”. *Applied Catalysis A: General* 522 (2016), pp. 54–69.

[144] B. Shen, T. Liu, N. Zhao, X. Yang, and L. Deng. “Iron-doped Mn-Ce/TiO2 catalyst for low temperature selective catalytic reduction of NO with NH3”. *Journal of Environmental Sciences* 22.9 (2010), pp. 1447–1454.

[145] M. Wiechen, M. M. Najafpour, S. I. Allakhverdiev, and L. Spiccia. “Water oxidation catalysis by manganese oxides: Learning from evolution”. *Energy and Environmental Science* 7.7 (2014), pp. 2203–2212.

[146] C. S. Lindberg, M. Y. Manuputty, P. Buerger, J. Akroyd, and M. Kraft. “Numerical simulation and parametric sensitivity study of titanium dioxide particles synthesised in a stagnation flame”. *Journal of Aerosol Science* 138.August (2019), p. 105451.

[147] C. Houtman, D. B. Graves, and K. F. Jensen. “CVD in Stagnation Point Flow: An Evaluation of the Classical 1D Treatment”. *Journal of The Electrochemical Society* 133.5 (1986), pp. 961–970.

[148] H. Zhang and J. F. Banfield. “Thermodynamic analysis of phase stability of nanocrystalline titania”. *Journal of Materials Chemistry* 8.9 (1998), pp. 2073–2076.

[149] V. Bayer, C. Franchini, and R. Podloucky. “Ab initio study of the structural, electronic, and magnetic properties of MnO(100) and MnO(110)”. *Physical Review B - Condensed Matter and Materials Physics* 75.3 (2007), pp. 1–9.

[150] N. Birkner and A. Navrotsky. “Thermodynamics of manganese oxides: Effects of particle size and hydration on oxidation-reduction equilibria among hausmannite, bixbyite, and pyrolusite”. *American Mineralogist* 97.8-9 (2012), pp. 1291–1298.

[151] J. M. Bergthorson, D. Goodwin, and P. Dimotakis. “Experiments and Modeling of Impinging Jets and Premixed (Article)”. *Office* 2005.December (2005), pp. 5–8.

[152] I. Wlokas, A. Faccinetto, B. Tribalet, C. Schulz, and A. Kempf. “Mechanism of iron oxide formation from iron pentacarbonyl-doped low-pressure hydrogen/oxygen flames”. *International Journal of Chemical Kinetics* 45.8 (2013), pp. 487–498.

[153] J. Z. Wen, C. F. Goldsmith, R. W. Ashcraft, and W. H. Green. “Detailed kinetic modeling of iron nanoparticle synthesis from the decomposition of Fe(CO)5”. *Journal of Physical Chemistry C* 111.15 (2007), pp. 5677–5688.

[154] A. Navrotsky, C. Ma, K. Lilova, and N. Birkner. “Nanophase transition metal oxides show large thermodynamically driven shifts in oxidation-reduction equilibria”. *Science* 330.6001 (2010), pp. 199–201.

[155] V. Mittal, H. Pitsch, and F. Egolfopoulos. “Assessment of counterflow to measure laminar burning velocities using direct numerical simulations”. *Combustion Theory and Modelling* 16.3 (2012), pp. 419–433.

[156] U. Niemann, K. Seshadri, and F. A. Williams. "Accuracies of laminar counterflow flame experiments". *Combustion and Flame* 162.4 (2015), pp. 1540–1549.

[157] R. F. Johnson, A. C. Vandine, G. L. Esposito, and H. K. Chelliah. "On the axisymmetric counterflow flame simulations: Is there an optimal nozzle diameter and separation distance to apply quasi one-dimensional theory?" *Combustion Science and Technology* 187.1-2 (2015), pp. 37–59.

[158] T. Yuan, Y.-h. Lai, and C.-k. Chang. "Numerical studies of heterogeneous reaction in stagnation flows using one-dimensional and two-dimensional Cartesian models". 154 (2008), pp. 557–568.

[159] N. Bouvet, D. Davidenko, C. Chauveau, L. Pillier, and Y. Yoon. "On the simulation of laminar strained flames in stagnation flows : 1D and 2D approaches versus experiments". *Combustion and Flame* 161.2 (2014), pp. 438–452.

[160] Y. Xiong and S. E. Pratsinis. "Gas phase production of particles in reactive turbulent flows". *Journal of Aerosol Science* 22.5 (1991), pp. 637–655.

[161] T. T. Kodas and M. J. Hampden Smith. *Aerosol Processing of Materials*. Ed. by Wiley-VCH. 1991.

[162] S. Kluge, L. Deng, O. Feroughi, F. Schneider, M. Poliak, A. Fomin, V. Tsionsky, S. Cheskis, I. Wlokas, I. Rahinov, T. Dreier, A. Kempf, H. Wiggers, and C. Schulz. "Initial reaction steps during flame synthesis of iron-oxide nanoparticles". *CrystEngComm* 17.36 (2015), pp. 6930–6939.

[163] S. K. Friedlander. *Smoke, Dust, and Haze: Fundamentals of Aerosol Behavior*. New York: Oxford University Press, 2000.

[164] F. Buciuman, F. Patcas, R. Craciun, and D. R. Zahn. "Vibrational spectroscopy of bulk and supported manganese oxides". *Physical Chemistry Chemical Physics* 1.1 (1999), pp. 185–190.

[165] C. Julien, M. Massot, S. Rangan, M. Lemal, and D. Guyomard. "Study of structural defects in γ-MnO2 by Raman spectroscopy". *Journal of Raman Spectroscopy* 33.4 (2002), pp. 223–228.

[166] E. D. Tolmachoff, A. D. Abid, D. J. Phares, C. S. Campbell, and H. Wang. "Synthesis of nano-phase TiO2 crystalline films over premixed stagnation flames". *Proceedings of the Combustion Institute* 32 II.November 2018 (2009), pp. 1839–1845.

[167] G. K. Burgess and R. G. Waltenberg. "The Emissivity of Metals and Oxides". *Physical Review Letters* 4 (1914), pp. 546–547.

[168] O. I. Arabi-Katbi, S. E. Pratsinis, P. W. Morrison, and C. M. Megaridis. "Monitoring the flame synthesis of TiO2 particles by in-situ FTIR spectroscopy and thermophoretic sampling". *Combustion and Flame* 124.4 (2001), pp. 560–572.

[169] G. T. Linteris, V. Knyazev, and V. Babushok. "PREMIXED FLAME INHIBITION BY MANGANESE AND TIN COMPOUNDS". April (2001).

[170] G. T. Linteris, V. D. Knyazev, and V. I. Babushok. "Inhibition of premixed methane flames by manganese and tin compounds". *Combustion and Flame* 129.3 (2002), pp. 221–238.

[171] U. Westblom, F. Fernandez Alonso, C. R. Mahon, G. P. Smith, J. B. Jeffries, and D. R. Crosley. "Laser-induced fluorescence diagnostics of a propane/air flame with a manganese fuel additive". *Combustion and Flame* 99.2 (1994), pp. 261–268.

[172] D. L. Hildenbrand and K. H. Lau. "Thermochemistry of gaseous manganese oxides and hydroxides". *The Journal of Chemical Physics* 100.11 (1994), pp. 8377–8380.

[173] A. Matraszek, M. Miller, L. Singheiser, and K. Hilpert. "Thermodynamic vaporization studies of the manganese oxide-yttria stabilized zirconia (YSZ) solid solution". *Journal of the European Ceramic Society* 24.9 (2004), pp. 2649–2656.

[174] N. A Fuchs. *Mechanics of Aerosols*. Pergamon, 1964.

[175] A. G. Gaydon and H. G. Wolfhard. *Flames: Their Structure, Radiation, and Temperature*. Chapman & Hall, 1979.

[176] J. Kojima, Y. Ikeda, and T. Nakajima. "Spatially resolved measurement of OH, CH, and C2 chemiluminescence in the reaction zone of laminar methane/air premixed flames". *Proceedings of the Combustion Institute* 28.2 (2000), pp. 1757–1764.

[177] C. Saggese, A. Cuoci, A. Frassoldati, S. Ferrario, J. Camacho, H. Wang, and T. Faravelli. "Probe effects in soot sampling from a burner-stabilized stagnation flame". *Combustion and Flame* 167 (2016), pp. 184–197.

[178] B. Zhao, Z. Yang, J. Wang, M. V. Johnston, and H. Wang. "Analysis of soot nanoparticles in a laminar premixed ethylene flame by scanning mobility particle sizer". *Aerosol Science and Technology* 37.8 (2003), pp. 611–620.

[179] Meng-Jiao Wang, C. A. Gray, S. A. Reznek, K. Mahmud, and Y. Kutsovsky. *Carbon Black*.

[180] F. C. Lockwood and J. E. Van Niekerk. "Parametric study of a carbon black oil furnace". *Combustion and Flame* 103.1-2 (1995), pp. 76–90.

[181] A. Javadi, M. Soltanieh, S. Sahebdelfar, D. Bastani, and K. Javadi. "Estimation of temperature and residence time of carbon black oil furnace industrial reactors".

Proceedings of 2006 ASME International Mechanical Engineering Congress and Exposition, IMECE2006 - Process Industries July 2016 (2006).

[182] A. Naseri and M. J. Thomson. “Development of a numerical model to simulate carbon black synthesis and predict the aggregate structure in flow reactors”. *Combustion and Flame* 207 (2019), pp. 314–326.

[183] M. Balthasar, F. Mauss, A. Knobel, and M. Kraft. “Detailed modeling of soot formation in a partially stirred plug flow reactor”. *Combustion and Flame* 128.4 (2002), pp. 395–409.

[184] K. Ono, M. Yanaka, S. Tanaka, Y. Saito, H. Aoki, O. Fukuda, T. Aoki, and T. Yamaguchi. “Influence of furnace temperature and residence time on configurations of carbon black”. *Chemical Engineering Journal* 200-202 (2012), pp. 541–548.

[185] G. Skillas, C. Becker, H. Mühlenweg, and J. Behnisch. “Simulation of particulates in a carbon black reactor”. *Journal of Nanoparticle Research* 7.1 (2005), pp. 15–27.

[186] F. A. Ishola, A. O. Inegbenebor, and F. A. Oyawale. “Thermal Modelling for A Pilot Scale Pyrolytic Furnace for Production of Carbon Black”. *Journal of Physics: Conference Series* 1378.3 (2019).

[187] F. Schneider, S. Suleiman, J. Menser, E. Borukhovich, I. Wlokas, A. Kempf, H. Wiggers, and C. Schulz. “SpraySyn-A standardized burner configuration for nanoparticle synthesis in spray flames”. *Review of Scientific Instruments* 90.8 (2019).

[188] R. Mueller, L. Mädler, and S. E. Pratsinis. “Nanoparticle synthesis at high production rates by flame spray pyrolysis”. *Chemical Engineering Science* 58.10 (2003), pp. 1969–1976.

[189] W. Y. Teoh, R. Amal, and L. Mädler. “Flame spray pyrolysis: An enabling technology for nanoparticles design and fabrication”. *Nanoscale* 2.8 (2010), pp. 1324–1347.

[190] L. Mädler, A. A. Lall, and S. K. Friedlander. “One-step aerosol synthesis of nanoparticle agglomerate films: Simulation of film porosity and thickness”. *Nanotechnology* 17.19 (2006), pp. 4783–4795.

[191] Koppers. *Coal Tar Distillate, Safety Data Sheet.* Tech. rep. 2020.

[192] S. Dasappa and J. Camacho. “Thermodynamic Barrier to Nucleation for Manganese Oxide Nanoparticles Synthesized by High-Temperature Gas-to-Particle Conversion”. *Energy and Fuels* 35.2 (2021), pp. 1874–1884.

[193] J. H. Kint. “A noncatalytic coating for platinum-rhodium thermocouples”. *Combustion and Flame* 14.2 (1970), pp. 279–281.

[194] C. R. Shaddix. “Correcting thermocouple measurements for radiation loss: A critical review”. *National Heat Transfer Conference*. 1999.

[195] S. Dasappa and J. Camacho. “Fuel molecular structure effect on soot mobility size in premixed C6 hydrocarbon flames”. *Fuel* 300.January (2021), p. 120973.

[196] P. B. Kuhn, B. Ma, B. C. Connelly, M. D. Smooke, and M. B. Long. “Soot and thin-filament pyrometry using a color digital camera”. *Proceedings of the Combustion Institute* 33.1 (2011), pp. 743–750.

[197] L. C. Nistor, J. Van Landuyt, V. G. Ralchenko, T. V. Kononenko, E. D. Obraztsova, and V. E. Strelnitsky. “Direct observation of laser-induced crystallization of a-C:H films”. *Applied Physics A Solids and Surfaces* 58.2 (1994), pp. 137–144.

[198] T. Jawhari, A. Roid, and J. Casado. “Raman spectroscopic characterization of some commercially available carbon black materials”. *Carbon* 33.11 (1995), pp. 1561–1565.

[199] J. Pan, J. A. Libera, N. H. Paulson, and M. Stan. “Flame stability analysis of flame spray pyrolysis by artificial intelligence”. *International Journal of Advanced Manufacturing Technology* 114.7-8 (2021), pp. 2215–2228.

[200] T. O’Haver. *https://terpconnect.umd.edu/˜toh/spectrum/*.

[201] A. G. Gaydon. *The Spectroscopy of Flames*. Second. Chapman & Hall, 1974.

[202] M. A. Catalan, W. F. Meggers, and O. Garcia-Riquelme. “The first spectrum of manganese, Mn I”. *Journal of Research of the National Bureau of Standards Section A: Physics and Chemistry* 68A.1 (1964), p. 9.

[203] H. P. Broida. “Rotational and vibrational ”temperatures” of CH in flames at atmospheric pressure”. *The Journal of Chemical Physics* 21.2 (1953), pp. 340–346.

[204] V. I. Perminov, A. I. Semenov, and N. N. Shefov. “On rotational temperature of the hydroxyl emission”. *Geomagnetism and Aeronomy* 47.6 (2007), pp. 756–763.

[205] R. Zaplotnik, G. Primc, and A. Vesel. “Optical emission spectroscopy as a diagnostic tool for characterization of atmospheric plasma jets”. *Applied Sciences (Switzerland)* 11.5 (2021), pp. 1–22.

[206] E. Goudeli, A. J. Gröhn, and S. E. Pratsinis. “Sampling and dilution of nanoparticles at high temperature”. *Aerosol Science and Technology* 50.6 (2016), pp. 591–604.

[207] J. S. Kim and M. A. Cappelli. “Temperature measurements in low-pressure, diamond-forming, premixed flames”. *Journal of Applied Physics* 84.8 (1998), pp. 4595–4602.

[208] Y. Wang, J. Fang, M. Attoui, T. S. Chadha, W. N. Wang, and P. Biswas. “Application of Half Mini DMA for sub 2nm particle size distribution measurement in

an electrospray and a flame aerosol reactor". *Journal of Aerosol Science* 71 (2014), pp. 52–64.

[209] S. Dasappa and J. Camacho. "Raman spectroscopy, mobility size and radiative emissions data for soot formed at increasing temperature and equivalence ratio in flames hotter than conventional combustion applications". *Data in Brief* 36 (2021), p. 107064.

[210] T. Schlebrowski, L. Beucher, H. Bazzi, B. Hahn, S. Wehner, and C. B. Fischer. "Changing Contents of Carbon Hybridizations in Amorphous Hydrogenated Carbon Layers (a-C:H) on Sustainable Polyhydroxybutyrate (PHB) Exhibit a Significant Deterioration in Stability, Depending on Thickness". *C — Journal of Carbon Research* 5.3 (2019), p. 52.

[211] E. K. Yapp, D. Chen, J. Akroyd, S. Mosbach, M. Kraft, J. Camacho, and H. Wang. "Numerical simulation and parametric sensitivity study of particle size distributions in a burner-stabilised stagnation flame". *Combustion and Flame* 162.6 (2015), pp. 2569–2581.

[212] S. Memarzadeh, E. D. Tolmachoff, D. J. Phares, and H. Wang. "Properties of nanocrystalline TiO2 synthesized in premixed flames stabilized on a rotating surface". *Proceedings of the Combustion Institute* 33.2 (2011), pp. 1917–1924.

[213] D. J. Morgan. "Comments on the XPS Analysis of Carbon Materials". *C* 7.3 (2021), p. 51.

[214] O. Orhan, E. Haffner-Staton, A. La Rocca, and M. Fay. "Characterisation of flame-generated soot and soot-in-oil using electron tomography volume reconstructions and comparison with traditional 2D-TEM measurements". *Tribology International* 104 (2016), pp. 272–284.

[215] A. J. Gröhn, S. E. Pratsinis, A. Sánchez-Ferrer, R. Mezzenga, and K. Wegner. "Scale-up of nanoparticle synthesis by flame spray pyrolysis: The high-temperature particle residence time". *Industrial and Engineering Chemistry Research* 53.26 (2014), pp. 10734–10742.

[216] N. K. Memon, S. D. Tse, J. F. Al-Sharab, H. Yamaguchi, A. M. B. Goncalves, B. H. Kear, Y. Jaluria, E. Y. Andrei, and M. Chhowal. "Flame synthesis of graphene films in open environments". *Carbon* 49.15 (2011), pp. 5064–5070.

[217] Y. Liang, K. Ku, Y. Lin, L. Yu, J. Wen, E. Lee, J. Libera, and J. Lu. "Process Engineering to Increase the Layered Phase Concentration in the Immediate Products of Flame Spray Pyrolysis". *ACS Applied Materials and Interfaces* 13.23 (2021), pp. 26915–26923.

[218] P. D. I. Milano. "Tesi di Dottorato di CHIARA SAGGESE Matricola 785658" (2014).

[219] T. P. Huelser, A. Lorke, P. Ifeacho, H. Wiggers, and C. Schulz. “Core and grain boundary sensitivity of tungsten-oxide sensor devices by molecular beam assisted particle deposition”. *Journal of Applied Physics* 102.12 (2007).

[220] M. Kang, E. D. Park, J. M. Kim, and J. E. Yie. “Manganese oxide catalysts for NOx reduction with NH3 at low temperatures”. *Applied Catalysis A: General* 327.2 (2007), pp. 261–269.

[221] M. Moghiman, N. Hosseini, M. H. Raad, and M. Javadi. “Experimental and numerical studies of carbon black formation through thermal decomposition of waste natural gas”. *ASME International Mechanical Engineering Congress and Exposition, Proceedings* 3.November (2009), pp. 239–245.

[222] R. L. Vander Wal and L. J. Hall. “Flame synthesis of Fe catalyzed single-walled carbon nanotubes and Ni catalyzed nanofibers: Growth mechanisms and consequences”. *Chemical Physics Letters* 349.3-4 (2001), pp. 178–184.

[223] N. G. Glumac and D. G. Goodwin. “Large-area diamond film growth in a low-pressure flame”. *Materials Letters* 18.3 (1993), pp. 119–122.

[224] B. C. Connelly, S. A. Kaiser, M. D. Smooke, and M. B. Long. “Two-Dimensional Soot Pyrometry with a Color Digital Camera”. *Joint Meeting of the U.S. Sections of the combustion Insitiute* 2.3 (2005).

[225] A. D’Anna. “Combustion-formed nanoparticles”. *Proceedings of the Combustion Institute* 32 I.1 (2009), pp. 593–613.

[226] F. Liu, W. Wang, W. Zheng, and Y. Wang. “Investigation of spatially resolved spectra of OH and N2+ in N2 and H2O mixture wire-plate positive pulsed streamer discharge”. *Spectrochimica Acta - Part A: Molecular and Biomolecular Spectroscopy* 69.3 (2008), pp. 776–781.

[227] J. S. Lee, M. H. Oh, P. Kumar, A. Khanna, R. K. Singh, and M. B. Ranade. “Mn-doped Zn 2SiO 4 phosphors synthesis using flame spray pyrolysis”. *Journal of Thermal Spray Technology* 20.5 (2011), pp. 1001–1008.

[228] G. Yasin, M. A. Khan, W. Q. Khan, T. Mehtab, R. M. Korai, X. Lu, M. T. Nazir, and M. N. Zahid. “Facile and large-scalable synthesis of low cost hard carbon anode for sodium-ion batteries”. *Results in Physics* 14.June (2019), p. 102404.

[229] K. H. Ahn, S. H. Sohn, C. H. Jung, and M. Choi. “In situ measurement of nano particle size distribution and charge characteristics in H2/O2/TEOS diffusion flame”. *Scripta Materialia* 44.8-9 (2001), pp. 1889–1892.

[230] S. Wang and K. Komvopoulos. “Structure evolution during deposition and thermal annealing of amorphous carbon ultrathin films investigated by molecular dynamics simulations”. *Scientific Reports* 10.1 (2020).

[231] M. Solakidou, Y. Georgiou, and Y. Deligiannakis. “Double-nozzle flame spray pyrolysis as a potent technology to engineer noble metal-TiO2 nanophotocatalysts for efficient H2 production”. *Energies* 14.4 (2021).

[232] H. W. Huang and Y. Zhang. “Flame colour characterization in the visible and infrared spectrum using a digital camera and image processing”. *Measurement Science and Technology* 19.8 (2008).

[233] T. R. Melton, F. Inal, and S. M. Senkan. “The effects of equivalence ratio on the formation of polycyclic aromatic hydrocarbons and soot in premixed ethane flames”. *Combustion and Flame* 121.4 (2000), pp. 671–678.

[234] A. Abid, G. Smith, M. Krause, A. Yin, and C. Sungail. “Gas phase sodium flame synthesis of non-oxide metallic powders”. *TechConnect Briefs 2018 - Advanced Materials* 1 (2018), pp. 74–77.

[235] N. Mironova-Ulmane, A. Kuzmin, V. Skvortsova, G. Chikvaidze, I. Sildos, J. Grabis, D. Jankoviča, A. Dindune, and M. Maiorov. “Synthesis and vibration spectroscopy of nano-sized manganese oxides”. *Acta Physica Polonica A* 133.4 (2018), pp. 1013–1016.

[236] J. Heinze, U. Meier, T. Behrendt, C. Willert, K. P. Geigle, O. Lammel, and R. Lückerath. “PLIF thermometry based on measurements of absolute concentrations of the OH radical”. *Zeitschrift fur Physikalische Chemie* 225.11-12 (2011), pp. 1315–1341.

[237] N.AFuchs and A.G Sutugin. “Coagulation rate of highly dispersed aerosols”. *Journal of Colloid Science* 20.6 (1964), pp. 492–500.

[238] C. Russo and A. Ciajolo. “Effect of the flame environment on soot nanostructure inferred by Raman spectroscopy at different excitation wavelengths”. *Combustion and Flame* 162.6 (2015), pp. 2431–2441.

[239] N. Wagner, A. M. Svensson, and F. Vullum-Bruer. “ Liquid-feed flame spray pyrolysis as alternative synthesis for electrochemically active nano-sized Li 2 MnSiO 4 ”. *Translational Materials Research* 3.2 (2016), p. 025001.

[240] G. De Falco, M. Commodo, M. Barra, F. Chiarella, A. D’Anna, A. Aloisio, A. Cassinese, and P. Minutolo. “Electrical characterization of flame-soot nanoparticle thin films”. *Synthetic Metals* 229.April (2017), pp. 89–99.

[241] Y. Wang, Z. Feng, W. Zhu, V. Gariépy, C. Gagnon, M. Provencher, D. Laul, R. Veillette, M. L. Trudeau, A. Guerfi, and K. Zaghib. “High capacity and high efficiency maple tree-biomass-derived hard carbon as an anode material for sodium-ion batteries”. *Materials* 11.8 (2018).

[242] G. A. Kelesidis, E. Goudeli, and S. E. Pratsinis. “Flame synthesis of functional nanostructured materials and devices: Surface growth and aggregation”. *Proceedings of the Combustion Institute* 36.1 (2017), pp. 29–50.

[243] Y. Liao, C. H. Li, Z. Y. Ye, C. Chang, G. Z. Wang, and R. C. Fang. "Analysis of optical emission spectroscopy in diamond chemical vapor deposition". *Diamond and Related Materials* 9.9 (2000), pp. 1716–1721.

[244] N. Cordonnier. "Scholar Commons Flame Spray Pyrolysis of Ce-Mn Solid Solutions for Catalytic Applications" (2019).

[245] A. Sadezky, H. Muckenhuber, H. Grothe, R. Niessner, and U. Pöschl. "Raman microspectroscopy of soot and related carbonaceous materials: Spectral analysis and structural information". *Carbon* 43.8 (2005), pp. 1731–1742.

[246] J. H. Bechtel and R. E. Teets. "Hydroxyl and its concentration profile in methane–air flames". *Applied Optics* 18.24 (1979), p. 4138.

[247] J. Jiang and A. Kucernak. "Electrochemical supercapacitor material based on manganese oxide: Preparation and characterization". *Electrochimica Acta* (2002).

[248] J. Kent. "A noncatalytic coating for platinum-rhodium thermocouples". *Combustion and Flame* 14 (1970), pp. 279–281.

[249] A. Eckmann, A. Felten, A. Mishchenko, L. Britnell, R. Krupke, K. S. Novoselov, and C. Casiraghi. "Probing the nature of defects in graphene by Raman spectroscopy". *Nano Letters* 12.8 (2012), pp. 3925–3930.

[250] O. M. Feroughi, S. Hardt, I. Wlokas, T. Hülser, H. Wiggers, T. Dreier, and C. Schulz. "Laser-based in situ measurement and simulation of gas-phase temperature and iron atom concentration in a pilot-plant nanoparticle synthesis reactor". *Proceedings of the Combustion Institute* 35.2 (2015), pp. 2299–2306.

[251] A. Münzer, L. Xiao, Y. H. Sehlleier, C. Schulz, and H. Wiggers. "All gas-phase synthesis of graphene: Characterization and its utilization for silicon-based lithium-ion batteries". *Electrochimica Acta* 272 (2018), pp. 52–59.

[252] L. G. Cançado, A. Jorio, E. H. Ferreira, F. Stavale, C. A. Achete, R. B. Capaz, M. V. Moutinho, A. Lombardo, T. S. Kulmala, and A. C. Ferrari. "Quantifying defects in graphene via Raman spectroscopy at different excitation energies". *Nano Letters* 11.8 (2011), pp. 3190–3196.

[253] J. Sellmann, I. Rahinov, S. Kluge, H. Jünger, A. Fomin, S. Cheskis, C. Schulz, H. Wiggers, A. Kempf, and I. Wlokas. "Detailed simulation of iron oxide nanoparticle forming flames: Buoyancy and probe effects". *Proceedings of the Combustion Institute* 37.1 (2019), pp. 1241–1248.

[254] Z. Li and H. Wang. "Thermophoretic force and velocity of nanoparticles in the free molecule regime". *Physical Review E - Statistical Physics, Plasmas, Fluids, and Related Interdisciplinary Topics* 70.2 (2004), p. 11.

[255] Z. Yin, A. Montello, W. R. Lempert, and I. V. Adamovich. “Measurements of temperature and Hydroxyl radical generation/decay in lean fuel-air mixtures excited by a repetitively pulsed nanosecond discharge”. *43rd AIAA Plasmadynamics and Lasers Conference 2012* 160 (2012), pp. 1594–1608.

[256] J. Camacho. “DEVELOPMENT OF A NOVEL HETEROGENEOUS FLOW REACTOR – SOOT FORMATION AND NANOPARTICLE CATALYSIS”. *Journal of Petrology* 369.1 (2013), pp. 1689–1699.

[257] F. Kapteijn, A. D. van Langeveld, J. A. Moulijn, A. Andreini, M. A. Vuurman, A. M. Turek, J. M. Jehng, and I. E. Wachs. “Alumina-supported manganese oxide catalysts. I. Characterization: Effect of precursor and loading”. *Journal of Catalysis* (1994).

[258] J. J. Chen, T. Zhang, M. Q. Zhang, Q. Y. Liu, X. N. Li, and S. G. He. “Size-Dependent Reactivity of Nano-Sized Neutral Manganese Oxide Clusters toward Ethylene”. *Chemistry - A European Journal* 23.62 (2017), pp. 15820–15826.

[259] A. Kaniyoor and S. Ramaprabhu. “A Raman spectroscopic investigation of graphite oxide derived graphene”. *AIP Advances* 2.3 (2012).

[260] C. De Martino, F. Demichelis, and A. Tagliaferro. “Determination of the sp3 sp2 ratio in a-C:H films by infrared spectrometry analysis”. *Diamond and Related Materials* 4.10 (1995), pp. 1210–1215.

[261] N. Zettervall. “Reduced chemical kinetic reaction mechanism for JP-10-air combustion”. *Energy and Fuels* 34.12 (2020), pp. 16624–16635.

[262] W. Li, G. V. Gibbs, and S. T. Oyama. *Mechanism of Ozone Decomposition on a Manganese Oxide Catalyst. 1. In Situ Raman Spectroscopy and Ab Initio Molecular Orbital Calculations*. Tech. rep. 1998.

[263] F. C. Tai, S. C. Lee, J. Chen, C. Wei, and S. H. Chang. “Multipeak fitting analysis of Raman spectra on DLCH film”. *Journal of Raman Spectroscopy* 40.8 (2009), pp. 1055–1059.

[264] M. Sokolowski, A. Sokolowska, A. Michalski, and B. Gokieli. “The ”in-flame-reaction” method for Al2O3 aerosol formation”. *Journal of Aerosol Science* 8.4 (1977).

[265] Puech, Kandara, Paredes, Moulin, Weiss-Hortala, Kundu, Ratel-Ramond, Plewa, Pellenq, and Monthioux. “Analyzing the Raman Spectra of Graphenic Carbon Materials from Kerogens to Nanotubes: What Type of Information Can Be Extracted from Defect Bands?” *C — Journal of Carbon Research* 5.4 (2019), p. 69.

[266] S. Dasappa and J. Camacho. “Evolution in size and structural order for incipient soot formed at flame temperatures greater than 2100 K”. *Fuel* 291.February (2021), p. 120196.

[267] K. J. Kadassery and D. C. Lacy. "Pentacarbonylmethylmanganese(i) as a synthon for Mn(i) pincer catalysts". *Dalton Transactions* 48.14 (2019), pp. 4467–4470.

[268] A. D. Abid, J. Camacho, D. A. Sheen, and H. Wang. "Evolution of soot particle size distribution function in burner-stabilized stagnation n-dodecane-oxygen-argon flames". *Energy and Fuels* 23.9 (2009), pp. 4286–4294.

[269] T. L. Zhao, Y. Xu, Y. H. Song, X. S. Li, J. L. Liu, J. B. Liu, and A. M. Zhu. "Determination of vibrational and rotational temperatures in a gliding arc discharge by using overlapped molecular emission spectra". *Journal of Physics D: Applied Physics* 46.34 (2013).

[270] J.-l. Liu, L.-z. Fan, and X. Qu. "Electrochimica Acta Low temperature hydrothermal synthesis of nano-sized manganese oxide for supercapacitors". *Electrochimica Acta* 66 (2012), pp. 302–305.

[271] Y. E. Zhu, H. Gu, Y. N. Chen, D. Yang, J. Wei, and Z. Zhou. "Hard carbon derived from corn straw piths as anode materials for sodium ion batteries". *Ionics* 24.4 (2018), pp. 1075–1081.

[272] M. Fahad, S. Ali, and Y. Iqbal. "Plasma diagnostics by optical emission spectroscopy on manganese ore in conjunction with XRD, XRF and SEM-EDS". *Plasma Science and Technology* 21.8 (2019).

[273] R. L. Axelbaum, D. P. Dufaux, C. A. Frey, and S. M. Sastry. "A Flame Process for Synthesis of Unagglomerated, Low-Oxygen Nanoparticles: Application to Ti and TIB2". *Metallurgical and Materials Transactions B: Process Metallurgy and Materials Processing Science* 28.6 (1997), pp. 1199–1211.

[274] F. Phillips, G. B. Burns, W. J. French, P. F. Williams, A. R. Klekociuk, and R. P. Lowe. "Determining rotational temperatures from the OH(8-3) band, and a comparison with OH(6-2) rotational temperatures at Davis, Antarctica". *Annales Geophysicae* 22.5 (2004), pp. 1549–1561.

[275] H. J. Seong and A. L. Boehman. "Evaluation of Raman parameters using visible Raman microscopy for soot oxidative reactivity". *Energy and Fuels* 27.3 (2013), pp. 1613–1624.

[276] T. S. Totton, A. J. Misquitta, and M. Kraft. "A quantitative study of the clustering of polycyclic aromatic hydrocarbons at high temperatures". *Physical Chemistry Chemical Physics* 14.12 (2012), pp. 4081–4094.

[277] F. Schulz, M. Commodo, K. Kaiser, G. De Falco, P. Minutolo, G. Meyer, A. D'Anna, and L. Gross. "Insights into incipient soot formation by atomic force microscopy". *Proceedings of the Combustion Institute* 37.1 (2019), pp. 885–892.

[278] G. Liu, H. Wang, N. Feng, L. Chen, J. Yu, J. Meng, F. Fang, L. Wang, H. Wan, and G. Guan. "Construction of substrate-dependent 3D structured MnO 2 catalysts for diesel soot elimination". *Applied Surface Science* (2019).

[279] M. Biswas, J. A. Libera, S. B. Darling, and J. W. Elam. "Polycaprolactone: A Promising Addition to the Sequential Infiltration Synthesis Polymer Family Identified through in Situ Infrared Spectroscopy". *ACS Applied Polymer Materials* 2.12 (2020), pp. 5501–5510.